1-1-2011

Analytical and experimental investigation of cracking in two-way reinforced concrete panels

Armin Ziari Shalmani
Ryerson University

ANALYTICAL AND EXPERIMENTAL INVESTIGATION OF CRACKING IN TWO-WAY REINFORCED CONCRETE PANELS

By

Armin Ziari Shalmani

M.A.Sc., Ryerson University, 2007

B.Sc., University of Tehran, 2004

A Dissertation

Presented to Ryerson University

in Partial Fulfillment of the

Requirements for the Degree of

Doctor of Philosophy

in the Program of

Civil Engineering

Toronto, Ontario, Canada, 2011

AUTHOR'S DECLARATION

I hereby declare that I am the sole author of this dissertation.

I authorize Ryerson University to lend this dissertation to other institution or individuals for the purpose of scholarly research.

_____
Armin Ziari Shalmani
September 2011

I further authorize Ryerson University to reproduce this dissertation by photocopying or by other means, in total or in part, at the request of other institution or individuals for the purpose of scholarly research.

_____
Armin Ziari Shalmani
September 2011

ANALYTICAL AND EXPERIMENTAL INVESTIGATION OF CRACKING IN TWO-WAY REINFORCED CONCRETE PANELS

Armin Ziari Shalmani, Doctor of Philosophy, 2011

Department of Civil Engineering
Ryerson University

ABSTRACT

In this study, the cracking behaviour of RC panels under a two-way loading condition is investigated analytically and experimentally. A modified FE bond layer model is introduced and shown to be much simpler to define, and yet, more accurate than perfect bond or link element bond models. FE analysis suggests a bi-linear curve for approximating the distribution of bond stresses at stabilized cracking. Several FE parametric studies are performed on a one-way tension member to obtain peak shear bond stresses, concrete tensile stresses due to internal restrained shrinkage, splitting tensile stresses caused by radial bond stresses, and the reduction in bond strength caused by longitudinal splitting cracks. The FE analysis of flexural beams suggests a new factor for estimation of the depth of effective tension area, which is defined through FE parametric study. In the experimental phase, three medium-scale RC panels are subjected to direct tension in one direction and bending in the perpendicular direction. The collected data consist of applied loads, steel and concrete stresses, crack propagation sequence, crack pattern, crack width, total elongation, and leakage observations. The crack pattern is mainly influenced by the shape of reinforcement mesh due to the presence of splitting tensile stresses. The formation of diagonal cracks depends on principal stresses that can be influenced by reinforcement ratio, ratio of loads in two directions, and clear concrete cover to bar diameter ratio. The bond strength is significantly weakened by the formation of orthogonal cracks along

reinforcing bars. The crack width is increased under repeated loading especially at the first cycle. Residual crack widths remain in place even after complete unloading. Observations indicate that the water leakage is influenced by the crack width gradient. Finally, it is shown that one-way crack prediction models underestimate the crack width of two-way panels. A new set of analytical equations is developed for the prediction of cracking load, minimum and maximum spacing of cracks, and maximum crack width in a two-way panel. These equations are shown to predict the cracking behaviour of the tested panels more accurately than any other previously proposed model.

ACKNOWLEDGMENTS

The author would like to express his sincere gratitude to his supervisor Dr. Reza Kianoush for having provided this great research opportunity. Without his continuous guidance, suggestions, and encouragements this study could not be accomplished. The author is also deeply grateful to the laboratory technical advisor, Nidal Jaalouk, for his kind assistance in conducting the experimental tests.

The financial support provided by Natural Sciences and Engineering Research of Canada (NSERC) in the forms of a Postgraduate Scholarship and a Research Grant are gratefully acknowledged.

DEDICATION

To

my parents

for their endless love and support in every step of my life

TABLE OF CONTENTS

CHAPTER 6 ANALYTICAL MODELING OF TWO-WAY CRACKS

LIST OF TABLES

LIST OF FIGURES

LIST OF APPENDICES

LIST OF SYMBOLS

a_{cr}	distance from the point considered to the surface of the nearest longitudinal bar
$a_{s,max}$	maximum size of aggregates
A_c	cross-sectional area
$A_{c,ef}$	effective tension area of concrete
$A_{c,efx}$	effective tension area of concrete for the section normal to direction x
A_{ctx}	effective stretched area of concrete in direction x
A_e	effective stretched area of concrete
A_s	area of tension reinforcement
$A_{s1,perbar}$	area of reinforcement in direction 1 per bar
$A_{s,\text{net}}$	net cross sectional area of steel ($A_{s,\text{gross}}$-A_{groove})
$A_{s,\text{gross}}$	gross cross sectional area of steel
A_{sx}	area of tension reinforcement in direction x
a'	distance from the compression face to the point at which the crack width is being calculated
b	section width
b_t	width of section at the centroid of tension steel
c_1	clear concrete cover to the nearest reinforcing bar in direction 1
c_c	clear concrete cover
$c_{c,eqx}$	equivalent clear concrete cover to the reinforcing bar in direction x
c_{cy}	clear concrete cover to the reinforcing bar in direction y
c_{min}	minimum cover to the tension reinforcement
d	effective depth of tension reinforcement
d_b	diameter of reinforcing bar
d_{b1}	diameter of the reinforcement in direction 1 (direction of the reinforcement closest to the concrete outer tensile fibre)
d_{bx}	diameter of the reinforcing bar in direction x
d_{by}	diameter of the reinforcing bar in direction y
d_c	damage variable in compressive stress/strain curve

d_c	concrete cover to the center of reinforcing bar
d_{c1}	distance from the concrete outer tensile fibre to the center of the reinforcing bar in direction 1
d_{cx}	concrete cover to the center of reinforcing bar in direction x
d_t	damage variable in tensile stress/strain curve
$d_{t,ef}$	depth of effective tension area
$d_{t,efx}$	depth of effective tension area of concrete for the section normal to direction x
$d'_{t,ef}$	partial depth of effective tension area
d_x	effective depth of reinforcement in direction x
E_s	modulus of elasticity of steel
$E_{s,\text{fictitious}}$	adjusted modulus of elasticity of steel
E_c	modulus of elasticity of concrete
E_{ci}	initial undamaged stiffness
f_{bb}	bearing stress
f_c'	compressive strength of concrete
$f_{cc,cube,14}$	cube compressive strength of concrete at 14 days
$f_{sp,cube,28}$	cube splitting tensile strength of concrete at 28 days
f_{ck}	characteristic compressive strength of concrete
f_{cm}	mean value of compressive strength of concrete
f_{ct}	tensile strength of concrete
$f_{ctm}(t)$	mean value of concrete tensile strength at time t
f_s	actual average service load steel stress level or 50% of the design yield strength
$f_{s,cr}$	steel stress at the crack
$f_{s,max}$	maximum allowed steel stress
G_f	fracture energy of concrete
G_{fo}	base value of fracture energy
G_I	grid index
h	over-all depth of the member
h_n	notional size of member
$I_{cr,tr}$	moment of inertia of the transformed cracked section
k_b	constant to account for the distribution and surface characteristics of bar for the bond stress
k_t	factor of effective tension area

k'_t	new factor of effective tension area
k'_{tx}	new factor of effective tension area for the section normal to direction x
kd	depth of neutral axis
kd_x	depth of neutral axis for the section normal to direction x
K	fracture coefficient
K_c	ratio of the second stress invariant on the tensile meridian to that on the compressive meridian at initial yield for any given value of the pressure invariant p such that the maximum principal stress is negative.
l	span length
l_F	span length in flexural direction
$l_{s,max}$	length over which slip occurs between steel and concrete in the vicinity of a crack (two times transmission length)
M_{max}	maximum bending moment at mid-span
N_r	cracking load
N_{rx}	stabilized cracking load for cracks normal to direction x
N_{sd}	tensile force in steel at crack
N_{sdx}	tensile force in steel in direction x at crack
p_s	perimeter of the cross section of steel reinforcing bar
P	center jack load
P_r	stabilized cracking load of flexural cracks (center jack load)
$\bar{p}$	hydrostatic pressure stress
$\bar{q}$	Mises equivalent effective stress
Q_{i1}	active steel ratio
RH	relative humidity of the ambient atmosphere
s	bar spacing
s_1	spacing of reinforcement in direction 1
s_2	spacing of the reinforcement in direction 2 perpendicular to direction 1
$s.w.$	self weight
s_x	spacing of reinforcing bars in direction x
s_y	spacing of reinforcing bars in direction y
S_{max}	maximum crack spacing
S_{min}	minimum crack spacing
S_{mx}	average crack spacing for cracks normal to direction x

S^{I}_{maxx}	maximum crack spacing at stabilized cracking for cracks normal to direction x assuming one-way loading condition
S^{I}_{minx}	minimum crack spacing for cracks normal to direction x assuming one-way loading condition
S^{II}_{maxx}	maximum crack spacing at stabilized cracking for cracks normal to direction x under two-way loading condition
S^{II}_{minx}	minimum crack spacing for cracks normal to direction x under two-way loading condition
t	age of concrete
t_s	age of concrete at the beginning of shrinkage
T	direct tension load (total of side jack loads)
T_r	stabilized cracking load of direct tension cracks (total of side jack loads)
T'	direct tension load (each side jack load)
T'_r	stabilized cracking load of direct tension cracks (each side jack load)
u	perimeter of the member in contact with atmosphere
u_t^{cr}	crack displacement
w	design surface crack width
w_c	stiffness recovery factor in compression
w_k	characteristic crack width
w_{maxx}	maximum crack width at stabilized cracking for cracks normal to direction x
w_t	stiffness recovery factor in tension
$w_{t,max}$	maximum crack width at tension face
y_{st}	distance from neutral axis to the level of tensile reinforcement
y_t	distance from neutral axis to tensile fibre
Z	crack control factor
α_e	modular ratio (E_s/E_c)
α_{sp}	peak shear bond stress reduction factor due to longitudinal splitting crack
β_b	average bond stress factor
β_e	empirical factor to assess average strain within $l_{s,max}$
β_g	crack width gradient factor (cover factor) (the ratio of distances to the neutral axis from the extreme tension fiber and from the centroid of the main reinforcement)
β_{gx}	crack width gradient factor for cracks normal to direction x
β_s	coefficient to describe the development of shrinkage with time

β_{sc}	coefficient related to the type of cement
β_{spy}	a factor accounting for the average splitting tensile stresses over the effective tension area caused by reinforcement in direction y
$\Delta\varepsilon_{sx}$	total variation of steel strain over transfer length $S^{II}_{maxx}/2$ for reinforcement in direction x
$\Delta\sigma$	variation of steel stress over the length Δx
Δx	finite length of steel reinforcing bar
ε_1	strain at the level considered ignoring the stiffening effect of the concrete in the tension zone
ε_2	strain due to the stiffening effect of concrete between cracks
ε_c	concrete total compressive strain
ε_{cEx}	concrete strain at the point of zero slip in direction x
ε_{cm}	average concrete strain within $l_{s,max}$
ε_{cmx}	average concrete strain within S^{II}_{maxx} in direction x
ε_{cs}	shrinkage strain (negative value)
ε_{cso}	notional shrinkage coefficient
ε_{cso}	base total shrinkage strain
$\varepsilon_{cs}(t,t_s)$	total shrinkage strain at time t
ε_m	average strain at the level where the cracking is being considered
ε_{s2}	steel strain at the crack
ε_{s2x}	steel strain at crack for reinforcement in direction x
$\varepsilon_{s,cr}$	steel strain at the crack
ε_{sE}	steel strain at the point of zero slip
ε_{sE1}	steel strain at the point of zero slip at pre-stabilized cracking
ε_{sm}	average steel strain within $l_{s,max}$
ε_{smx}	average steel strain within S^{II}_{maxx} for reinforcement in direction x
ε_{sr2}	steel strain at crack at the cracking load level
ε_t	concrete total tensile strain
ε^{el}_{0c}	undamaged elastic compressive strain
ε^{el}_{0t}	undamaged elastic tensile strain
ε^{in}_{c}	compressive inelastic strain

ε_c^{pl}	compressive equivalent plastic strain
ε_t^{cr}	cracking strain
ε_t^{pl}	tensile equivalent plastic strain
ϕ_s	diameter of reinforcing bar
γ_c	unit weight of concrete
ρ_s	reinforcement ratio (A_s/bd)
$\rho_{s,ef}$	effective reinforcement ratio ($A_s/A_{c,ef}$)
$\rho_{s,efx}$	effective reinforcement ratio in direction x
ρ_{sx}	reinforcement ratio for direction x
σ_{b0}	initial equibiaxial compressive yield stress
σ_c	concrete compressive stress
σ_{c0}	initial uniaxial compressive yield stress
σ_{cEx}	concrete stress at the point of zero slip in direction x
σ_{csox}	concrete stress in direction x due to internally restrained shrinkage based on a total shrinkage strain of 50 $\mu\varepsilon$
σ_{csx}	concrete tensile stress in direction x due to internally restrained shrinkage
σ_{s2}	steel stress at the crack
$\sigma_{s,cr}$	steel stress at the crack
σ_{sE}	steel stress at the point of zero slip
σ_{sE1}	steel stress at the point of zero slip at pre-stabilized cracking
σ_{spy}	average splitting tensile stress in the effective end region caused by reinforcement in direction y
σ_{sr2}	steel stress at crack at the cracking load level
σ_{sr2x}	steel stress at crack at cracking load level for reinforcement in direction x
$\sigma_{sy,crx}$	tensile stress in reinforcement in direction y when cracking occurs normal to direction x
σ_t	concrete tensile stress
τ_{bk}	lower fractile value of the average bond stress
$\tau(x)$	bond stress distribution function
τ_t	shear bond stress
$\tau_{t,ave}$	average shear bond stress

τ_{tp}	peak shear bond stress
$\tau_{t,peak}$	peak shear bond stress
$\tau_{tp,sp}$	peak shear bond stress in a tie member with longitudinal splitting crack
τ_{tpx}	peak bond stress for reinforcement in direction x
ψ	dilation angle measured in the p-q plane at high confining pressure
ϵ	flow potential eccentricity

CHAPTER 1

INTRODUCTION

1.1 General Remarks

Reinforced concrete (RC) is one of the most widely used materials in the construction industry. Aside from its numerous advantages, concrete is very weak in tension. The low tensile strength of the concrete results in the formation of cracks under very low tensile forces. The tensile reinforcement is basically placed in the concrete to carry tensile forces after concrete is cracked. The layout and the amount of tensile reinforcement can alter the final pattern and the width of cracks.

The relationship between the reinforcement and the cracking characteristics of RC structures has been the subject of numerous previous studies. Despite their considerable contributions to the conceptual understanding of the RC cracking behaviour, these studies have failed to deliver a unanimous approach for the prediction of the crack width. Furthermore, they have been focused primarily on simple one-way loading conditions, such as pure tension or pure bending, which are rare to occur in the actual structures.

The issue of concrete cracking is even more critical for infrastructures designed and operated under the serviceability limit states, such as gaseous or liquid containing tanks, nuclear power plants, etc. The prevention or control of cracks in these types of structures is extremely important, as cracks can be detrimental to the functionality and durability of these structures. The components of these structures are dominantly under two-way state of stresses, which is not properly reflected in the recommendations of the current crack control design codes.

Besides several improvements in the understanding of the one-way cracking phenomenon, this study will enhance the knowledge of the actual two-way cracking behaviour of the liquid containing tank wall under service loads. The outcome of this study will provide numerous advancements in the over-simplified crack control design methods currently practiced for two-way structural members. As a result, a more sophisticated approach will be in hand to design adequately safe and durable infrastructures, and hence, the losses imposed by inappropriate design procedures will be minimized.

1.2 Objectives and Scope

Most design codes neglect the bi-axial nature of the internal forces in RC liquid or gaseous containing structures. The integrity of these types of structures must remain intact throughout their service life and should not be compromised for simple design methods. For that reason, the control of two-way cracking should be properly reflected in their design procedure. This study is aimed to provide a more rational perspective and awareness of the actual cracking behaviour of these types of structures. Design recommendations can be drawn based on the outcome of this study. On the path to achieve this ultimate goal several objectives will be pursued, which are pointed out as follows,

- Reviewing previous experimental and analytical attempts on the prediction of one-way and two-way cracking behaviour especially those that are adopted by design codes.

- Experimentally investigating the cracking and leakage behaviour of RC panels under a two-way loading condition comparable to internal forces in the wall of a liquid containing tank, i.e. a direct tension in one direction and a bending moment in the perpendicular direction.

- Improving the modeling of the bond mechanism in the finite element (FE) analysis of RC structures, and evaluating the capability of FE method in predicting different aspects of cracking.

- Identifying the main parameters influencing the one-way and two-way cracking of RC elements, and formulating them using an improved and validated FE modelling technique.

- Developing a new crack prediction model for two-way structural components.

- Evaluating the accuracy of the proposed model against the experimental data and the other models available in the literature.

1.3 Layout of the Dissertation

Following this introduction Chapter, a literature review on the reinforced concrete cracking is presented in Chapter 2. Various parameters influencing the cracking are described through the one-way crack theory. A close attention is given to the understanding of the bond mechanism between the steel reinforcing bar and the surrounding concrete. A number of well-known crack prediction models, widely adopted by various design Codes, are also introduced. Several previous experimental and analytical studies on the two-way cracking behaviour of RC structures are also mentioned.

The one-way cracking is analytically investigated in Chapter 3. A nonlinear FE model based on the concrete fracture energy is introduced. Three different FE bond models are described and their efficiency is investigated. With the use of the verified FE model, several parametric studies are performed to determine the shear bond stress and the depth of the effective tension area of the concrete.

Chapter 4 reports on an experimental study of the two-way cracking phenomenon. Three medium-scale RC panels are tested under a two-way loading condition that would resemble the wall of a circular tank. The water leakage is also examined through a few selected cracks. The collected and post-processed data are thoroughly presented in Chapter 5. After further analysis of the experimental results, a number of new findings are pointed out that can help to improve the understanding of the two-way cracking phenomenon.

The two-way cracking is analytically investigated in Chapter 6. Several FE parametric studies are performed to estimate the internally restrained shrinkage stresses, the splitting tensile stresses caused by the transverse reinforcement, and the amount of damage to the bond strength due to the formation of the longitudinal splitting cracks. A new set of equations are developed to predict the cracking load, the minimum and the maximum spacing of cracks, and the maximum crack width in a two-way system. The accuracy of the proposed model is evaluated against some other crack prediction models using the experimental data of the tested panels.

Finally, a brief summary of the entire work of this study is given in Chapter 7. The outcomes and conclusions of this research are pointed out, and suggestions are made for future research.

CHAPTER 2

LITERATURE REVIEW

2.1 Introduction

The behaviour of concrete under tension is associated with cracking at a very low tensile stress. As a result, cracks can be commonly observed in any reinforced concrete structure even at the service load level. An excessive cracking or crack width can impair serviceability (reduction of stiffness, large deflections, risk of leakage, …), durability, and aesthetics of the structure. Usually, a limiting value for the maximum probable crack width is implicitly or explicitly used as the basis for the crack control recommendations of various design Codes. For instance, the maximum allowable crack widths recommended by ACI 350 (2006) for flexural cracks in environmental structures are 0.23 *mm* and 0.27 *mm* for severe and normal exposures, respectively. However, a limiting crack width of 0.1 mm is recommended by ACI 224R (2001) for water-retaining structures.

Cracking in reinforced concrete is a complex phenomenon, which is very difficult to predict if not impossible. The complexity and the randomness of cracking are stemmed from both a complicated interaction at the interface of the reinforcing bars and the surrounding concrete and the high inhomogeneity of the concrete material. For the prediction of such a random event, one should always consider a probability of a marginal discrepancy from the actual observations. Fortunately, for the purpose of designing a structure, only the highest or the lowest possible values of the crack related parameters are of significance. This makes the crack control an achievable goal as it is observed that these values can be calculated with a higher confidence.

The maximum crack width can be influenced by a number of parameters, such as, steel strain, bar diameter, bond condition, concrete cover, confining pressure, bar spacing, loading rate, loading duration, shrinkage strains, restraint condition, etc. Many attempts are undertaken by various researchers to formulate the cracking, however, a substantial disagreement can be observed between these various methods. This is partly due to the fact that incorporating all the influential parameters into one single crack prediction formula is just not feasible. As a result, the crack prediction models, especially the empirical models, are greatly influenced by the range of parameters considered in the development of that model.

The rise of tensile stresses in the concrete, and hence, the cracking can be from two major causes, namely, the restrained volumetric change and the external applied loads. The focus of this study will be on the prediction of cracks caused by the external applied loads in externally unrestrained members, nevertheless, any effect of the concrete shrinkage strains and the internal restraint due to the presence of the reinforcement will be considered. It is worth mentioning that, in an externally restrained member, the restrained volumetric change can increase the steel stress at the crack, and hence, the crack width. The same equations recommended here may be used for the prediction of the crack width in an externally restrained member if this raise in the steel stress is considered. However, the calculation of these steel stresses caused by the externally restrained volumetric change is not in the scope of this study.

The mechanism of cracking and the influential parameters are explained in this Chapter. A brief review of a number of well-known crack prediction models widely used in various design standards is also presented. Most of these models are based on the cracking behaviour of one-way members. As of to date, no distinguished method of crack control for two-way members is adopted by any design Code. This is because a very limited number of studies are available in the literature regarding the cracking of two-way members. The main goal of this study is to improve the understanding of two-way cracking through both experimental and analytical techniques.

2.2 One-Way Cracking Theory

A reinforced concrete tie element with a single embedded rebar under concentric tension is the simplest structural component that can be used to investigate the cracking. Such an element with a circular section is shown in Fig. 2.1. The tie element can be subjected to tension by pulling the extruded reinforcing bar at both ends. Such an element not only represents the RC elements under direct tension, but also, it can represent the tension chord between two consecutive flexural cracks.

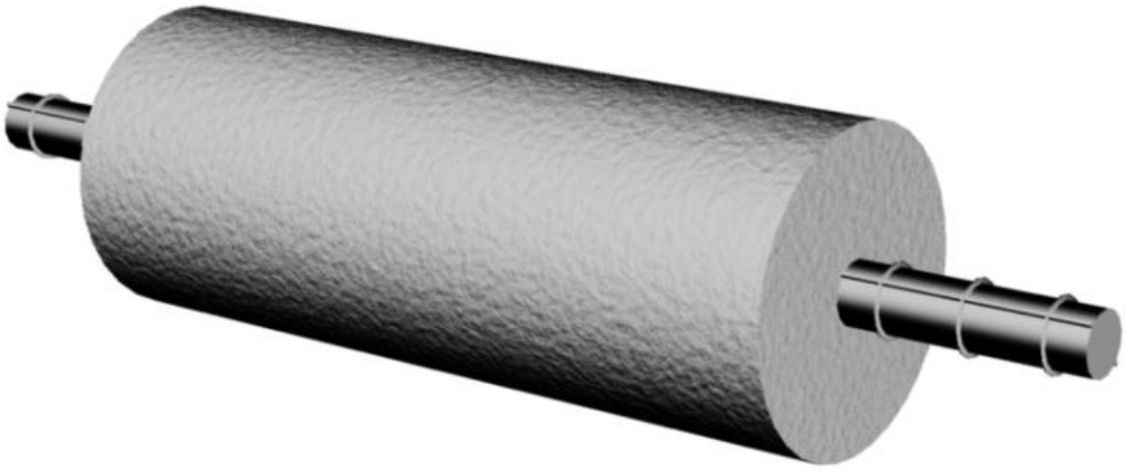

Fig. 2.1 Cylindrical tie element

Once the pulling force is applied, it will transfer from the reinforcing bar to the surrounding concrete through the bond stresses. The strain distribution along the RC element at various stages of loading is shown in Fig. 2.2. This is a simplified model that has been widely used to predict the cracking behaviour. This model will be explained here with reference to the CEB-FIP MC90 (1990). Understanding the underlying concept of this model is helpful in recognizing the importance of various parameters involved in the formation of cracks.

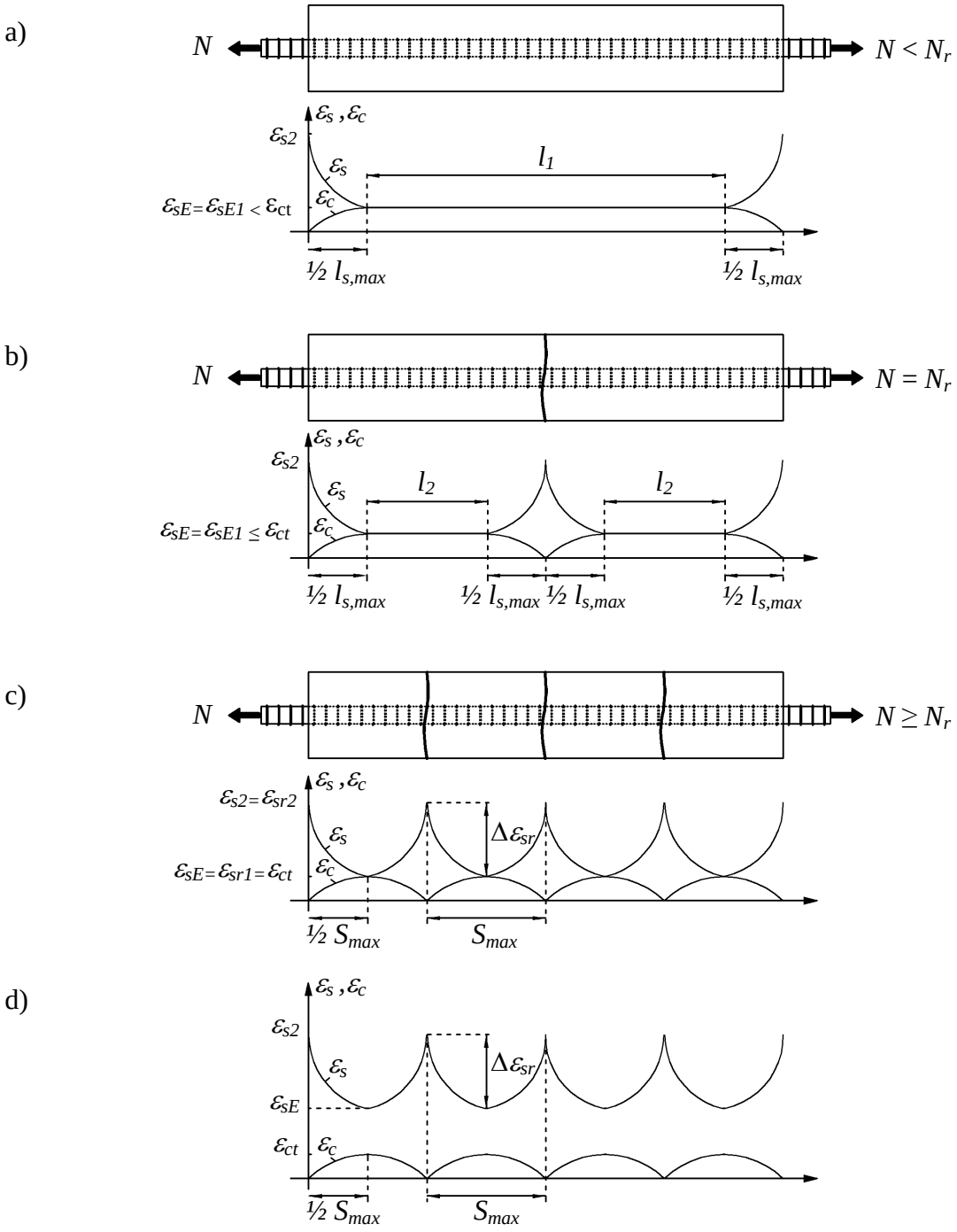

Fig. 2.2 Strain distribution in a RC tie element, a) prior to cracking, b) crack formation(pre-stabilized cracking), c) stabilized cracking, d) post-stabilized cracking

The strain distribution in the steel and the concrete prior to the onset of cracking is shown in Fig. 2.2(a). This case can also be regarded as the strain distribution between two pre-existing cracks under a load smaller than the cracking load. Moving away from the two loaded ends, the steel strain decreases from its maximum value while the concrete strain increases from zero value. The difference between the two strains is accommodated by the slip mechanism at the interface of the concrete and steel. The two strains will meet each other at the point of zero slip at some distance from the loaded end, so called the transmission length l_t. The parameter $l_{s,max}$ is defined as twice the size of transmission length.

Cracking can only take place anywhere inside the zero slip portion of the tie element indicated with length l_1 in Fig. 2.2(a). This means that cracks could not be spaced smaller than the transmission length. The formation of the first crack with corresponding strain redistribution is shown in Fig. 2.2(b). This happens when the strain in concrete at the point of zero slip reaches its tensile cracking strain. Figure Fig. 2.2(b) is also applicable to the reloading of a cracked tie element in which stabilized cracking has not yet reached (pre-stabilized cracking).

The $l_{s,max}$ can be found by integrating bond forces over the distance of transmission length and setting it equal to the total change of force in the reinforcing steel over the same distance. Therefore,

$$\int_0^{1/2 l_{s,\max}} \pi\phi_s \times \tau(x)dx = (\sigma_{s2} - \sigma_{sE}) \times \pi\phi_s^2 / 4 \qquad (2.1)$$

where $l_{s,max}$ = length over which slip occurs between steel and concrete in the vicinity of a crack (two times transmission length); ϕ_s = diameter of reinforcing bar; $\tau(x)$ = bond stress distribution function; σ_{s2} = steel stress at the crack; and σ_{sE} = steel stress at the point of zero slip.

The bond stress distribution function $\tau(x)$ in Eq. 2.1 must be found from experimental tests. This function may be found based on the steel strain distribution from a direct tension test or calculated with the use of the bond-slip relationship from pull-out tests. Bond stress is one of the most influential parameters on the crack width. Over-estimation of bond stresses will result in under-estimated spacing of cracks. This parameter will be discussed later in more detail. To

simplify the calculations, a constant value is assumed for $\tau(x)$ in CEB MC90. Accordingly, solving Eq. 2.1 with a constant bond stress gives,

$$l_{s,\max} = 2\frac{\sigma_{s2} - \sigma_{sE}}{4\tau_{bk}}\phi_s \qquad (2.2)$$

where τ_{bk} = lower fractile value of the average bond stress ($1.8f_{ctm}(t)$ for short term/instantaneous loading of pre-stabilized and post-stabilized cracking or long term/repeated loading of post-stabilized cracking, $1.35f_{ctm}(t)$ for long term/repeated loading of pre-stabilized cracking); and $f_{ctm}(t)$ = mean value of concrete tensile strength at time t at which the crack appeared.

Another simplifying assumption in this model is that at each section the strain in concrete is uniform over the effective area of concrete in tension ($A_{c,ef}$). This enables an easier calculation of steel stress at the point of zero slip (σ_{sE}). However, this needs a proper outline for calculation of the effective tension area. The depth of effective tension area ($d_{t,ef}$) is schematically shown in Fig. 2.3. The CEB MC90 gives a simple estimation of this depth for members under direct tension or flexural loads, as follows,

$$d_{t,ef} = \begin{cases} \text{Lesser of} \begin{cases} 0.5h \\ 2.5d_c \end{cases} & \text{direct tension members} \\ \text{Lesser of} \begin{cases} 2.5d_c & \text{single rebar layer} \\ 2.5(h-d) & \text{multi rebar layer} \\ (h-kd)/3 & \end{cases} & \text{flexural members} \end{cases} \qquad (2.3)$$

where $d_{t,ef}$ = depth of effective tension area; h = over-all depth of the member; d_c = concrete cover to the center of reinforcing bar; d = effective depth of tension reinforcement; and kd = depth of neutral axis.

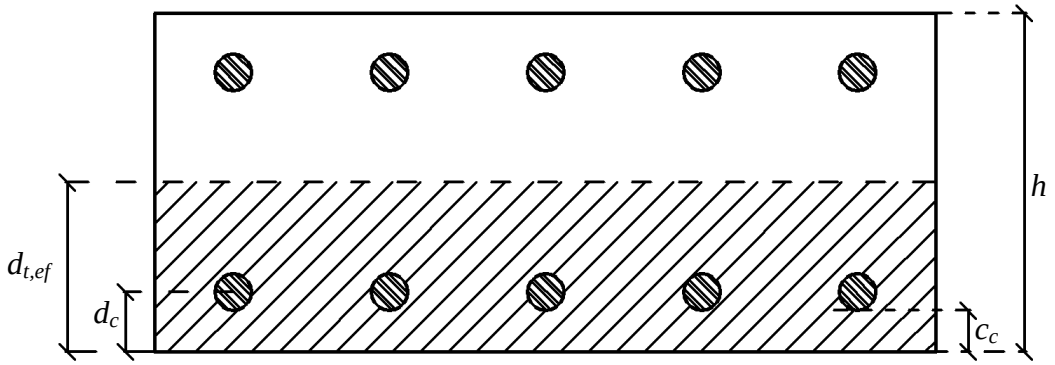

Fig. 2.3 Effective tension area of concrete

Over-estimation of concrete effective tension area is a conservative error in terms of the crack width, as it results in an under-estimated σ_{sE}, which in turn results in an over-estimated transmission length. This happens especially for elements with larger concrete covers in which the strain distribution differs from uniform over the depth of the concrete cover. On the other hand, another effect of this assumption is that the calculated crack width is an average crack width through the depth of the section. The crack width is smaller near the reinforcing bar and increases as it moves towards the concrete surface, more significantly in the case of flexural cracks. Therefore, when the width of a flexural crack at the concrete surface is desired, this model needs some modifications to take this effect into account.

The stress in steel at the point of zero slip at pre-stabilized cracking (σ_{sE1}) can be calculated as follows,

$$\sigma_{sE} = \sigma_{sE1} = E_s \varepsilon_{sE1} = E_s \varepsilon_{cE1} = E_s \frac{N_{sd}}{E_c (A_{c,ef} + \alpha_e A_s)} = \frac{\alpha_e N_{sd}}{A_{c,ef} (1 + \alpha_e \rho_{s,ef})} \qquad (2.4)$$

where E_s = modulus of elasticity of steel; N_{sd} = tensile force in steel at crack; E_c = modulus of elasticity of concrete; $A_{c,ef}$ = effective tension area of concrete; α_e = modular ratio (E_s/E_c); A_s = area of steel in tension; and $\rho_{s,ef}$ = effective reinforcement ratio ($A_s/A_{c,ef}$).

Substituting Eq. 2.4 into Eq. 2.2 knowing that $\sigma_{s2} = N_{sd} / A_s$ gives,

$$l_{s,\max} = \frac{\sigma_{s2}}{2\tau_{bk}} \phi_s \frac{1}{1+\alpha_e \rho_{s,ef}} \tag{2.5}$$

The above equation is applicable to the stage of crack formation (pre-stabilized cracking). Hypothetically, this equation may also be applied to reloading of a stabilized cracking system at loads lower than cracking load ($N_{sd} < N_r$) ignoring residual strains and slips. When the tensile load N_{sd} reaches the cracking load N_r, the $l_{s,max}$ reaches its maximum value, which is similar to the maximum crack spacing (S_{max}) as shown in Fig. 2.2(c). This stage is called stabilized cracking. In a worst case scenario, increasing load beyond this stage will not change the spacing of two cracks that are just S_{max} apart as shown in Fig. 2.2(d). The minimum spacing of cracks cannot be smaller than the transmission length at stabilized cracking, that is, half the maximum crack spacing (S_{min} = ½ S_{max}). The cracking load N_r can be calculated as follows,

$$N_r = f_{ctm}(t)(A_{c,ef} + \alpha_e A_s) = f_{ctm}(t) A_{c,ef}(1+\alpha_e \rho_{s,ef}) \tag{2.6}$$

and hence, the steel stress at crack at the cracking load level (σ_{sr2}) is,

$$\sigma_{sr2} = \frac{N_r}{A_s} = \frac{f_{ctm}(t) A_{c,ef}(1+\alpha_e \rho_{s,ef})}{A_s} = \frac{f_{ctm}(t)(1+\alpha_e \rho_{s,ef})}{\rho_{s,ef}} \tag{2.7}$$

Therefore, the stabilized cracking condition may be assumed to be reached when,

$$N_{sd} > N_r \xrightarrow{or} \sigma_{s2} > \sigma_{sr2} \xrightarrow{from \quad Eq.\,2.7} \rho_{s,ef}\sigma_{s2} > f_{ctm}(t)(1+\alpha_e \rho_{s,ef}) \tag{2.8}$$

At this stage the maximum crack spacing is established and can be calculated from Eq. 2.5 by substituting σ_{s2} with σ_{sr2} from Eq. 2.7, as follows,

$$l_{s,\max} = S_{\max} = \frac{f_{ctm}(t)}{2\tau_{bk}\rho_{s,ef}} \phi_s \xrightarrow{\tau_{bk} = 1.8 f_{ctm}(t)} S_{\max} = \frac{\phi_s}{3.6\rho_{s,ef}} \tag{2.9}$$

The width of a crack at all stages of loading can be defined as the integration of the relative deformation of the concrete and the steel over the length $l_{s,max}$ in the vicinity of that crack. As the width of a crack is not constant through the depth of concrete cover, if this crack width gradient is of interest, the relative deformation must be integrated at each depth separately to calculate the crack width at that depth. Alternatively, the average width of a crack at the reinforcing steel level can be calculated by using the average concrete strain over the depth of the section. Based on CEB MC 90, the design crack width may be calculated as,

$$w_k = l_{s,\max}(\varepsilon_{sm} - \varepsilon_{cm} - \varepsilon_{cs}) \tag{2.10}$$

where w_k = characteristic crack width; ε_{sm} = average steel strain within $l_{s,max}$; ε_{cm} = average concrete strain within $l_{s,max}$; and ε_{cs} = shrinkage strain (negative value).

This crack width is called characteristic crack width as the model targets cracks that have more than 5% probability of occurrence. This model is expected to give a characteristic crack width that is 1.7 times the actual average crack width. To calculate the average crack width at post-stabilized cracking stage the model suggests using $S_{ave} = {}^2/_3 S_{max}$ for $l_{s,max}$ in calculations. The mean steel and concrete strains must also be modified as will be seen later.

The average steel and concrete strains at pre-stabilized cracking may be calculated based on Fig. 2.2(b) as,

$$\varepsilon_{sm} - \varepsilon_{cm} = (\varepsilon_{s2} - \beta_e(\varepsilon_{s2} - \varepsilon_{sE1})) - \beta_e\varepsilon_{sE1} = \varepsilon_{s2} - \beta_e\varepsilon_{s2} = (1-\beta_e)\varepsilon_{s2} \tag{2.11}$$

and at stabilized cracking as,

$$\varepsilon_{sm} - \varepsilon_{cm} = (\varepsilon_{s2} - \beta_e(\varepsilon_{sr2} - \varepsilon_{sr1})) - \beta_e\varepsilon_{sr1} = \varepsilon_{s2} - \beta_e\varepsilon_{sr2} \tag{2.12}$$

where β_e = empirical factor to assess average strain within $l_{s,max}$ (0.6 for short term/instantaneous loading of pre-stabilized and post-stabilized cracking and long term/repeated loading of pre-stabilized cracking, 0.38 for long term/repeated loading of stabilized cracking)

It must be noted that the factor β_e is the integration parameter for a mean value of a given function. If a constant bond stress is assumed, the resulting steel and concrete strain curves will be linear. Thus, theoretically, the factor β_e must be 0.5 for such a model. However, in CEB MC90 model a different value than 0.5 is recommended for β_e based on the experimental data. This implies that the model uses the constant bond stress assumption only to calculate the crack spacing and not for the steel and concrete strain predictions. This improves the final results for calculation of the characteristic crack width.

To calculate the average crack width, the concrete and steel strains must be modified. In this case, the CEB MC90 model uses the constant bond assumption to modify the mean stresses. Therefore, a reduced accuracy may be expected in this model for calculation of the average crack width. Accordingly, with the assumption of a constant bond stress the mean concrete strain over the transmission length is expected to decrease by the same ratio that the transmission length is reduced meaning reduced by a ratio of $^2/_3$. An increase in the mean steel strain should also be considered in a similar manner. Accordingly, the mean strains at stabilized cracking corresponding to the average crack spacing are recommended as follows:

$$\varepsilon_{sm} - \varepsilon_{cm} = (\varepsilon_{s2} - \beta_e \frac{2}{3}(\varepsilon_{sr2} - \varepsilon_{sr1})) - \beta_e \frac{2}{3}\varepsilon_{sr1} = \varepsilon_{s2} - \frac{2}{3}\beta_e \varepsilon_{sr2} \qquad (2.13)$$

2.3 Mechanism of Bond

Based on the crack theory explained in the previous section, the bond stress is a very influential parameter on the crack width. The mechanism of the interaction at the steel/concrete interface is studied in detail in this section. The relative movement of the reinforcing bar and the surrounding concrete is called bond-slip, which is the main reason for the creation of bond forces. The bond behaviour can be characterized into two various categories of short and long slips. Long slips can happen where an adequate amount of development length is not provided for the reinforcing bar, and hence, it can be pulled a large distance (above 3 *mm*) out of the concrete, for instance at the structural joints. However, in all other cases of RC cracking the amount of slip is very small (below 1 *mm*), therefore, only the short slip bond behaviour is considered in this study.

There are three mechanisms that may contribute to the bonding forces, namely, chemical adhesion, friction, and mechanical interaction (Lutz and Gergely 1967). For the short-slip bond of deformed bars the primary contributing mechanism is the mechanical interaction between the bar lugs and the concrete, while the other two mechanisms are of a secondary importance. The bond mechanism is graphically illustrated in Fig. 2.4.

The chemical adhesion breaks down at low bond stresses, and the bond will be maintained by the bearing force of the lugs on the concrete. Diagonal micro-cracks will form at the tip of the bar lugs, which accommodates the main portion of the total slip. These cracks will cause the formation of diagonal compression struts around the bar lugs. At higher bond stresses, the crushed concrete entrapped in front of the bar lug produces a wedging effect, which is the cause for the radial component of the bond force. Therefore, the stress caused by the resultant of all bond forces, indicated as the bearing bond stress τ_b in Fig. 2.4, is at some angle to the bar axis. This angle is not constant at all levels of bond stress. Bond-slips caused by the concrete crushing and frictional sliding can also contribute to the total bond-slip.

The bearing bond stress has two components, namely, the tangential/shear bond stress τ_t and the radial bond stress σ_r. The shear bond stress is highly dependent on the radial bond stress, especially at higher bond stress levels. In other words, if the radial bond stress fails, the tangential bond stress will diminish as well. The shear bond stress is the main component for determination of the cracking behaviour in one-way structures. Therefore, most studies have been focused on directly finding the shear bond stress. There is not much attention given to the determination of the radial bond stresses, which is an influential parameter in cracking behaviour of two-way structures.

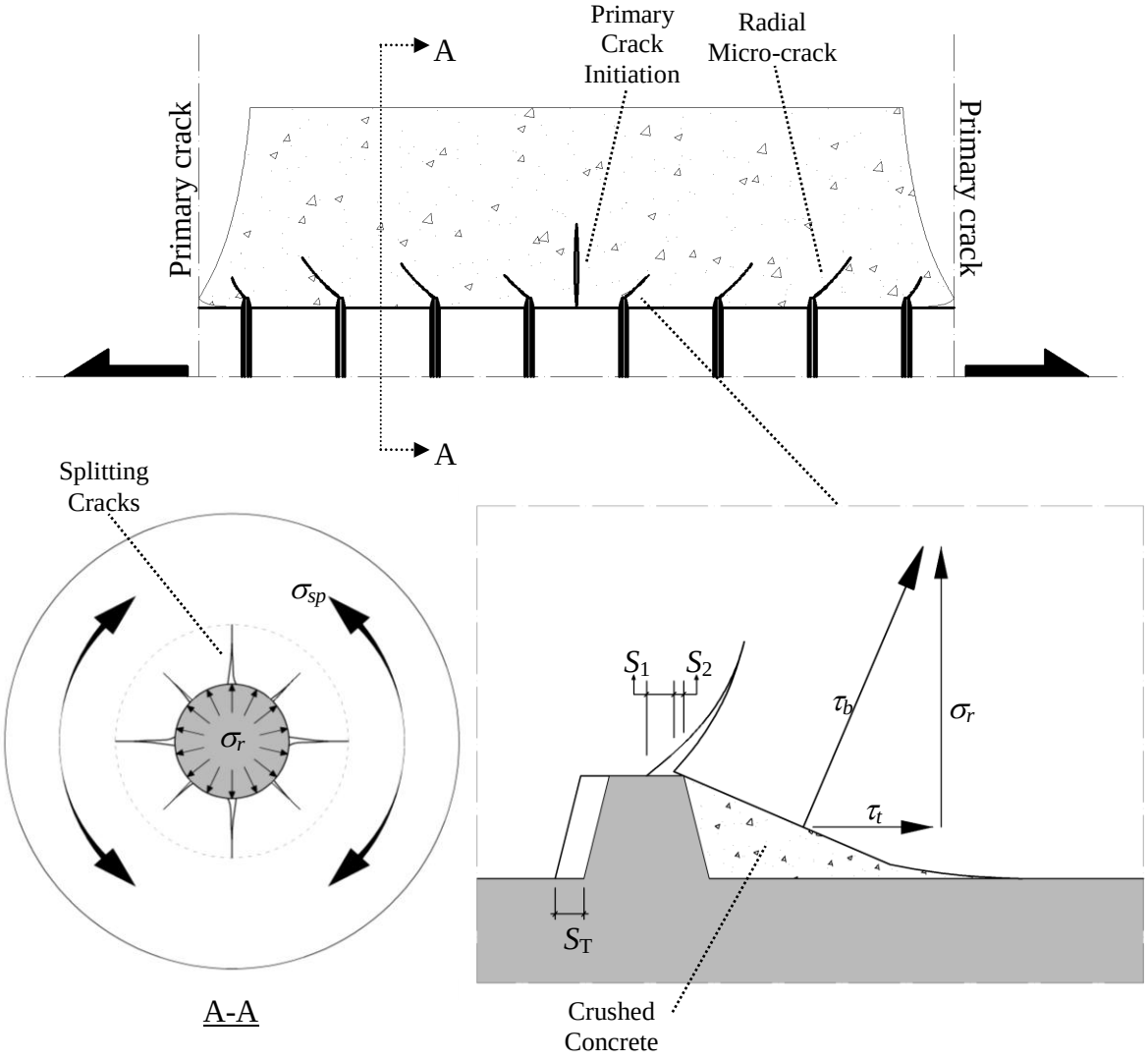

σ_{sp} : splitting tensile stress
τ_b : bearing bond stress
τ_t : tangential/shear bond stress
σ_r : radial bond stress

S_T : total slip
S_1 : slip due to microcracking
S_2 : slip due to concrete crushing and frictional sliding

Fig. 2.4 Local bond mechanism

The radial bond stresses σ_r, are balanced by the splitting tensile stresses σ_{sp}. Whenever, the splitting tensile stresses reach up to the tensile strength of concrete, longitudinal splitting cracks will form around the bar as shown in section A-A in Fig. 2.4. For small concrete covers without transverse reinforcement, the formation of splitting cracks in the full-depth of the concrete cover will cause the total failure of the bond stresses.

Direct determination of the local bond stress/slip relationship through experimental tests always encounters technological limitations. This is because the slip can only be measured at some distance to the reinforcing bar so as not to interfere with the bond itself. Therefore, the local bond stress/slip is usually calculated indirectly from the steel stress distribution from short slip tests.

2.3.1 Kankam test

An experimental investigation of short-slip bond stresses was performed by Kankam (1997). He performed double pullout tests on prismatic RC tie elements. These tie elements had a square section of 150×150 *mm* and an embedment length of 200 *mm*. The concrete mix used for these elements had a maximum aggregate size of 10 *mm*, a water to cement ratio of 0.5, and an average concrete cube strength of 50 *MPa* on the test day (14 days after casting). Three types of reinforcing bars were used, namely, plain round bar, cold-worked ribbed bar, and hot-rolled ribbed bar. The diameter of all reinforcing bars was 25 *mm* and their modulus of elasticity was found to be approximately 200 *GPa*. The reinforcing bars were longitudinally cut in half and a groove was machined in each half-bar to provide enough room for the installation of the strain gauges. This method of strain gauge installation has the least interference with the actual bond mechanism. A zero-slip condition was enforced at the mid-length of the specimen by providing a transverse anchor through a circular hole on the reinforcing bar at mid-span. The detailing of the machined bars is shown in Fig. 2.5. The bond stress/slip relationships were drawn from the steel stress variation along the reinforcing bars. It was shown that the bond stress/slip relationship changes with the varying longitudinal distance to the crack, and also, with the varying steel stress. A typical variation of the bond stress along the bar axis for the hot-rolled ribbed bar is shown in Fig. 2.6. It can be seen that the peak bond stress is biased toward the location of the loading end (crack).

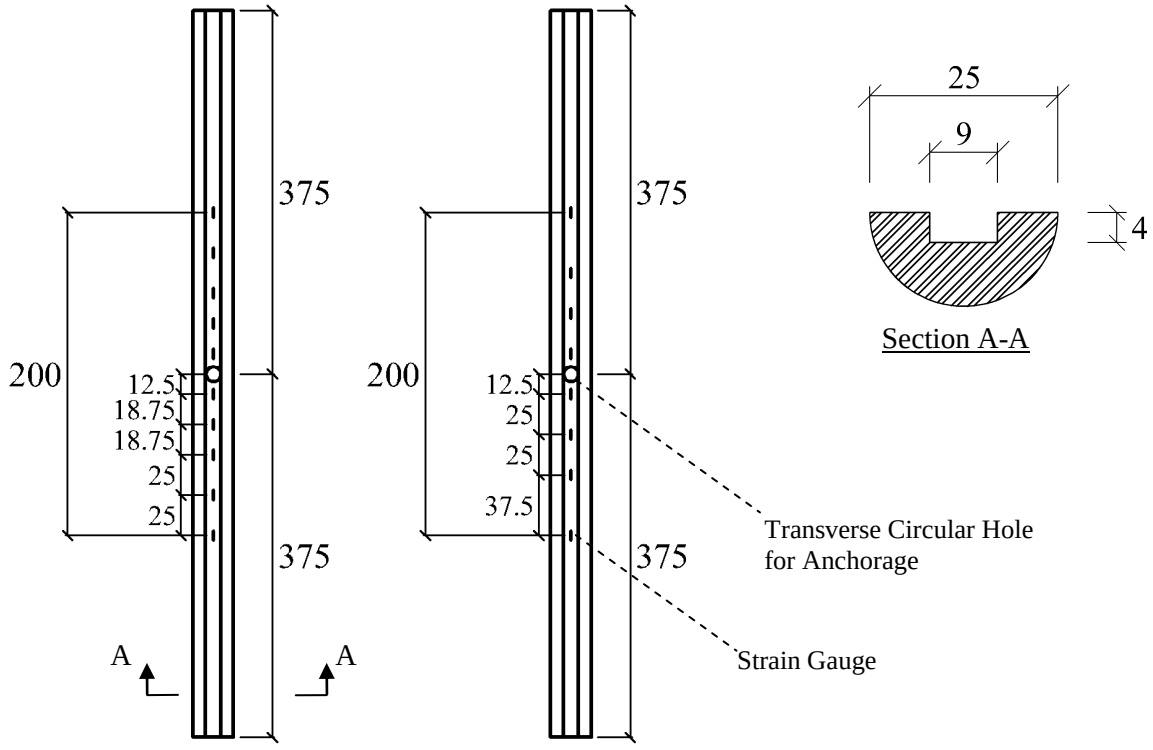

Fig. 2.5 Details of machined bar and positions of electrical resistance strain gauges for Kankam tests (dimensions in *mm*)

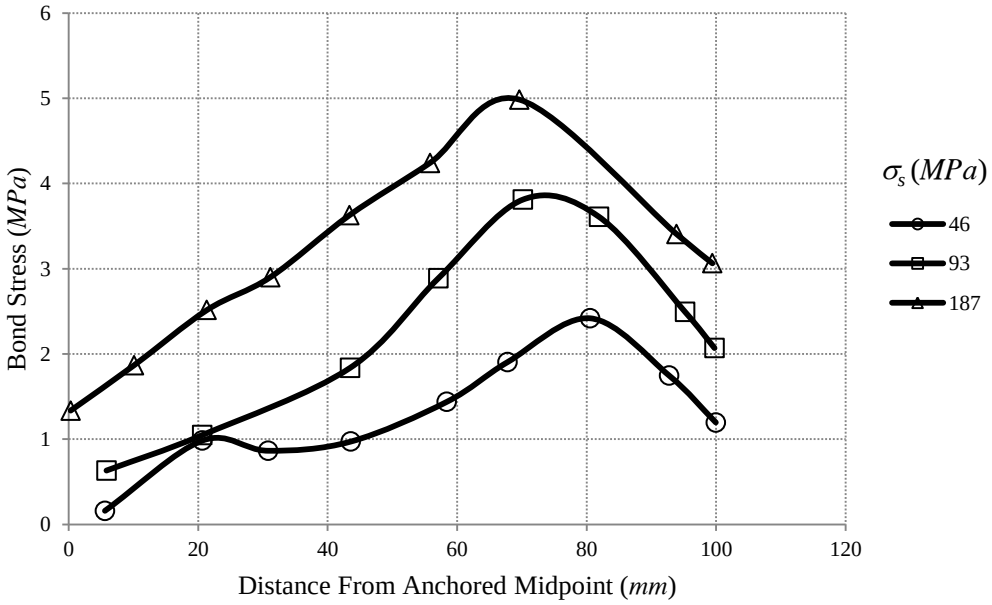

Fig. 2.6 Distribution of bond stress along the reinforcing bar, Kankam test

2.3.2 Tammo test

If it is assumed that the bond-slip is mainly accommodated via micro-cracking at the interface layer, this will produce a large crack width gradient through the concrete cover. This is because the concrete closer to the reinforcing bar is further stretched due to micro-cracking than the concrete away from reinforcing bar. This was observed in a test by Tammo and Thelandersson (2009). They conducted several double-pullout tests on square section RC tie elements. The focus in their experiment was on the width of cracks and its gradient through the depth of the concrete cover. With that in mind, a unique configuration of LVDT (Linear Variable Differential Transformer) displacement transducers was arranged at the loading end of the RC tie element, as shown in Fig. 2.7. With this arrangement the movement of the concrete relative to the reinforcing bar at two different depths of the concrete cover (at a distance 11 *mm* from the bar surface and at the concrete surface) could be measured. These measurements were representing half the width of an actual crack, and hence, they were doubled and referred to as the fictitious crack width so as to be comparable to the actual crack width. The width of a crack at concrete surface formed at the mid-length of the tie element was also reported (w_{cr}).

A typical result of these tests is shown in Fig. 2.8. It can be seen that the crack width gradient is increasing with the increasing steel stress. The crack width gradient is very negligible at steel stresses lower than 150 *MPa*, while it increases up to almost 0.06 *mm* at steel stress of 300 *MPa*.

A very small bond-slip ($w_{11}/2$) in a range of 0.05 *mm* can be observed at a distance 11 *mm* to the bar surface at service load levels (σ_s = 200 *MPa*). This value can be expected to be lower at the steel/concrete interface. In other words, the local bond-slip can be much smaller than 0.05 *mm*. The bond-slip reported by Kankam (1997) is also in the range of 0.06 *mm* for a steel stress of 160 *MPa*. This shows that the current experimental techniques are only capable of giving the bond-slip at some distance to the bar surface, and they are not representing the bond-slip at the steel/concrete interface. Therefore, the direct usage of the experimental bond stress-slip relationships in the FE modeling of the bond interaction at the interface layer can be to some extent erroneous.

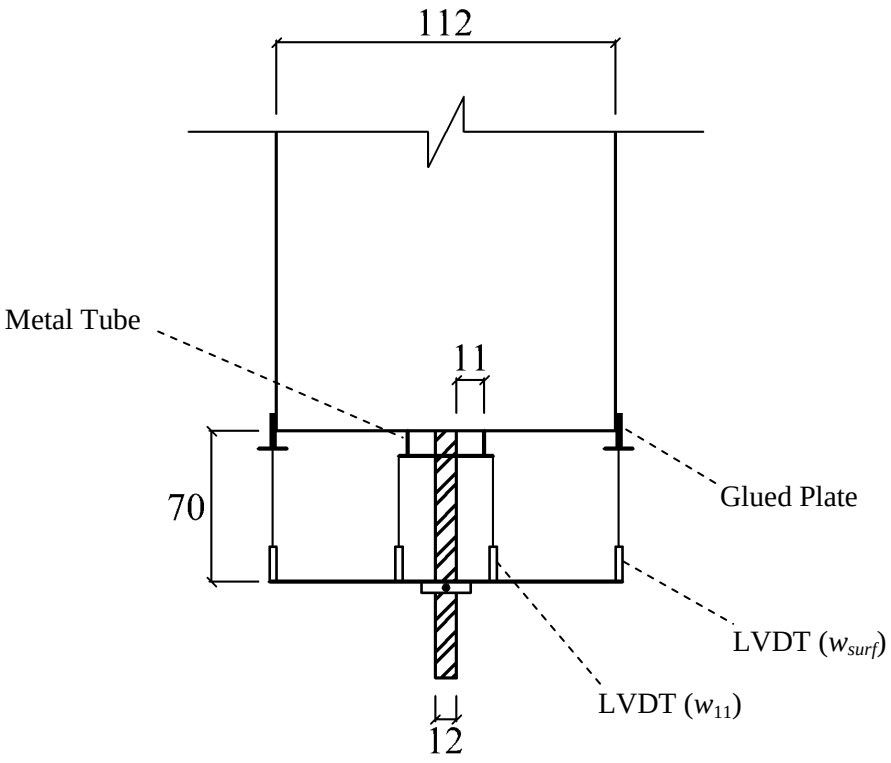

Fig. 2.7 Detailing of LVDT displacement transducers mounted at loading ends of tie element, Tammo test

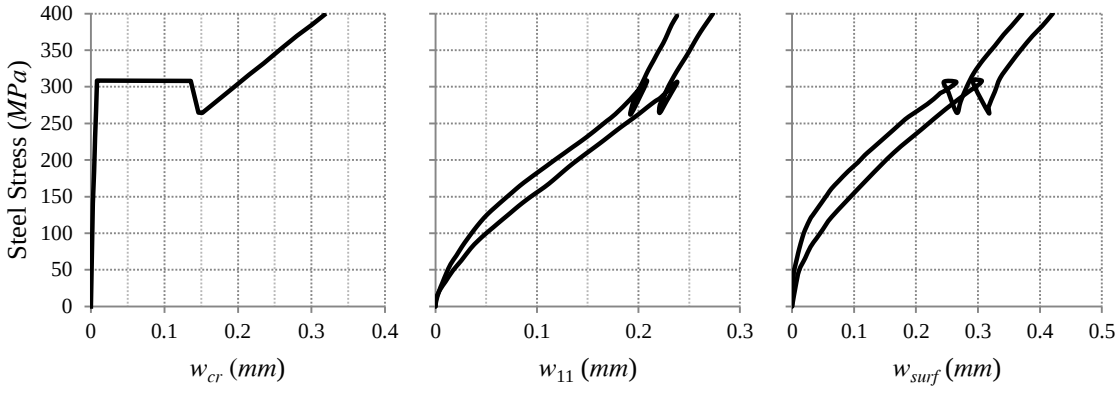

Fig. 2.8 Results of LVDT displacements for Tammo test

2.4 Crack Control Provisions of Various Design Codes

There are numerous crack prediction models available in the literature mainly for simple loading conditions of concentric tension and pure bending moment. These models can be categorized into three main types of empirical, semi-empirical, and analytical. Some of these models have been used as the basis for the crack control recommendations of various design Codes. In the following, the approach of various design Codes with the underlying crack prediction models will be introduced. In this study, the effectiveness and drawbacks of these models will be revealed.

New Zealand Standard NZS 3106 (1986)

Although, experiments show that the crack widths are highly dependent on the steel stress, limiting the stress in the reinforcing steel cannot be a standalone method of crack control. This over simplification can be seen in New Zealand Standard NZS 3106 (1986) in which the crack control is sought solely through limiting the steel stress for pure tension and pure bending loads (110 *MPa* for members in direct tension and for members thinner than 225 *mm* in bending, 138 *MPa* for members thicker than 225 *mm* in bending). A sound crack control must be based on a crack prediction model that incorporates as many influential parameters as practically possible in its calculations.

BS 8007 Code (1987)

The BS 8007 Code (1987) limits the maximum design crack widths to 0.2 and 0.1 *mm* for severe or very severe exposure and critical aesthetic appearance, respectively. These limits are generalized for all types of cracks. It is also stated that the crack widths may be deemed to be satisfactory when the steel stress is limited to 100 and 130 *MPa* for crack widths of 0.1 and 0.2 *mm*, respectively. Formulations are also provided for direct calculation of the width of flexural and direct tension cracks. These formulations are based on the work done by Beeby (1970, 1971). Accordingly, the width of flexural cracks may be calculated as follows,

$$w = \frac{3a_{cr}\varepsilon_m}{1+2\left(\frac{a_{cr}-c_{\min}}{h-kd}\right)} \tag{2.14}$$

where, w = design surface crack width, a_{cr} = distance from the point considered to the surface of the nearest longitudinal bar, c_{min} = minimum cover to the tension reinforcement, h = overall depth of the member, kd = depth of neutral axis, and ε_m = average strain at the level where the cracking is being considered, which is given by,

$$\varepsilon_m = \varepsilon_1 - \varepsilon_2 \tag{2.15}$$

where, ε_1 = strain at the level considered ignoring the stiffening effect of the concrete in the tension zone (should be modified to allow for the direct strain when the member is under combined flexural and tensile stresses), and ε_2 = strain due to the stiffening effect of concrete between cracks, which is given by,

$$\varepsilon_2 = \frac{b_t(h-kd)(a'-kd)}{3E_s A_s(d-kd)} \tag{2.16}$$

Where, b_t = width of section at the centroid of tension reinforcement, a' = distance from the compression face to the point at which the crack width is being calculated, E_s = modulus of elasticity of reinforcement, A_s = area of tension reinforcement, and d = effective depth.

The recommended equation for the width of direct tension cracks by BS 8007 Code (1987) is as follows,

$$w = 3a_{cr}\varepsilon_m \tag{2.17}$$

in which,

$$\varepsilon_2 = \frac{2b_t h}{3E_s A_s} \tag{2.18}$$

Equations 2.16 and 2.18 correspond to the maximum crack width of 0.2 *mm* and must be multiplied by 1.5 for maximum crack widths of 0.1 *mm*. It can be noticed that the elongation of concrete between cracks is ignored in this model.

CEB-FIP Model Code (1990)

A more rigorous method of crack control is provided in CEB-FIP Model Code (1990). The crack control is achieved by limiting a characteristic crack width defined as follows,

$$w_k = l_{s,\max}\left(\varepsilon_{sm} - \varepsilon_{cm} - \varepsilon_{cs}\right) \tag{2.19}$$

where, w_k = characteristic design crack width (1.7 times the average crack width), $l_{s,max}$ = length over which slip between steel and concrete occurs (1.5 times the average crack spacing), ε_{sm} = average steel strain within $l_{s,max}$, ε_{cm} = average concrete strain within $l_{s,max}$, and ε_{cs} = strain of concrete due to shrinkage (must be introduced algebraically).

The shrinkage strain ε_{cs} in Eq. 2.19 is taken as the total shrinkage strain. This is a conservative assumption because the bond between the concrete and the steel always creates some restraint against free contraction of the concrete between cracks. This would reduce the influence of shrinkage on the crack width in externally unrestrained members.

Basically, the total shrinkage strain after the time that the bond is sufficiently developed between the concrete and the steel comprises of two components, i.e. a part that is internally restrained by the reinforcement and a part that is unrestrained. The unrestrained part is due to the fact that slip always may occur between the reinforcement and the concrete. Different effects on the crack width may be resulted from each of these shrinkage strain components that should be carefully considered in the prediction model.

The unrestrained shrinkage can directly increase the crack width and that is the part of shrinkage that must be used as ε_{cs} in the Eq. 2.19. The unrestrained shrinkage is higher for concrete away from the reinforcement as the internal restraint is lower at those regions. Also, unrestrained shrinkage is higher at the vicinity of the crack as a higher slip occurs at that region.

The internally restrained shrinkage can increase the tensile stresses in the concrete, which is balanced by a decrease in steel stresses between cracks. This change in stresses is lower at the vicinity of the crack where a higher slip takes place and tends to increase at locations of zero slip away from the crack. In externally unrestrained members the internally restrained shrinkage does not directly influence the crack width, however, it can reduce the crack spacing by increasing the concrete tensile stresses, and hence, reducing the cracking load. On the other hand, in externally restrained members, the internally restrained shrinkage can increase the stresses in the reinforcement at crack, which eventually results in an increase in the crack width. This effect is also considered in the CEB-FIP MC90 (1990) under cl.7.4.3.1.2, which states that where cracking is also due to imposed deformations, the steel strain at cracks due to imposed loads (ε_{s2}) should be increased by that caused by imposed deformations. However, if the imposed deformation is due to the shrinkage strains and the total shrinkage strain is already considered in the Eq. 2.19 instead of the unrestrained shrinkage, increasing the steel strain due to externally restrained shrinkage effects is just over-conservative. The prediction of the cracking in an externally restrained member is not in the scope of this study. The readers are encouraged to see a study by Kianoush et al. (2007) regarding a FE approach to the prediction of the externally restrained shrinkage cracks. The effect of shrinkage on the crack width is further studied in Section 5.3 of this thesis.

The CEB-FIP MC90 model will be explained in more detail in Section 3.2 of the following Chapter.

ACI 350-01 (2001)

In ACI 350-01 (2001), the crack control in one-way flexural members is introduced by limiting the quantity of a factor defined as follows,

$$Z = f_{s,cr}\sqrt[3]{d_c A_e} \qquad (2.20)$$

where, $f_{s,cr}$ = the steel stress at crack, d_c = distance from center of bar to extreme tension fiber, and A_e = effective stretched area of concrete (area of concrete symmetric with reinforcing steel divided by number of bars).

The value of Z should not exceed 20 and 17 MN/m for normal and severe environmental exposures, respectively. The Z factor is simply a different arrangement of the Gergely-Lutz (1986) expression with corresponding maximum crack widths of 0.27 and 0.23 mm for normal and severe environmental exposures, respectively. The Gergely-Lutz equation is as follows,

$$w_{t,\max} = 1.1\times 10^{-5}\beta_g f_s \sqrt[3]{d_c A_e} \qquad (2.21)$$

where, $w_{t,max}$ = maximum crack width at tension face, and β_g = the ratio of distances to the neutral axis from the extreme tension fiber and from the centroid of the main reinforcement. f_s is in *MPa*, d_c is in *mm*, and A is in mm^2.

In determination of the maximum allowed values of Z, β is approximated as 1.2 for beams. The limiting values of Z are recommended to be reduced by a factor of (1.2/1.35) for slabs. The Gergely-Lutz equation is not applicable to d_c values larger than 63.5 *mm* (2.5 *in*), therefore, when the concrete clear cover exceeds 50 *mm* (2 *in*) the Code permits the calculation of d_c based on a clear cover of 50 *mm*. In that case, it is stated that the additional cover is regarded as added protection.

The aim of presenting the Gergely-Lutz formulation in a different form was to avoid the impression of predicting the precise crack width and to rather emphasize the importance of the reinforcement layout in the section. The aforementioned method is still allowed in the new ACI 350-06 (2006) presented in appendix C as an alternative method to the new approach.

ACI 350-06 (2006)

The new method of crack control in ACI 350-06 (2006) is based on a model developed by Frosch (1999). The Frosch model is also the basis for the recommendations of the ACI318-99 (1999) for controlling the width of flexural cracks. In his study, he showed the inapplicability of the Gregely-Lutz model (Eq. 2.21) to the concrete covers greater than 50 *mm*. In view of this, he proposed a different equation which he extracted from a pioneering work done by Broms (1965). In his model, the maximum crack spacing is taken to be twice the controlling cover distance (d^*). Accordingly, the proposed equation in its original form is as follows,

$$w_{t,\max} = 2\beta_g \varepsilon_{s,cr} d^* = 2\beta_g \frac{f_{s,cr}}{E_s}\sqrt{d_c^2 + \left(\frac{s}{2}\right)^2} \qquad (2.22)$$

where $w_{t,max}$ = maximum crack width at the tension face (*mm*); β_g = crack width gradient factor (the ratio of distances to the neutral axis from the extreme tension fiber and from the centroid of the main reinforcement); $\varepsilon_{s,cr}$ = steel strain at the crack; d^* = controlling cover distance (*mm*); $f_{s,cr}$ = steel stress at the crack (*MPa*); d_c = concrete cover to the center of reinforcing bar (*mm*); and s = bar spacing (*mm*).

The crack control recommendations of the ACI 350-06 are basically the rearrangement of the Eq. (2.22) for determination of the limiting steel stresses with a known maximum crack width and a clear concrete cover of 50 *mm*. It states that the maximum allowed steel stress should be calculated as:

$$f_{s,\max} = \frac{56000}{\beta\sqrt{s^2 + 4(50 + d_b/2)^2}} \qquad \text{normal environmental exposure} \qquad (2.23)$$

$$f_{s,\max} = \frac{45500}{\beta\sqrt{s^2 + 4(50 + d_b/2)^2}} \qquad \text{severe environmental exposure} \qquad (2.24)$$

where, $f_{s,max}$ = maximum allowed steel stress (*MPa*) (should not be more than 250 *MPa*, and need not be less than 140 and 165 *MPa* in Eq. 2.23 for one-way and two-way members, respectively, and 115 and 140 *MPa* in Eq. 2.24 for one-way and two-way members, respectively), s = bar spacing (*mm*), and d_b = bar diameter (*mm*).

Clear concrete covers more than 50 *mm* are not considered in the above two equations, therefore, where the appearance of the concrete surface is of concern the Code imposes a limit on the bar spacing for concrete covers to the center of reinforcing bars exceeding 75 *mm*. Accordingly, the bar spacing must be limited to a value given by,

$$s = \frac{94600}{f_s} - 2.5c_c < 300\ mm \qquad (2.25)$$

where, c_c = clear concrete cover (*mm*).

The Eq. (2.25) is the linear approximation of the Eq. (2.22) while it is rearranged for determination of the bar spacing with a known maximum crack width for clear concrete covers greater than 50 *mm*.

The ACI 350-06 does not provide any explicit measure to control the direct tension cracks. Direct tension cracks can penetrate the full-depth of the section, which can provide an opening for the gas or liquid to seep out. In an experimental study by the author (2009b), it is observed that the leakage can begin at a very low crack width of 0.04 *mm*. However, a reduction in the rate of leakage is observed over time. This can be due to the mechanical obstruction caused by the micro-scale debris or the self-healing capacity of un-hydrated cement paste when it is exposed to water. The leakage problem associated with the direct tension cracks requires them to be controlled under more stringent crack width limitations especially in liquid or gaseous containing structures.

The abovementioned formulas are valid for members under pure bending moments. In a previous study by the author (2009a), it is shown that the Frosch and Gergely-Lutz models overestimate the crack width for members under combined uni-axial tension and bending. This overestimation tends to increase as the direct tension forces in the section increases with respect to the bending moment.

2.5 Two-Way Cracking

As of to date, no distinguished method has been provided by any design Code for controlling cracks in two-way members. The number of studies in the literature regarding this issue is also very limited. A prototype of a prestressed concrete containment vessel (scale of 1:14) was tested by MacGregor et al. (1980a). The wall of the vessel was hinged at the base, and it was reinforced

and prestressed in hoop and meridional directions. The behaviour of the vessel was monitored under increasing internal water pressure up to the failure. The obtained crack pattern is shown in Fig. 2.9. Horizontal and vertical cracks were formed due to the hoop tension force and the vertical moment in the wall. It can be noticed that the crack pattern closely reflects the shape of the reinforcing mesh. They (Simmonds et al. 1979, MacGregor et al. 1980b) also performed tests on uni-axially, and bi-axially loaded prestressed reinforced concrete wall segments. In another study, they (Rizkalla et al. 1979) examined the air leakage through a direct tension crack, and developed a theoretical equation to predict the leakage rate.

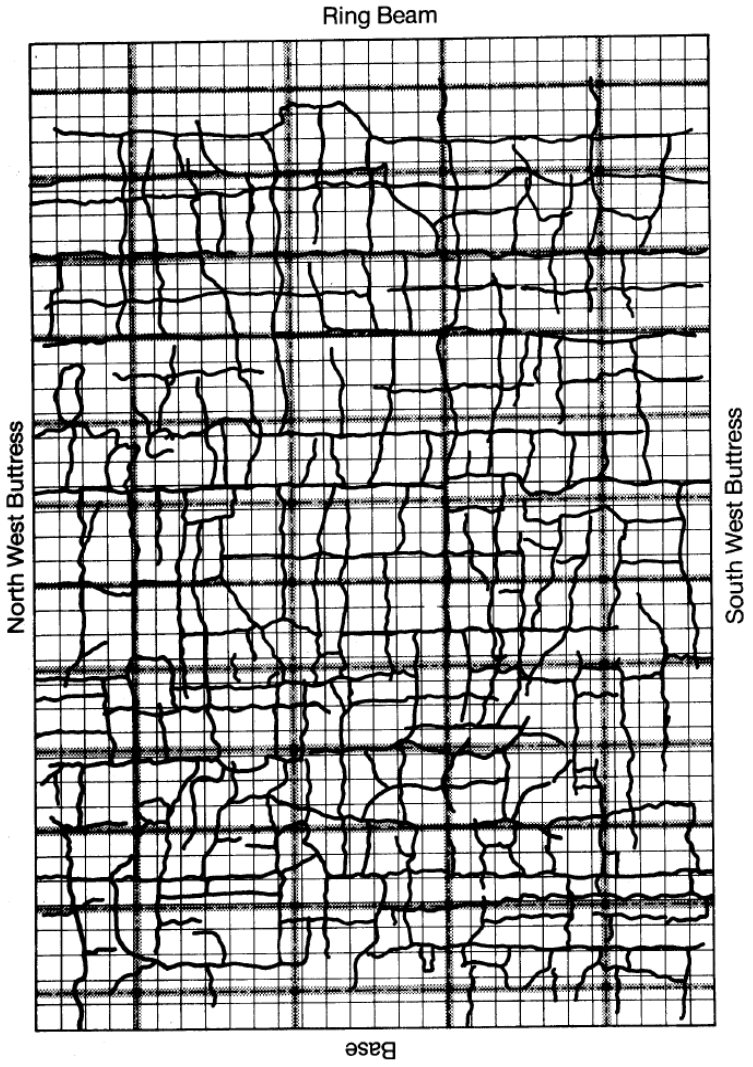

Fig. 2.9 Crack pattern of the wall of a prestressed containment vessel tested by MacGregor et al. (courtesy of MacGregor et al. (1980a))

In a recent study, prestressed reinforced concrete panels representing a segment of the concrete containment wall were tested under biaxial tension by Cho et al. (2004). The focus of their tests was on the crack pattern and the mean stress/strain response of the tested panels. Similar tests were performed by Dawood and Marzouk (2010). The focus in their tests was on the crack spacing and the crack width.

One extensive contribution to the understanding of the cracking behaviour of two-way slabs is due to a pioneering work performed by Nawy et al. (1971, 1972). They performed more than 90 tests on two-way slabs reinforced with deformed welded wire fabrics under various loadings, span ratios, and boundary conditions. The crack width was found to be a function of the grid index, the reinforcement stress, and the cover factor. A correlation was also recognized between the crack pattern and the grid index. The statistical analysis of all the experimental data along with the underlying fracture hypothesis resulted in the following equation for the estimation of the maximum crack width,

$$w_{t,\max} = K\beta_g f_s \sqrt{G_I} \tag{2.26}$$

where $w_{t,max}$ = maximum crack width at the face of concrete caused by flexural load at the service level (*mm*); K = fracture coefficient given in Table 2.1 (mm^2/N); β_g = crack width gradient factor (ratio of the distance from the neutral axis to the tensile face of the slab to the distance from the neutral axis to the centroid of the reinforcement grid); f_s = actual average service load steel stress level or 50% of the design yield strength (*MPa*); and G_I = grid index.

The grid index G_I in the Eq. 2.26 is defined as,

$$G_I = \frac{d_{b1} s_2}{Q_{i1}} \tag{2.27}$$

where d_{b1} = diameter of the reinforcement in direction 1 (direction of the reinforcement closest to the concrete outer tensile fibre; crack width prediction is made in this direction) (*mm*); s_2 = spacing of the reinforcement in direction 2 perpendicular to direction 1; and Q_{i1} = active steel ratio.

The active reinforcement ratio Q_{i1} is also defined as,

$$Q_{i1} = \frac{\text{reinforcement area per unit width}}{\text{effective tension area of concrete per unit width}} = \frac{A_{s1,perbar} \diagup s_1}{1 \times (d_{b1} + 2c_1)} = \frac{\pi d_{b1}^2 \diagup 4s_1}{2d_{c1}} = \frac{\pi}{8} \cdot \frac{d_{b1}^2}{s_1 d_{c1}} \tag{2.28}$$

where, $A_{s1,perbar}$ = area of reinforcement in direction 1 per bar; s_1 = spacing of reinforcement in direction 1; c_1 = clear concrete cover to the nearest reinforcing bar in direction 1; and d_{c1} = distance from the concrete outer tensile fibre to the center of the reinforcing bar in direction 1.

Substituting Eq. 2.28 into Eq. 2.27, the grid index can be written as,

$$G_I = \frac{8}{\pi} \cdot \frac{s_1 s_2 d_c}{d_{b1}} \tag{2.29}$$

The fracture coefficient K in Eq. 2.26 is dependent on the loading, boundary conditions, and the span ratio of the slab. The value of this coefficient is given in Table 2.1.

Table 2.1 Fracture coefficient K for slabs and plates

Loading Type	Span Ratio	Boundary Condition	$K(\times 10^{-5})$ $(in^2/kips)$	$K(\times 10^{-6})$ (mm^2/N)
Concentrated	1.0	4 edges restrained	2.1	3.0
	1.0	4 edges simply supported	2.1	3.0
Uniformly Distributed	0.5	4 edges restrained	1.6	2.3
	0.7	4 edges restrained	2.2	3.2
	0.7	3 edges restrained, 1 edge hinged	2.3	3.3
	0.7	2 edges restrained, 2 edges hinged	2.7	3.9
	1.0	4 edges restrained	2.8	4.1
	1.0	3 edges restrained, 1 edge hinged	2.9	4.2
	1.0	2 edges restrained, 2 edges hinged	4.2	6.1

One possible limitation of the Nawy's model, which interestingly has not gained any attention, is the questionable applicability of this model to the normally reinforced concrete slabs. The

Nawy's equation was developed based on the experimental data of slabs that were reinforced with welded wire fabrics. Unlike the normal reinforcement, the reinforcing bars cannot slip relative to each other at welded joints of a wire fabric. This will cause the creation of some forces, so called bearing forces, between the transverse reinforcement and the concrete. This effect may change the bond behaviour and the cracking mechanism of the slab. The bearing force was recognized by Desayi and Kulkarni (1976) in their prediction model for the crack spacing in a two-way slab. They verified their model against the experimental data of the Nawy's tests. Their recommended equation for the calculation of the crack spacing is in the following form,

$$S_{mx} = \frac{k_t f_{ct} A_{ctx}}{\left(\pi d_{bx} k_b \tau_t / s_x\right) + \left(d_{by} f_{bb} / s_y\right)} \tag{2.30}$$

where S_{mx} = average crack spacing for cracks normal to direction x; k_t = constant to account for the distribution of tensile stress in effective tension area; f_{ct} = tensile strength of concrete; A_{ctx} = effective stretched area of concrete per unit width in tension in direction x; d_{bx} = diameter of bars in direction x; k_b = constant to account for the distribution and surface characteristics of bar for the bond stress; τ_t = shear bond stress; s_x = spacing of bars in direction x; d_{by} = diameter of bars in direction y; f_{bb} = bearing stress; and s_y = spacing of bars in direction y.

A similar approach is used by Dawood and Marzouk (2010) to predict the crack spacing in bi-axially loaded concrete panels reinforced with normal reinforcement mesh. However, the presence of bearing stresses in a normally reinforced concrete member in which the reinforcing bars are free to slip at the mesh joint is uncertain.

The cracking in normal and high strength concrete two-way flexural slabs was also investigated by Rizk and Marzouk (2010). They recommended an analytical formulation for the prediction of the crack spacing based on the concepts of the bond stress and the splitting tensile stress. The recommended equation for the calculation of the crack spacing in one of two main orthogonal directions is as follows,

$$S_{mx} = \frac{k_t f_{ctm} A_{ctx} - 0.67 d_{by} f_{ctm}}{\frac{2}{3} \pi d_{bx} \tau_{tp} n_x} \quad (2.31)$$

where S_{mx} = average crack spacing for cracks normal to x reinforcement; k_t = ratio of the average tensile stress area to the actual tensile stress area within the effective embedment thickness; f_{ctm} = mean value of concrete tensile strength at time that crack forms; A_{ctx} = effective stretched area of concrete in direction x; d_{by} = diameter of bars in direction y; d_{bx} = diameter of bars in direction x; τ_{tp} = peak shear bond stress; and n_x = number of bars in direction x per unit width.

In development of this model, a parabolic distribution was assumed for the bond stresses, which contradicts the bond stress behaviour shown in Fig. 2.6. Also, a triangular distribution was assumed for splitting tensile stresses. The peak shear bond stress was taken to be constant for all geometrical conditions. These over-simplifications will be improved through the results of this study.

2.6 Summary

In this Chapter, the theory of one-way cracking is explained with the aid of CEB MC90 model, and the main influential parameters are introduced. The interaction between concrete and steel is identified as one important parameter in the crack width prediction models, and hence, described in more detail. Also, the crack control provisions of several design Codes are reviewed. Additionally, a number of previous studies on the cracking behaviour of two-way members are explained.

CHAPTER 3

FE PARAMETRIC STUDY OF ONE-WAY CRACKING

3.1 Introduction

In a reinforced concrete structure, different members or elements may undergo various types and combinations of loadings. This may add to the complexity of the resulting cracks. The ultimate goal of this study is to investigate the crack control under two-way loading conditions. As the first step towards the final and a more general solution, the problem is dealt with in its simplest form in this Chapter, i.e. one-way cracks. One-way cracks are those that develop under one-way loading conditions. Two types of one-way loading conditions will be investigated in sequence based on their complexity, namely, concentric tension, and pure bending moment.

In this study, the analytical approach is chosen among other techniques to develop a crack control model. This is because the analytical model is inexpensive as compared to the empirical model. Also, it can easily be modified to cover a wide range of applications in which experiments may not be economically feasible. The first step in developing such a model is to understand the mechanics of cracking. Once the underlying physics is understood, the simplified mathematical formulation can be established. For this purpose, two different sources will be used together to acquire the necessary information. One is the experimental data produced either by others or in this study, and the other one is the finite element (FE) technique. While the experimental data is useful for both understanding of the actual behaviour and validating

analytical models, the FE technique is a powerful tool to study complex events such as mechanical interactions, stress distribution, cracking, etc.

In this Chapter, a FE model for reinforced concrete is introduced. Different techniques for modeling the bond behaviour between the steel and concrete elements are examined. A new type of bond layer model is shown to be effective in simulating the actual mechanism of bond. The recommended FE model is verified against the experimental data from the literature. This FE model is used to perform several parametric studies for determination of the distribution of the bond stress, and the effective tension area.

3.2 FE Modeling of RC Tension Members

To further investigate direct tensile cracks and the validity of the one-way crack theory explained in the previous Chapter, the finite element (FE) technique will be used. The application of FE in modeling reinforced concrete cracking dates back to more than 40 years ago (Ngo and Scordelis 1967). At that time, the reinforced concrete model was very simple. Predefined crack patterns combined with a linear material model were used to represent the concrete. Link elements were also used between concrete and steel elements to represent the bond-slip mechanism. Since those pioneering times, the reinforced concrete FE model has enjoyed continuous advancements. Today's state of the art concrete models can efficiently capture the highly non-linear tensile cracking behaviour of concrete. To better understand these models, the fracture theory of concrete cracking will be explained first.

3.3 Fracture Theory of Quasi-Brittle Materials

In fracture mechanics, materials can be categorized into three different types, namely, brittle, quasi-brittle, and plastic. For all these material types, the rupture initiates when the tensile stress reaches up to the tensile strength. However, the post-cracking behaviour is different for each of these types. For a brittle material, the tensile stress across the crack will drop quickly to zero causing the crack to abruptly penetrate through the section. On the other hand, for the other two types, a micro-cracked region will form at the tip of the crack so called fracture process zone.

For the crack to propagate, a certain amount of energy must be provided, which will be consumed in the fracture process zone. This energy is called the fracture energy and is defined as the amount of energy needed for the formation of a unit area of a crack. For that reason, the post-cracking stress/strain curve of these materials shows a gradual decrease to zero rather than a sudden drop.

The size of the fracture process zone is quite small for plastic materials, which makes the linear elastic fracture mechanics relevant for this type of materials. However, the size of the fracture process zone is quite large for quasi-brittle materials such as concrete, meaning several times the aggregate size. When the size of the structure is small relative to the size of the fracture process zone (less than 100 times the aggregate size, Bazant 1979), some sensitivity to the size of the structure can be observed in the structural behaviour. This means most laboratory size specimens exhibit some degree of size effects. For that reason, nonlinear fracture mechanics must be used for a quasi-brittle material such as concrete.

While most existing formulas for the crack prediction are based on the strength criterion, Bazant and Oh (1983a) suggested that a fracture mechanics model would be a more appropriate approach for a notch-sensitive material such as concrete. The strength criterion is sufficient to indicate when the initiation of a crack takes place. However, a certain amount of energy must be supplied afterwards so that a distinct crack could form. As mentioned before, this energy is called the fracture energy G_f and is regarded as the material property of the concrete. By definition, the fracture energy is the amount of energy needed for the formation of a unit area of a crack, which is equal to the area under post-cracking stress-strain diagram times the effective width of the fracture process zone. They also pointed out that inherent to the inhomogeneities of the concrete the fracture process zone is longer than several times the aggregate size. This means in a realistic crack model the crack growth could only take place in increments several times the aggregate size. This is especially appropriate for smaller scale members in which an infinitesimal growth of the crack is just meaningless. Their proposed model predicts the crack spacing by equating the energy consumed in the formation of a crack to the strain energy release happening in the concrete regions near that crack. In this model, the crack is assumed to form through the entire depth of the cover at once, which is more appropriate for small concrete covers.

Fracture energy based models best suit the numerical analysis such as finite element, however, for analytical calculations they yield bulky equations yet after several simplifications such as constant bond stress, uniform transverse strain distribution, or a crack formation step for the full depth of the cover at once, as attempted by Bazant and Oh (1983a). An argument can be made on whether such a complex model is worthwhile after numerous simplifications. Here in this study the fracture energy models will be used through the FE modeling only. The results of FE analysis will be incorporated in an analytical model, which will be developed based on the strength based criterion due to its simplicity for practical use.

Two slightly different approaches are commonly used in the FE modeling of the concrete fracture, namely, the fictitious crack model developed by Hillerborg et al. (1976) and the crack band model developed by Bazant and Oh (1983b). In the former, the post-cracking behaviour of concrete is defined by a stress/crack opening displacement curve. This curve will be automatically converted to stress/strain by the program. This is achieved by dividing the crack opening displacement by a characteristic crack length, which depends on the mesh geometry and formulation. The mesh sensitivity is reduced with this approach as the concrete behaviour is determined primarily by the opening at the crack rather than its strain. In the latter approach, i.e. the crack band model, the post-cracking behaviour is defined directly by the stress/strain curve. This approach can induce some mesh sensitivity if the same stress/strain curve is used for different mesh sizes. In this way the deformation of a concrete element is influenced by its length rather than the opening at the crack, as the deformation is the product of the strain and the length of that element. Therefore, the mesh size must be considered for the definition of the stress/strain curve to reduce this effect. The two approaches must yield nearly identical results if the mesh size effect is considered in the definition of the stress/strain curve.

In this study, ABAQUS 6.7 (Hibbitt et al. 2007) is adopted as the finite element computer platform. The stress/crack opening displacement approach is used for the concrete post-cracking material model to eliminate the mesh sensitivity. Also, wherever possible, the mesh sizes are chosen to have an aspect ratio very close to 1 to reduce the mesh sensitivity induced by the definition of the characteristic crack length. From several different material models available in

ABAQUS for concrete, Damaged Plasticity is selected. This model is briefly explained in the following Section.

3.4 Damaged Plasticity Model

The damage plasticity model in ABAQUS is based on the models proposed by Lubliner et al. (1989) and by Lee and Fenves (1998). The model is a continuum, plasticity-based, damage model that provides a general capability for the analysis of concrete structures under monotonic, cyclic and/or dynamic loading under low confining pressures. Under low confining pressures, concrete behaves in a brittle manner, and the main failure mechanisms are cracking in tension and crushing in compression.

The concrete damaged plasticity model uses an isotropic linear elastic behaviour for the material prior to yield. The model makes use of the yield function of Lubliner et al. (1989) with the modifications proposed by Lee and Fenves (1998) to account for different evolution of strength under tension and compression. The evolution of the yield surface is controlled by two hardening variables, namely the tensile equivalent plastic strain ε_t^{pl} and the compressive equivalent plastic strain ε_c^{pl}, linked to failure mechanisms under tension and compression loading, respectively. The model also assumes nonassociated potential plastic flow. The flow potential used for this model is the Drucker-Prager hyperbolic function. The plastic flow potential function and the yield surface make use of two stress invariants of the effective stress tensor, namely the hydrostatic pressure stress $\bar{p}$ and the Mises equivalent effective stress $\bar{q}$. The definition of various parameters associated with this model and their assumed values are explained in the following,

ψ = the dilation angle measured in the *p*-*q* plane at high confining pressure taken to be 34°.

ϵ = Flow potential eccentricity, which is a small positive number that defines the rate at which the hyperbolic flow potential approaches its asymptote. The default value of 0.1 is accepted.

σ_{b0}/σ_{c0} = the ratio of the initial equibiaxial compressive yield stress to initial uniaxial compressive yield stress. The default value of 1.16 is used.

K_c = the ratio of the second stress invariant on the tensile meridian to that on the compressive meridian at initial yield for any given value of the pressure invariant p such that the maximum principal stress is negative. The default value of 2/3 is used.

For the reason that, the failure mode of all models used in this study is governed primarily by the tensile cracking, the above parameters do not have a major effect and their default values can be acceptable. To define the compressive behaviour of concrete beyond the elastic range, the uniaxial compressive stress/strain curve must be defined in terms of the stress/inelastic strain ε_c^{in}. The inelastic strain is shown in Fig. 3.1 and is defined as,

$$\varepsilon_c^{in} = \varepsilon_c - \varepsilon_{0c}^{el} = \varepsilon_c - \frac{\sigma_c}{E_{ci}} \tag{3.1}$$

where ε_c = concrete total compressive strain; ε_{0c}^{el} = undamaged elastic compressive strain; E_{ci} = initial undamaged stiffness; and σ_c = concrete compressive stress.

The tensile stress/strain curve of concrete is shown in Fig. 3.2. An elastic behaviour is assumed for concrete prior to cracking. The tensile behaviour of concrete in post-cracking range is defined with a softening curve in terms of the stress/cracking strain ε_t^{cr}. The cracking strain is defined as,

$$\varepsilon_t^{cr} = \varepsilon_t - \varepsilon_{0t}^{el} = \varepsilon_t - \frac{\sigma_t}{E_{ci}} \tag{3.2}$$

where ε_t = concrete total tensile strain; ε_{0t}^{el} = undamaged elastic tensile strain; and σ_t = concrete tensile stress.

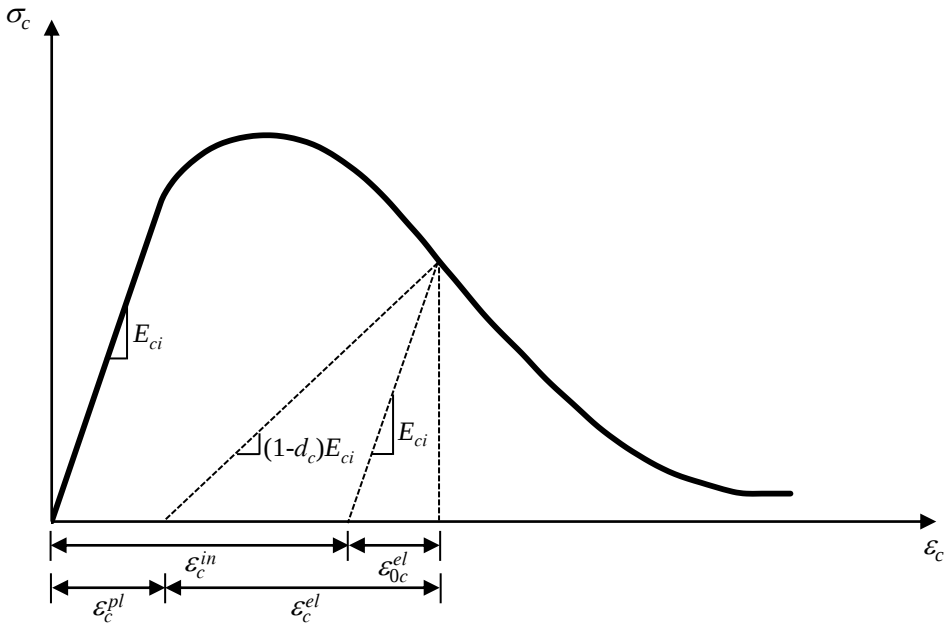

Fig. 3.1 Compressive stress/strain curve for damaged plasticity model

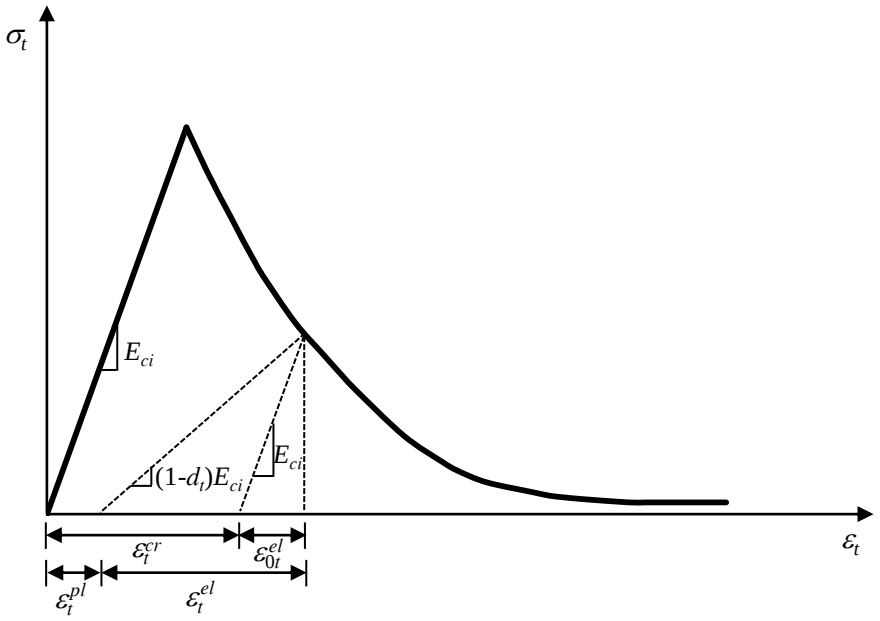

Fig. 3.2 Tensile stress/strain curve for damaged plasticity model

Alternatively, the post-cracking behaviour can be defined with stress/cracking displacement u_t^{cr} curve. The area under this curve must be equal to the fracture energy of the concrete G_f. Various methods are recommended by different researchers for the definition of this curve. These methods will be explained later in this Chapter. The program will convert this curve to the stress/cracking strain curve by dividing the crack displacement u_t^{cr} by the characteristic crack length. The characteristic crack length represents the effective width of the fracture process zone and depends on the element geometry and formulation. In damaged plasticity model this length is a typical length of a line across an element for a first-order element, and half of the same typical length for a second-order element. This definition will induce some mesh sensitivity for elements with large aspect ratios depending on the direction of the crack. Therefore, elements with aspect ratios closer to one are used to minimize this effect.

As it is shown in Figs. Fig. 3.1 and Fig. 3.2, the unloading path for the stress/strain curve can be arbitrarily described by defining damage variables d_c and d_t in compression and in tension, respectively. In the case of a cyclic loading condition, this model is also capable of defining the load reversal path for the stress/strain curve through stiffness recovery factors w_c and w_t in compression and in tension, respectively. As all models in this study deal with monotonic loading conditions only, the definition of these parameters is not a great concern. Therefore, zero values are considered for damage variables and default values of stiffness recovery factors are adopted, meaning 1 and 0 for w_c and w_t, respectively

3.5 Solution Techniques

The response of a reinforced concrete structure under an increasing static load is highly nonlinear, which involves collapse behaviour due to cracking. In other words, at the moment of cracking the load-displacement response exhibits a negative stiffness and the structure must release strain energy to remain in equilibrium. In FE modeling, one approach to treat such a problem is by including inertia effects through a dynamic analysis. The explicit dynamic solution technique is among this type of analysis. Another approach is to find the static equilibrium states during the unstable phase of the response using the modified Riks method. The explicit dynamic

solution technique is used here as the main solution scheme and the static Riks method is used only to make a comparison.

The explicit dynamic solution technique is a direct-integration dynamic procedure that uses the central-difference operator. The explicit central-difference operator satisfies the dynamic equilibrium equations at the beginning of the increment t, the accelerations calculated at time t are used to advance the velocity solution to time $(t + \Delta t/2)$ and the displacement solution to time $(t + \Delta t)$. Because the displacements and velocities are calculated in terms of quantities that are known at the beginning of an increment, the global mass and stiffness matrices need not be formed and inverted, which means that each increment is relatively inexpensive. However, the size of the time increment has a limit to prevent the method from generating large, rapidly growing errors. This is because the central-difference operator is only conditionally stable.

The stability time limit for the central-difference method is closely related to the time required for a stress wave to cross the smallest element dimension in the model. Therefore, the method is computationally attractive for problems in which the total dynamic response time that must be modeled is only a few orders of magnitude longer than this stability limit. This method can also be used for slow quasi-static processes in which it is appropriate to use mass scaling to reduce the wave speed or to speed up the total response time if the rate-dependency is not included in the material behaviour.

Artificially increasing the material density is called “mass scaling,” which reduces the ratio of the event time to the time for wave propagation across an element while leaving the event time fixed. This allows rate-dependent behaviour to be included in the analysis. If the rate-dependency is not an issue speeding up the time of simulation can have the same effect. Mass scaling must be used with care to ensure that the inertia forces do not dominate and change the solution

The modified static Riks method is used for cases where all loads are proportional to a single scalar parameter. The Riks method uses the load magnitude as an additional unknown and it solves simultaneously for loads and displacements. The basic algorithm to solve the nonlinear equilibrium equations is the Newton method. The solution is obtained as a series of increments,

with iterations to obtain equilibrium within each increment. Increments must be kept small to ensure correct modeling. In the load-displacement space, the increment size is limited by moving a given distance along the tangent line to the current solution point and then searching for equilibrium in the plane that passes through that point, which is orthogonal to the same tangent line.

3.6 Preliminary Verification of FE Technique

To assess the performance and accuracy of the aforementioned FE modeling techniques in predicting the behaviour of reinforced concrete structures, a simple case study conducted by Kankam (1997) is selected. This study is explained in the Section 2.3.1 of the previous Chapter. The steel stress variation along the hot-rolled deformed reinforcing bar reported in this test will be used for comparison with the results of FE modeling.

3.6.1 Estimation of material properties

Because the modulus of elasticity and the tensile strength of concrete were not reported, they can be estimated based on its compressive strength. Two various formulations are considered, namely, the CEB-FIP MC90 (1990) and the ACI 209R-92 (1992) recommended formulas. The CEB MC90 recommended formulas are as follows,

$$E_c = E_{co}\left[f_{cm} / f_{cmo}\right]^{1/3} \tag{3.3}$$

$$f_{ctm} = f_{ctko,m}\left(\frac{f_{ck}}{f_{cko}}\right)^{2/3} \tag{3.4}$$

$$f_{cm} = f_{ck} + \Delta f \tag{3.5}$$

where f_{cm} = mean value of compressive strength of concrete; f_{ctm} = mean value of tensile strength of concrete; f_{ck} = characteristic compressive strength of concrete (strength below which 5% of all

possible strength measurements for the specified concrete may be expected to fall) ; E_{co} = 2.15 x 10^4 *MPa*; f_{cmo} = 10 *MPa*; $f_{ctko,m}$ = 1.40 *MPa*; f_{cko} = 10 *MPa*; and Δf = 8 *MPa*.

For comparison, the recommendations of the ACI 209R-92 (1992) for the calculation of concrete properties will also be considered as follows,

$$E_c = g_{ct}\left[\gamma_c{}^3 f_c'\right]^{1/2} \tag{3.6}$$

$$f_{ct} = g_t\left[\gamma_c f_c'\right]^{1/2} \tag{3.7}$$

where γ_c = unit weight of concrete (kg/m^3); f_c' = compressive strength of concrete (*MPa*); f_{ct} = tensile strength of concrete; g_{ct} = 0.043; and g_t = 0.0069.

To define the post-cracking curve of concrete for use in FE modeling, the fracture energy of concrete is needed. To approximate the fracture energy of concrete (G_f), the recommended formulation of CEB-FIP MC90 (1990) is used here as follows,

$$G_f = G_{fo}(f_{cm}/f_{cmo})^{0.7} \tag{3.8}$$

where G_{fo} = base value of fracture energy ($N.mm/mm^2$)(0.025, 0.030, 0.058 for maximum aggregate sizes of 8, 16 and 32 mm, respectively).

Three different models for post-cracking stress/displacement behaviour of concrete will be investigated in this study, namely, Bazant and Oh (1983b), Hillerborg (1976), and CEB-FIP MC90 (1990). These models are shown in Fig. 3.3. The corresponding defining parameters for these models are presented in Table 3.1 and Table 3.2.

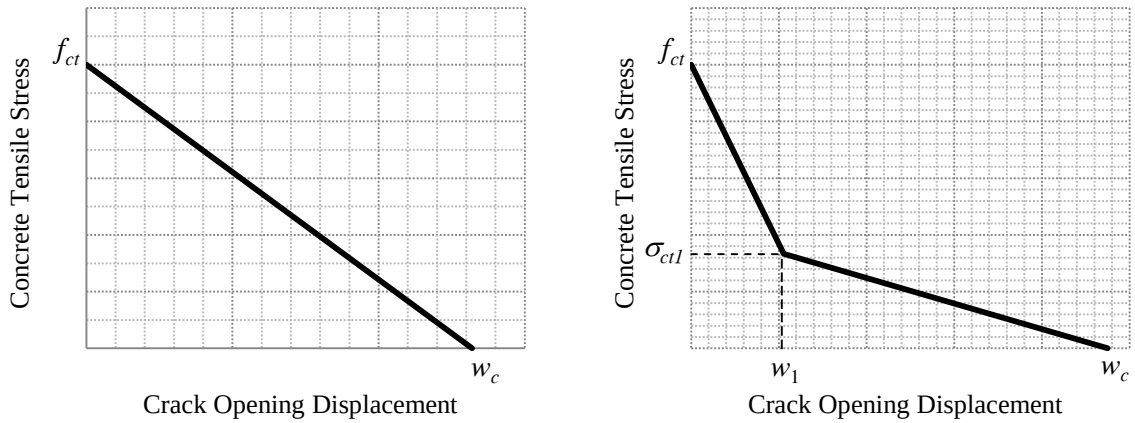

(a) (b)

Fig. 3.3 Post-cracking stress/strain curves a) Bazant & Oh, b) Hillerborg and CEB

Table 3.1 Post-cracking stress/displacement curve parameters corresponding Fig. 3.3.

	w_c	w_1	σ_{ct1}
Bazant & Oh	$2G_f/f_{ct}$	-	-
Hillerborg	$3.6G_f/f_{ct}$	$0.8G_f/f_{ct}$	$f_{ct}/3$
CEB	$\alpha_F G_f/f_{ct}$	$(2\text{-}0.15\alpha_F)G_f/f_{ct}$	$0.15f_{ct}$

Table 3.2 Coefficient α_F in CEB model

$a_{s,max}$ (mm)	8	16	32
α_F	8	7	5

$a_{s,max}$: maximum size of aggregates

For the FE modeling of Kankam test the square section of the tie element is transformed to an equivalent circular section. In this way, the RC tie member can be modeled with axisymmetric elements, which are much more computationally time-efficient than 3D elements. Also to preserve the diameter of the reinforcing bar, the reduction in the cross section area of the bar due to the presence of the groove is considered through an adjustment of the modulus of elasticity of steel as follows,

$$E_{s,\text{fictitious}} = \frac{A_{s,\text{net}}}{A_{s,\text{gross}}} E_s \tag{3.9}$$

where $E_{s,\text{fictitious}}$ = adjusted modulus of elasticity of steel, $A_{s,\text{net}}$ = net cross sectional area of steel ($A_{s,\text{gross}}$-A_{groove}), $A_{s,\text{gross}}$ = gross cross sectional area of steel, and E_s = actual modulus of elasticity of steel.

The specifications of the Kankam test and the estimated material properties based on the Eqs. 3.3 to 3.9 are summarized in Table 3.3. The post-cracking stress/displacement curves of concrete, which are used for FE modeling calculated based on Fig. 3.3 and Table 3.1 are shown in Table 3.4 and Fig. 3.4. The area under each of these curves is equal to the fracture energy of concrete, however, each curve suggests a different trend for the development of the crack opening displacement with the concrete stress. A bi-linear curve is adopted for modeling the compressive stress/strain behaviour of concrete. The strain at ultimate compressive stress is assumed to be 0.0022 *mm*/*mm* and the resulting curve is shown in Fig. 3.5. The inelastic strains calculated based on Eq. 3.1 are also shown in this figure, which will be used as an input for FE modeling.

Table 3.3 Test data and estimated properties for Kankam test

	Specimen Cross Section (mm)	Length of Embedment (mm)	d_b (mm)	Groove Area (mm^2)	$A_{s,net}$ (mm^2)	Approx. E_s (GPa)	$a_{s,max}$ (mm)	$f_{cc,cube,14}$ (MPa)
Test Data	150×150	200	25	76	415	200	10	50

	Equivalent Circular Section (mm)	Steel Poisson's Ratio ν_s	Assumed E_s (GPa)	Fictitious E_s (GPa)	γ_c (kg/m^3)	α_F	Concrete Poisson's Ratio ν_c
Equivalent & Assumed Data	169.3	0.3	214	181	2400	8	0.18

	f_c' (MPa)	E_c (MPa)			f_{ck} (MPa)	f_{ct} (MPa)			G_f (CEB) ($N.mm/mm^2$)
		ACI209R	CEB	Assumed		ACI209R	CEB	Assumed	
Estimated Data	40	31975	34129	33000	32	2.14	3.04	2.50	0.066

d_b: diameter of reinforcing bar

$f_{cc,cube,14}$: cube compressive strength of concrete at 14 days

Table 3.4 Various post-cracking models for FE modeling of Kankam test

	Bazant & Oh		Hillerborg			CEB		
w (mm)	0.00	0.05	0.00	0.02	0.10	0.00	0.02	0.21
σ_{ct} (MPa)	2.50	0.00	2.50	0.83	0.00	2.50	0.38	0.00

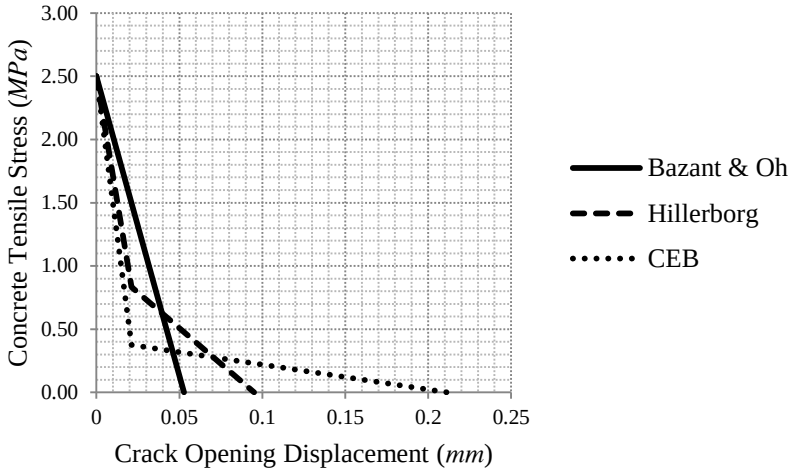

Fig. 3.4 Various post-cracking models for FE modeling of Kankam test

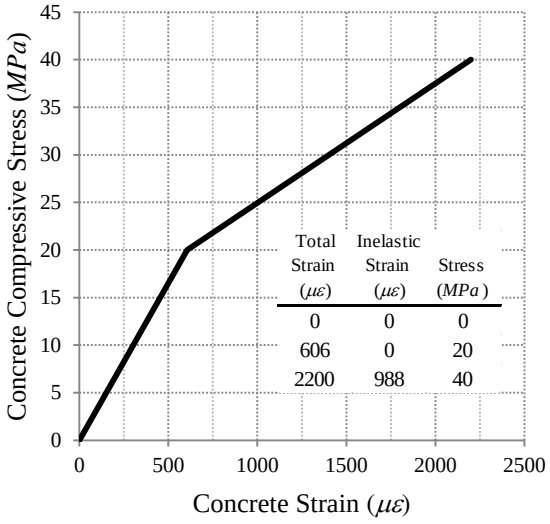

Fig. 3.5 Compressive stress/strain curve of concrete for FE modeling of Kankam test

3.6.2 Details of FE model

The tension RC prism tested by Kankam (1997) is transformed to an equivalent cylindrical tie element. In this way, the use of axisymmetric elements will make the modeling much more efficient. The geometry and the boundary conditions of the FE model are shown in Fig. 3.6. The pulling force condition in the test is equivalently simulated through a displacement control condition. A displacement that smoothly ramps up from zero to its maximum value throughout the loading step is prescribed at the loading end of the steel elements. With this method, in the case of a dynamic analysis, the unwanted accelerations due to cracking will be minimized. The damaged plasticity model explained earlier in this Chapter is used for the concrete material. As the steel behaviour beyond its yielding point is not of interest in this study, an elastic model is used for the steel material. The aforementioned explicit dynamic solution technique is used for all models unless stated otherwise. A perfect bond condition is provided at the steel/concrete interface, meaning, the concrete and the steel elements share the same nodes at their connecting interface.

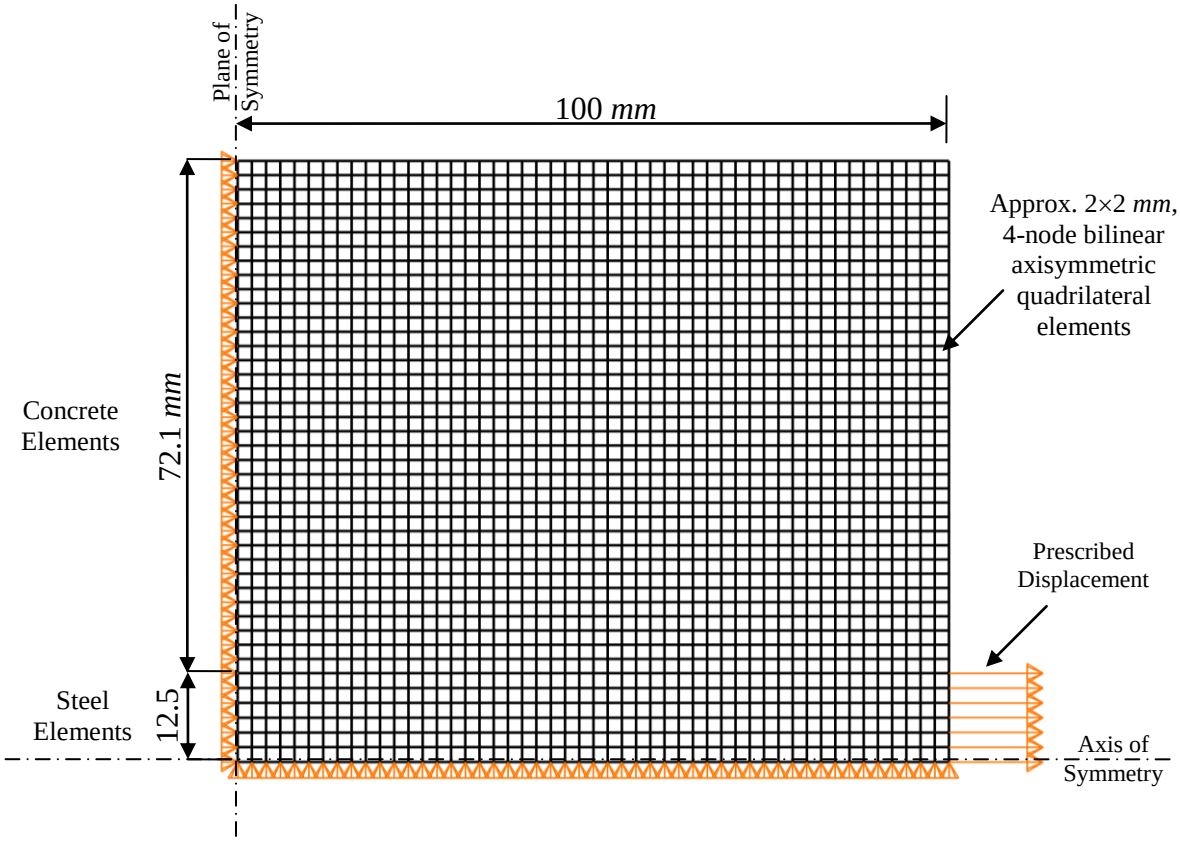

Fig. 3.6 FE model for Kankam specimen with perfect bond condition

3.6.3 Results of FE analysis

The variation of the steel strain along the reinforcing bar is the selected variable for comparison of the FE results with the experimental data. This variable is directly related to the tangential/shear bond stresses. The FE results for three different post-cracking models, introduced earlier in this Chapter, are shown in Fig. 3.7. These models show a similar trend at lower loading levels with the maximum steel stresses of about 100 *MPa*, however, they shift away from each other at higher loading levels with the maximum steel stresses of about 200 *MPa*. All results are in a good range compared to the experimental data with the CEB model showing the lowest and the Bazant and Oh model the highest shear bond strength.

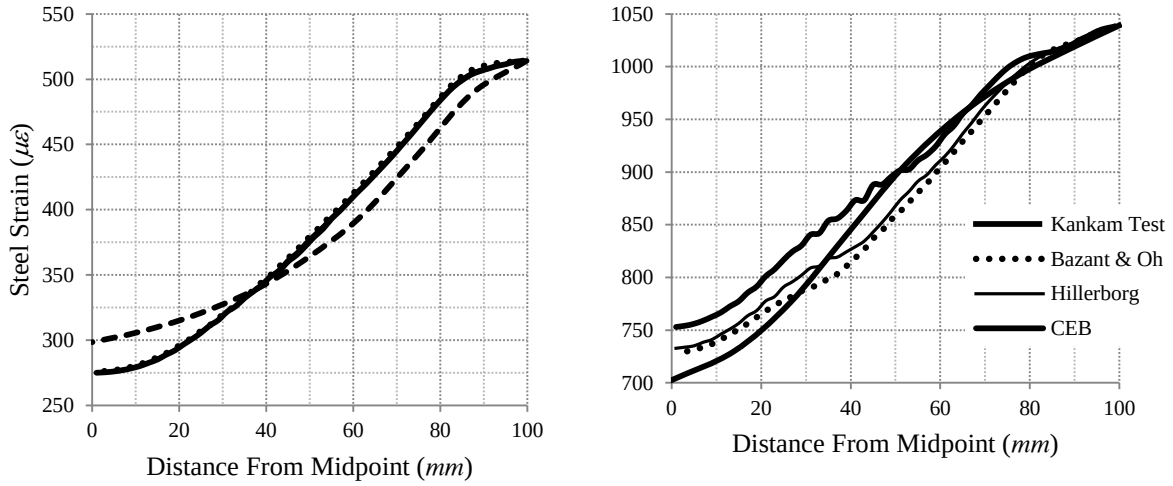

(a) (b)

Fig. 3.7 Steel strain variation, comparison of various post-cracking curve models, a) $T = 50\ kN$, b) $T = 98\ kN$

The sensitivity of the model to the number of time increments for the full loading step is investigated in Fig. 3.8 and Fig. 3.9. Although the steel strain variation has not shown a significant change with the number of increments in Fig. 3.8, a slight change is noticeable looking at the principle strain contours in Fig. 3.9. The higher the number of time increments, the higher accuracy is expected from the model. Although the number of increments is very high, the processing time of each increment is efficiently short. The formation of a secondary crack close to the reinforcing bar is also noticeable in the Fig. 3.9. This behaviour is in confirmation of the

experimental observations reported by Goto and Otsuka (1979). They observed the formation of diagonal secondary cracks around the reinforcing bar.

The sensitivity of the model to the size of elements is investigated in Fig. 3.10. Increasing the element size does not affect the steel strain variations and hence the overall response of the structure to any considerable extent. However, the concrete strain contours are observed to be altered, which is expected for such a big change in the mesh size.

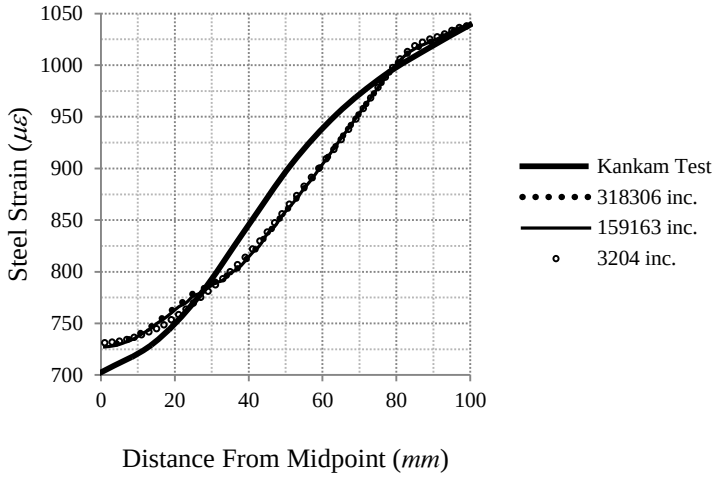

Fig. 3.8 Sensitivity to the number of time increments

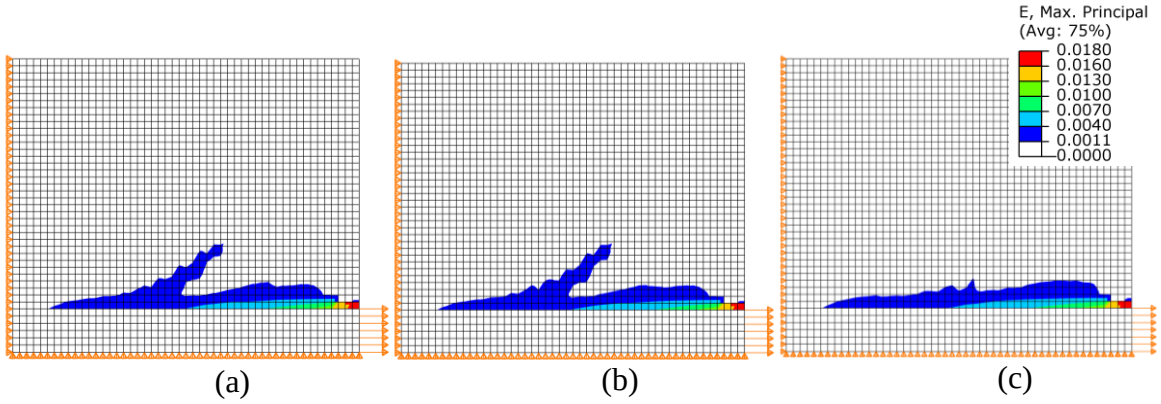

Fig. 3.9 Sensitivity to the number of increments, reduced contour of the principle tensile strain, a) 318306 inc., b) 159163 inc., c) 3204 inc.

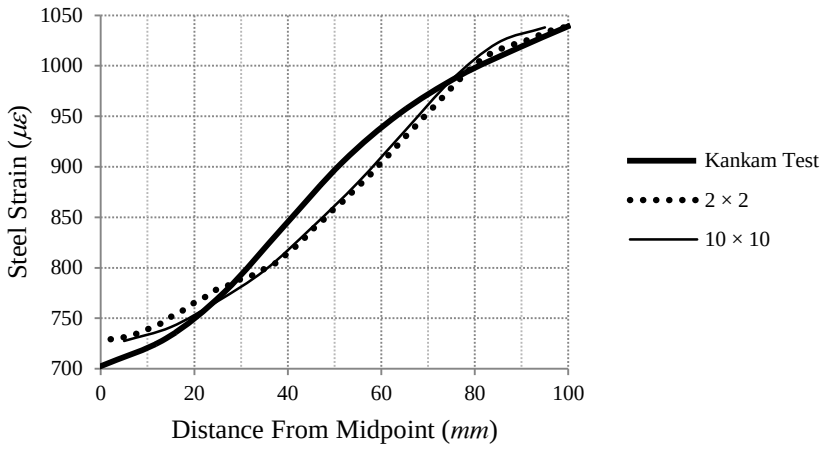

Fig. 3.10 Sensitivity to the mesh size

The influence of the tensile strength of concrete on the steel strain variation is shown in Fig. 3.11. It is clear that the bond strength is closely related to the tensile strength of concrete. Therefore, a proper estimation of the tensile strength of concrete is essential for an accurate modeling of the bond behaviour.

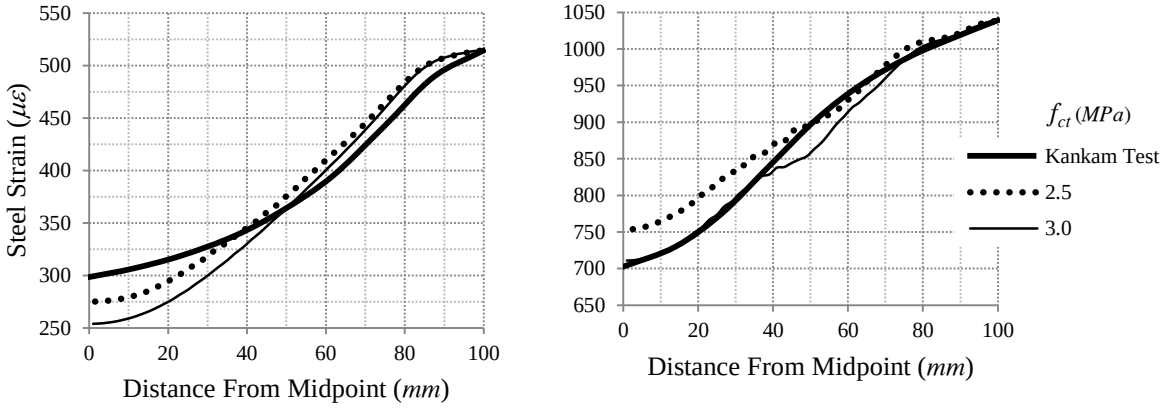

(a) (b)

Fig. 3.11 Sensitivity to the tensile strength of concrete, a) T = 50 kN, b) T = 98 kN

As explained before, two different solution techniques are used here to verify the performance of the FE modeling. Therefore, for a selected model the solution technique is changed from the explicit dynamic to the static Riks. The results are compared with each other in Fig. 3.12. The two results are in a good agreement to each other. Despite its much lower number of increments, it takes much longer time for the analysis to complete with the static Riks solution technique than with the explicit dynamic solution technique. Additionally, the static Riks solution technique shows a higher sensitivity to the number of increments. It can be concluded that for the same level of accuracy, the explicit dynamic solution technique is much more cost-effective than the static Riks solution technique.

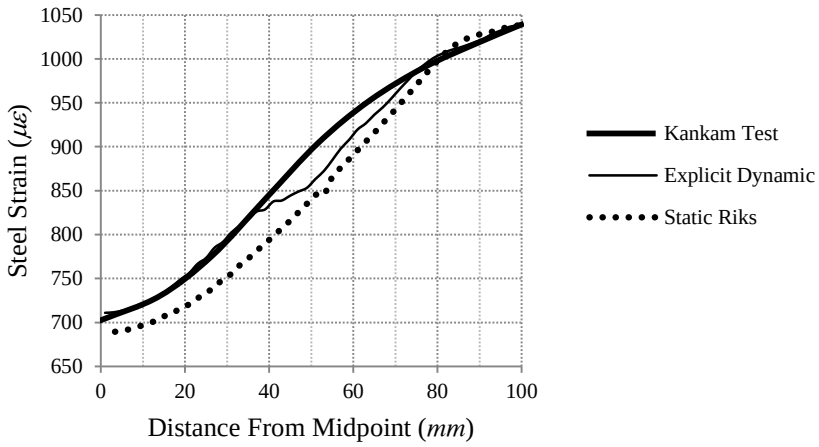

Fig. 3.12 Comparison of results for explicit dynamic and static Riks solution techniques

3.7 Various Bond Models

To further improve the accuracy of the FE modeling for the crack prediction of RC structures, the attention is paid to the modeling of the interaction between the steel and the concrete. A valid FE modeling of the bond phenomenon must be able to correctly make a prediction of all components of the bond stress. The mechanism of bond at the steel and concrete interface is explained in detail in Section 2.3. In the following two different methods for modeling the bond mechanism are introduced, namely, the diagonal link elements, and bond layer model. The results of these models will be compared with the perfect bond model.

3.7.1 Diagonal link elements

If it is assumed that the bond-slip occurs mainly due to micro-cracking and the bond force is primarily transfers through diagonal compression struts around the bar lugs, then the bond interaction can be modeled with diagonal link elements. These diagonal link elements conventionally replace a layer of concrete elements close to the reinforcing bar to represent the diagonal compression struts. However, a different method is proposed here to model the diagonal bond forces.

As explained in Section 2.3, the diagonal nature of the bond forces can rise from two sources. One source is the formation of diagonal compression struts due to the micro-cracking, and the other one is the wedging action in front of the bar lug. The effect of micro-cracking is already considered in the tensile behaviour of concrete elements next to the steel elements. This means that even for a perfect bond model the effect of micro-cracking at the bond interface is to some extent simulated. However, the effect of wedging action, which results in an increase in the radial bond forces is not considered in the perfect bond model.

To simulate the wedging action, diagonal link elements can be used to connect the nodes of steel elements to the nodes of concrete elements at the interface layer without replacing the concrete elements. In this manner, the effect of diagonal bond force caused by the wedging action is added to the perfect bond model. These diagonal elements can be formulated dimensionless, or alternatively, they can connect the nodes of an inner layer of steel elements to the nodes of concrete elements at the interface layer at a desired angle. This type of bond model is shown in Fig. 3.13. The steel and the concrete elements have separate nodes at the interface layer. The nodes of steel elements shown with solid squares are connected to the nodes of concrete elements shown with solid triangles using diagonal link elements (connector elements in ABAQUS). Since the direction of the bond stress can be reversed due to cracking, the link elements are provided in both longitudinal directions. The link elements are placed at two different angles of 45° and 30° as shown in Fig. 3.13 (a) and (b), respectively. In this way, the effect of the angle of link elements on the bond behaviour can also be examined.

The force/displacement behaviour of the link elements is shown in Fig. 3.14. A nonlinear elastic behaviour is adopted, meaning, the unloading path is the same as the loading path. This behaviour is also defined in a way to ensure that these elements are not taking any tensile force, and they only act in compression. For simplicity, these elements are assumed to behave as rigid as practically possible in compression i.e. with the stiffness of 10^7 *N*/*mm*. In this way, the bond-slip due to the concrete crushing and the frictional sliding is kept very limited.

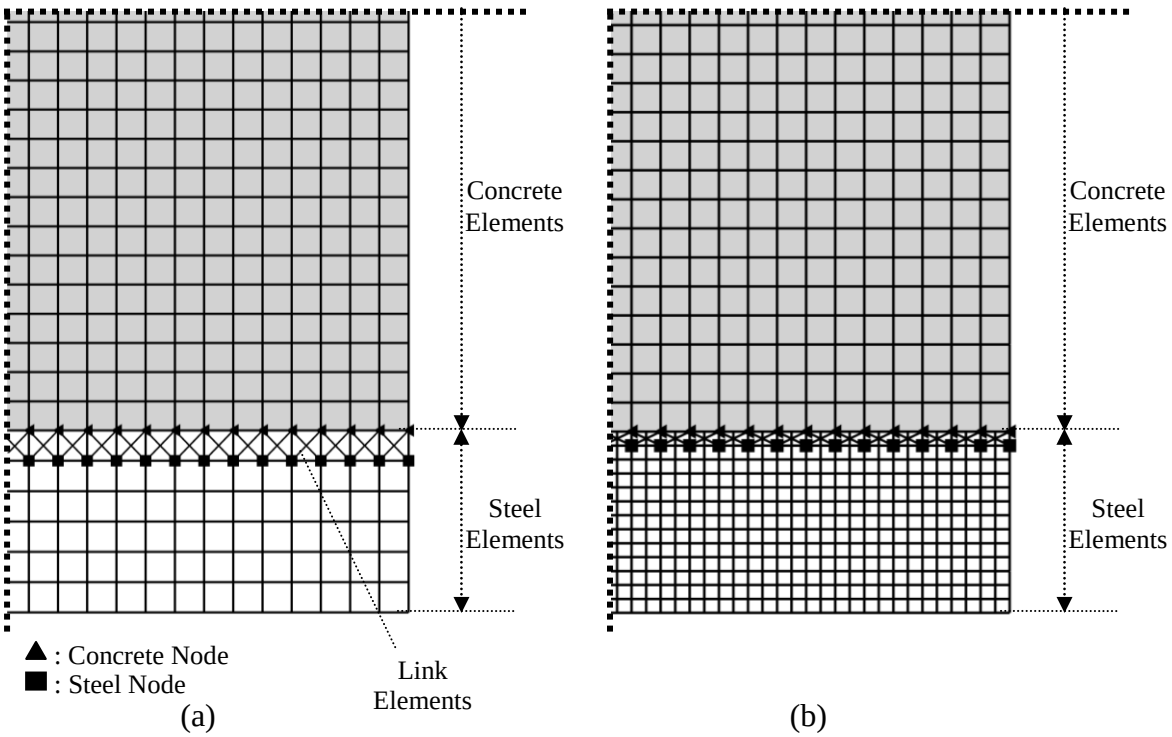

Fig. 3.13 Bond models with link elements, a) 45º inclination, b) 30º inclination

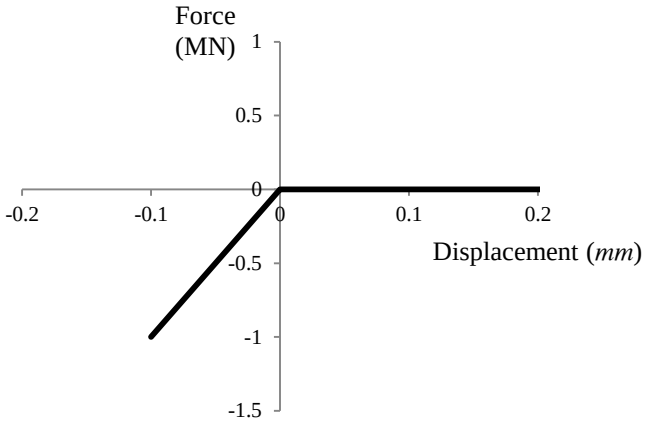

Fig. 3.14 Non-linear elastic behaviour of bond link elements

3.7.1.1 Verification of diagonal link element bond model

The diagonal link element bond model is incorporated in the FE model of the Kankam tension prism, explained in the Section 3.6. The results for the steel strain variation along the bar axis is shown in Fig. 3.15. It can be seen that the steel strain variation, and thus, the shear bond stress is nearly the same for the 45° link element, the 30° link element, and the perfect bond models. A slight difference in these results indicates that the perfect bond model produces the highest and the 45° link element bond model produces the lowest shear bond stresses. It must be noted that the model has a large enough concrete cover to prevent the formation of full-depth splitting cracks. Therefore, the similarity in the results of shear bond stresses may be reduced for smaller concrete covers. This is because of the fact that a noticeable difference is observed in the results of radial bond stresses, as shown in Fig. 3.16. In this figure, the splitting tensile stress variations are drawn along the radial axis at the face of the loading end (x = 100 *mm*) and also along the bar axis at a section with 20 *mm* radial distance from the face of the bar. It can be seen that the perfect bond model significantly underestimates the radial bond stresses estimated by the link element bond models. This behaviour is a sign for a deficiency in the perfect bond modeling approach.

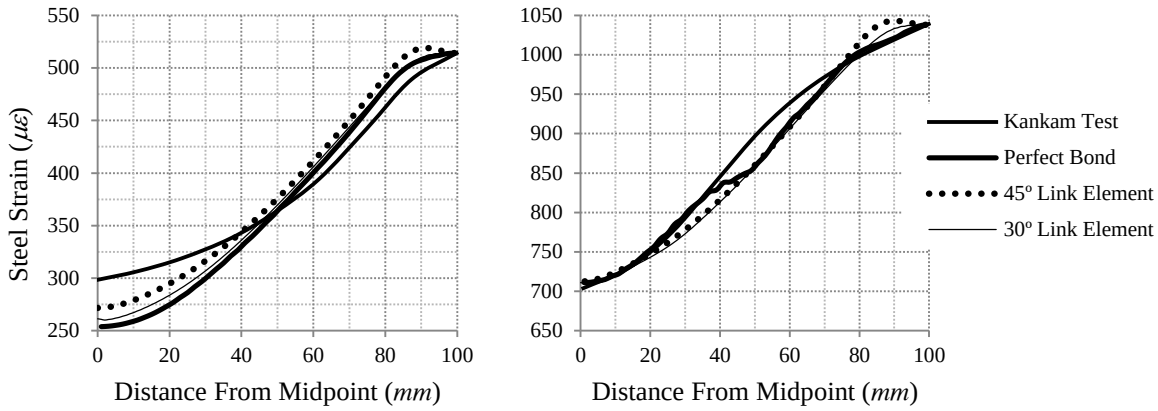

Fig. 3.15 Comparison of steel strain variation for perfect and link element bond models

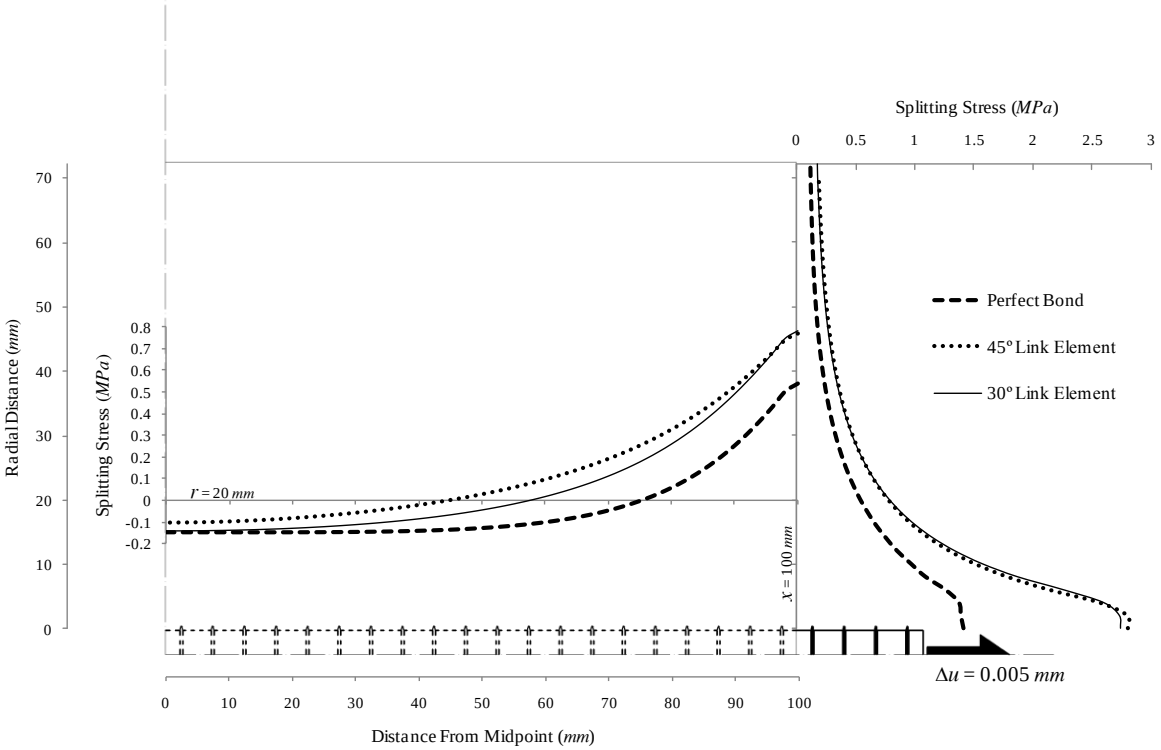

Fig. 3.16 Splitting tensile stress variation along radial and bar axes for various bond models

3.7.2 Bond layer model

Thus far, it is found that the perfect bond model has two flaws. One is to generate inadequate amount of tangential bond-slip, which results in higher tangential bond stresses, and the other

one is to produce inadequate radial bond stresses. The link element approach is a more accurate bond modeling method, however, defining these link elements in a model is quite time consuming, which makes it impractical for large structures. Additionally, the application of link elements in three dimensional models is associated with many difficulties and it needs special considerations. One method to simplify the application of link elements is to formulate them into the constitutive law of a two dimensional element. This is done by de Groot et al. (1981). Their model, so called, bond layer model, is consisted of several elastic link elements, which are mathematically combined in a two dimensional element. In this approach, a layer of concrete elements next to the reinforcing bar is replaced by the bond layer elements. The bond layer elements represent a layer of concrete that is micro-cracked just next to the reinforcing bar.

As an alternative approach to the bond layer model, which is created based on the combination of several elastic link elements, the material property of concrete elements next to the reinforcing bar can be modified in such a way that can improve the bond interaction. Accordingly, extremely reduced value of the tensile strength and the fracture energy of concrete will be used for these elements. In this manner, the force transfers from the reinforcing bar to the adjacent concrete through diagonal compressive stresses rather than tangential tensile stresses. This is in agreement with the actual bond behaviour in which early micro-cracks will cause the formation of diagonal compression struts. In reality, these micro-cracks also form in a very early stages of loading because of high concentration of stresses at the bar lugs. The only property modified in the bond layer elements is the definition of the post-cracking curve for the same concrete material model previously used. The definition of this curve is presented in Table 3.5. This curve is arbitrarily defined based on trial and error. The results are not sensitive to the definition of this curve as long as a very low tensile strength and fracture energy is used for this curve, so that, the tensile stresses diminish at very early stages of loading.

Table 3.5 Definition of post-cracking curve for bond layer elements

w (mm)	0.00	0.05	0.10
σ_{ct} (MPa)	0.02	0.009	0.00

3.7.2.1 Verification of bond layer model

The bond layer model is incorporated in the FE model of the Kankam tension prism, explained in the Section 3.6. The results of FE analysis are compared with the experimental data, and also with the results of other models in Fig. 3.17. For the steel strain variation shown in Fig. 3.17(a), the perfect bond model gives the highest variation of steel stresses, and hence, the highest shear bond stresses among other models. The bond layer model gives the lowest shear bond stresses similar to the experimental data. For splitting tensile stresses shown in Fig. 3.17(b), as it is expected, the bond layer model results are somewhere in-between the results of the perfect bond model and the link element models. This is because the perfect and the link element bond models represent the lowest and the highest extreme boundaries of the radial bond stresses, respectively. This shows the capability of bond layer model technique in properly simulating the bond mechanism.

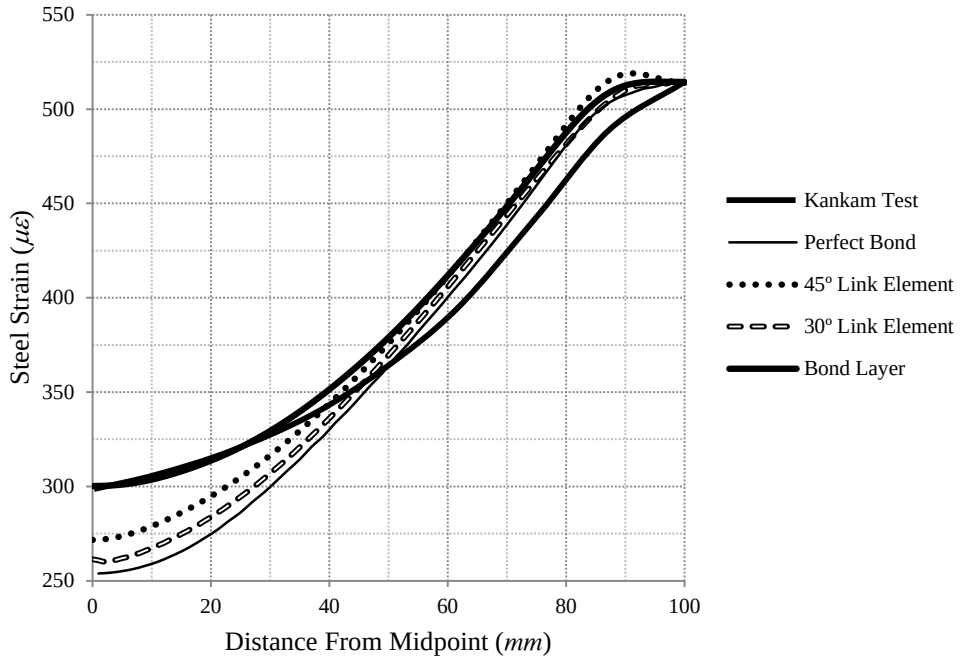

(a)

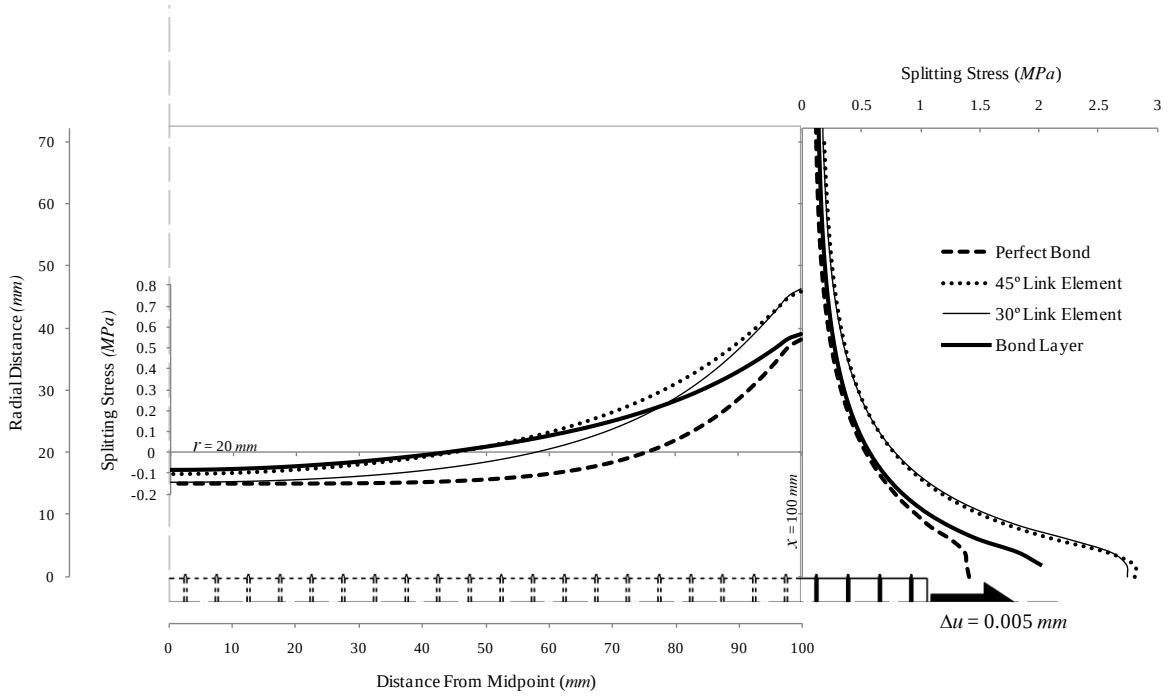

(b)

Fig. 3.17 Comparison of bond layer model and other bond models, a) steel strain variation along the bar axis, b) splitting tensile stress variation along radial and bar axes

3.8 Validation of Proposed FE Model

To further assess the accuracy of the proposed FE technique, which incorporates the bond layer model, another case study reported by Tammo and Thelandersson (2009) is considered in this section. Their experiment is explained in Section 2.3.2 of previous Chapter. One of the tested tie elements from their experiment is selected among others for this study.

3.8.1 Estimation of material properties

The reported data of the Tammo test and the estimated properties based on Eqs. 3.3 to 3.9 are given in Table 3.6. The post-cracking stress/displacement curve of concrete, which is used for the FE modeling, calculated based on the CEB model in Fig. 3.3 and Table 3.1, is given inTable 3.7. The compressive stress/strain curve of concrete along with the inelastic strains to be used as an input for the FE model is shown in Fig. 3.18.

Table 3.6 Test data and estimated properties for Tammo test

	Specimen Cross Section (mm)	Length of Embedment (mm)	d_b (mm)	$A_{s,net}$ (mm^2)	E_s (GPa)	γ_c (kg/m^3)	$a_{s,max}$ (mm)	$f_{cc,cube,28}$ (MPa)	$f_{sp,cube,28}$ (MPa)
Test Data	112×112	500	12	113	206	2313	16	36.5	2.95

	Equivalent Circular Section (mm)	Steel Poisson's Ratio ν_s	α_F	Concrete Poisson's Ratio ν_c
Equivalent & Assumed Data	126.4	0.3	7	0.18

	f_c' (MPa)	E_c (MPa)			f_{ck} (MPa)	f_{ct} (MPa)				G_f (CEB) ($N.mm/mm^2$)
		ACI209R	CEB	Assumed		ACI209R	CEB	$0.9f_{sp}$	Assumed	
Estimated Data	29.2	25848	30730	30000	21.2	1.79	2.31	2.66	2.66	0.053

$f_{sp,cube,28}$: cube splitting tensile strength of concrete at 28 days

Table 3.7 CEB post-cracking model for FE model of Tammo test

	CEB		
w (mm)	0.00	0.02	0.14
σ_{ct} (MPa)	2.66	0.40	0.00

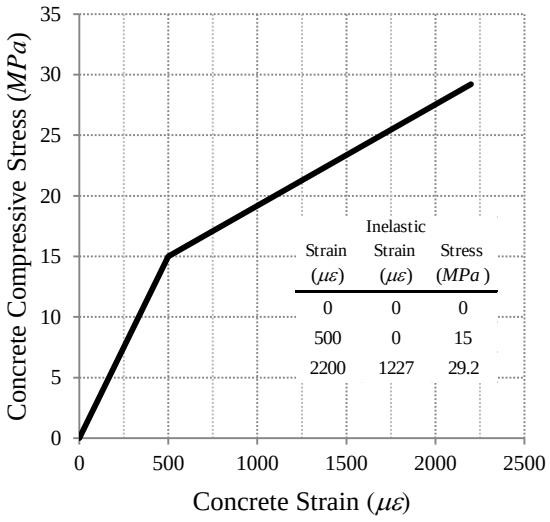

Fig. 3.18 Concrete compressive stress/strain curve for FE model of Tammo test

3.8.2 Details of FE model

The geometry and the boundary conditions of the FE model are shown in Fig. 3.19. The full length of the RC tie member is modeled due to the unsymmetric geometry imposed by a primary crack that will be formed within the length of the member. Two various bond models, namely, perfect bond model and bond layer model are used for comparison. For the bond layer model, the definition of the post-cracking curve for a layer of concrete elements just next to the steel elements is defined based on the data given in Table 3.5. The prescribed displacement applied to one end of the steel reinforcing bar is gradually increased throughout the loading step.

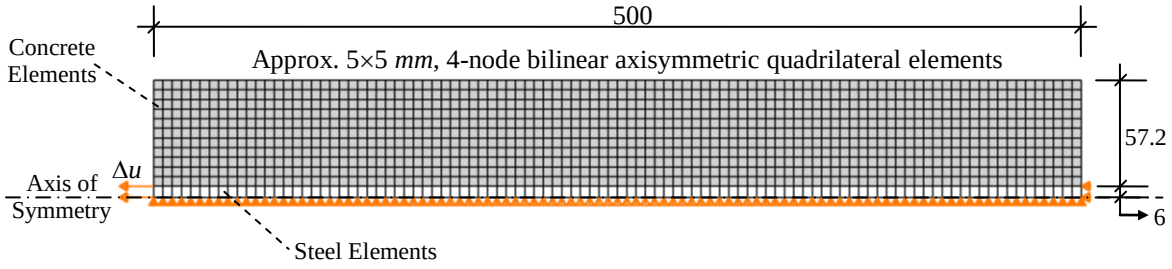

Fig. 3.19 FE model for Tammo specimen (dimensions in *mm*)

3.8.3 Results of FE analysis

The results of the FE model with a perfect bond condition are compared with the experimental data in Fig. 3.20. It can be seen that the FE results are in a good range of the experimental data, especially for the width of the crack at the mid-length of the member (w_{cr}). It must be noted that the significant drop in the steel stress after the formation of each crack is due to the displacement control loading condition used in the FE model. The initial crack is formed at a steel stress of about 300 *MPa* similar to the test data. However, another crack is formed at a steel stress of about 390 *MPa*, which is not in agreement with the experimental observations. This can be an indication of slightly over-estimated shear bond stresses in the perfect bond model. On the other hand, the formation of a second crack is not observed in the results of the FE model with a bond layer condition as shown in Fig. 3.21. Also, the results for the fictitious crack widths are in a closer range of the experimental data in this model than those in the perfect bond model.

The variation of the shear bond stress along the bar axis is shown in Fig. 3.22. It can be seen that the shear bond stress typically increases from zero at the crack to its peak value and then reduces to zero halfway the spacing between two consecutive cracks. Also, the location of the peak bond stress is biased toward the location of the crack. The shape of the bond stress variation curve is not following any low-order polynomial curve. This behaviour contradicts the assumption of parabolic curves in formulating the shear bond stress as made by other researchers (Rizk and Marzouk 2010).

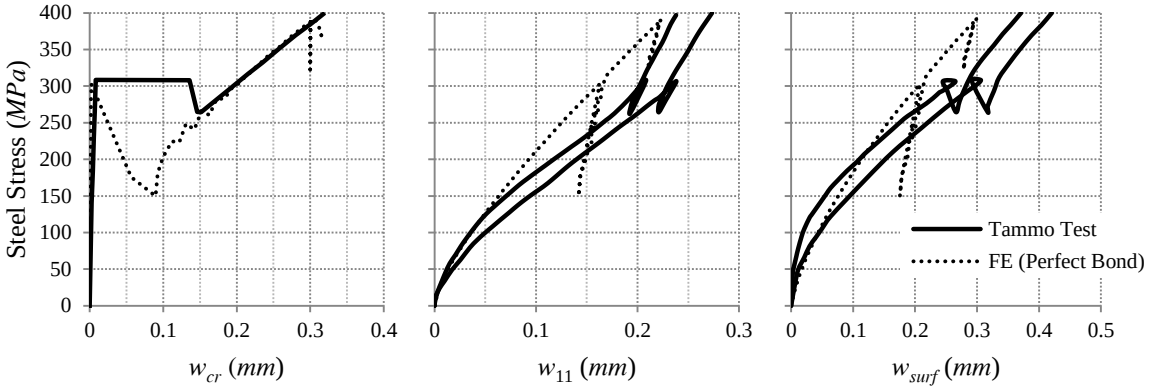

Fig. 3.20 Results of FE model with perfect bond condition for Tammo test

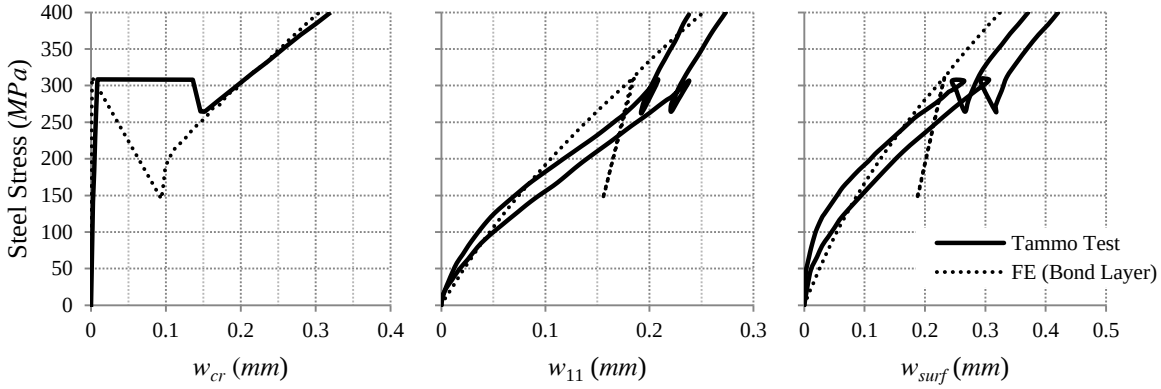

Fig. 3.21 Results of FE model with bond layer condition for Tammo test

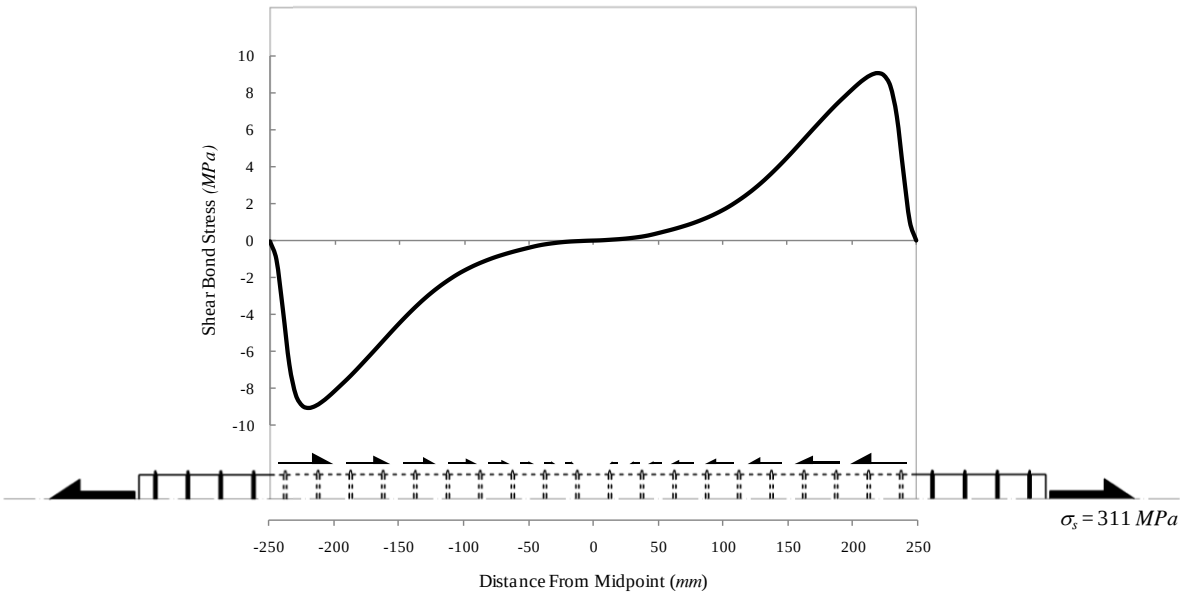

(a)

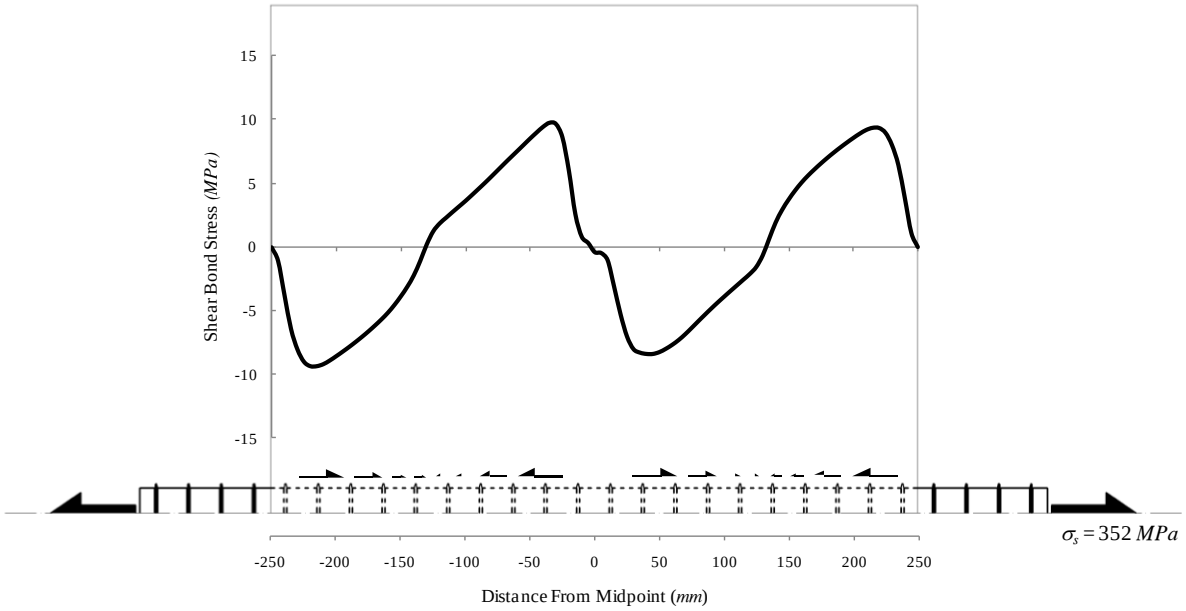

(b)

Fig. 3.22 FE shear bond stresses for Tammo test with bond layer model a) right before cracking, b) after cracking

The results of the splitting tensile stresses at different steel stress levels are also shown in Fig. 3.23. These stresses are drawn along the radial axis through the concrete cover at a section close to the loading end, and also, along the longitudinal axis at a concrete cover depth of 30 *mm*

distance to the surface of the reinforcing bar. The splitting tensile stresses are at their peak value at the loading end, and they gradually decrease to zero halfway between two consecutive cracks. It can be seen that the splitting tensile stresses can easily reach up to the tensile strength of concrete even at low steel stresses of about 100 *MPa*. This implies that the consideration of the splitting tensile stresses is imperative for the accuracy of any crack prediction model in two-way systems.

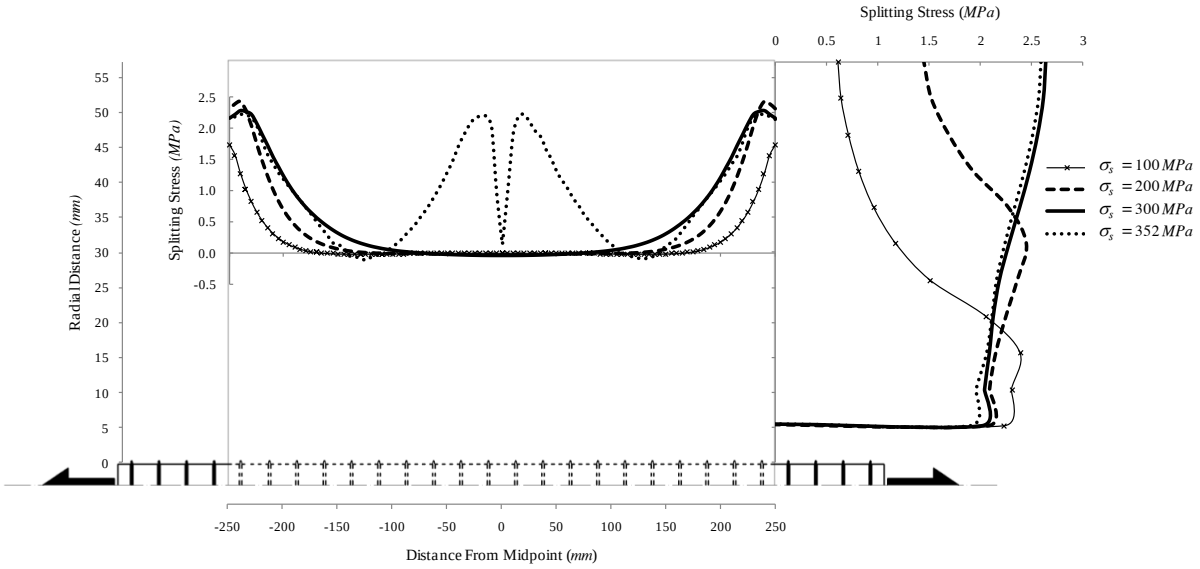

Fig. 3.23 FE splitting tensile stresses along radial and bar axes at different steel stresses for Tammo test with bond layer model

As explained before, the bond stress is composed of two components, namely, shear/tangential and normal/radial bond stresses. These stresses are compared for the perfect bond and the bond layer FE models just before the formation of the first crack at the steel stress of 300 *MPa* in Fig. 3.24. It can be seen that, while the shear bond stresses are quite similar for the two bond models in Fig. 3.24 (a), the perfect bond model significantly underestimates the radial bond stresses as compared to the bond layer model in Fig. 3.24 (b). This shows the inadequacy of the perfect bond model in simulating the bond mechanism, specifically the normal bond stresses, which are the underlying cause for the formation of the splitting tensile stresses.

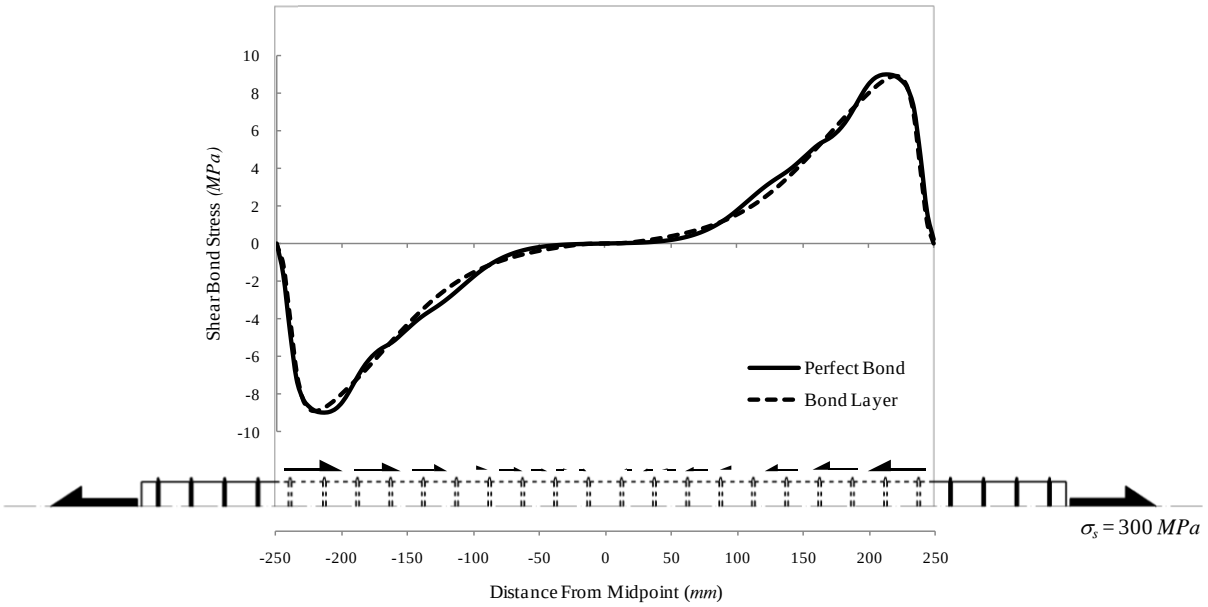

(a)

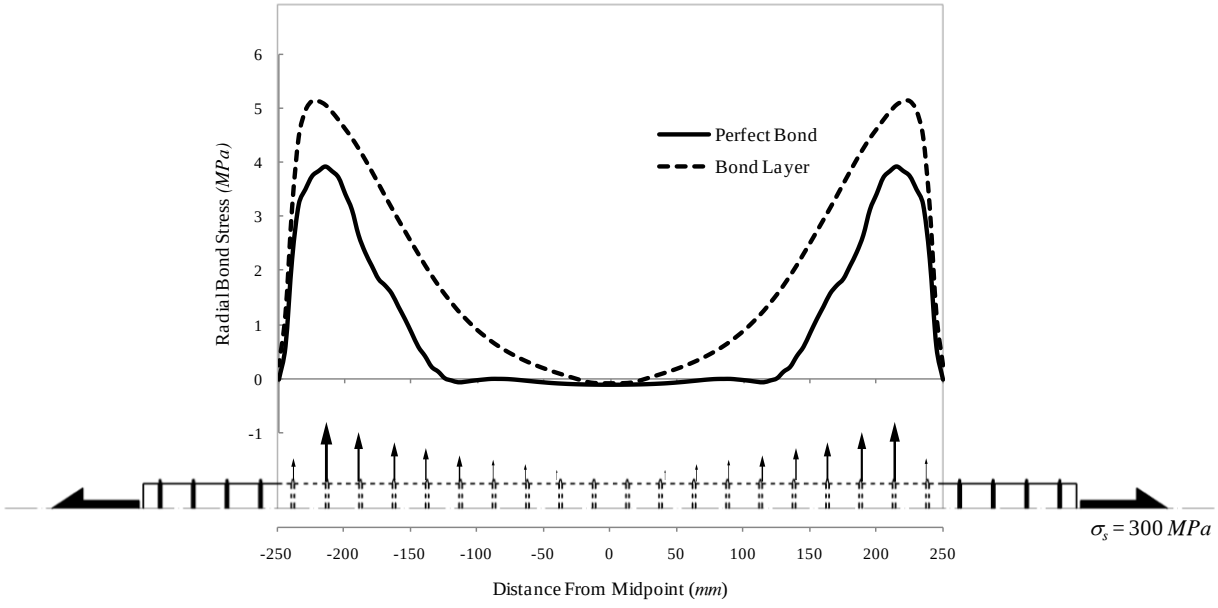

(b)

Fig. 3.24 Comparison of bond stresses for perfect bond and bond layer models, a) shear bond stresses, b) radial bond stresses

The FE results of the splitting tensile stresses for the perfect bond and the bond layer models are compared in Fig. 3.25. As it is expected, higher normal bond stresses in the bond layer model has caused the creation of larger splitting tensile stresses in this model than in the perfect bond model. The structural responses for the two bond models are compared in Fig. 3.26. It can be

seen that the FE model with the perfect bond condition behaves a bit stiffer than with the bond layer condition. However, in spite of the same response at the steel stress of about 390 *MPa* for the two models, two extra cracks are formed in the perfect bond model, which contradicts the experimental observations.

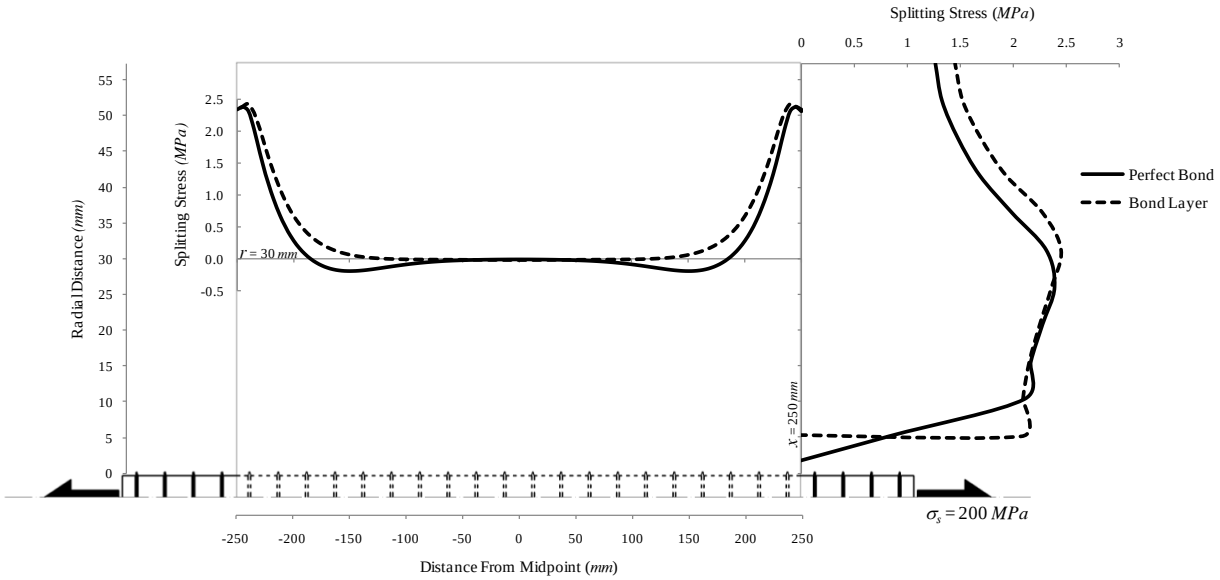

Fig. 3.25 Splitting tensile stress variation along radial and bar axes, comparison of perfect bond and bond layer models

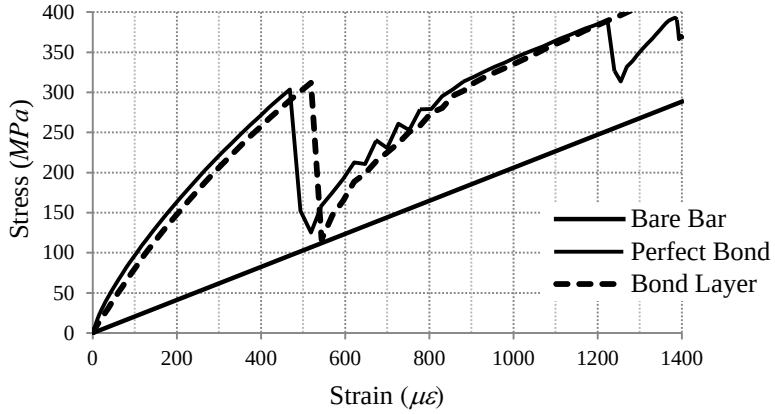

Fig. 3.26 Comparison of mean stress/strain curves for perfect bond and bond layer models

3.9 Approximation of Shear Bond Stress

Essential to any crack prediction model is a proper prediction of the shear bond stress. The shear bond stress at stabilized cracking obtained in the previous Section from the FE analysis of Tammo test is shown in Fig. 3.27. Despite showing a somewhat irregular pattern, the shear bond stress variation can be adequately approximated by a multi-linear curve. This approach at worse may slightly underestimate the bond stress, which in turn will result in a conservative overestimation of the crack spacing and the crack width. The most significant parameter to define such a curve is the peak shear bond stress. The peak shear bond stress has a close relationship with the tensile strength of the concrete, the confining pressure, the effective tension area or the clear concrete cover. It also changes with the level of the reinforcing steel stress. Such a relationship will be established through a parametric study using the FE analysis.

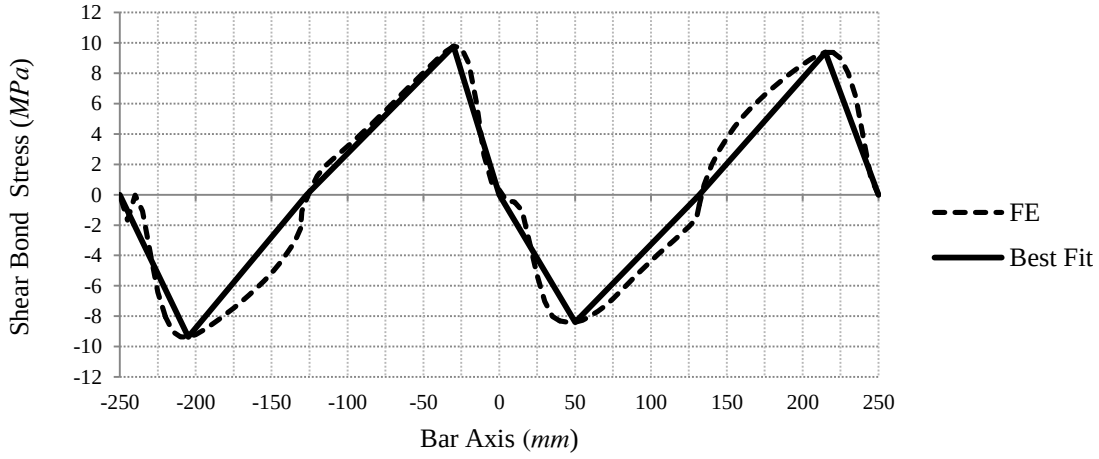

Fig. 3.27 Approximation of the shear bond stress at stabilized cracking

3.9.1 Parametric study of peak shear bond stress

To find the peak shear bond stress in various structural conditions, a FE parametric study is conducted on the RC tie elements in tension. For this purpose, the model used for Tammo test in Section 3.8 is modified several times to include the effect of different clear concrete covers, keeping everything else the same. These models represent the unconfined condition, meaning, a structural member without the confining effect of the transverse reinforcement or the confining

pressure from any other source. The effect of the confinement is also considered in another set of models. To create the confining condition, the radial displacements for the nodes of the concrete elements at the surface of the member are restrained as shown in Fig. 3.28. The resulting peak shear bond stresses at different steel stress levels are obtained from each of these models and presented in Table 3.8 and Table 3.9 for unconfined and confined conditions, respectively. For more clarification, these results are also depicted in charts shown in Fig. 3.29 and Fig. 3.31. It is obvious that the peak shear bond stress is increasing with the increasing clear concrete cover. However, at service load levels, the effect of the concrete cover on the peak shear bond stress is very negligible for clear concrete covers larger than $4d_b$. It can also be seen that the peak shear bond stress is increasing with the increasing level of the steel stress. This increase is more pronounced for stresses below 300 *MPa* and it becomes insignificant for stresses above that level. To create a design guide than can be used for determination of the peak shear bond stress in various structural conditions, the FE obtained peak shear bond stresses in Fig. 3.29 and Fig. 3.31 are normalized as shown in Fig. 3.30 and Fig. 3.32 for unconfined and confined conditions, respectively. These graphs will be used in this study to determine the peak shear bond stress for all types of structures and loadings, including one-way and two-way members in direct tension or bending moment. This is because the tension tie element can represent a region around the reinforcing steel that is under tensile stresses, so called the effective tension area or the tension chord, in any type of structural member. However, the equivalent clear concrete cover must be used in these charts for structures in confined conditions.

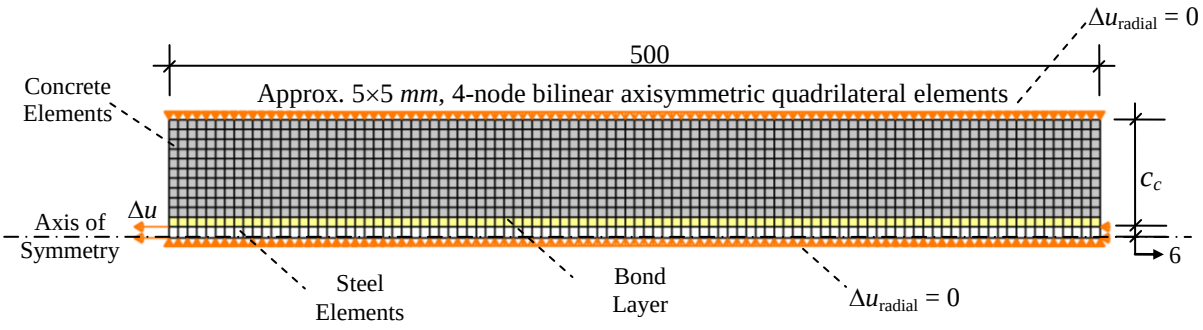

Fig. 3.28 Geometry and boundary conditions of FE model for parametric study of shear bond stresses with confined condition (dimensions in *mm*)

Table 3.8 Peak shear bond stresses for different clear concrete covers at various steel stress levels (unconfined condition)

c_c/d_b	$\tau_{t,peak}/f_{ct}$			
	$\sigma_s\ (MPa)$			
	100	200	300	400
6.07	1.65	2.65	3.45	4.06
4.77	1.64	2.63	3.35	3.89
4.33	1.63	2.59	3.38	3.55
3.9	1.63	2.55	3.10	3.18
3.47	1.59	2.59	2.81	3.00
3.03	1.56	2.32	2.59	2.70
2.6	1.56	2.05	2.28	2.41
2.17	1.48	1.80	1.96	2.06
1.73	1.29	1.52	1.66	1.68
1.30	0.98	1.24	1.30	1.33

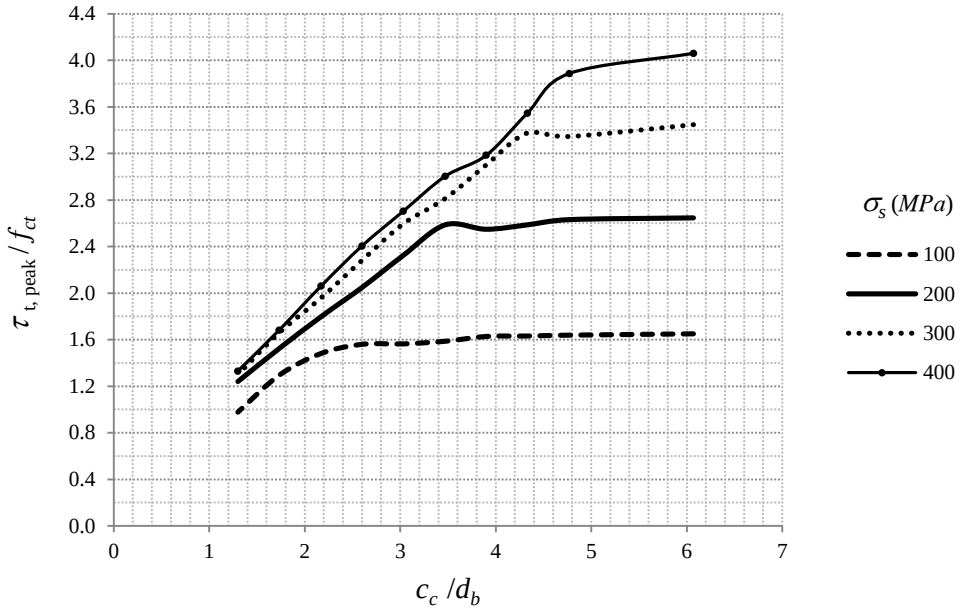

Fig. 3.29 Peak shear bond stress versus clear concrete cover versus steel stress (unconfined condition)

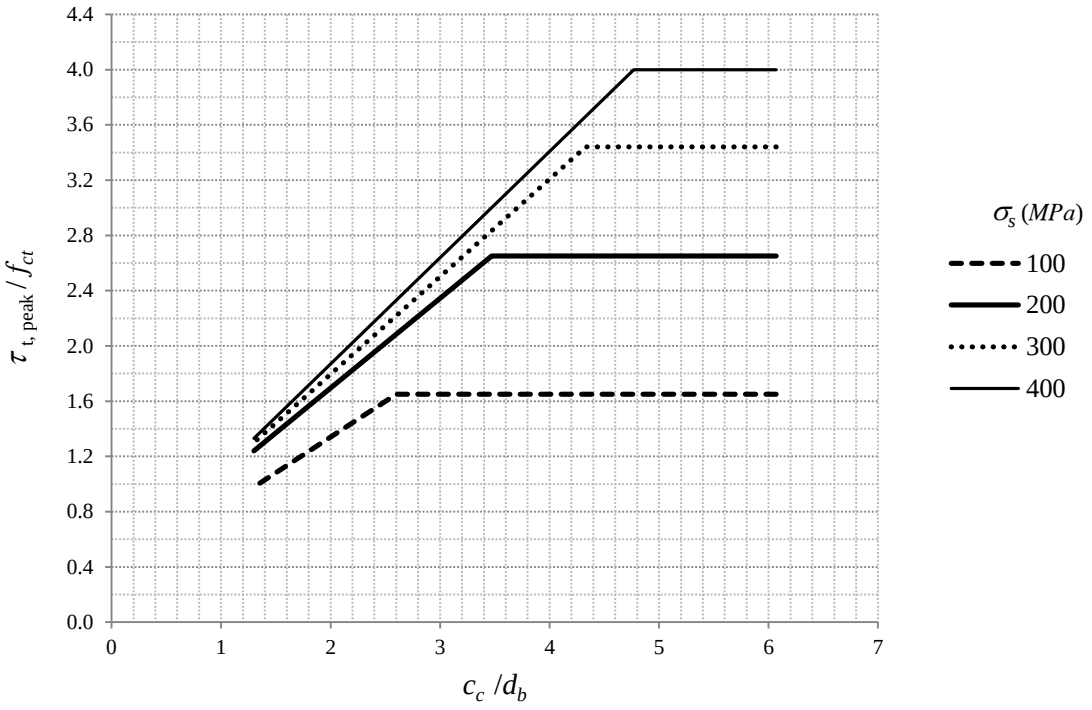

Fig. 3.30 Normalized peak shear bond stress versus clear concrete cover versus steel stress (unconfined condition)

Table 3.9 Peak shear bond stresses for different clear concrete covers at various steel stress levels (confined condition)

c_c/d_b	$\tau_{t,peak}/f_{ct}$			
	σ_s (MPa)			
	100	200	300	400
6.07	1.71	2.87	3.82	4.61
4.77	1.73	2.93	3.89	4.95
4.33	1.77	2.95	4.00	4.84
3.9	1.76	2.94	3.96	3.97
3.47	1.78	2.96	3.44	3.98
3.03	1.79	2.73	3.29	3.67
2.6	1.81	2.35	2.85	2.77
2.17	1.78	2.15	2.43	2.65
1.73	1.57	1.86	1.84	1.88
1.30	1.16	1.45	1.50	1.60

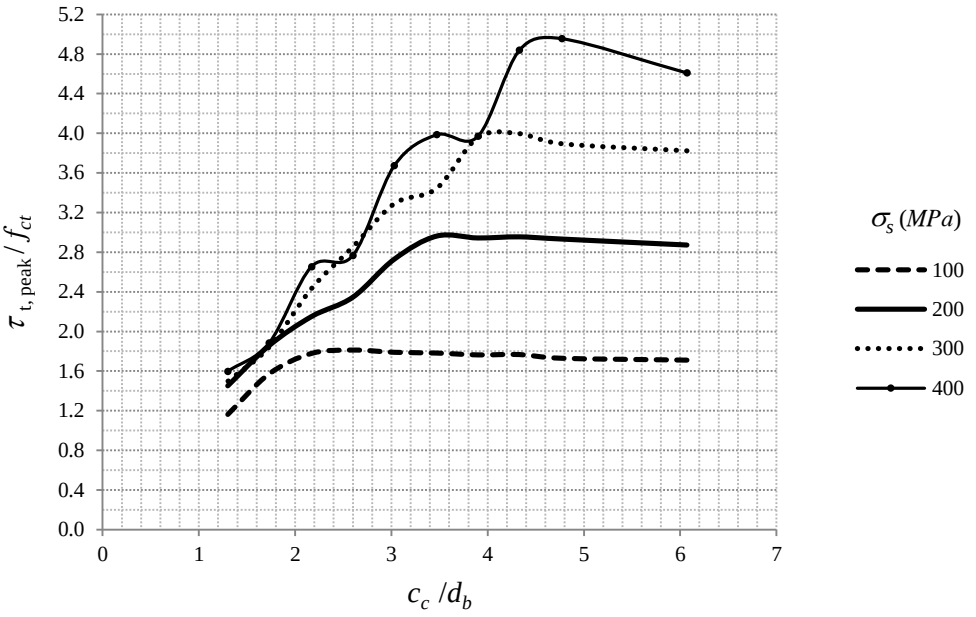

Fig. 3.31 Peak shear bond stress versus clear concrete cover versus steel stress (confined condition)

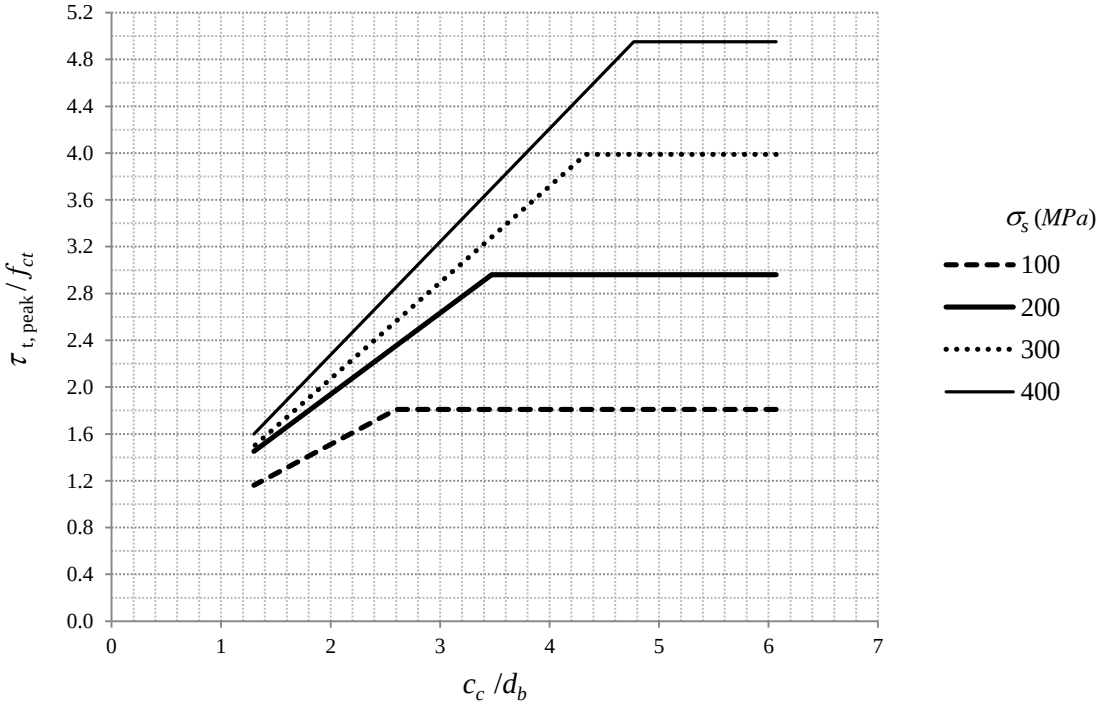

Fig. 3.32 Normalized peak shear bond stress versus clear concrete cover versus steel stress (confined condition)

3.9.2 Average shear bond stress

The average shear bond stress is an influential parameter in the calculation of the crack spacing. Since the shear bond stress is approximated to have a triangular distribution in Fig. 3.27, the average shear bond stress ($\tau_{t,ave}$) is half the peak shear bond stress (τ_{tp}). Therefore, the average shear bond stress is defined as,

$$\tau_{t,ave} = \frac{\tau_{tp}}{2} \tag{3.10}$$

3.9.3 Mean steel and concrete strains

The mean tensile strain in the concrete and the reinforcing steel between two consecutive cracks are important parameters in finding the crack width. These parameters are directly related to the distribution of the shear bond stresses. This correlation is illustrated in Fig. 3.33. A linear distribution of the shear bond stress means a parabolic distribution of the concrete and steel strains. The factor β_e, described in Eqs. 2.11 and 2.12 for the CEB MC90 cracking model, is an empirical integration parameter that can relate the mean value to the peak value of the concrete or steel strains. As it can be seen in Fig. 3.33, the value of the factor β_e is between two extreme boundary values of 0.66 and 0.33 depending on the location of the peak shear bond stress. The recommendations of the CEB MC90 model for the value of this factor are 0.6 for short term/instantaneous loading of pre-stabilized and post-stabilized cracking and long term/repeated loading of pre-stabilized cracking, and 0.38 for long term/repeated loading of stabilized cracking, which are both within the boundary limits. Since the FE analysis shows that the location of the peak shear bond stress is closer to the location of the crack, the value of 0.6 for this parameter is a very reasonable approximation.

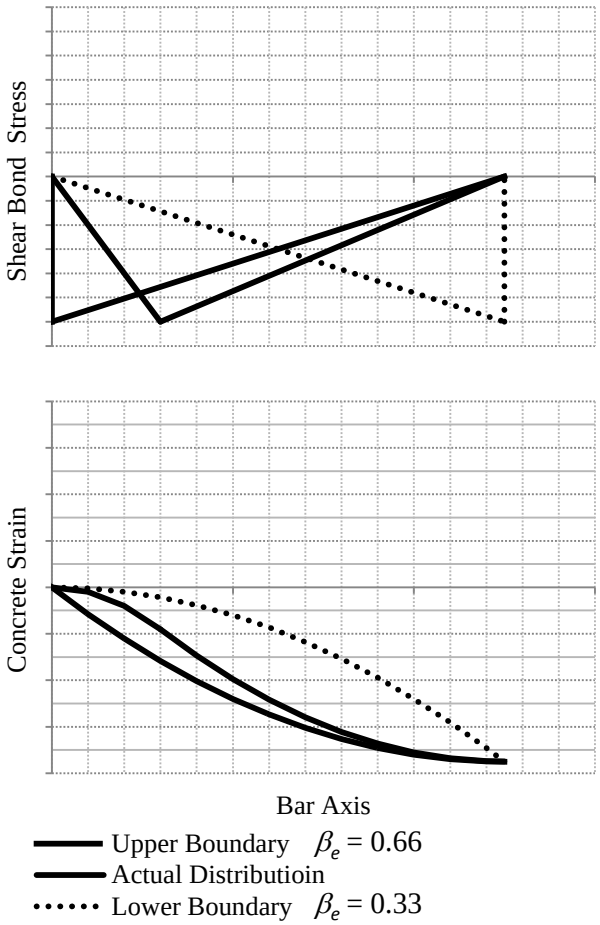

Fig. 3.33 Correlation of shear bond stress and concrete strain distributions, determination of factor β_e

3.10 Effective Tension Area of Concrete

As explained before, in a RC member when a steel reinforcing bar is in tension, the tensile force will transfer from the steel to the concrete surrounding the reinforcing bar through the bond mechanism. The distribution of the tensile stresses in this region of tensioned concrete is not uniform. The concrete tensile stresses are at their highest in the immediate vicinity of the reinforcing bar and they gradually decrease with increasing radial distance to the reinforcing bar. An area of concrete with a uniform distribution of tensile stresses that produces the same total tensile stresses as in the actual distribution is called effective tension area. Using this parameter instead of the non-uniform tensile stress distribution in the calculations of the crack width greatly simplifies these calculations.

3.10.1 Direct tension members

The FE analysis of the axially symmetric tension tie elements, it is observed that the concrete tensile stresses are almost uniformly distributed over the entire section mid-way between two consecutive cracks right before cracking. This happens even for clear concrete covers of 6 times the bar diameter. However, this is not the case for tension members in which the reinforcing bar is placed biased in the section.

The recommendation of the CEB MC90 model for the effective tension area of concrete for RC members in direct tension is explained earlier in Eq. 2.3 and Fig. 2.3. Accordingly, the depth of the effective tension area, $d_{t,ef}$, is taken as the lesser of the depth allocated to each reinforcing bar (half the depth of the section in the example) and 2.5 times the concrete cover to the center of the reinforcing bar. The latter governs when the over-all depth of the member is higher than 5 times the concrete cover for two layers of the reinforcement. In that case, the effective tension area of concrete will be less than the total area of the section, which will result in smaller crack spacings, and hence, crack widths. This can be misleading because this recommendation stipulates smaller concrete covers for better crack control. When the concrete cover is excessively small with no transverse reinforcement, the risk of spalling of the concrete cover or the formation of longitudinal splitting cracks is higher. In that case, the bond will fail before the concrete longitudinal stress can reach to the cracking stress, which results in large crack spacings and crack widths. This indicates a poor design for the layout of the reinforcing bars, which does not take a full advantage of the cross-sectional area of the member.

The recommendation of the CEB MC90 model for the effective tension area of concrete in direct tension members is adopted here. However, the adverse effect of small concrete covers is considered in this study through the calculation of the shear bond stress based on the recommendations given in the Section 3.9.1.

3.10.2 Flexural members

The effective tension area of concrete around the tensile reinforcement in a flexural member is investigated through a parametric study. A flexural beam with a single reinforcing bar is selected for this purpose. The geometry and the boundary conditions for this beam are schematically shown in Fig. 3.34. The cross section of the reinforcing bar is approximated with a square section instead of a circular section. This would eliminate the FE mesh transitions and irregularities by using 3D hexahedron brick elements for the entire model. The bending moment is preferably simulated through a prescribed rotational displacement at two ends of the beam rather than a prescribed flexural load.

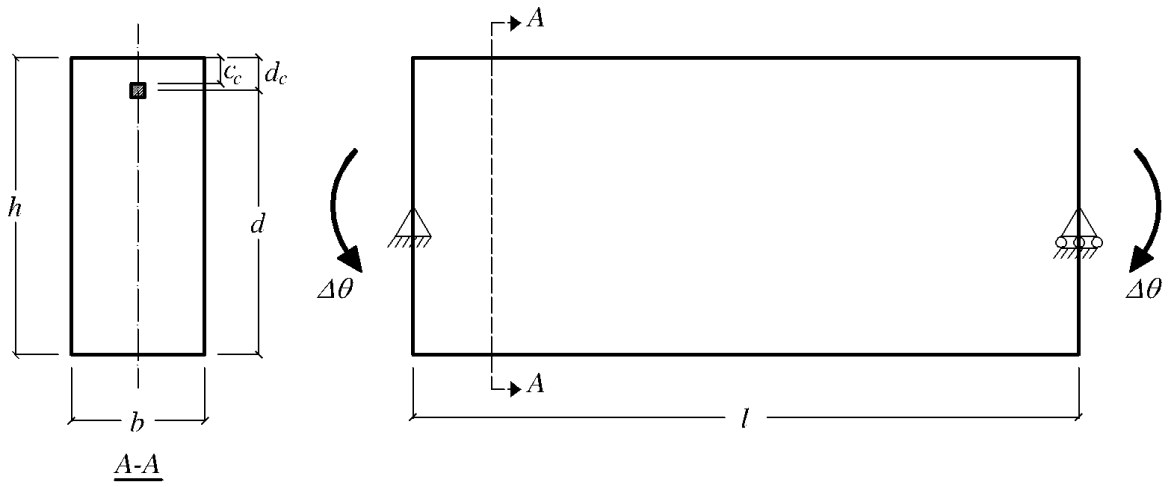

Fig. 3.34 Schematic of the flexural beam used for parametric study of effective tension area

3.10.2.1 Details of FE model

A typical FE model for this flexural beam is shown in Fig. 3.35. Only half the section of the beam is modeled due to a geometrical symmetry. The tensile strength of concrete elements is deliberately reduced for two sections at two ends of the beam. This is to create weak planes at two faces of the beam so that the cracks would first occur at these two locations at a very early stage of loading. In this way, the tensile force is transferred to the concrete through the bonding force. In other words, the FE model represents a segment of a beam between two flexural cracks.

The material properties selected for this model are similar to those previously described in Section 3.8.1 for the FE model of Tammo prisms.

In the parametric study, the height of the beam section is changed while all other properties are kept constant for different models. In this way, the only varying parameter is the reinforcement ratio. This parameter is chosen here because it has the most influence on the depth of the effective tension area.

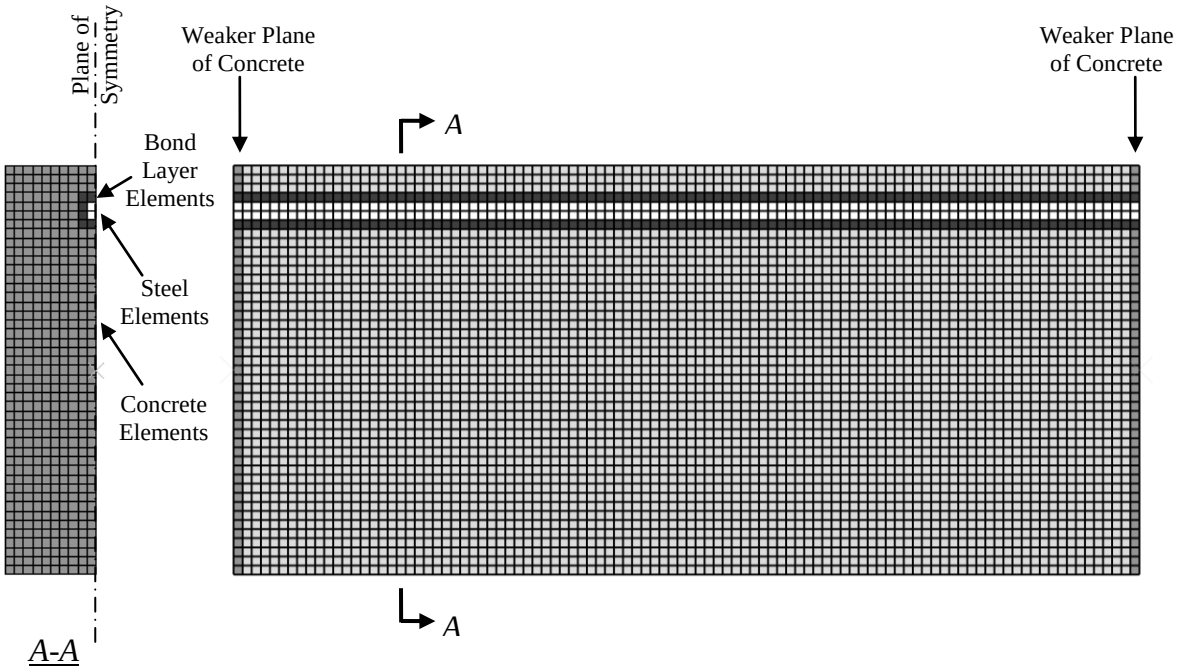

Fig. 3.35 FE model for the flexural beam

3.10.2.2 Results of FE analysis

The reduced contour of the tensile stresses and the crack pattern through the depth of the beam section are shown for three different section heights in Fig. 3.36. The higher tensile stresses are shown with darker colors in the stress contours. The depth of neutral axis at a crack section (*kd*) is also indicated in these figures. It is clear that the tensile stresses in the concrete are more concentrated in a region in the vicinity of the reinforcing bar between two cracks. It can also be

seen that the spacing of cracks is smaller for the smaller section heights or the higher reinforcement ratios.

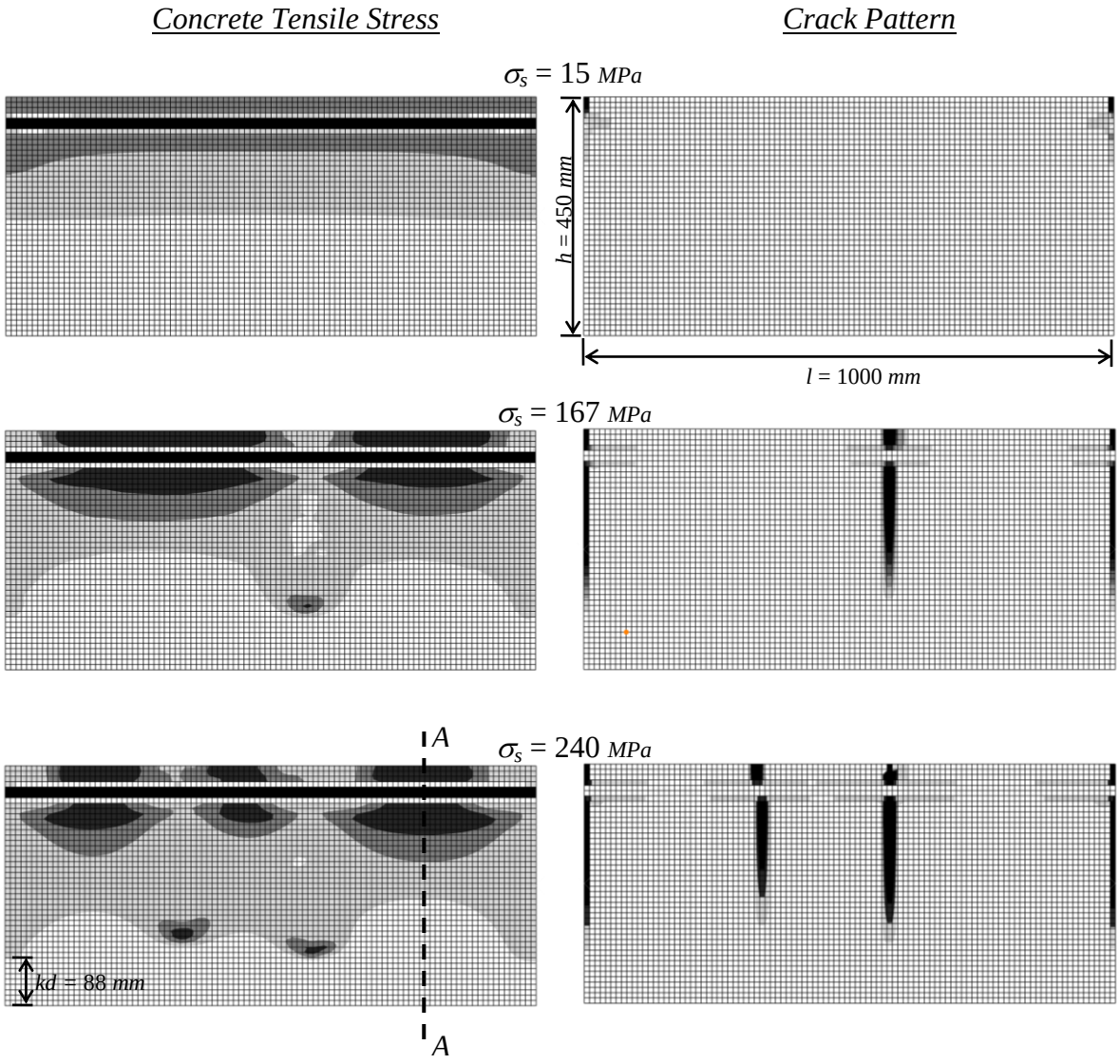

(a)

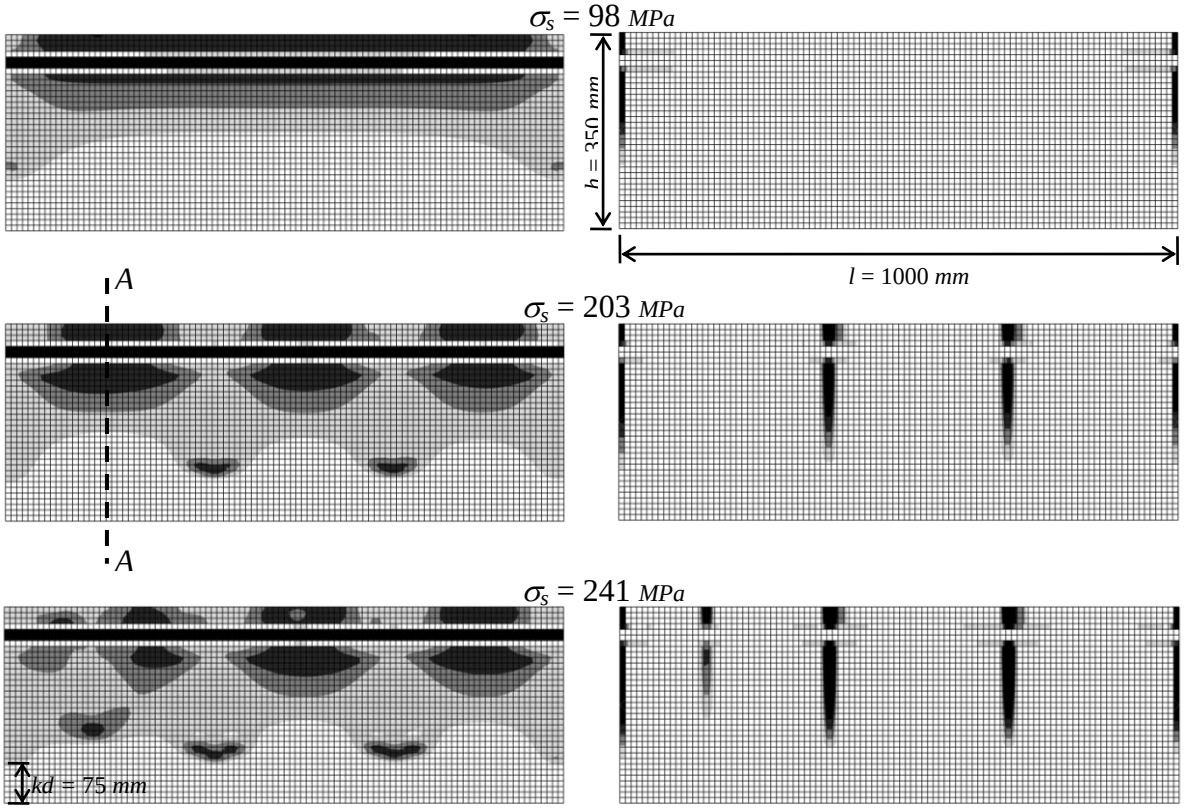
σ_s = 98 MPa
h = 350 mm
l = 1000 mm
A
σ_s = 203 MPa
A
σ_s = 241 MPa
kd = 75 mm

(b)

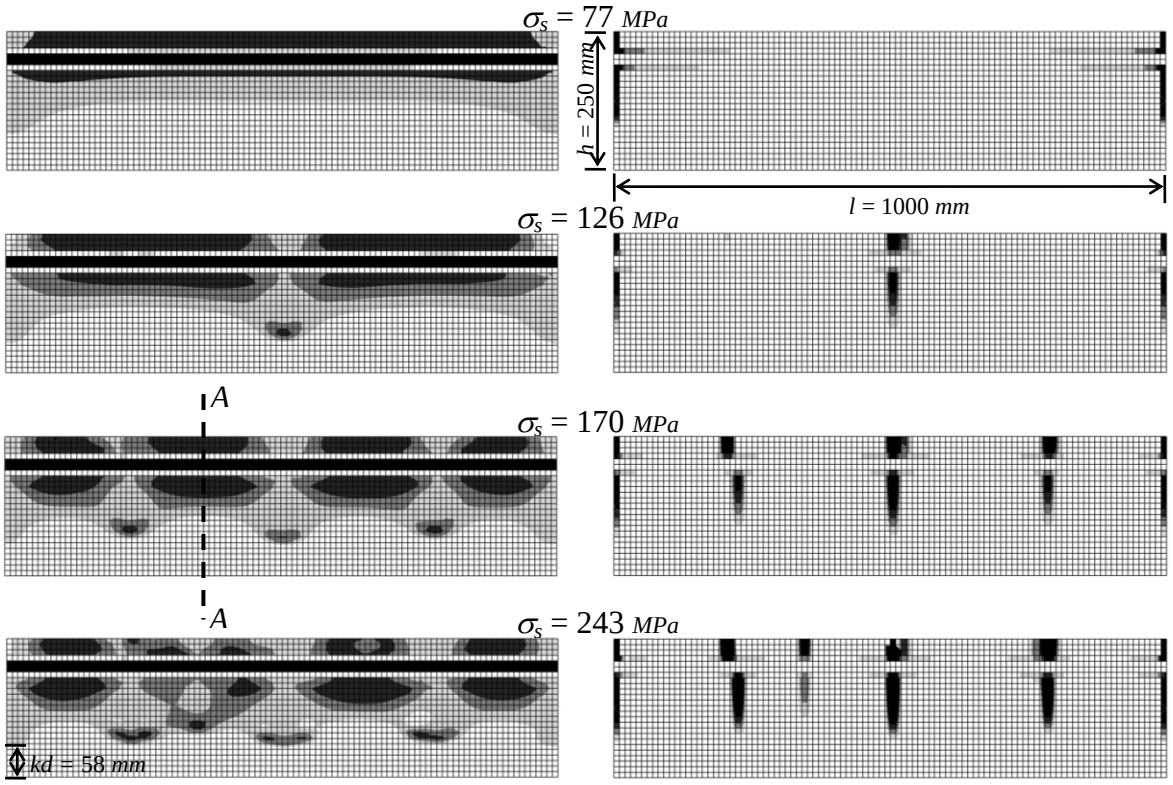

(c)

Fig. 3.36 Tensile stress contour and crack pattern at various steel stress levels, a) h = 450 *mm*, b) h = 350 *mm*, c) h = 250 *mm*

The distribution of the concrete tensile stresses through the depth of a section at mid-length between two consecutive cracks (indicated as the section A-A in Fig. 3.36) at various steel stresses is obtained for each model and shown in Fig. 3.37. The distribution curve is linear at low steel stresses and it changes to a non-linear curve with more weight around the reinforcing bar. The tensile stresses in the section at service load are normalized in Fig. 3.38. This means for the small portion of this curve where the tensile stresses are in the post-cracking stage, these stresses are adjusted to the tensile strength of concrete. Subsequently, this normalized curve is approximated with an equivalent block of uniformly distributed tensile stresses, meaning, both curves produce the same total tensile stress. This equivalent tension block represents the effective tension area of concrete. The depth of the effective tension area, $d_{t,ef}$, is indicated for each model.

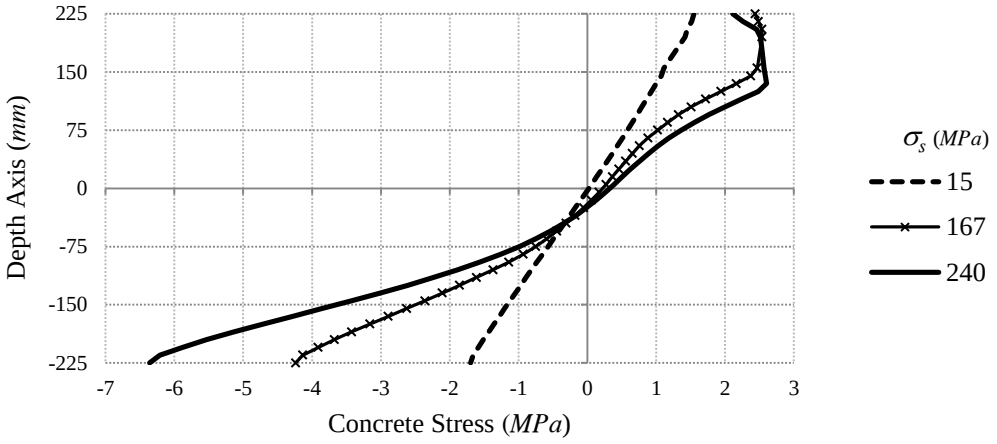

(a)

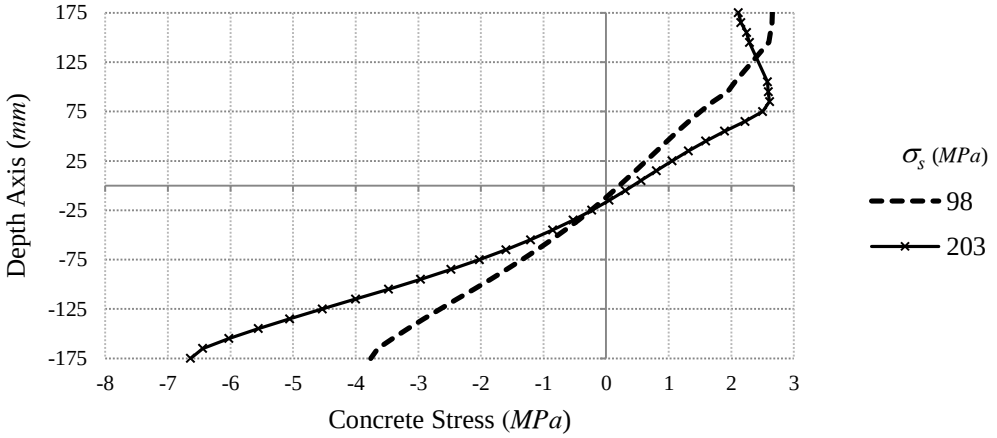

(b)

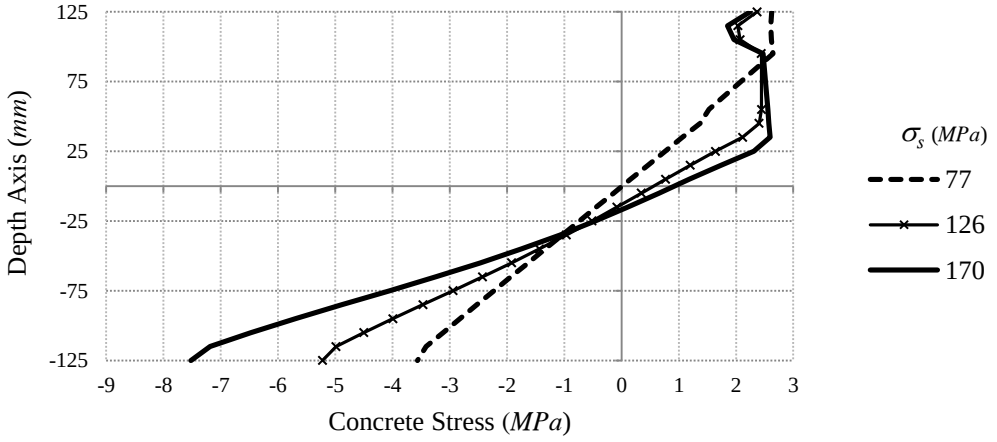

(c)

Fig. 3.37 Concrete stress distribution in section A-A in Fig. 3.36 at various steel stresses, a) h = 450 *mm*, b) h = 350 *mm*, c) h = 250 *mm*

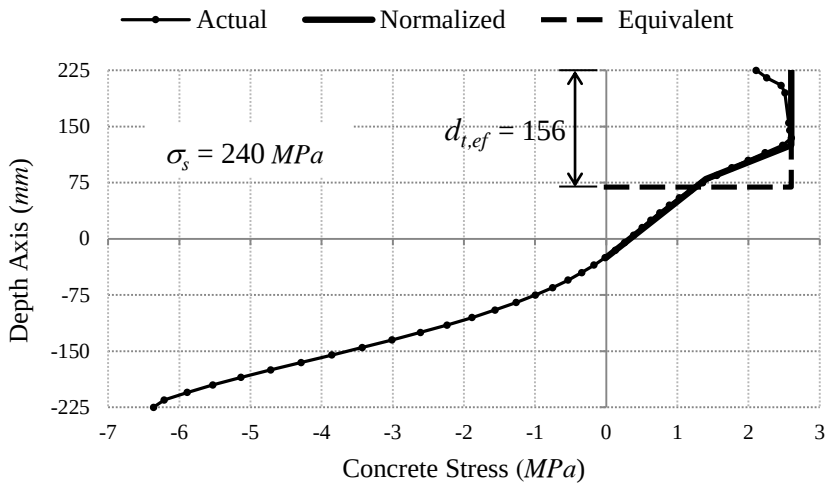

(a)

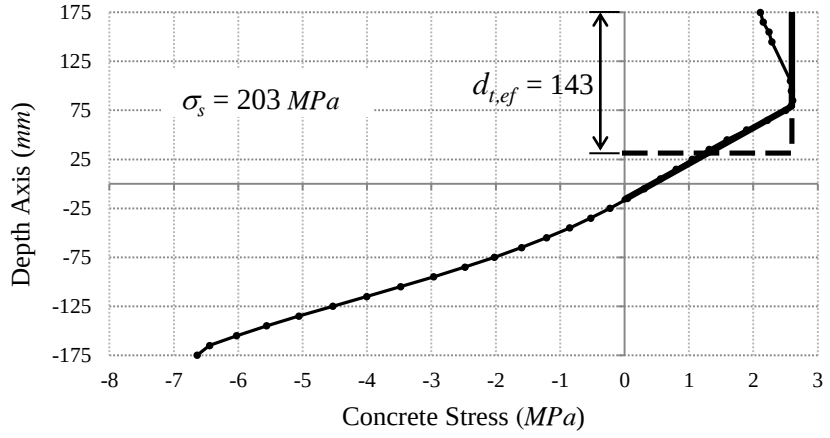

(b)

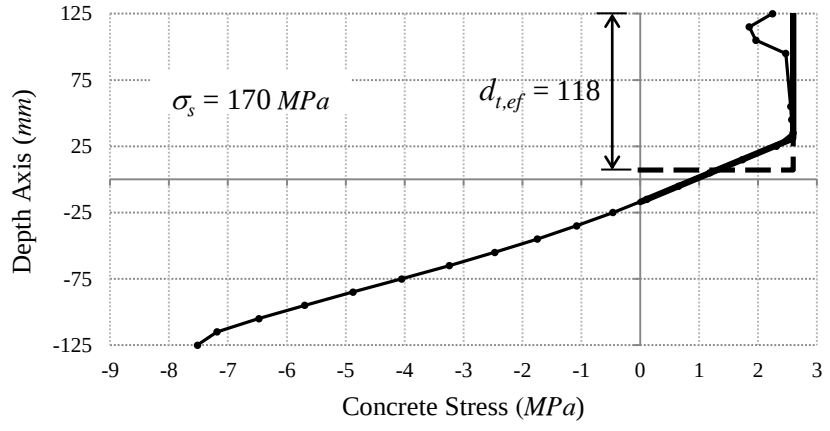

(c)

Fig. 3.38 Approximating effective tension area at section A-A in Fig. 3.36 at service load, a) h = 450 *mm*, b) h = 350 *mm*, c) h = 250 *mm*

The aforementioned parametric study is also performed for a beam with the over-all depth of 550 *mm*.

All the results of this parametric study are summarized in Table 3.10. The depth of neutral axis, *kd*, in this table is theoretically calculated based on the following equation,

$$kd = \left(\sqrt{2\rho_s \alpha_e + (\rho_s \alpha_e)^2} - \rho_s \alpha_e \right) d \qquad (3.11)$$

where ρ_s = reinforcement ratio (A_s/bd); α_e = modular ratio (E_s/E_c); and d = effective depth of tensile reinforcement.

This theoretical *kd* is used for all subsequent calculations, and the *kd* found in FE analysis is given just for comparison. Most previous studies define the depth of effective tension area, $d_{t,ef}$, as follows,

$$d_{t,ef} = k_t (h - kd) \qquad (3.12)$$

where k_t = factor of effective tension area; and h = height of beam section.

The results of FE analysis show that the tensile stresses are uniform through the depth of the concrete cover. This will be confirmed later in this Chapter through another parametric study on the effect of concrete cover. Therefore, it seems more appropriate to define the $d_{t,ef}$ as a combination of two depths as follows,

$$d_{t,ef} = d'_{t,ef} + d_c \qquad (3.13)$$

where $d'_{t,ef}$ = partial depth of effective tension area; d_c = concrete cover to the center of reinforcing bar.

The partial depth of effective tension area, $d'_{t,ef}$, is then defined based on the effective depth of tensile reinforcement, *d*, rather than the height of the beam section *h*, as follows,

$$d'_{t,ef} = k'_t(d - kd) \tag{3.14}$$

where k'_t = new factor of effective tension area.

The abovementioned factors of effective tension area k_t and k'_t are calculated based on the results of FE analysis and given in the Table 3.10. The variations of these factors with varying reinforcement ratio are also drawn in Fig. 3.39, and Fig. 3.40. These charts can be used as a design guide to calculate the effective tension area of concrete.

Table 3.10 Summary of the parametric study for effective tension area of concrete in flexure (effect of reinforcement ratio)

h (mm)	b (mm)	d (mm)	d_b (mm)	c_c (mm)	l (mm)	ρ_s (d_b^2/bd)	kd *FEM* (mm)	kd *theor.* (mm)	$d_{t,ef}$ (mm)	$d'_{t,ef}$ $d_{t,ef}$ -d_c (mm)	k_t $d_{t,ef}/(h-kd)$	k'_t $d'_{t,ef}/(d-kd)$
550	200	2.5b = 500	20	$2d_b$ = 40	1000	0.004	109	104	154	104	0.35	0.26
450	200	2.0b = 400	20	$2d_b$ = 40	1000	0.005	88	92	156	106	0.44	0.34
350	200	1.5b = 300	20	$2d_b$ = 40	1000	0.007	75	78	143	93	0.53	0.42
250	200	1.0b = 200	20	$2d_b$ = 40	1000	0.010	58	62	118	68	0.63	0.49

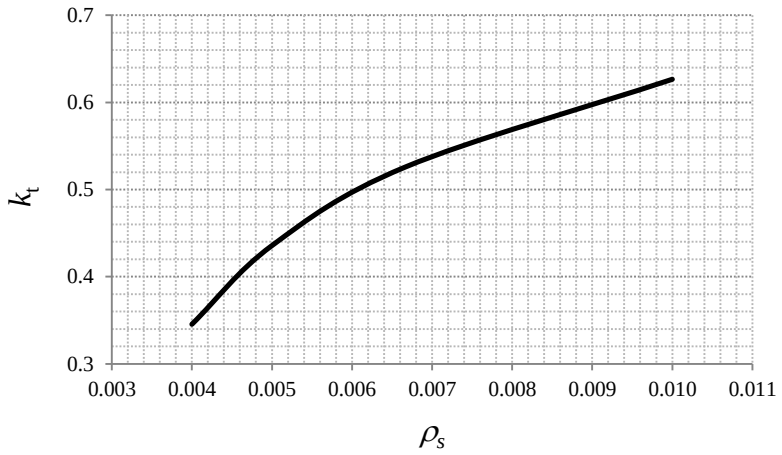

Fig. 3.39 Factor of effective tension area (k_t) vs. reinforcement ratio

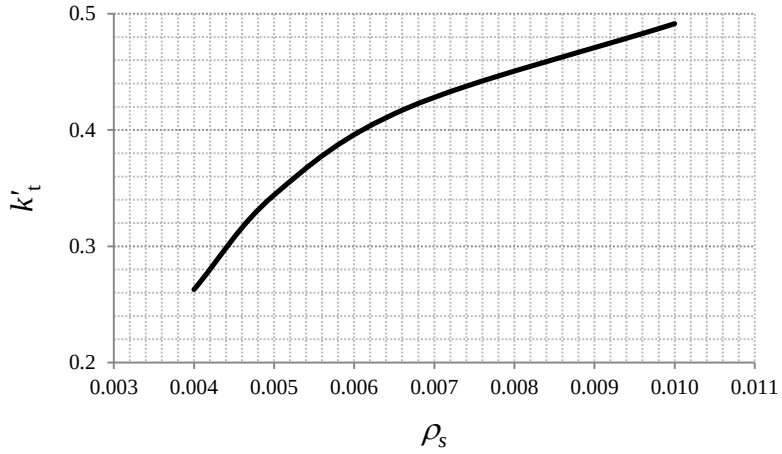

Fig. 3.40 New factor of effective tension area (k'_t) vs. reinforcement ratio

3.10.2.3 Comparison with previous models

The model developed in this study for the depth of effective tension area is compared with two other models proposed by others, namely, Gilbert (2005) and CEB-FIP MC90 (1990) models. Gilbert developed his model based on the tension chord model proposed by Marti et al. (1998). The Gilbert model suggests a value of 0.5 for the factor k_t in Eq. 3.12. The recommendation of CEB model for calculation of the depth of effective tension area in flexural members is given in Eq. 2.3.

The results of these two models along with those of the proposed model, which is developed based on the FE analysis in the previous section, are compared in Fig. 3.41. It can be seen that the Gilbert model overestimate the effective tension area for reinforcement ratios smaller than 0.006. On the other hand, the CEB model seems to be largely underestimating the effective tension area for all values of reinforcement ratios. This can result in underestimating the crack spacings, and thus, crack widths.

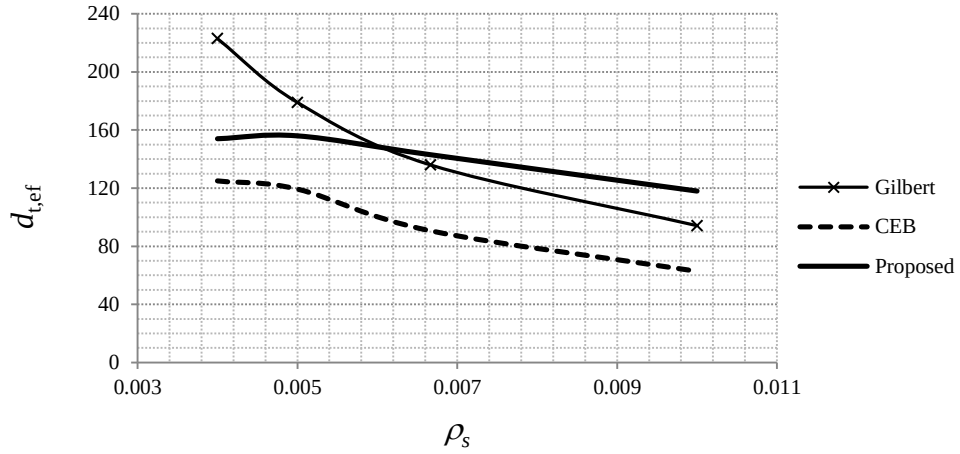

Fig. 3.41 Comparison of various models for the depth of effective tension area

3.10.2.4 Effect of concrete cover

The effect of concrete cover on the distribution of stresses in the beam section, and also on the shear bond stresses is investigated through a parametric study. For this purpose, the FE model previously defined for a beam with h = 450 mm in Fig. 3.36(a) is chosen. The clear concrete cover is changed in this model while everything else is kept constant. The distribution of concrete stresses through the depth of the beam at a section between two consecutive cracks is shown in Fig. 3.42 for these models. It can be seen that the concrete cover has no significant effect on the distribution of concrete stresses. Additionally, the concrete stresses are uniform through the concrete cover. This implies that, the proposed parameters $d'_{t,ef}$ and k'_t in Eq. 3.14 are more relevant than k_t in Eq. 3.12 to calculate the depth of effective tension area, because they are defined independent of the concrete cover.

In this study, it is observed that the number of primary cracks reduces for smaller concrete covers. This is an indication of a reduction in the shear bond stresses. This can be confirmed by looking at the variation of shear bond stresses along the bar axis as shown in Fig. 3.43 for various clear concrete covers. It is obvious that the peak shear bond stress is less for smaller clear concrete covers. Using these results, the peak shear bond stress is drawn versus the clear concrete cover for various steel stresses in Fig. 3.44. Comparing this chart with Fig. 3.30, it can be seen that the two bond behaviours are in the same range, meaning, the recommendations of Fig. 3.30, and Fig. 3.32 are valid for all types of loading.

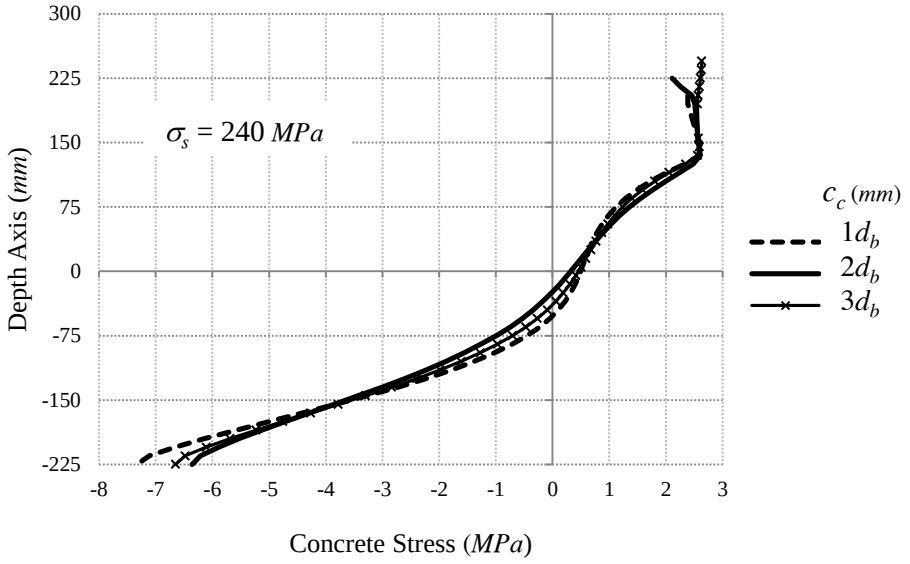

Fig. 3.42 Effect of clear concrete cover on concrete stress distribution through the depth of beam section (d = 400 *mm*, b = 200 *mm*, d_b = 20 *mm*)

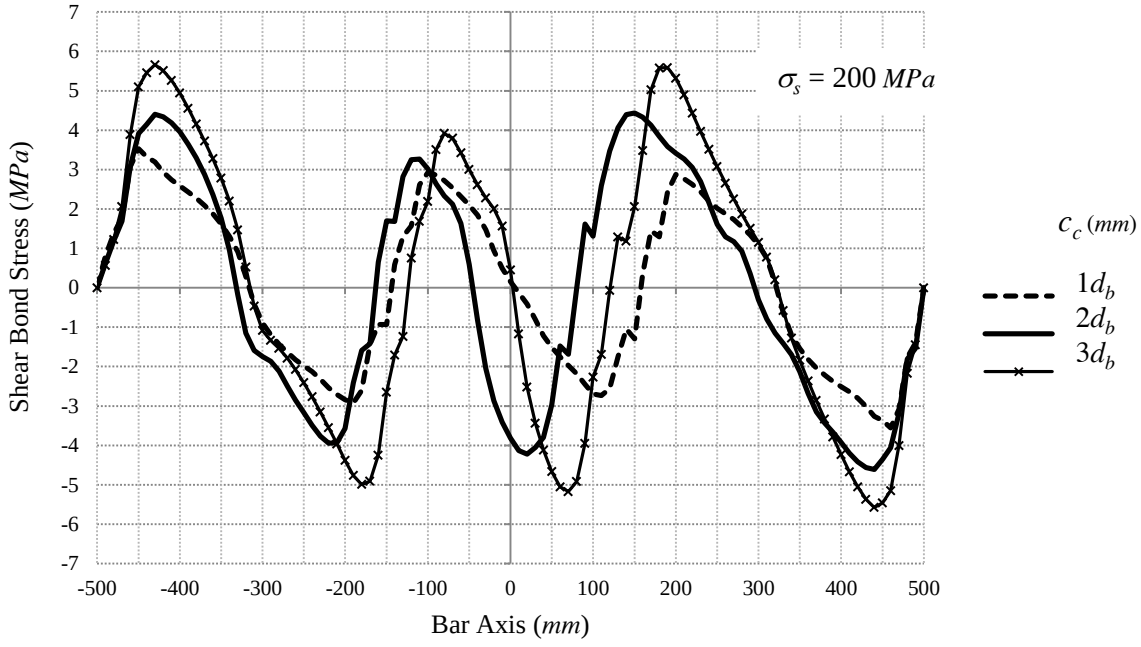

Fig. 3.43 Variation of shear bond stress along the bar axis in a flexural beam, effect of concrete cover (d = 400 *mm*, b = 200 *mm*, d_b = 20 *mm*)

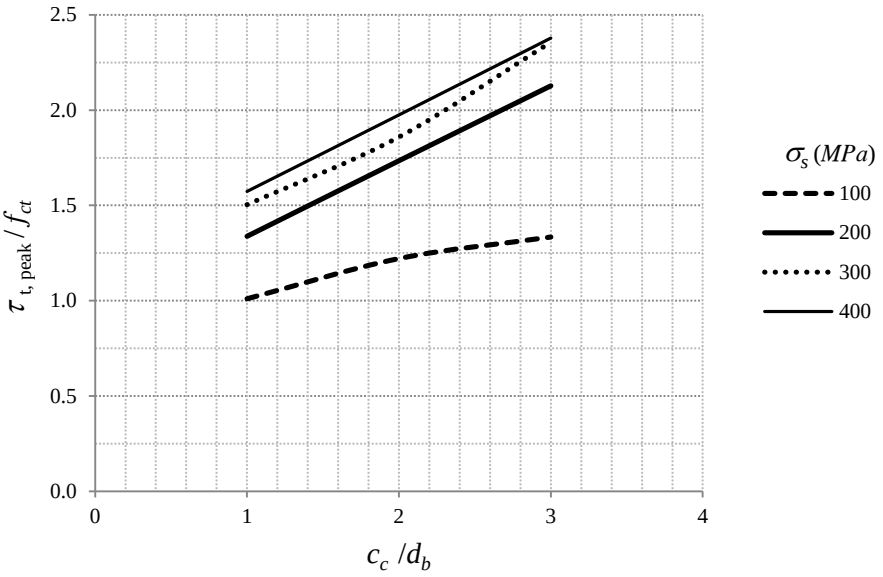

Fig. 3.44 Peak shear bond stress vs. clear concrete cover vs. steel stress

3.11 Crack Width Gradient

Although using a larger concrete cover will result in a better bond strength, it increases the crack width at the surface due to the crack width gradient, as shown in Fig. 3.45. It can be seen that the width of a flexural crack increases with increasing distance to the neutral axis. This effect is neglected in the CEB model, as it calculates the width of cracks at the reinforcing bar level. Whether the crack width at the surface of concrete or the crack width at the reinforcing bar level in flexural members should be the basis for the crack control can be debated. To calculate the width of flexural cracks at the concrete surface, the crack width at the reinforcing bar level must be multiplied by the crack width gradient factor (or cover factor), β_g, calculated as follows,

$$\beta_g = \frac{h - kd}{d - kd} \tag{3.27}$$

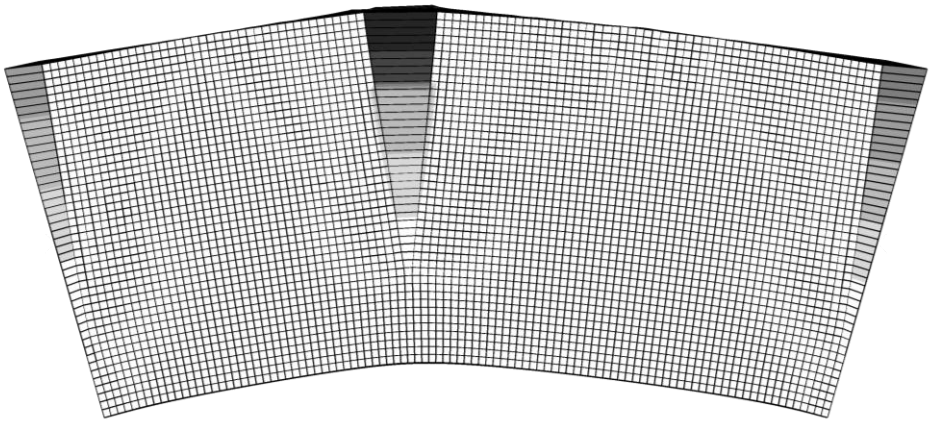

Fig. 3.45 Exaggerated deformed shape of flexural cracking

3.12 Summary

The one-way cracking behaviour of reinforced concrete members is analytically investigated in this Chapter. A non-linear FE model for concrete, namely, damaged plasticity model, with two different solution techniques, namely, dynamic explicit and static Riks, are introduced. The accuracy of this model is verified using the experimental data from the Kankam test on RC tension tie elements. The sensitivity of this model to various parameters, including the post-cracking curve of concrete, the number of time increments, the mesh size, and the tensile strength of concrete, is examined. Also, it is found that the dynamic explicit formulation is a more time-efficient solution technique than the static Riks formulation.

To improve the accuracy of the abovementioned model, the attention is paid to the interaction mechanism between the reinforcing bar and the surrounding concrete. Three different approaches are compared with each other, namely, the perfect bond, the diagonal link element, and the bond layer models. It is found that the perfect bond model underestimates the amount of bond-slip due to an underestimated angle of the bond force with respect to the bar axis. This problem is alleviated in the other two bond models in which the radial bond stress, and hence, the angle of the bond force is larger. The accuracy of these models is verified using an experimental data from the Tammo test on tension tie elements.

Based on the results of the validated FE model with the bond layer model, the tangential bond stress is approximated with a bilinear curve. The peak shear bond stress is determined through a FE parametric study, which includes the effect of the clear concrete cover, the bar diameter, the tensile strength of concrete, the steel stress, and the confinement condition. The recommendations are presented in a chart format for design purposes. Additionally, a parametric study is performed to study the effective tension area of concrete in flexural members. A new factor is recommended for determination of this area.

CHAPTER 4

EXPERIMENTAL INVESTIGATION OF TWO-WAY CRACKING

4.1 Introduction

Thus far in this study, the mechanism of cracking for a member under a simple one-way loading condition is thoroughly reviewed. However, there are many instances in which the RC structural member is under a more complicated two-way loading condition, such as, elements of a nuclear plant containment structure, the walls of a gaseous or liquid containing structure, two-way slabs in buildings, etc. The mechanism of cracking in this type of elements is not as good established as that of the one-way cracking, with many unknowns still remained unexplored. Also, as of to date, a very limited experimental data is available in the literature on the two-way cracking phenomenon. An effective experimental study should report on all aspects of cracking, including the crack propagating sequence, the measurable crack pattern, the crack width, and the steel and concrete strains. One goal of this study is to contribute to such an experimental database for a future reference.

In this Chapter, the procedure of three medium-scale experiments on the cracking and leakage behaviour of RC panels subjected to a two-way loading condition is reported. The effects of the reinforcement ratio and the spacing of the reinforcing bars are considered. The RC panels are subjected to pure tension in one direction and to bending moment in the other. This type of loading is directly applicable to the wall of a liquid containing circular tank under hydrostatic pressure. This loading condition may also occur at the base of a rectangular or circular tank wall

due to combination of hydrostatic loading and restraint volumetric change. Moreover, the results of this experiment can help to understand the fundamentals of the two-cracking phenomenon, which can be applied to any type of two-way loading.

4.2 Case Study

As a case study for the loading condition of the experimental tests, the internal forces in a wall of a liquid containing circular tank are selected. The control of cracking is highly important for this type of structures so as to maintain their performance throughout their service life. The wall of this structure is under two-way loading condition, meaning, a pure tension force in hoop/circumferential direction and a bending moment in meridional/vertical direction. The experimental tests are aimed to represent a segment of this tank wall. Therefore, the internal forces in the actual structure are needed to create a similar loading condition in the laboratory.

To obtain the internal forces existing in the actual structure, a fixed-base open-top circular water tank with a diameter of 20 *m*, a height of 5 *m*, and a thickness of 300 *mm* is selected for the FE modeling. The wall of this tank is modeled with two different types of elements, namely, three dimensional (3D) shell elements with both linear elastic and nonlinear behaviours and axisymmetric shell elements with linear elastic behaviour. The axisymmetric elements should not be used for the nonlinear analysis, because the tank wall is axially symmetric only prior to cracking. For 3D modeling, just a quarter of the tank in the plan view is modeled due to the geometrical symmetry. Three dimensional shell elements (S4R) with the size of 125×125 *mm* and the thickness of 300 *mm* are used in this model. The hydrostatic pressure due to water inside the tank and the gravity loads due to the self-weight of the structure are considered. Because of the fact that these external loads are not large enough to cause cracking in the concrete, linear elastic and nonlinear models both yield the same results. Therefore, the axisymmetric elements with a linear elastic behaviour are also used for comparison. The deformed shapes of these models are shown in Fig. 4.1.

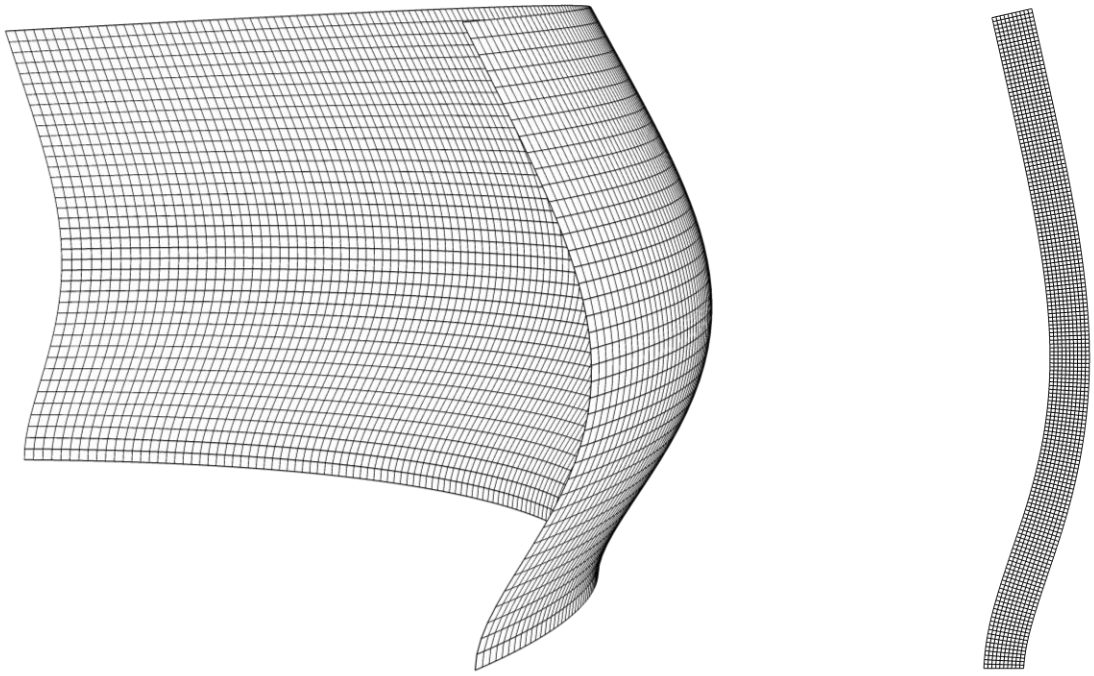

(a) (b)

Fig. 4.1 Deformed shape of the wall of a circular tank, a) 3D shell elements, b) axisymmetric shell elements

The results of FE analysis for the internal forces of the wall are shown in Fig. 4.2. The variation of the hoop tension force and the vertical bending moment over the height of the wall are shown in Fig. 4.2(a) and (b), respectively. The positive sign of the bending moment means that the outside surface of the wall is in tension. It can be seen that the most critical combination of two-way internal forces occurs at about the mid-height of the wall. According to these figures, a combination of a hoop tension force of 231 *kN per unit width of the wall* and a vertical bending moment of 8.7 *kN.m per unit width of the wall* will be used as the basis to prescribe the initial ratio of the two-way loading in the experimental test. This ratio will be kept constant at initial loading stages and will be changed for the final loading stages to produce some data on the effect of loading ratio.

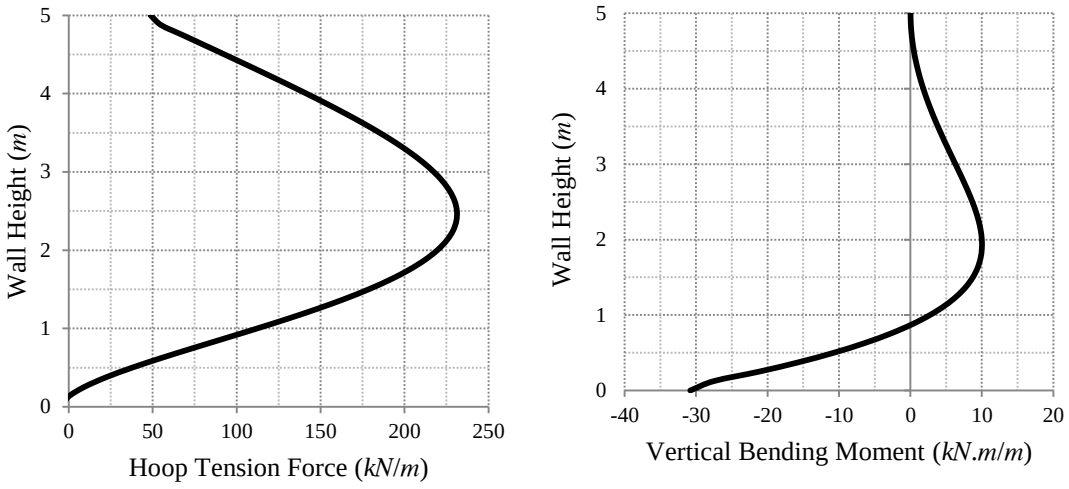

(a) (b)

Fig. 4.2 Results of FE analysis for internal forces in the wall of a circular water tank, a) hoop tension force, b) vertical bending moment

4.3 Loading Configuration

As shown in the previous section, the wall of a circular tank is under a unique two-way loading condition. To create a similar condition in the laboratory, RC panels that represent a segment of this wall are subjected to a comparable loading condition. The loading configuration and the boundary conditions for these tests are shown in Fig. 4.3. With this loading scheme the RC panel is under a direct tension force *T* in one direction and a bending moment caused by the force *P* in the orthogonal direction. The boundary conditions are carefully selected to create a free to slide condition along the axis of direct tension and a simply supported condition for the flexural direction. The spacing of the direct reinforcing bars are selected to be 300 *mm*, which is the maximum allowed bar spacing for environmental structures based on ACI350-06 (2006). The loads *T* and *P* must be increased simultaneously in small increments to maintain a fixed two-way loading ratio. The relative magnitude of these loads can be determined based on the target internal forces of the actual structure obtained in the previous section.

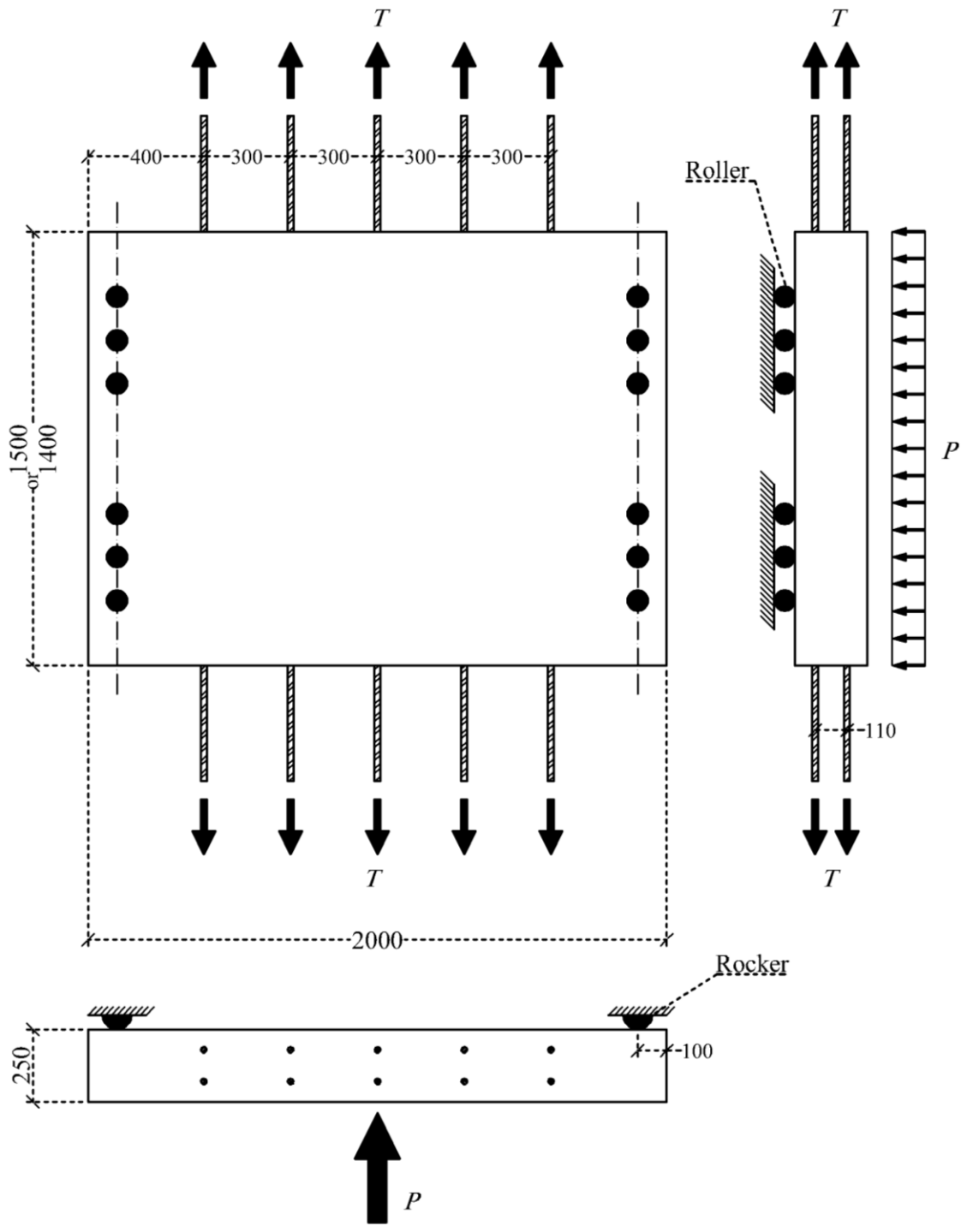

Fig. 4.3 Loading configuration and boundary conditions (dimensions in *mm*)

In the calculation of the direct tension force, only the middle portion of the RC panel is considered to be effectively under uniform direct tension, as shown in Fig. 4.4.

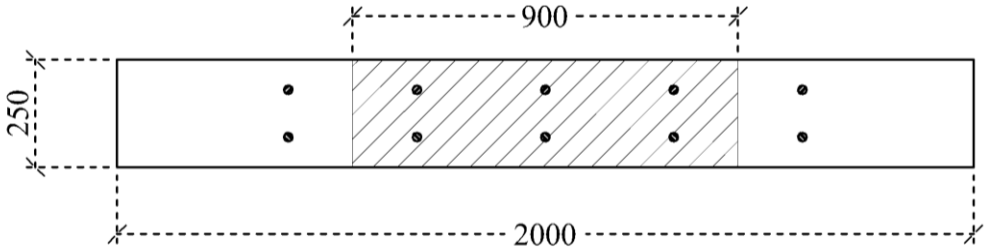

Fig. 4.4 Area of the section considered in uniform direct tension

The correlation of the forces *T* and *P* can be calculated as follows,

$$T = 231\,N/mm \times 900\,mm \times \frac{10}{6} = 346500\,N$$

$$M_{\max} = \frac{P - s.w.}{2} \times 900 = 450(P - s.w.) \qquad \text{(I)}$$

$$M_{\max} = 8673\,N.mm/mm \times (1500 \text{ or } 1400)\,mm = 13009500 \text{ or } 12142200\,N.mm \qquad \text{(II)}$$

$$\text{(I)}, \text{(II)} \rightarrow P - s.w. = \frac{13009500 \text{ or } 12142200}{450} = 28910 \text{ or } 26982\,N$$

$$\Rightarrow \frac{T}{P - s.w.} = \frac{346500}{28910 \text{ or } 26982} \cong 12 \text{ or } 12.8 \qquad (4.1)$$

Where M_{max} = maximum bending moment; and *s.w.* = self-weight of panel And the mounted equipments.

The above correlation of forces *T* and *P* will be used to prescribe the loading plan of the experiments at service load levels.

4.4 Test Setup

A unique test setup that can reproduce the abovementioned two-way loading condition is carefully designed as shown in Fig. 4.5. This figure shows the plan view of the test setup. The reinforcing bars extruded out of the RC panel are fixed to the rigid wall at north-side and pulled away from the south-side. This would create the direct tension force in the RC panel in north-south direction. Two RC distributing beams are used at the two extruded north and south ends to uniformly distribute the tensile force between direct reinforcing bars. These beams are designed to work as a deep beam in which the forces are primarily transferred through compression struts. The pulling force is applied using two jacks on the east and west sides of the RC panel, which are pushing the steel I-beam against the rigid wall via large diameter solid round bars. The steel I-beam transfers these forces from the side jacks to two points in the middle of the south RC distributing beam, which are symmetric with the two fixing points of the north-side RC distributing beam. This is to ensure the deep beam behaviour of these RC beams.

The section A-A in Fig. 4.5 is shown in Fig. 4.6. The roller supports are provided to ensure a free to slide boundary condition in the direction of the direct tension loading. Another jack is placed at the bottom center of the RC panel to apply a uniformly distributed line load over the width of the RC panel. This can also be seen in Fig. 4.7, which shows the section B-B in Fig. 4.5. The bottom center jack applies an upward pushing force while the two ends of the RC panel are fixed to the rigid floor with free to rotate rocker supports. This would create a bending moment in the RC panel in the east-west direction. For more clarification, a number of section views of the test setup in Fig. 4.5 are shown in Fig. 4.8. The layout and detailing of the reinforcement for the RC distributing beam are shown in Fig. 4.9 and Fig. 4.10.

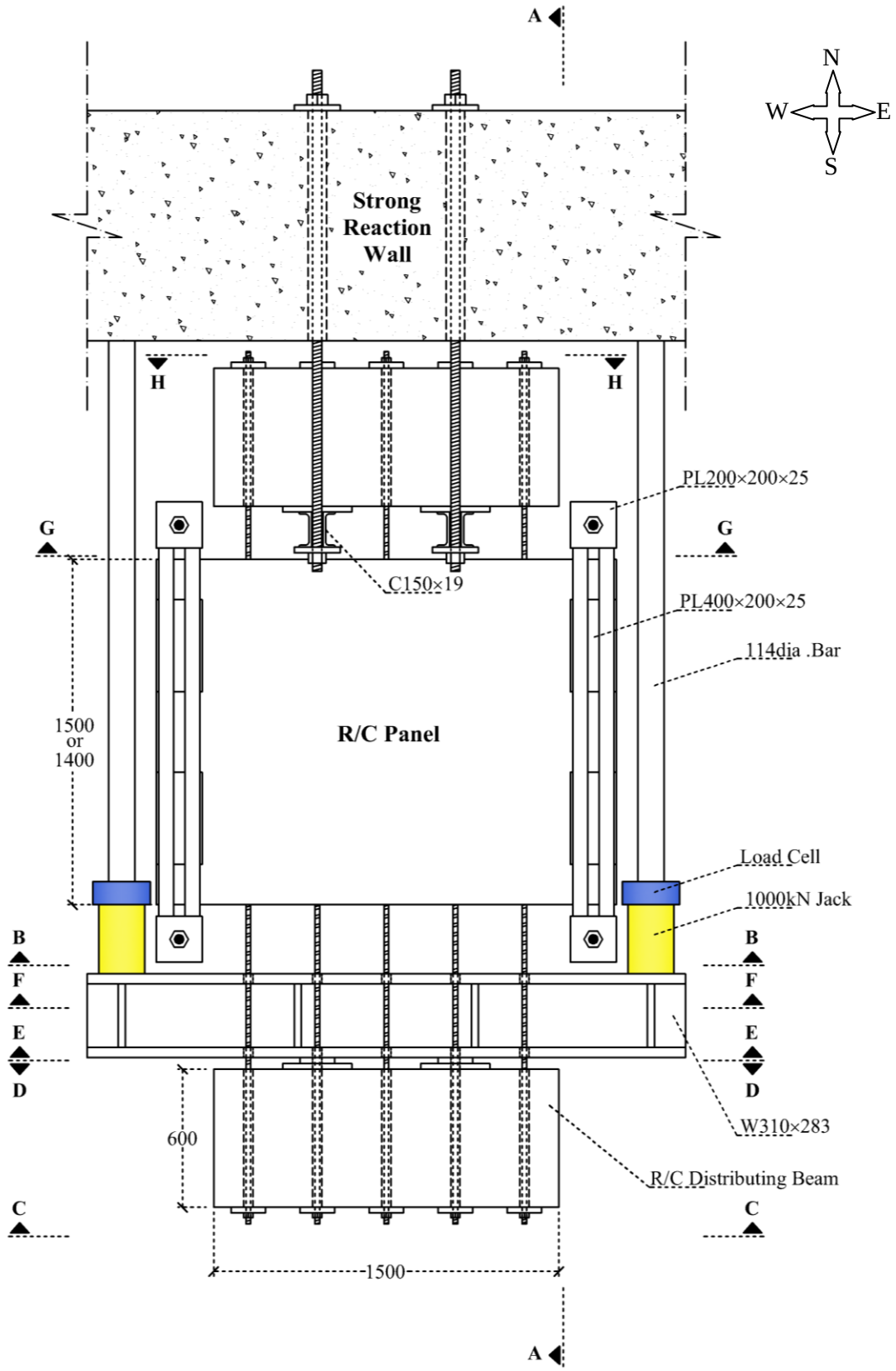

Fig. 4.5 Plan view of the test setup (dimensions in *mm*)

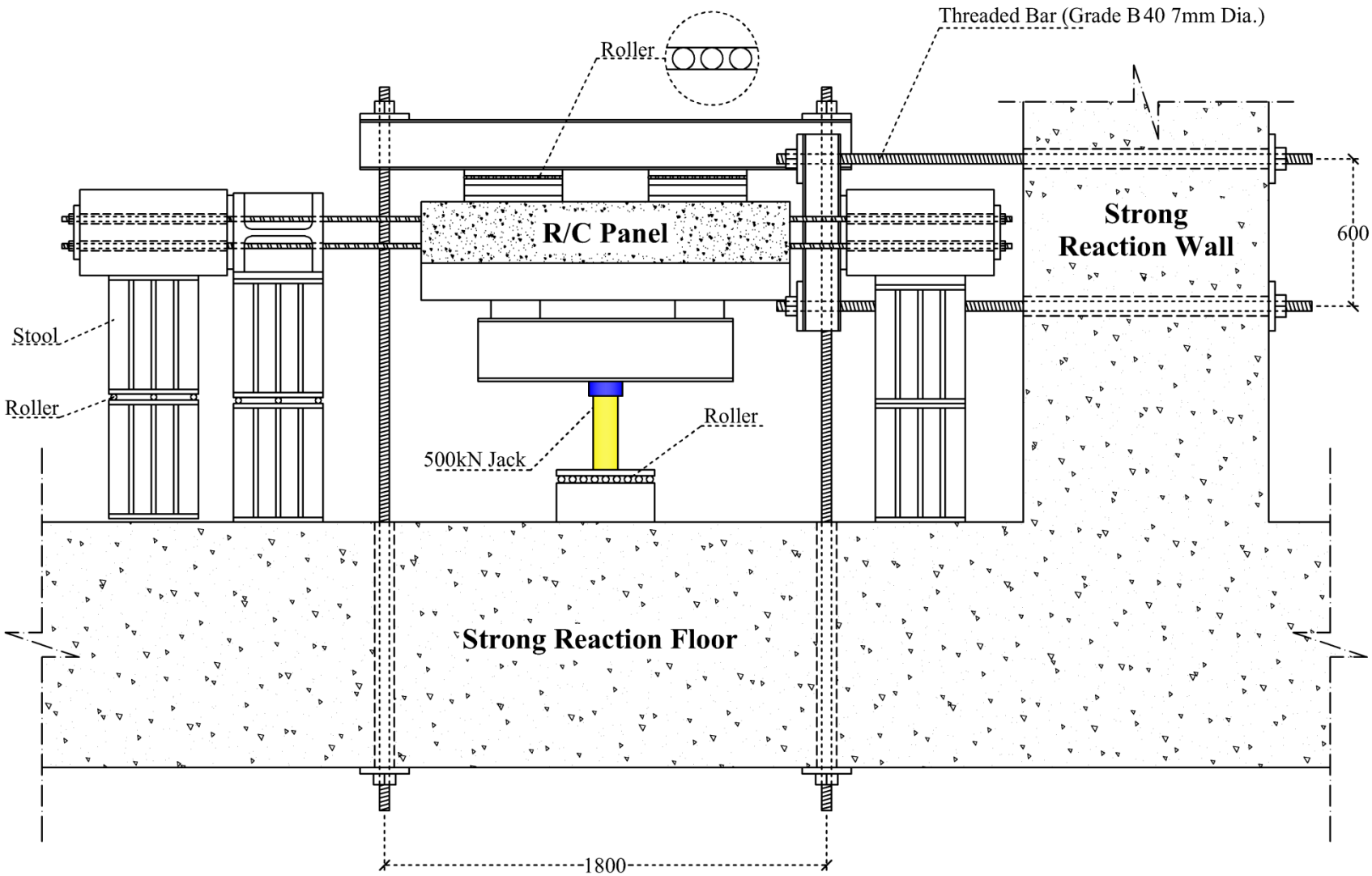

Fig. 4.6 Section A-A in Fig. 4.5 (dimensions in *mm*)

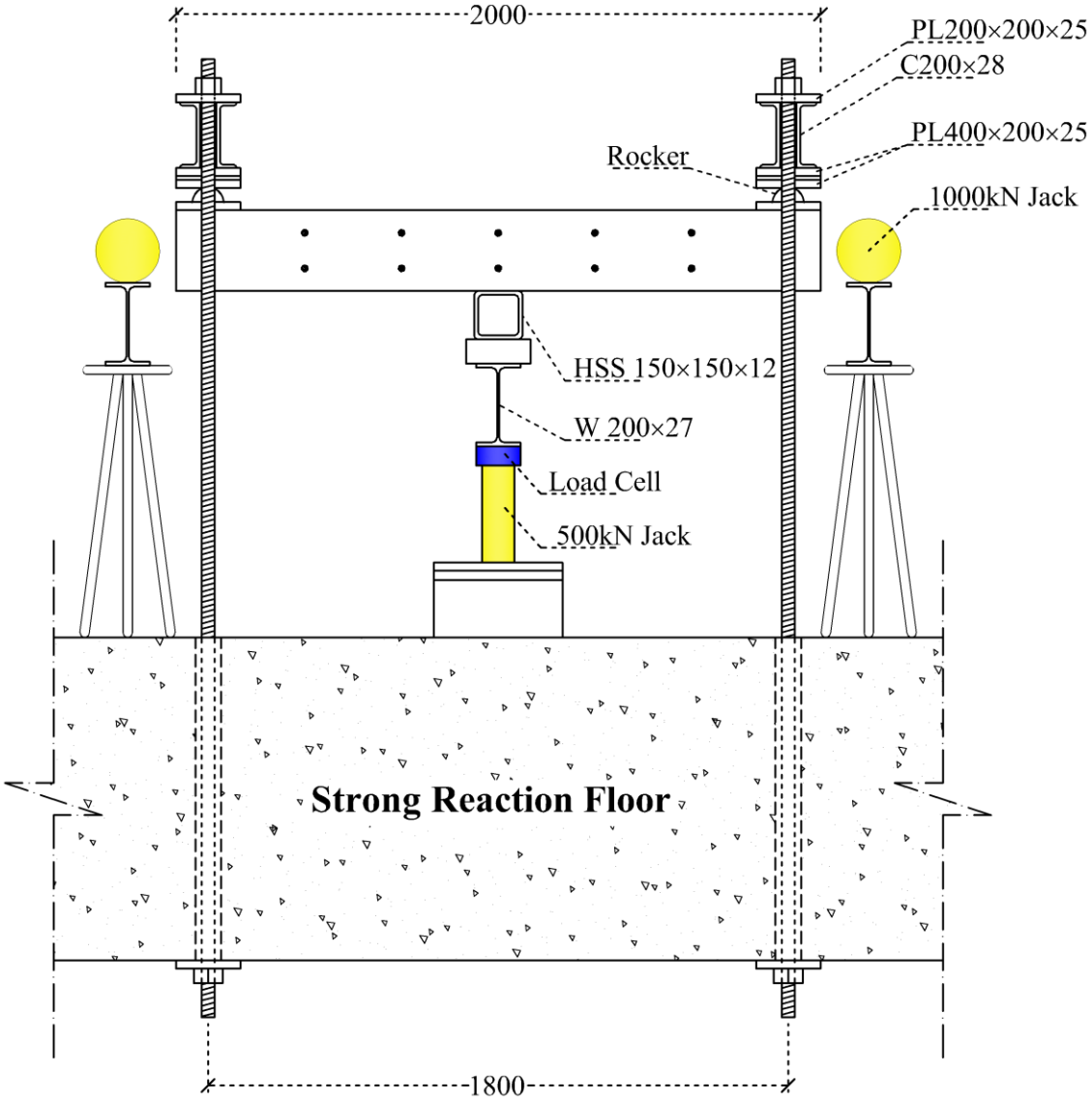

Fig. 4.7 Section B-B in Fig. 4.5 (dimensions in *mm*)

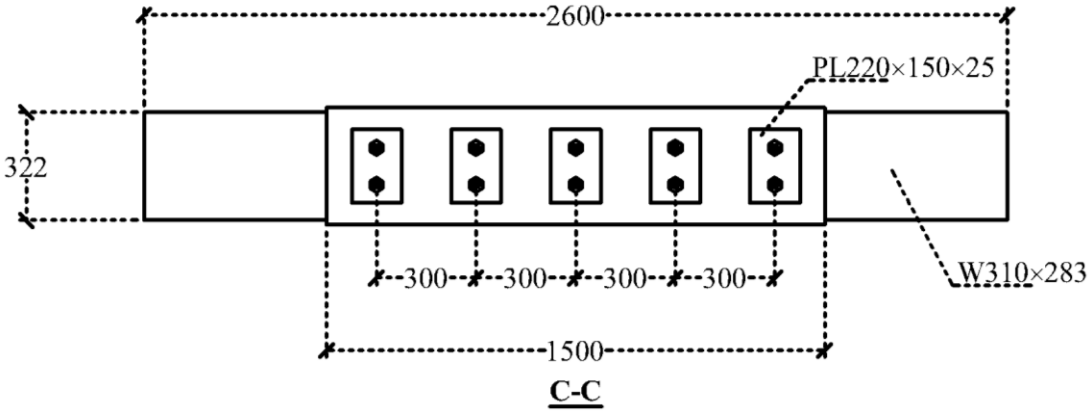

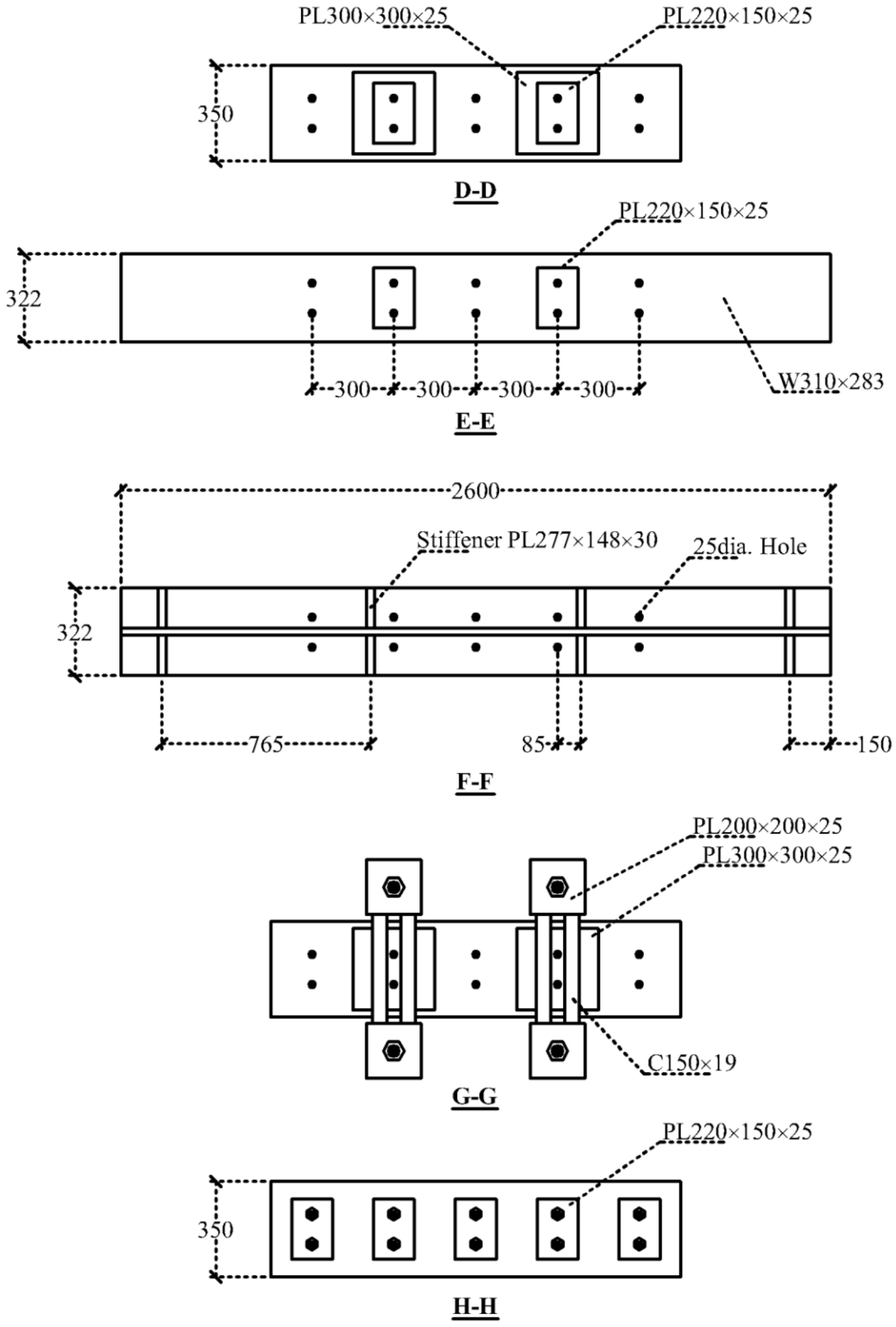

Fig. 4.8 Different section views in Fig. 4.5 (dimensions in *mm*)

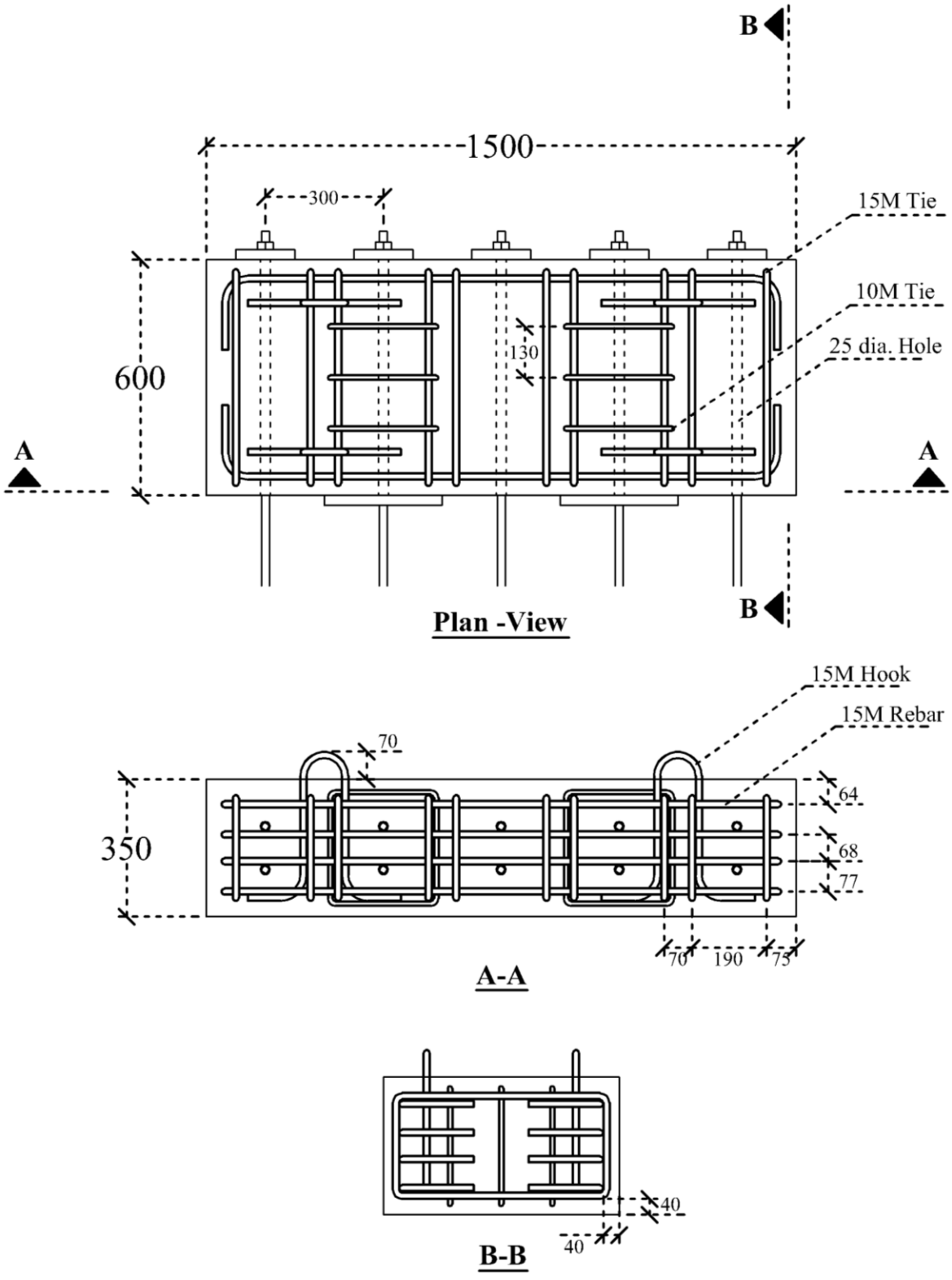

Fig. 4.9 Reinforcement layout of RC distributing beam

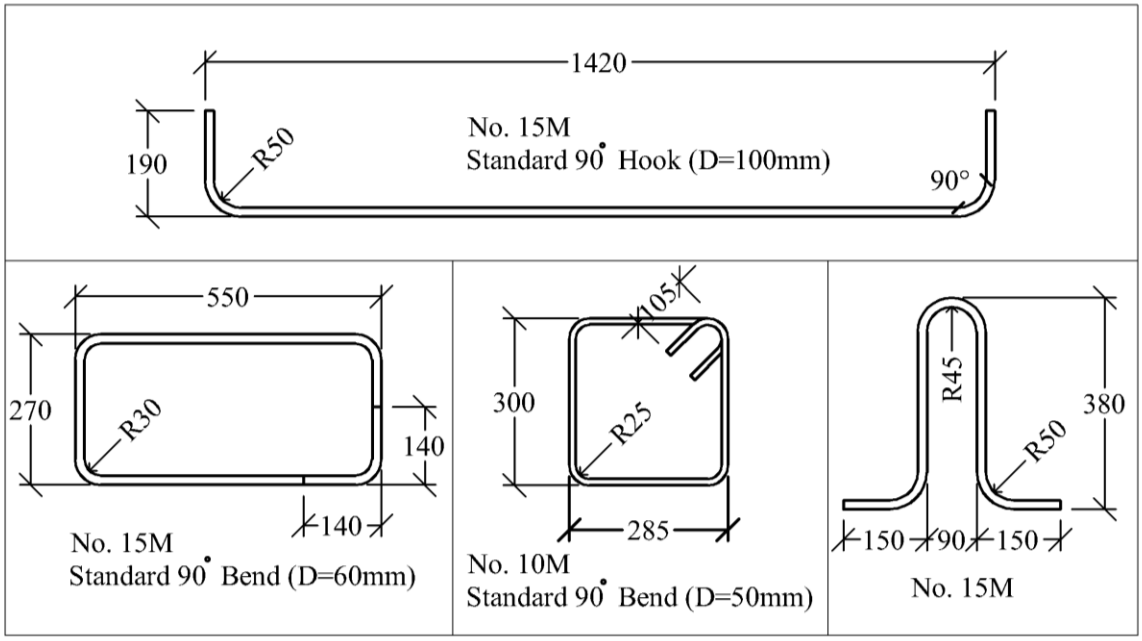

Fig. 4.10 Details of reinforcing bars used in RC distributing beam

4.5 Specifications of RC Panels

The effect of two different parameters on the two-way cracking behaviour will be investigated, namely, the reinforcement ratio and the spacing of the reinforcing bars. For that reason, three RC panels are built, which are labelled as A, B, and C, as shown in Fig. 4.11. The RC panels A and B, shown in Fig. 4.11(a), have the same dimensions and reinforcement layout, however the size of direct and flexural reinforcing bars is reduced from No. 20M in panel A to No. 15M in panel B to investigate the effect of a changing reinforcement ratio. Additionally, a third RC panel, panel C shown in Fig. 4.11(b), is built to investigate the effect of the bar spacing. This is achieved comparing the panels A and C, in which the reinforcement ratio is kept constant for flexural reinforcement while the spacing of the flexural reinforcing bars are reduced from 300 *mm* in panel A to 200 *mm* in panel C. Accordingly, to keep the reinforcement ratio constant in flexural direction, the size of flexural reinforcing bars and the width of flexural section are proportionally reduced in panel C. The dimensions and detailing of reinforcing bars used in RC panels are shown in Fig. 4.12.

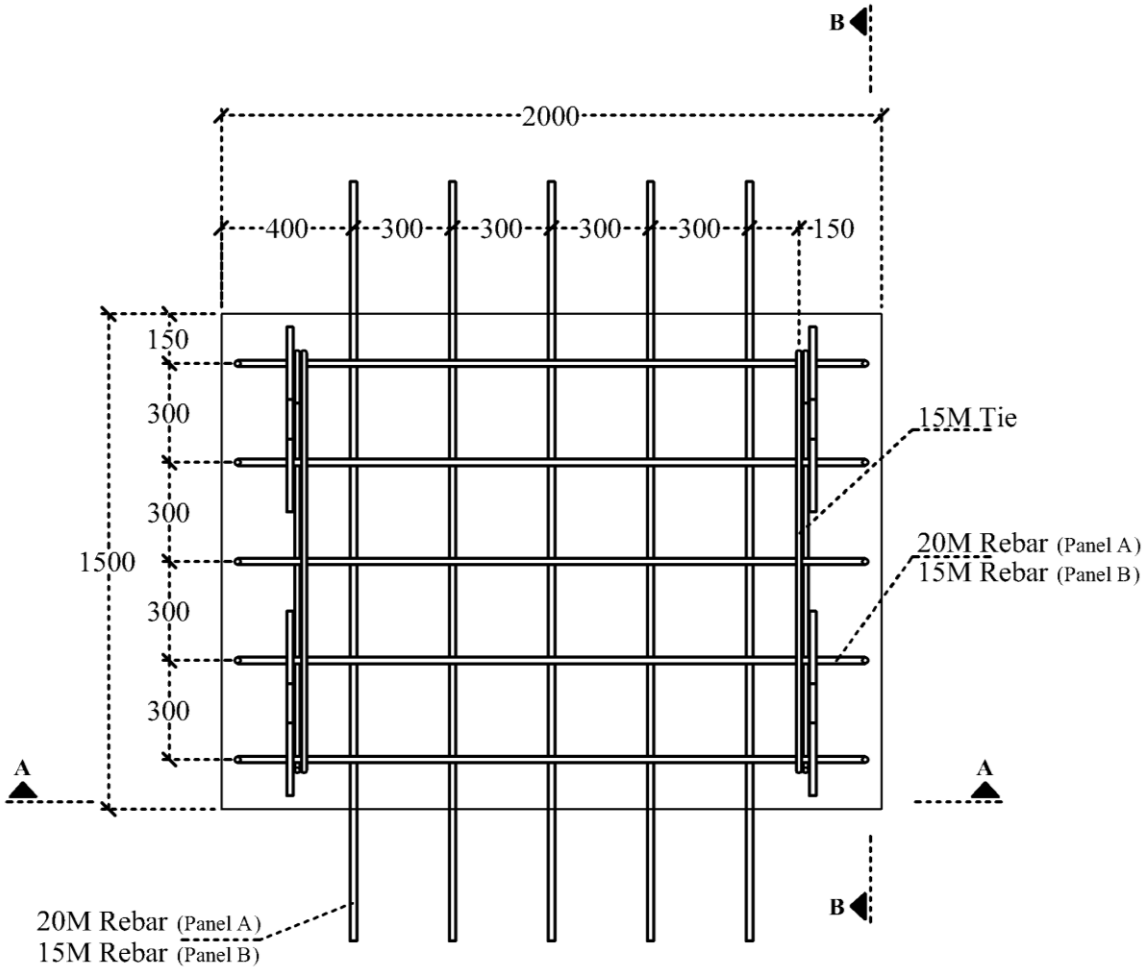

Plan -View

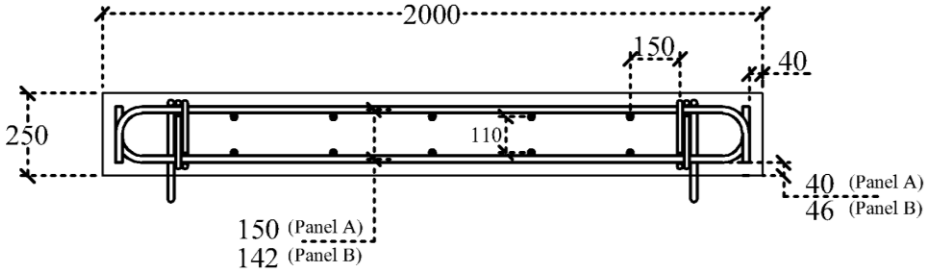

A-A

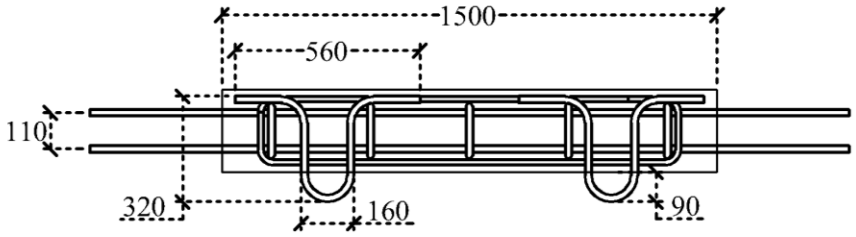

B-B

(a)

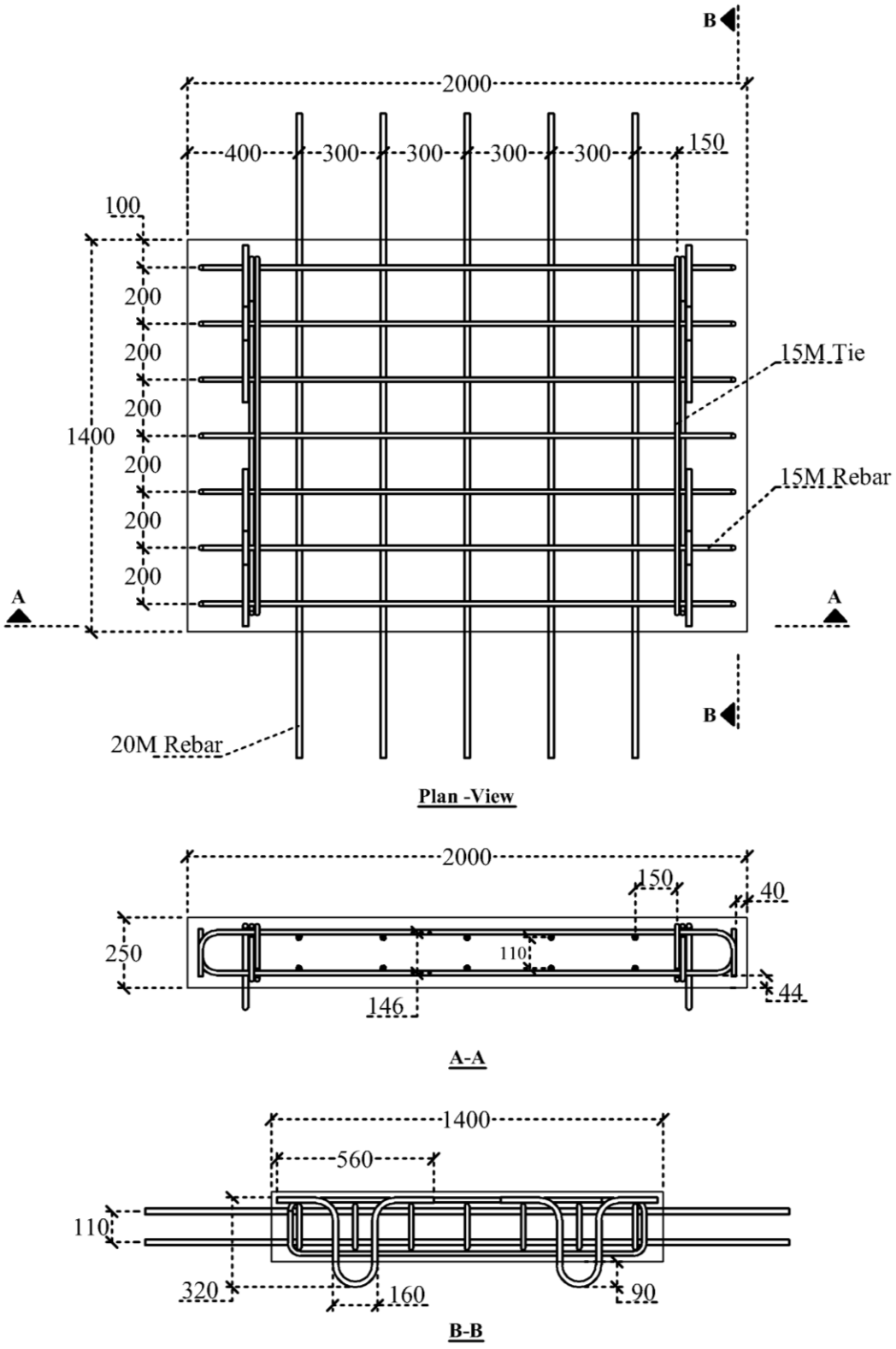

(b)

Fig. 4.11 Reinforcement layout of RC panels, a) panels A and B, b) panel C (dimensions in *mm*)

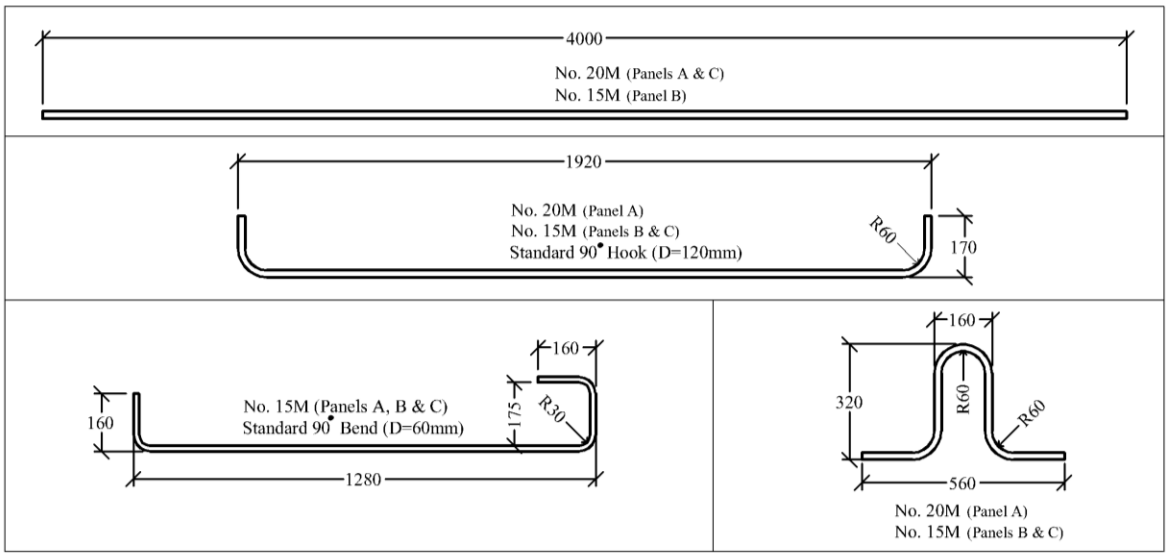

Fig. 4.12 Detailing of reinforcing bars used in RC panels

4.6 Instrumentations

The steel reinforcing bars in RC panels are instrumented with electrical resistance strain gauges (10 *mm* gauge length) at various locations. The RC panels are also instrumented with electrical resistance strain gauges (120 *mm* gauge length) attached to the concrete at top and bottom surfaces of these panels. The labelling of these gauges is defined in Fig. 4.13. The locations of these strain gauges are shown in Fig. 4.14 and Fig. 4.15 for steel and concrete strain gauges, respectively. These strain readings can help to detect the moment of crack initiation, the bond behaviour, and the variation of steel stresses. These data are also useful in verifying the mathematical modeling of the cracking behaviour. As it is shown in Fig. 4.15, an LVDT (Linear Variable Differential Transformer) displacement transducer is also mounted on top of the RC panel to measure the elongation of the RC panel along the axis of direct tension.

After formation of cracks, the widths of these cracks are measured either manually or automatically. A microscope that has a scale graduated into 0.02 *mm* divisions is used for manual measurement of the crack width. This microscope is shown in Fig. 4.16. Two types of crack displacement transducers are used for automatic measurement of the crack width, namely, PI-2-50 and KG-5A, as shown in Fig. 4.17. These gauges have sensitivities of 2000 and 800 *micro-*

strain/*mm*, respectively. These gauges are mounted on a number of cracks at various locations. The locations and labeling of these gauges will be shown later on the crack patterns.

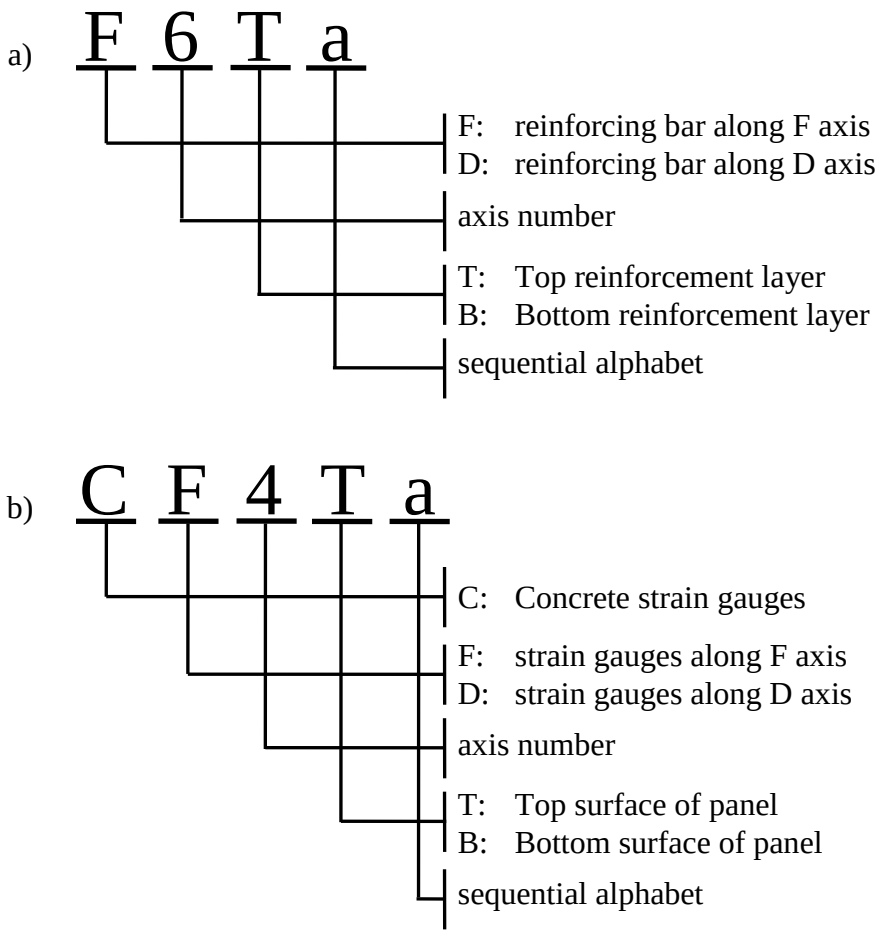

Fig. 4.13 Strain gauge designations, a) steel strain gauges, b) concrete strain gauges

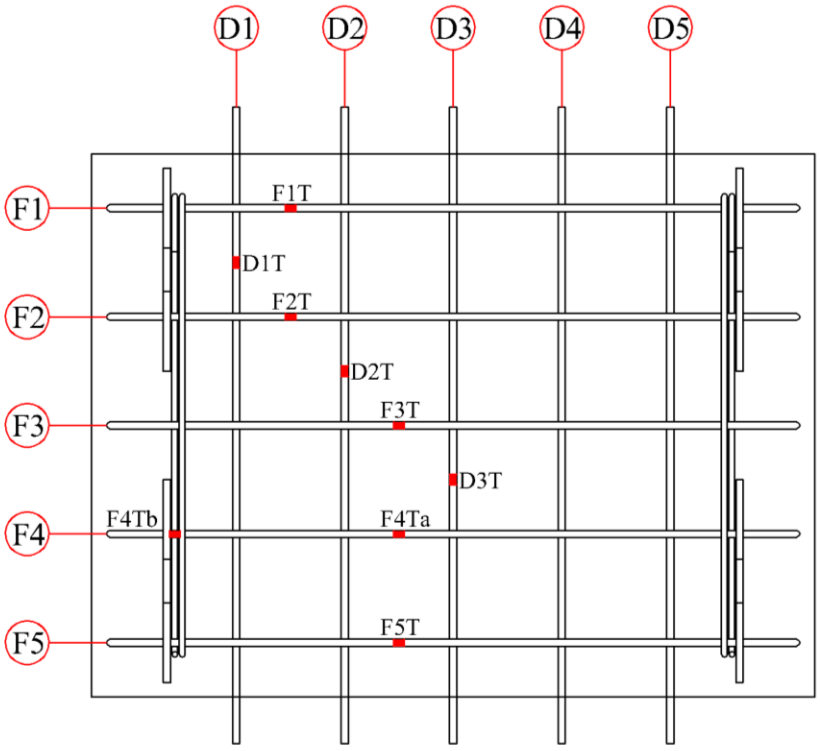

Top Reinforcement Layer

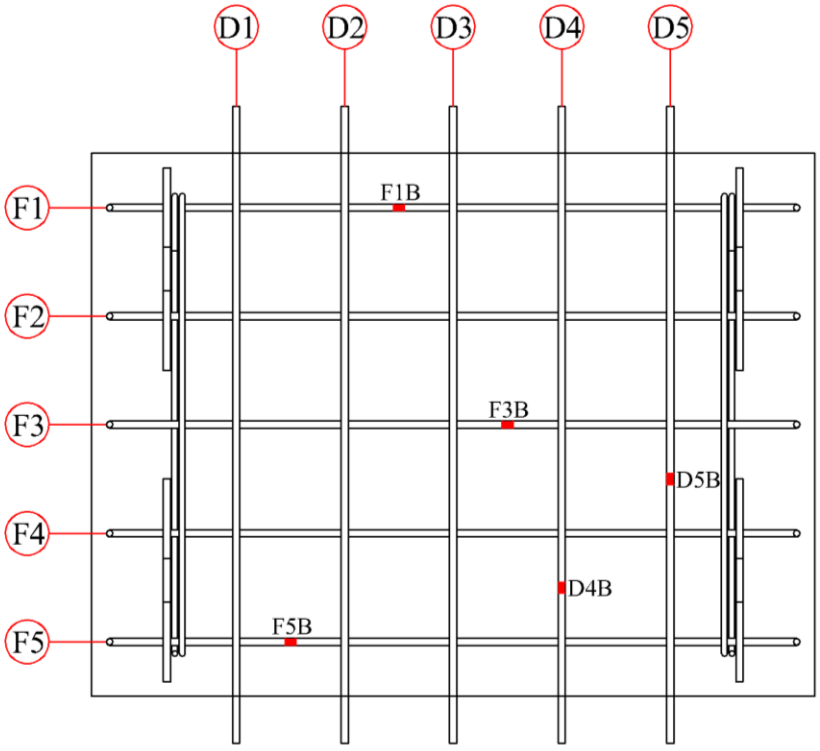

Bottom Reinforcement Layer

(a)

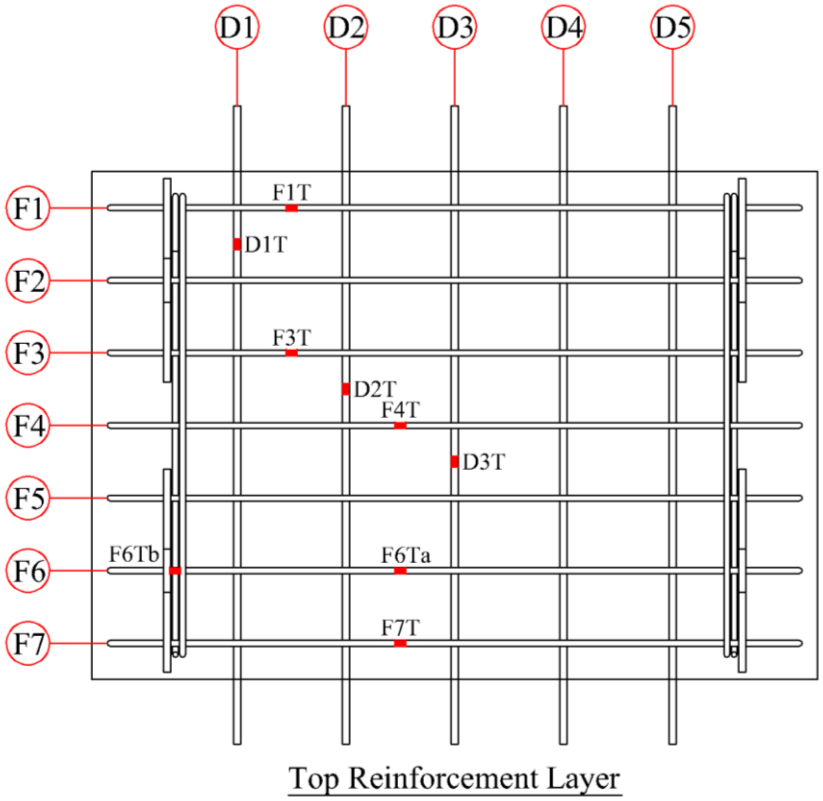

Top Reinforcement Layer

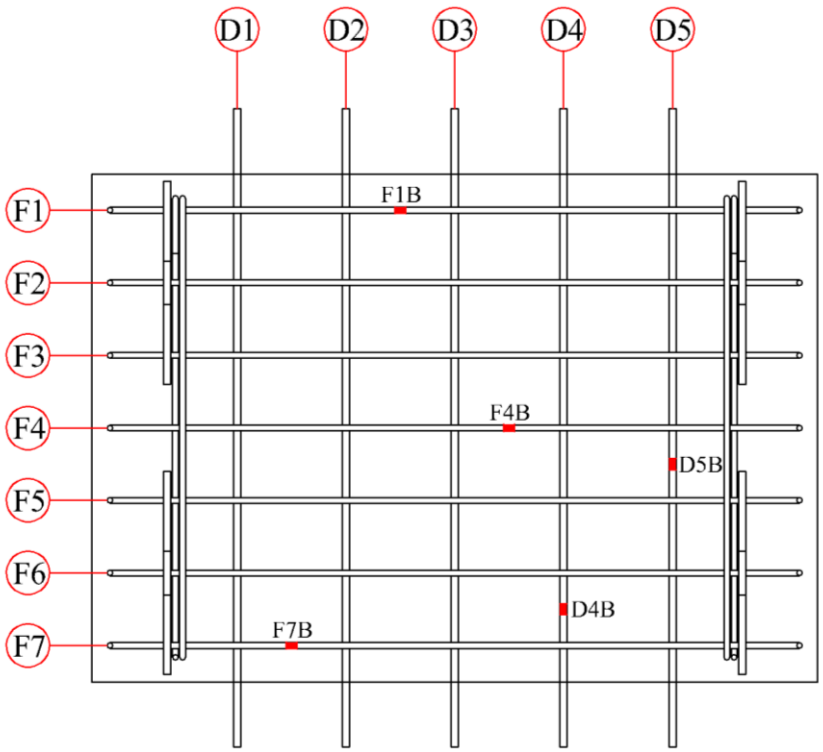

Bottom Reinforcement Layer

(b)

Fig. 4.14 Steel strain gauges, a) panels A and B, b) panel C

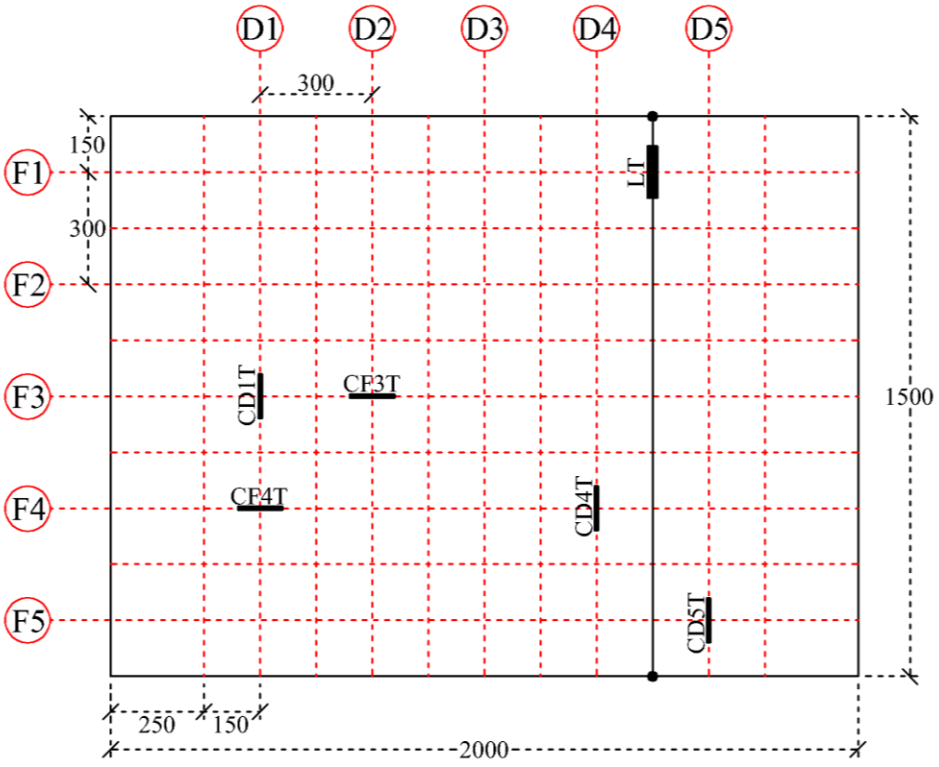

Top Surface

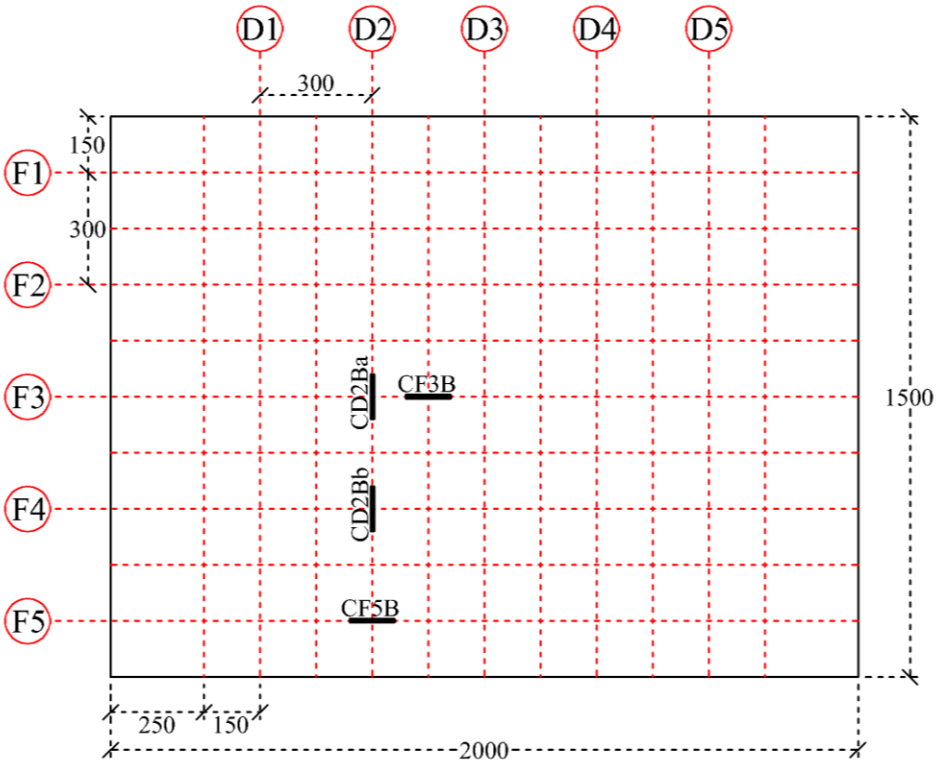

Bottom Surface

(a)

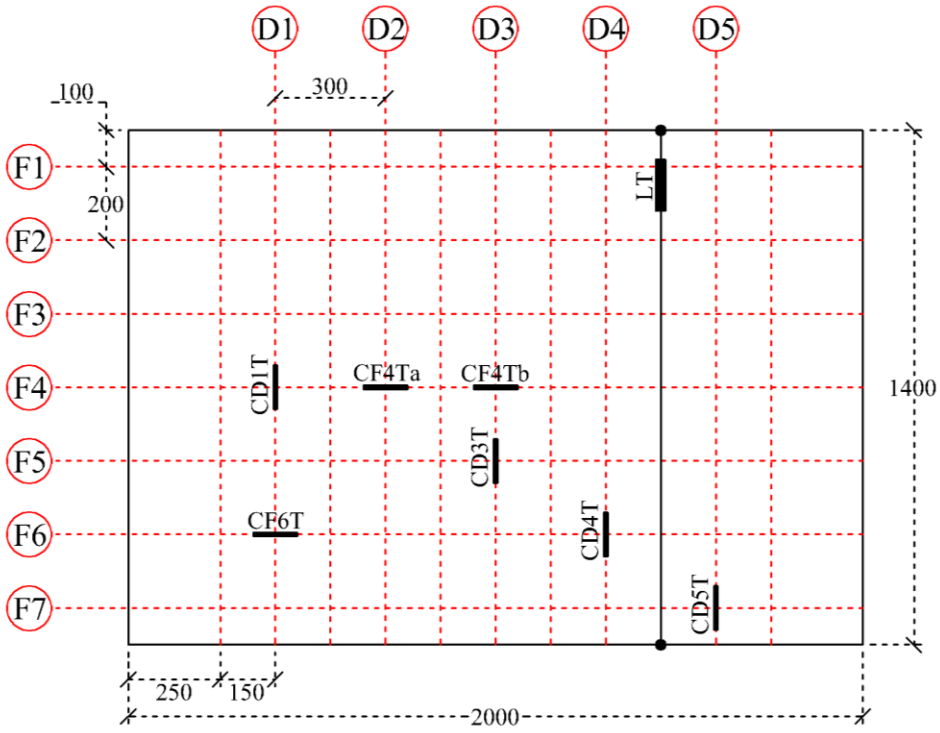

Top Surface

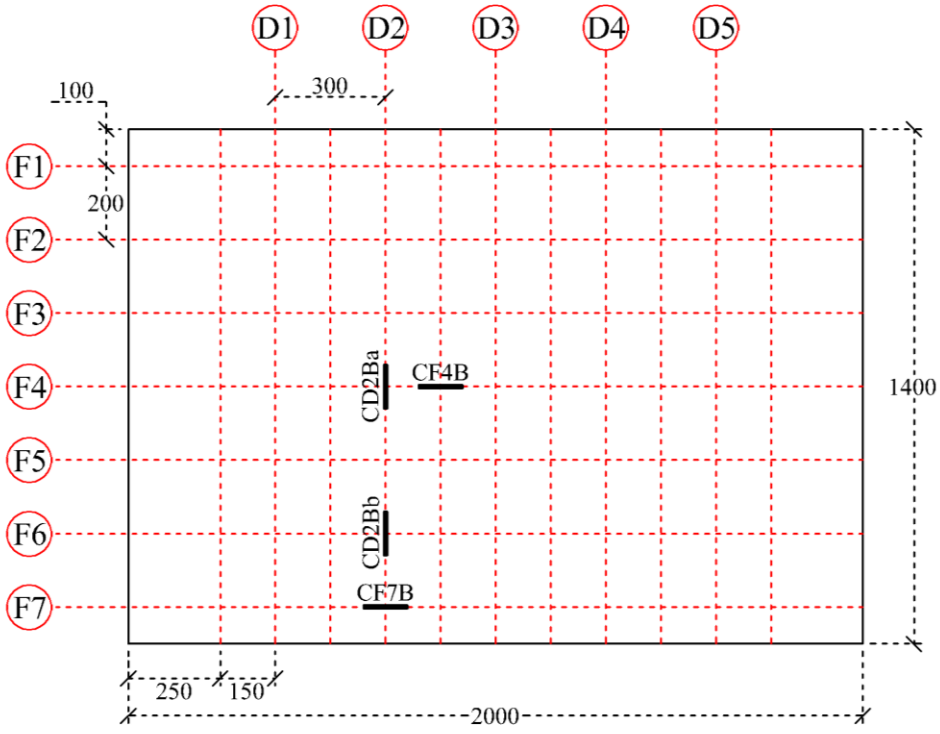

Bottom Surface

(b)

Fig. 4.15 Concrete strain gauges and LVDT, a) panel A and B, b) panel C

Fig. 4.16 Crack microscope

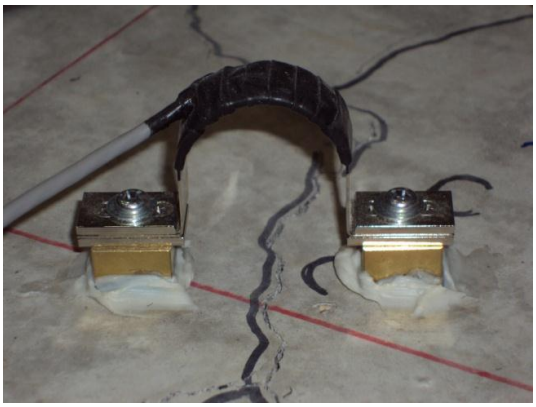

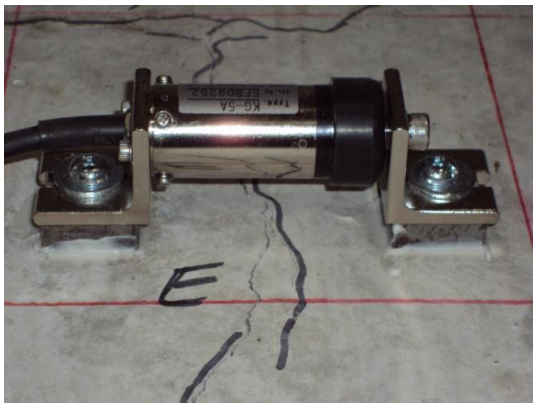

(a) (b)

Fig. 4.17 Crack displacement transducers, a) PI-2-50, b) KG-5A

4.7 Preparation of Test Setup

After finalizing the design and planning of the test setup, the construction phase of the experimental test is started. Based on the design sketches, different components of the test setup are obtained from the supplier. Additional cutting, drilling and welding are performed in the final preparation of these parts.

4.7.1 Installation of steel strain gauges

The procedure for the installation of strain gauges on the steel reinforcing bars is shown in Fig. 4.18. First the reinforcing bar is slightly grinded to create a smooth surface, Fig. 4.18(a). Then the steel surface is cleaned with the isopropyl alcohol, conditioner, and neutralizer. While it is aligned with the bar longitudinal axis, the strain gauge is glued on the surface with the appropriate gauge cement, Fig. 4.18(b). At this stage, the gauge wires are connected and soldered to the extension wires. Electric tape is used to insulate the wires from the steel bar. A layer of water proof coating and another piece of electric tape on top of it are used to cover the strain gauge, Fig. 4.18(c). Finally, everything is covered with a piece of aluminum tape to ensure better water and damage proof conditions, Fig. 4.18(d).

(a)

(b)

(c)

(d)

Fig. 4.18 Installation procedure of steel strain gauges, a) smoothed surface, b) gluing, c) waterproof coating, d) aluminum wrap

4.7.2 Casting RC panels and distributing beams

The wooden formworks are built for RC panels and RC distributing beams. The reinforcing bars are placed into these formworks while the strain gauge extension wires are collected at one side, as shown in Fig. 4.19. The panels are built upside down to achieve a smooth flat top surface for easier crack observations.

A ready-mix concrete from the supplier with the w/c ratio of 0.4, the slump of 150 *mm*, and the maximum aggregate size of 20 *mm* is used for these specimens. The concrete for three panels is casted at three different times, and hence, from different concrete batches. The fresh concrete is

slowly poured into the formwork and vibrated with care so as not to damage the steel strain gauges, as shown in Fig. 4.20(a). The concrete surface is troweled to achieve a flat finishing surface. Concrete cylinder and beam samples are also made from each concrete batch that will be used for the property test of concrete.

The fresh concrete is cured on-site for all specimens and samples, as shown in Fig. 4.20 (b) and (c). Right after casting, the fresh concrete is covered with plastic sheets. After a few hours, when the concrete surface is hardened and started to become dry, the concrete surface is sprayed with water and covered with wet burlaps and plastic sheets. This procedure is continued for seven days, and then the specimens are demolded and exposed to the laboratory environment without any further curing.

(a)

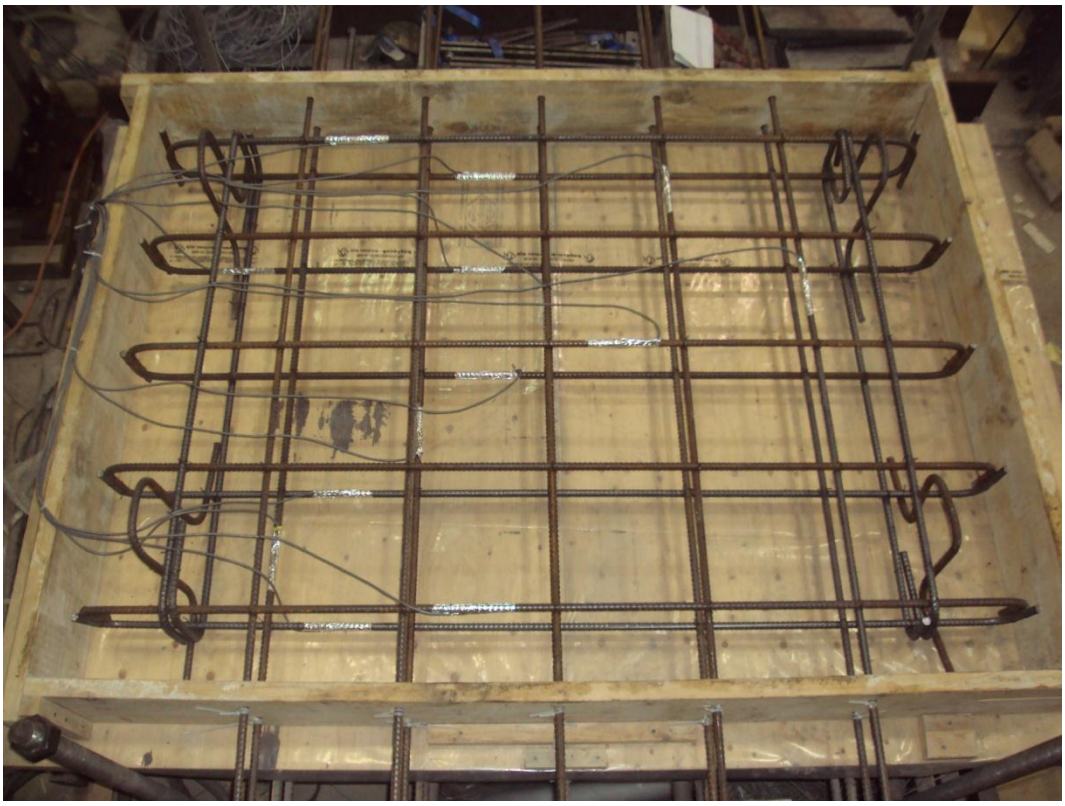

(b)

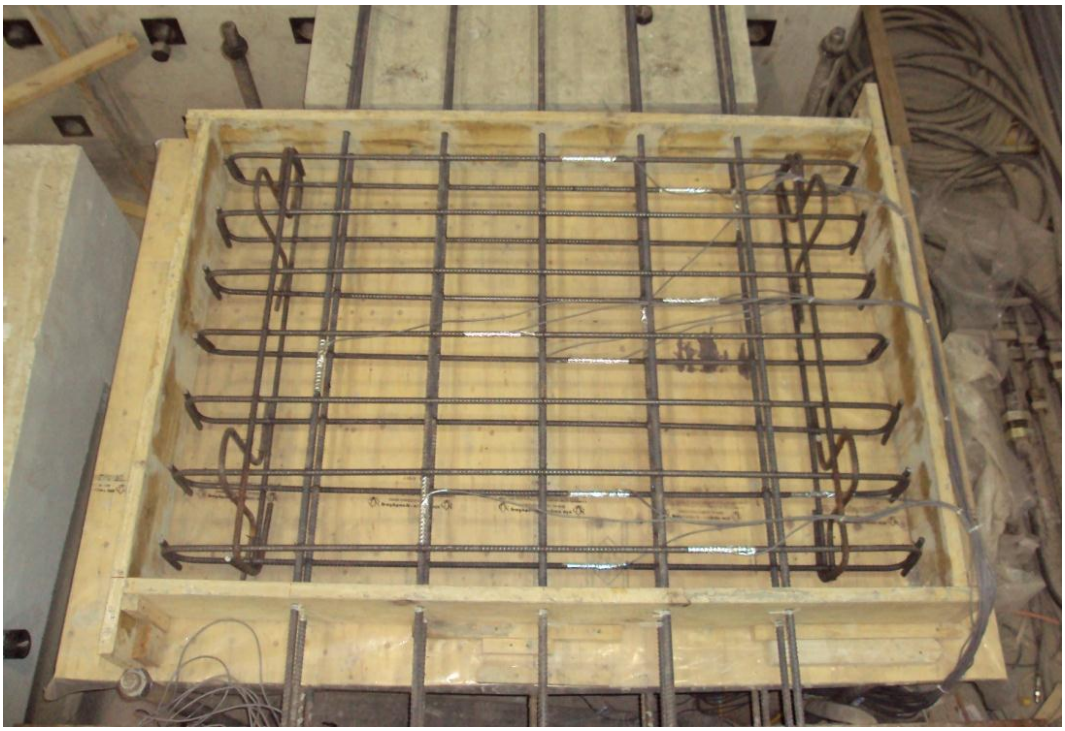

(c)

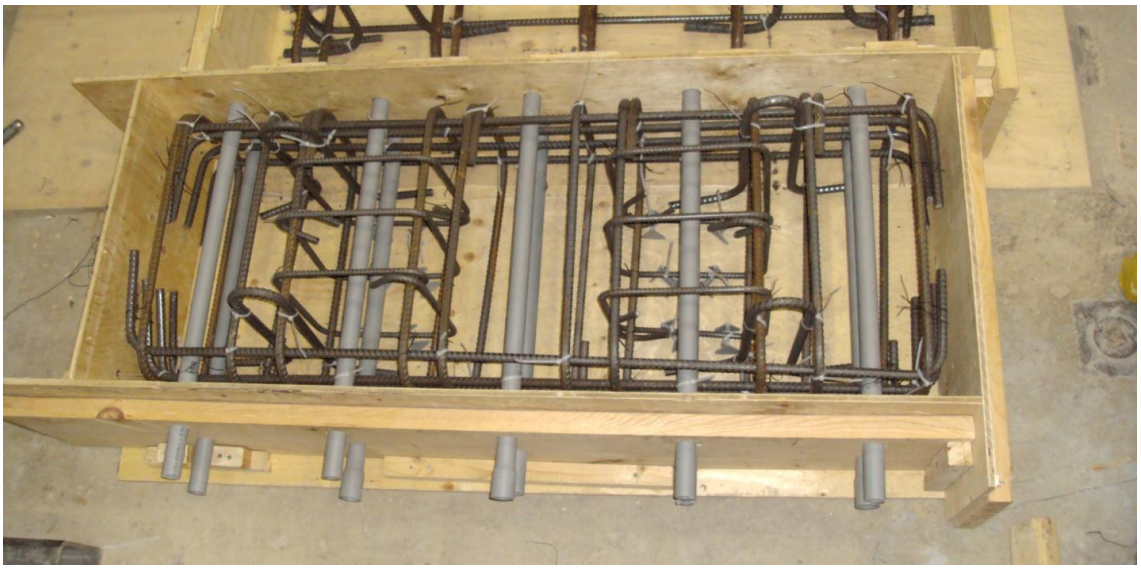

(d)

Fig. 4.19 Formwork and reinforcement cage, a) panel A, b) panel B, c) panel C, d) RC distributing beam

(a)

(b)

(c)

Fig. 4.20 Concrete casting, a) freshly casted concrete, b) on-site curing of panels, c) on-site curing of samples

4.7.3 Assembling test setup

All different components of the test setup are assembled together based on the design sketches given earlier in this Chapter. A typical test setup is shown in Fig. 4.21. As the panels are built upside down, they are flipped over before putting them into the test setup. Orthogonal red grid lines are drawn on the top and bottom surfaces of the panels for easy positioning of the instrumentations, and also to precisely locate and scale the crack patterns. To fix the direct tension reinforcing bars at two ends, after the final precise alignment, high strength bolts are welded to the reinforcing bars as shown in Fig. 4.22.

(a)

(b)

(c)

Fig. 4.21 Test setup, a) top view, b) side jack, c) bottom center jack

(a) (b)

Fig. 4.22 Fixed end detailing of direct reinforcing bars, a) before welding, b) after welding

4.7.4 Installation of concrete strain gauges

A number of electrical strain gauges are installed on the concrete surface at certain locations according to the Fig. 4.15. Before installation of these gauges, a layer of epoxy adhesive coating is applied to the concrete surface right at locations where the gauge is to be installed, and it is left to cure for 24 hours. This smooth coating layer would ensure a good bond between the strain gauge and the concrete surface. The subsequent steps of the installation procedure for the strain gauges is the same as those installed on the steel reinforcing bars explained earlier in this section. A typical strain gauge installed on the concrete surface is shown in Fig. 4.23.

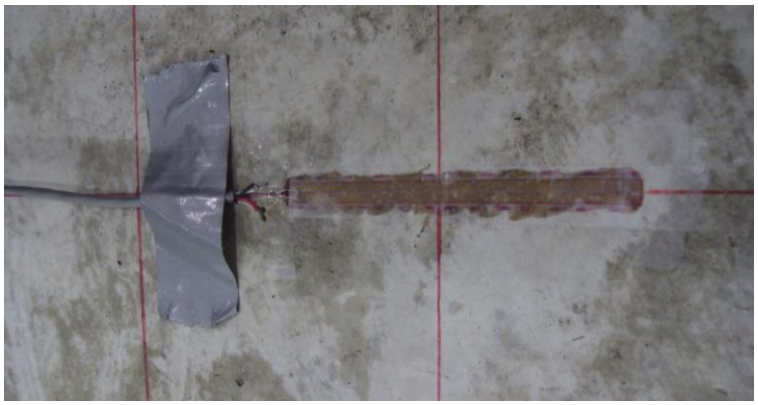

Fig. 4.23 Strain gauge attached to concrete surface

4.8 Concrete Property Tests

Three types of concrete property tests are conducted on the concrete samples, namely, the cylinder compressive test, the cylinder splitting test, and the third-point beam test. These tests would give the compressive strength, the splitting tensile strength, and the modulus of rupture of the concrete, respectively. The apparatuses used for these tests are shown in Fig. 4.24. These tests are conducted in accordance with the ASTM standards (C39/C39M-05 (2005), C496/C496M-04 (2004), and C78-08 (2008)). All concrete property tests are performed at 28 days and on the day RC panels are tested, except the cylinder compressive tests for which additional tests at 14 days are also performed. The results of the concrete property tests are summarized in Table 4.1. The mean value of the results after 28 days will be used in the future calculations due to the scatter of these results.

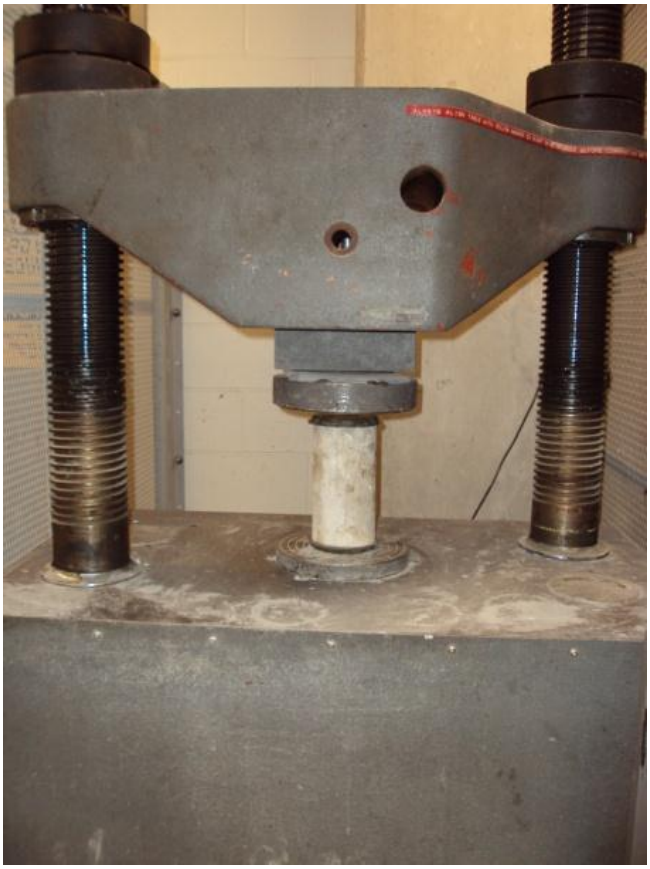

(a)

(b)

(c)

Fig. 4.24 Apparatus for concrete property test, a) compressive cylinder test, b) cylinder splitting test, c) third-point beam test

Table 4.1 Results of concrete property tests

Panel	Days	Cylinder (100×200 *mm*) Compressive Strength (*MPa*)	Mean Compressive Strength (*MPa*)	Cylinder (100×200 *mm*) Split Tensile Strength (*MPa*)	Mean Split Tensile Strength (*MPa*)	Third-Point Beam (76×102×406 *mm*) Modulus of Rupture (*MPa*)	Mean Modulus of Rupture (*MPa*)
A	14	33.1	34.4				
		35.6					
	28	47.5		2.3		4.6	
		33.8		3.3		4.6	
		45.2		2.4			
	116 (Test Day)	34.0	41.9	4.2	3.3	5.9	5.4
		37.2		3.4		6.4	
		50.9		4.1			
		44.5					
B	14	39.9	31.9				
		29.5					
		26.2					
	28	46.7		2.7		5.1	
		47.7		2.5		4.8	
		47.2		4.1			
	73 (Test Day)	46.4	46.0	2.7	3.1	5.3	5.2
		44.9		3.1		5.7	
		41.2		3.6			
		47.7		2.5			
				3.1			
				3.7			
				3.3			
				3.0			
C	14	31.8	32.2				
		32.0					
		32.6					
	28	33.6		3.3		4.2	
		37.7		3.2		4.6	
		39.3					
	63 (Test Day)	37.1	37.4	3.0	3.1	4.0	4.6
		34.8		3.6		5.6	
		39.6		2.4			
		34.6		3.2			
		38.9		2.8			
		40.8		3.2			

4.9 Testing Stages

The testing of the RC panels is performed in a number of stages. The loads are applied through two side jacks and one bottom center jack. These hydraulic jacks are operated with manual pumps. The correlations of these loads at different stages are given in Fig. 4.25, Fig. 4.26, and Fig. 4.27 for panels A, B, and C, respectively. For panels A and B, the loads are applied in increments of 1 kN for the center jack and 6 kN for the side jacks. For panel C, the loads are applied in increments of 1.4 kN for the center jack and 9 kN for the side jacks.

Generally, in the 1st stage the two-way loads are applied simultaneously in a constant ratio up to the observation of the first set of cracks (Fig. 4.25(a), Fig. 4.26(a), Fig. 4.27(a)). The constant two-way loading ratio at this stage is based on those calculated in Eq. 4.1. The self-weight (*s.w.*) in this equation is taken to be approximately 29 *kN* for all panels based on the scaling performed in the lab. The crack lines are marked with a black ink marker as soon as they are initiated. Photos are also taken at each cracking load level to record the crack propagation sequence. The width of cracks at this stage is measured with the microscope. As soon as the first set of cracks is observed, the panels are unloaded for the installation of the crack gauges. These gauges are mounted on several cracks at various locations. A concrete adhesive is used to attach these gauges to the concrete surface.

In the next stage, the panels are reloaded again with the same constant two-way loading ratio to record the crack widths (Fig. 4.25(b), Fig. 4.26(b) and (c), Fig. 4.27(b)). The loading is stopped below the yield level of steel reinforcing bars. The main goal of these experiments, which is to observe the two-way cracking behaviour at the service load level, is accomplished after completing this stage. The subsequent testing stages are performed to collect additional useful information.

In the next stage, the panel is loaded in direct tension only (Fig. 4.25(c), Fig. 4.26(d), Fig. 4.27(c)). While the center jack load is kept at the self-weight level, the side jack loads are increased up to the same maximum level of the previous stage. This stage is not meant to represent the one-way cracking behaviour, but it can provide information on the differences in the behaviour of a two-way cracked member under two-way and one-way loading conditions.

After unloading, the panels are reloaded in one-way bending (Fig. 4.25(d), Fig. 4.26(e), and Fig. 4.27(d)). For this purpose, while the side jack loads are kept at the zero level, the center jack loading is continued up to the same previously reached maximum level. The panels are unloaded again after completing this stage.

In the final stage, the panels are first loaded in a constant two-way loading ratio similar to that of the 1st stage up to the yield level of direct tension reinforcing bars. Then the side jack loads are kept constant while the center jack loading is continued up to the yield level of the flexural reinforcing bars (Fig. 4.25(e), Fig. 4.26(f), Fig. 4.27(e)). The newly formed cracks are marked with a blue or green ink marker. This stage is repeated for leakage tests of panel B and C (Fig. 4.26(g), and Fig. 4.27(f)). The leakage test of panel A is performed during the 2nd stage. The leakage tests will be explained in the following Section.

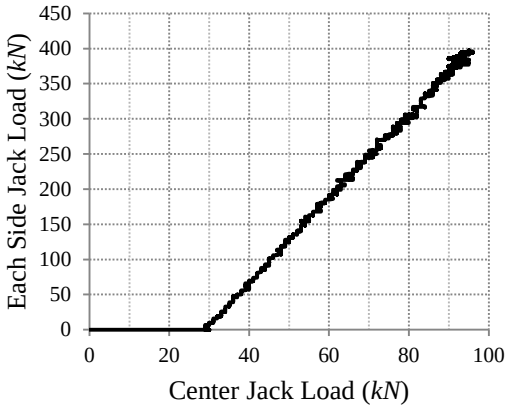

(a)

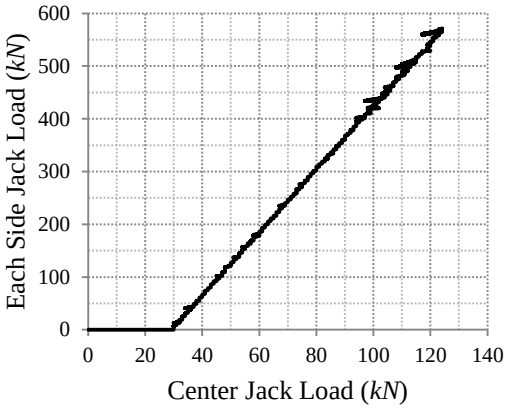

(b)

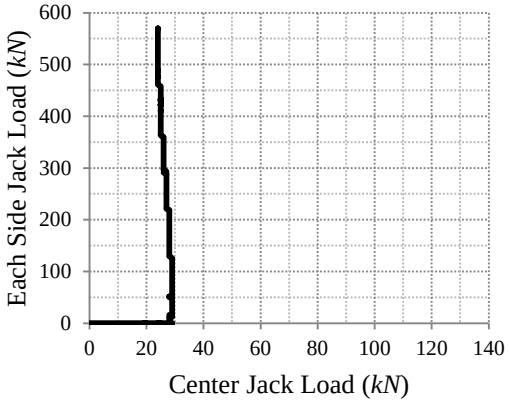

(c)

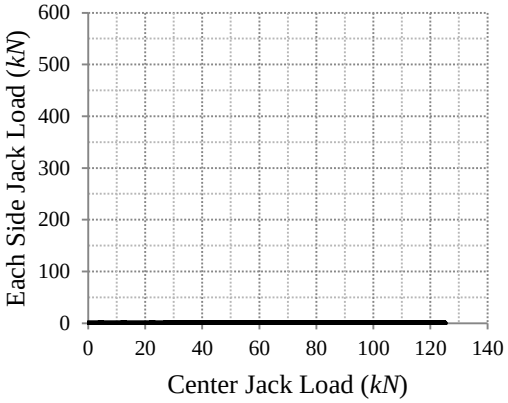

(d)

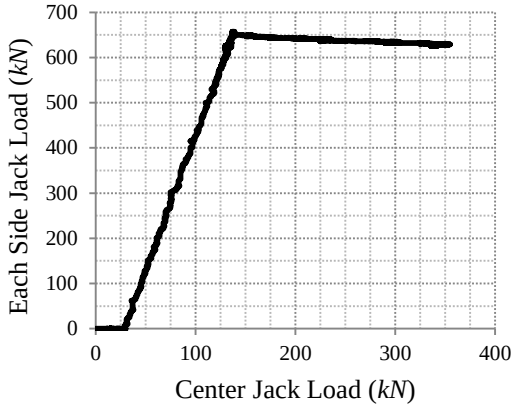

(e)

Fig. 4.25 Loading of panel A, a) 1st stage, b) 2nd stage, c) one-way tension, d) one-way bending, e) 3rd stage

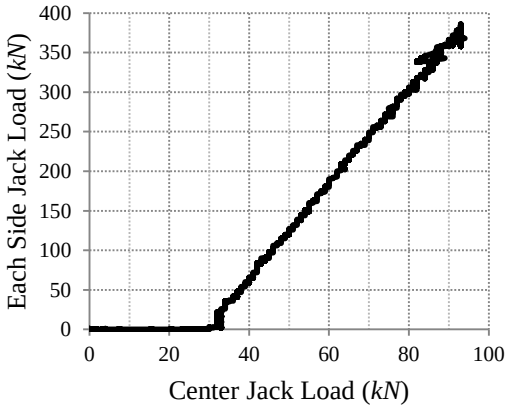

(a)

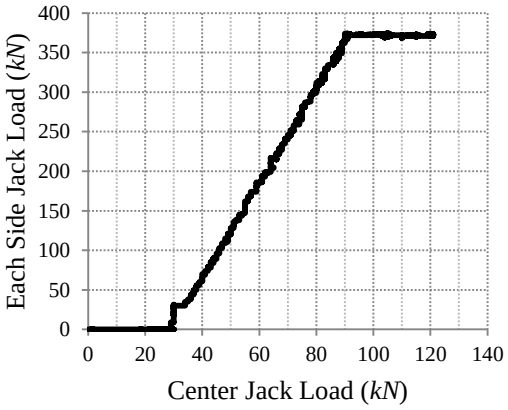

(b)

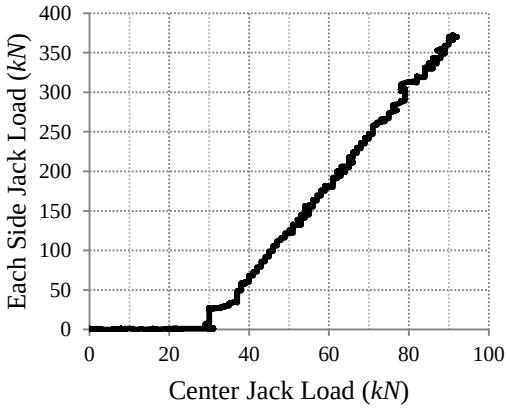

(c)

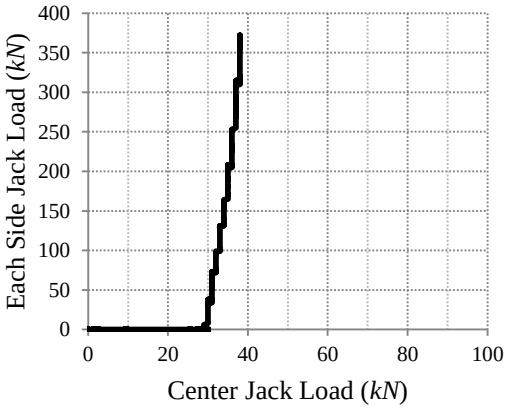

(d)

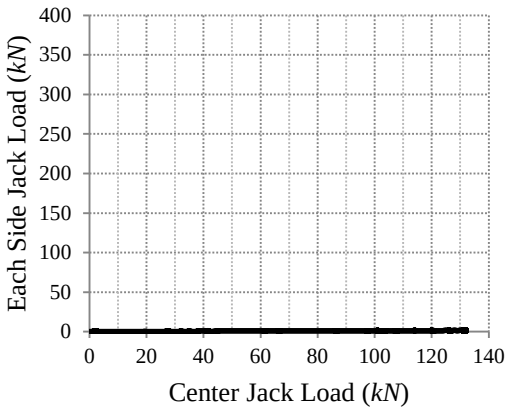

(e)

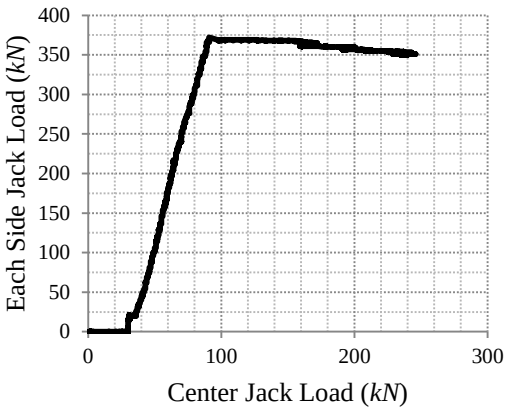

(f)

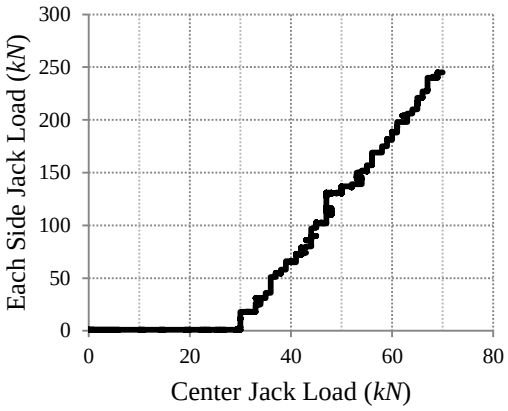

(g)

Fig. 4.26 Loading of panel B, a) 1st stage, b) 2nd stage, c) 3rd stage, d) one-way tension, e) one-way bending, f) 4th stage, g) 5th stage

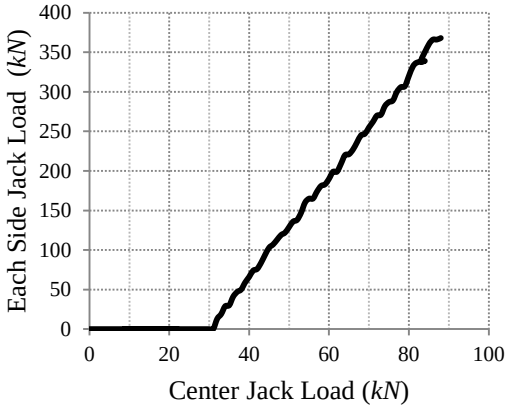

(a)

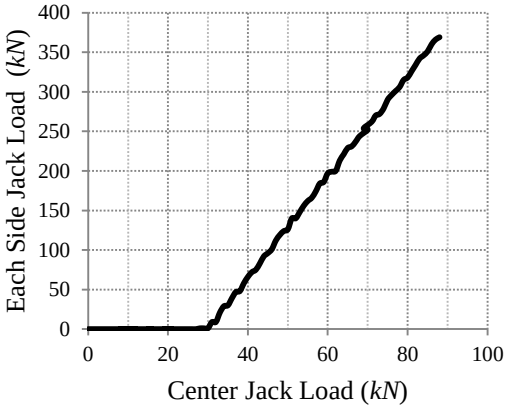

(b)

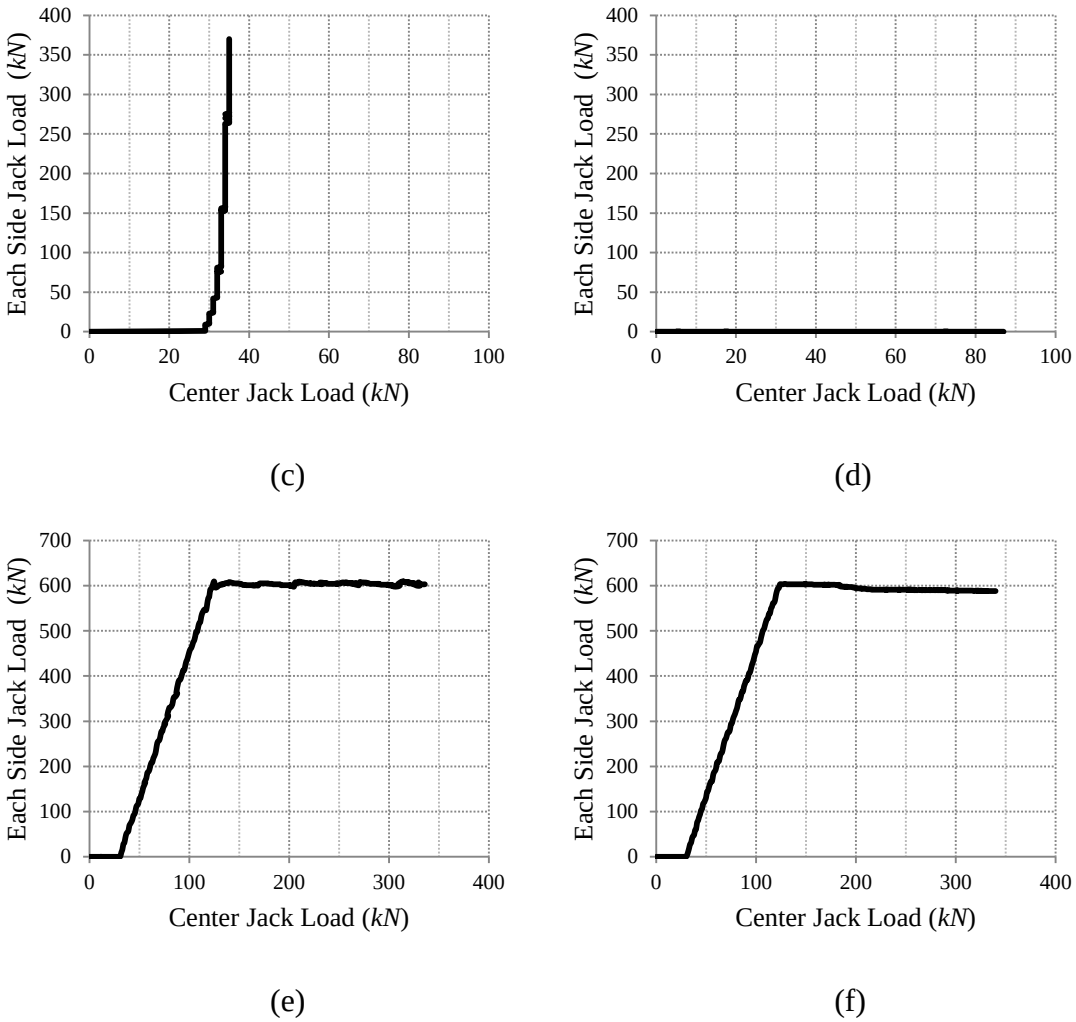

Fig. 4.27 Loading of panel C, a) 1st stage, b) 2nd stage, c) one-way tension, d) one-way bending, e) 3rd stage, f) 4th stage

4.10 Leakage Tests

The most adverse effect of cracks on the serviceability of liquid or gaseous containing structures is the risk of leakage associated with cracking. Therefore, the possibility of leakage through cracks is examined for the three tested panels. These leakage tests are not meant to quantify the leakage rate or flow, but only aimed to inspect the leakage behaviour through visual observations. A chamber that can maintain pressurized water over a cracked region of the panel is designed as illustrated in Fig. 4.28.

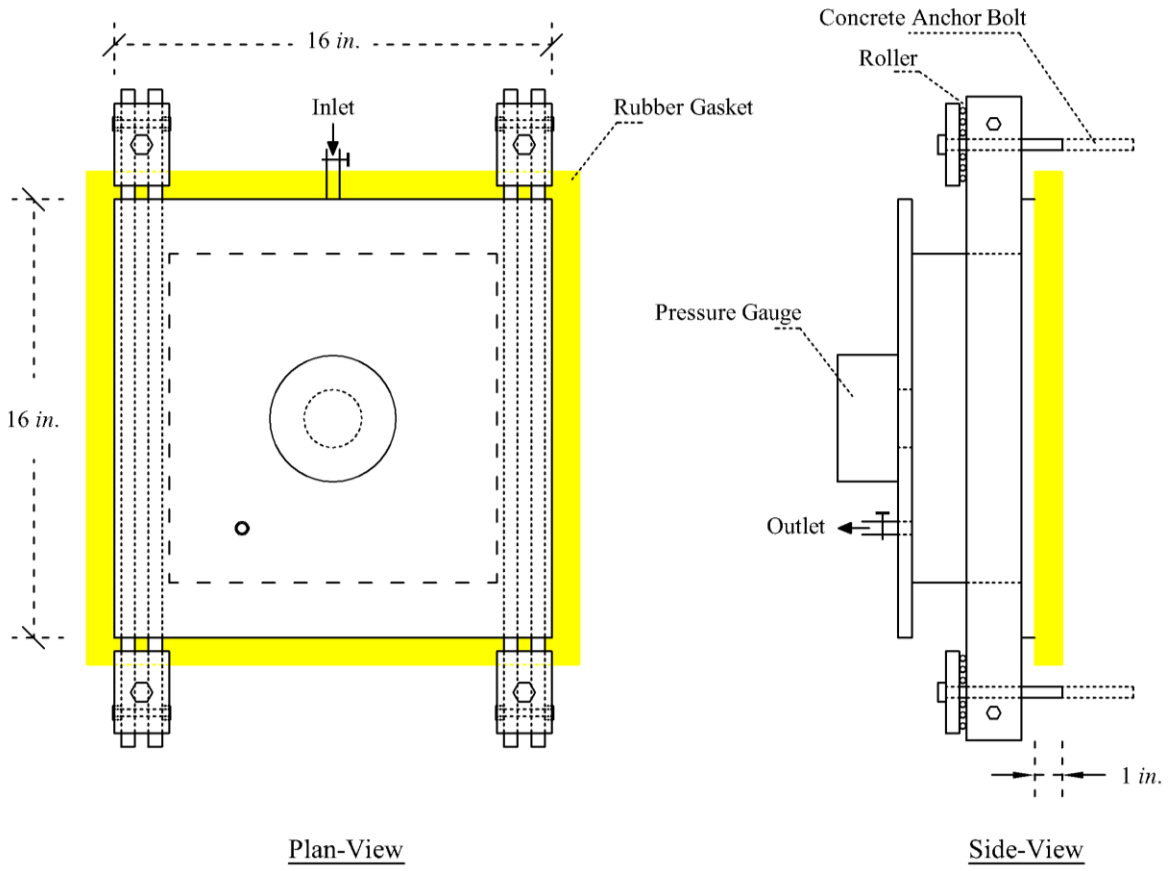

Fig. 4.28 Detailing of water pressure chamber

A rubber gasket is used between the chamber and the concrete surface to provide flexibility for free deformation of the RC panel. Also, free to slide roller support conditions are provided along the direct tension axis for free elongation of the RC panel. In this manner, the presence of chamber does not affect the response of the RC panel in any way. The chamber is attached to the RC panel by four ¼ *in.* anchor bolts. A water resistant silicone sealant is used at the top and bottom surfaces of the rubber gasket to ensure a completely sealed condition at all attaching surfaces. The inlet of the chamber is connected to the city water system. The inlet is equipped with a valve to control the water flow and the water pressure inside the chamber. The water pressure inside the chamber can be monitored by a pressure gauge attached to the chamber. This pressure is kept constant at 5 *m* head of water during the test. The water pressure chamber is mounted on a cracked region of the RC panel as shown in Fig. 4.29. The mounting location of the chamber will be shown on the crack pattern for each panel in the next Chapter.

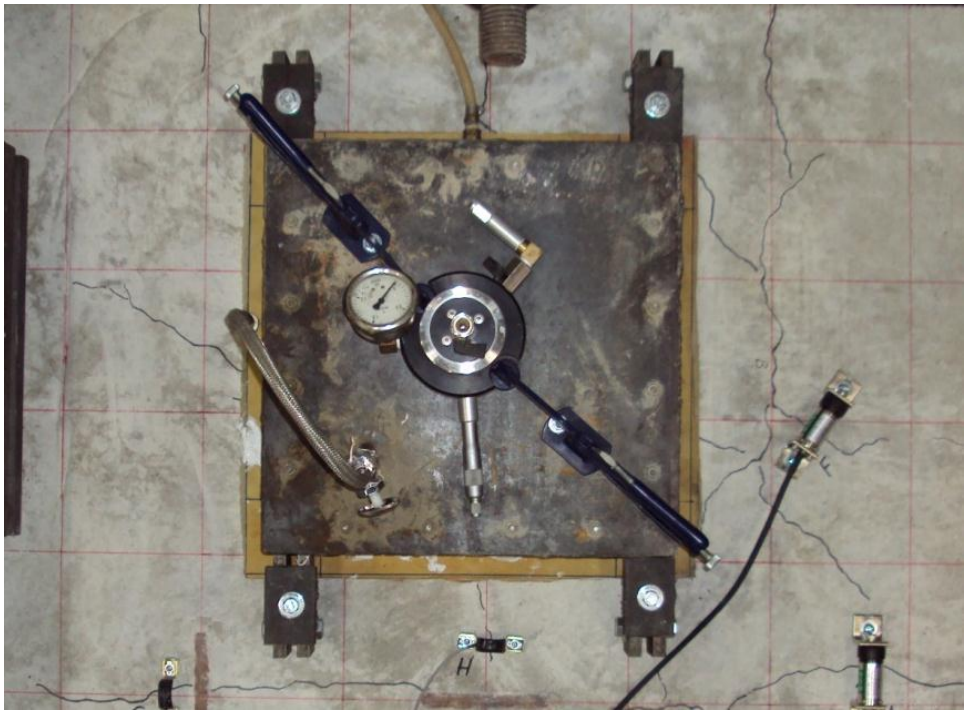

(a)

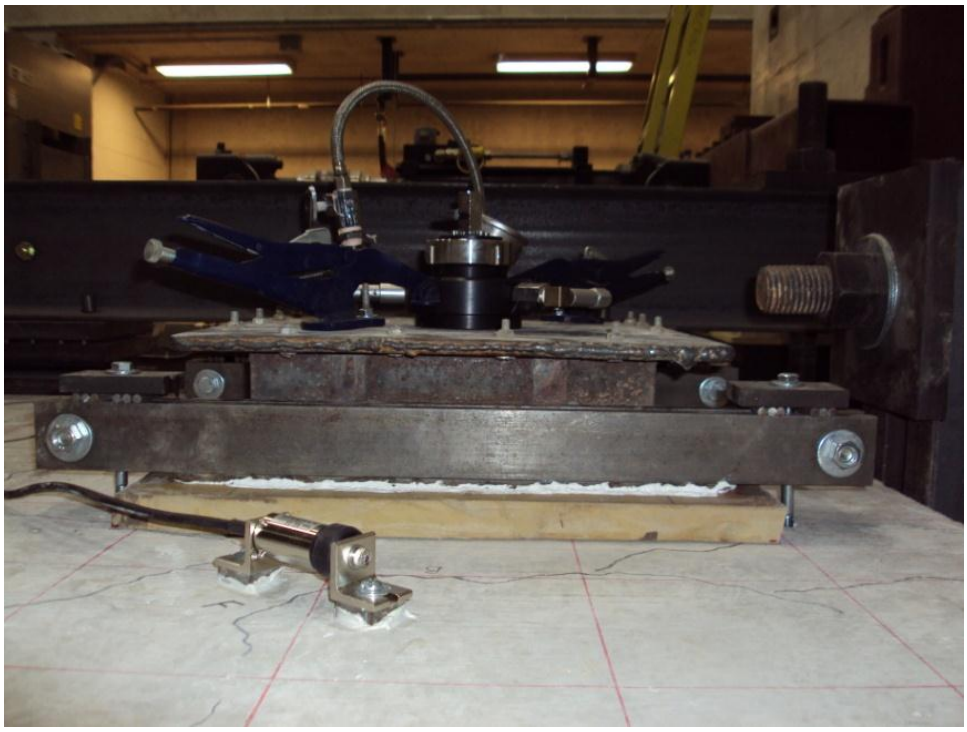

(b)

Fig. 4.29 Water pressure chamber, a) plan view, b) side view

4.11 Summary

The report of an experimental study on the two-way cracking behaviour of RC panels is presented in this Chapter. The RC panels are subjected to direct tension in one direction and bending in the other direction perpendicular to the first direction. This loading condition resembles the two-way internal forces that exist in the wall of a circular liquid containing tank. A unique test setup is designed and constructed for this purpose. Three different RC panels are tested to consider the effects of the reinforcement ratio and the bar spacing. These tests are performed in several stages of one-way and two-way loading cycles. Also, the extent of water leakage through these panels is examined by exposing a few selected cracks to pressurized water.

CHAPTER 5

TEST RESULTS AND DISCUSSIONS

5.1 Introduction

The collected data from the experiments described in the previous Chapter are examined and presented in this Chapter. These data include crack patterns, strain of steel reinforcing bars, strain at the concrete surface, elongation of the panel, crack width, and water leakage observations. Further analysis of these results has revealed a number of new findings that can improve the understanding of the two-way cracking phenomenon. These findings are discussed at the end of this Chapter.

5.2 Crack Patterns

The crack patterns at various stages of loading are given in Fig. 5.1. These crack patterns are mostly consisted of orthogonal cracks that reflect the shape of the reinforcement mesh. This is due to the effect of splitting tensile stresses. Orthogonal cracks are dominant when the combination of splitting and orthogonal stresses is larger than the principal diagonal stresses. Also, crack patterns show that a few cracks are formed at some angle to the main orthogonal axes. The diagonal cracks are more obvious in panel B (Fig. 5.1(b)) especially in 4th stage at which the two-way loading ratio is not constant. This can be due to a lower reinforcement ratio, and hence lower splitting tensile stresses in this panel along with a two-way loading ratio that produces larger diagonal principal stresses at the instant of cracking. Therefore, based on the loading ratios and the properties of panel B, it may be stated that the inclined cracking is more probable for the two-way loading ratios closer to 1, the reinforcement ratios less than 0.005, and

the clear cover to bar diameter ratios more than 2.5. For a properly reinforced concrete wall, such as panel A, the cracks will dominantly form in an orthogonal pattern. Therefore, the focus of this study will be on the prediction of the orthogonal cracks. The formation of diagonal cracks can be avoided by providing an adequate amount of reinforcement.

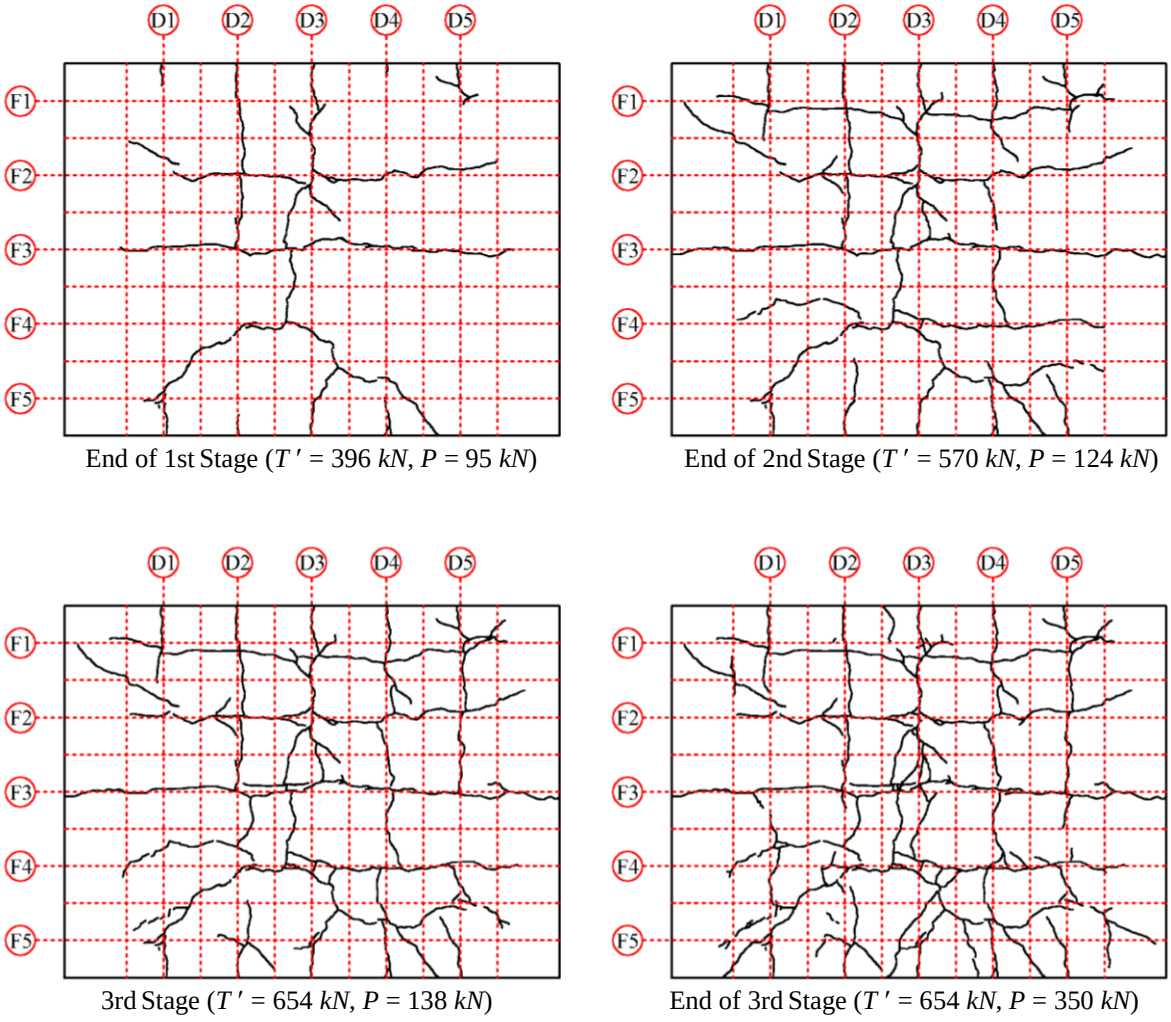

End of 1st Stage (T' = 396 *kN*, P = 95 *kN*)

End of 2nd Stage (T' = 570 *kN*, P = 124 *kN*)

3rd Stage (T' = 654 *kN*, P = 138 *kN*)

End of 3rd Stage (T' = 654 *kN*, P = 350 *kN*)

(a)

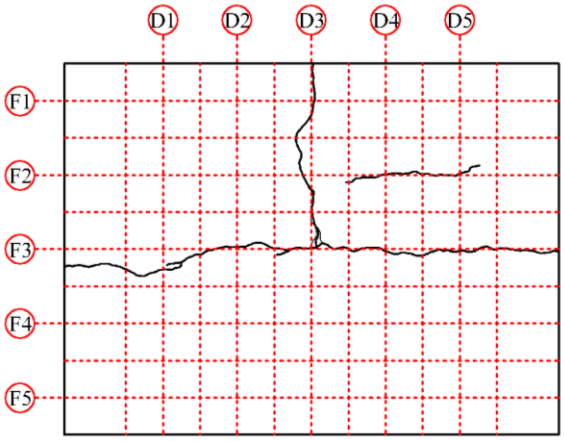

End of 1st Stage (T' = 354 *kN*, P = 88 *kN*)

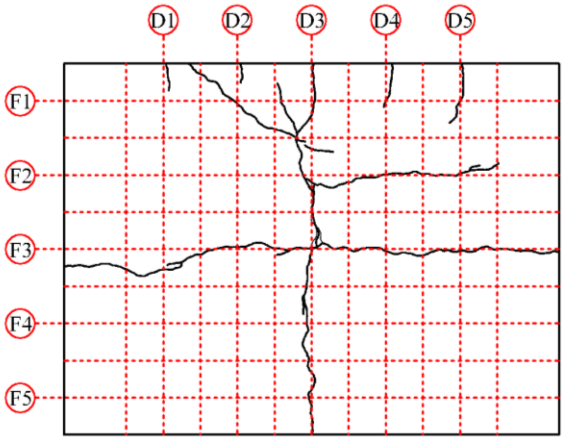

2nd Stage (T' = 372 *kN*, P = 105 *kN*)

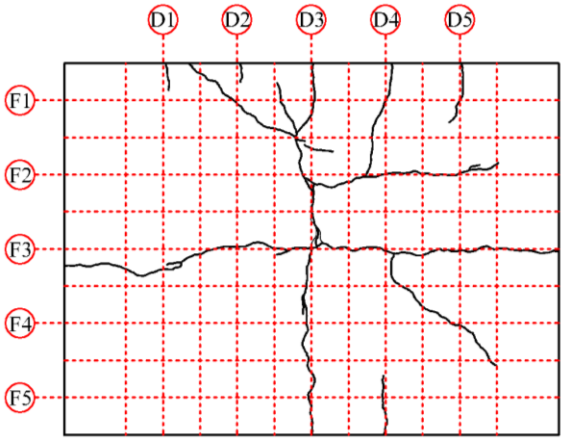

End of 2nd Stage (T' = 372 *kN*, P = 120 *kN*)

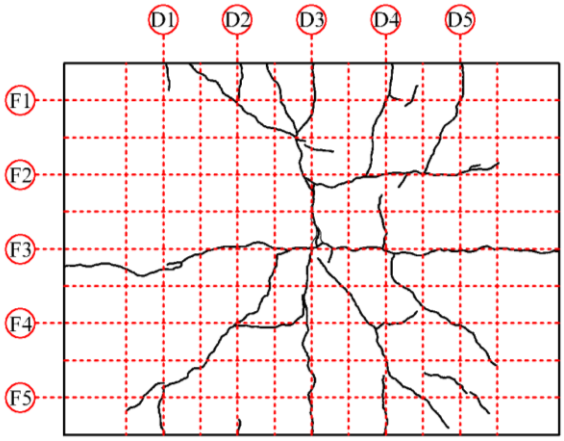

4th Stage (T' = 372 *kN*, P = 200 *kN*)

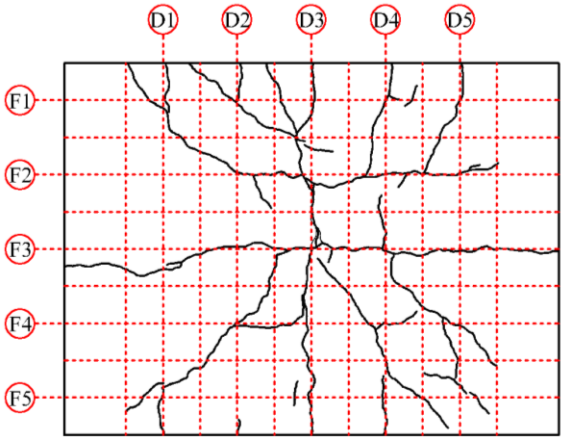

End of 4th Stage (T' = 372 *kN*, P = 245 *kN*)

(b)

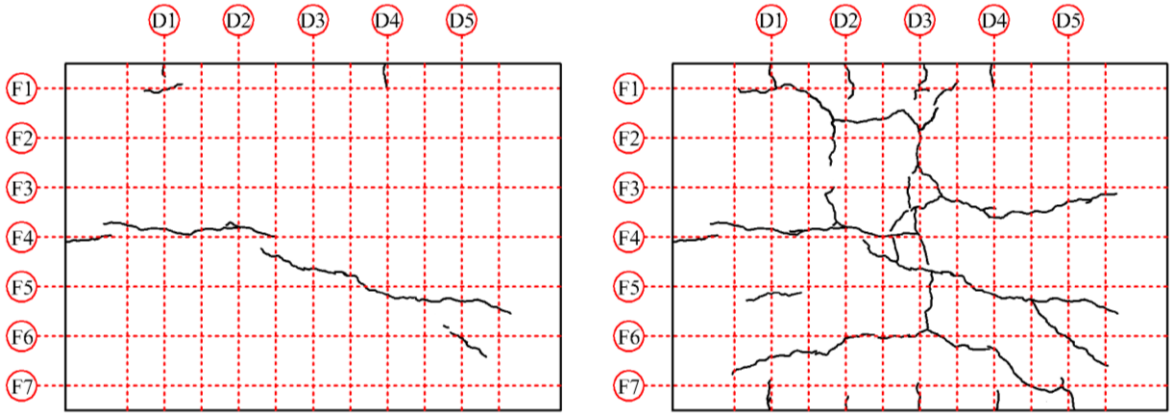

1st Stage (T' = 306 *kN*, P = 76.6 *kN*) End of 1st Stage (T' = 369 *kN*, P = 86.4 *kN*)

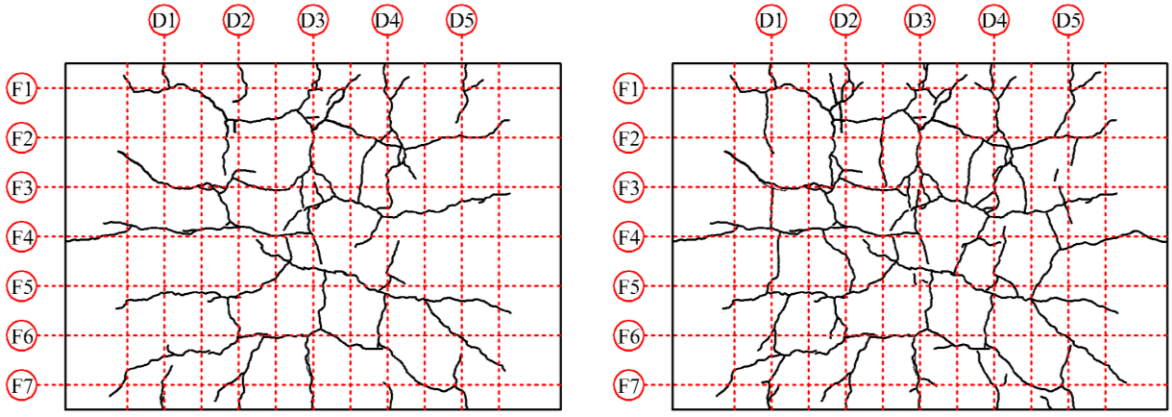

3rd Stage (T' = 603 *kN*, P = 122.8 *kN*) End of 3rd Stage (T' = 603 *kN*, P = 336 *kN*)

(c)

T' : each side jack load
P : center jack load

Fig. 5.1 Crack pattern at various loading stages, a) panel A, b) panel B, c) panel C

5.3 Crack Propagation Contour and Designations

The crack propagation for each panel is shown with a coloured contour in Fig. 5.2. Also shown in this Figure are the designated locations and orientations of the measured crack widths. The cracks designated for measurement are tried to be mainly primary cracks. The cracks labelled with subscript “b” are measured from the bottom surface of the panel.

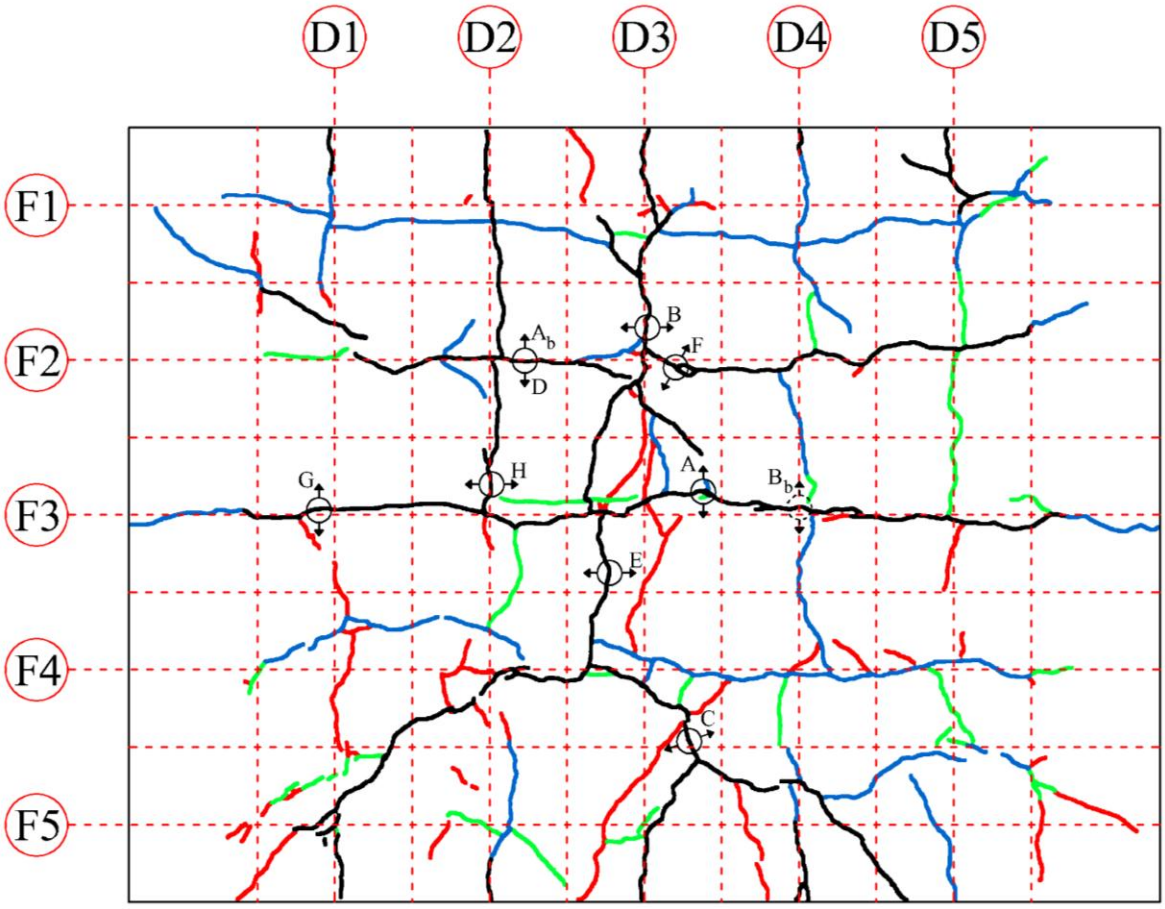

end of 1st stage at $T' = 396\ kN$, $P = 95\ kN$

end of 2nd stage at $T' = 570\ kN$, $P = 124\ kN$

3rd stage at $T' = 654\ kN$, $P = 138\ kN$

end of 3rd stage at $T' = 654\ kN$, $P = 350\ kN$

(a)

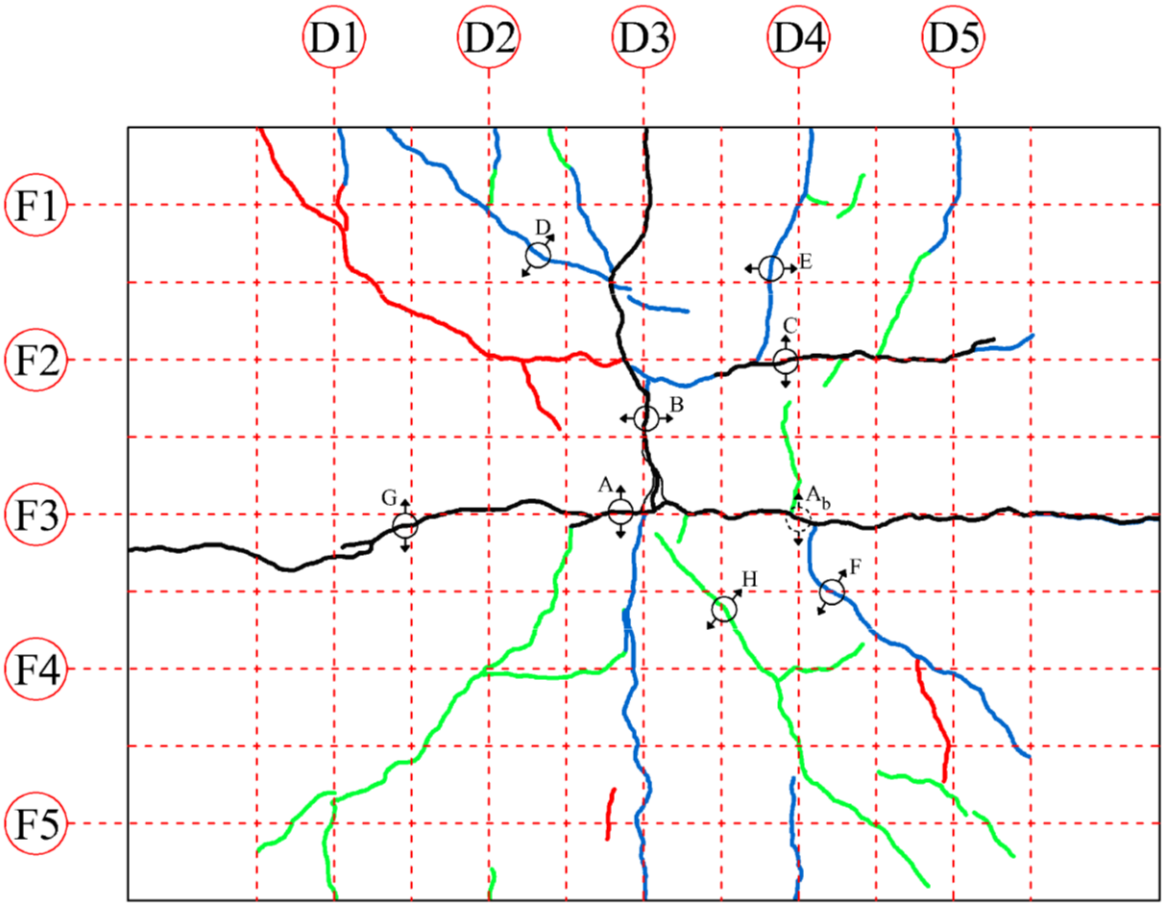

1st stage at $T' = 354\ kN$, $P = 88\ kN$

end of 2nd stage at $T' = 372\ kN$, $P = 120\ kN$

4th stage at $T' = 372\ kN$, $P = 200\ kN$

end of 4th stage at $T' = 372\ kN$, $P = 245\ kN$

(b)

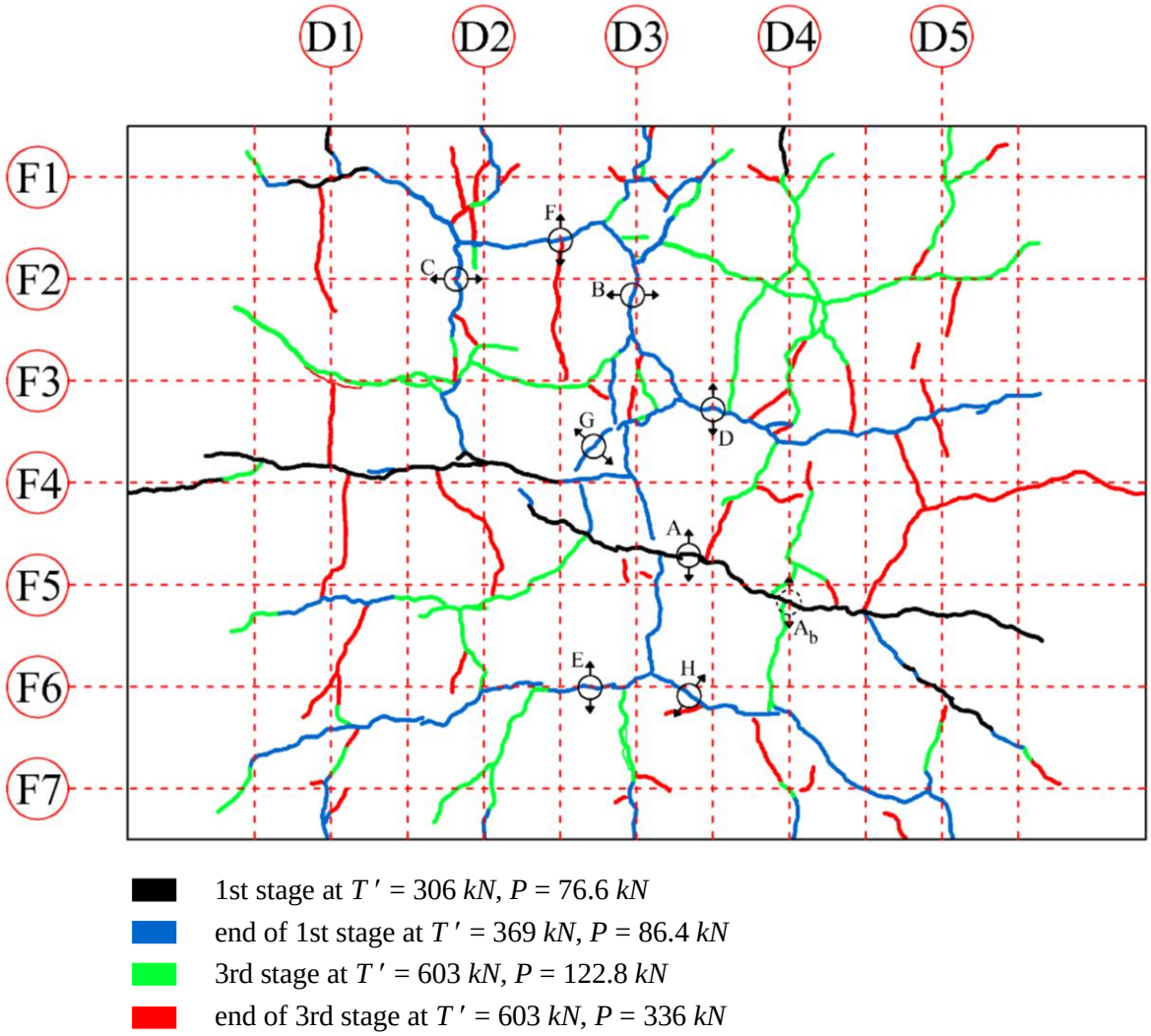

(c)

Fig. 5.2 Crack propagation contour and crack designations, a) panel A, b) panel B, c) panel C

5.4 Measured Crack Widths Using Microscope

As mentioned in the previous Chapter, the width of cracks is measured with a microscope at the initial cracking stage. The results of these readings are summarized in Table 5.1. It must be noted that the cracks are not completely closed even for a fully unloaded panel. This means once a crack is formed, a residual crack width always remains in place even after complete unloading. The amount of this residual crack width is dependent on the maximum achieved tensile stress of steel at the crack during the loading process. In other words, a panel that is loaded to a higher

steel stress level has a higher residual crack width after unloading. The residual crack width phenomenon can be attributed to the irregularities of the two surfaces inside the crack and the irreversible slip at the bond layer of the steel and the concrete. After yielding of the steel, the residual steel strain and the excessive bond-slip will result in extremely higher residual crack widths. The residual crack widths measured right before the installation of the crack displacement transducers will be added to the subsequent readings of these gauges.

Table 5.1 Crack widths measured with microscope

Panel	Test Stage	Each Side Jack (kN)	Center Jack (kN)	Crack Width (mm)									
				A	B	C	D	E	F	G	H	A_b	B_b
A	1st	378	92	0.20	0.20	0.32	0.20						
		396	95	0.24	0.24	0.36	0.22						
		0 (unload)	0 (unload)	0.04	0.10	0.10	0.06	0.10	0.10	0.02	0.04	0.08	0.06
B	1st	354	88	0.50									
		0 (unload)	0 (unload)	0.08								0.00	
	2nd	312	81		0.06								
		342	86		0.08	0.06							
		372	105		0.26	0.28							
		372	120				0.24	0.08	0.02				
		0 (unload)	0 (unload)		0.04	0.02	0.02	0	0	0.10			
	4th	0 (unload)	0 (unload)								0.18		
C	1st	306	76.6	0.32									
		369	86.4	0.40	0.10	0.06	0.14	0.32	0.22	0.10			
		0 (unload)	0 (unload)	0.06	0.02	0.02	0.02	0.06	0.02	0.02	0.06	0.02	

5.5 Steel and Concrete Strains

All the electrical gauges are connected to a data acquisition system, which records the gauge readings with the rate of 5 readings per second. The collected data from steel and concrete strain gauges in all panels for all testing stages are presented in Section A.1. The steel and concrete strains are drawn versus either each side jack load or the center jack load. The results are presented in separate groups for better clarity. Typical results are also shown in this section for easy reference.

Typical results of steel strains for panel A are given in Fig. 5.3. The steel strains show a sudden increase at the instant of cracking. The magnitude of this change in the steel strain depends on the location of the gauge and its distance to the crack. The closer is the gauge to a crack the higher is the change in its readings. It can also be seen that a residual steel strain remain even after unloading of the panel, which is an indication of the residual crack widths. These residual strains are accounted for by adding them to the strain readings at the beginning of each subsequent testing stage.

Generally, it can be seen that the steel strains are higher under two-way loading condition (Fig. 5.3(b)) than under one-way loading condition (Fig. 5.3(c) and (d)). There are two attributing factors to this phenomenon. One is the inclination of some cracks. Widening of such a crack can raise the steel strains of reinforcing bars in both orthogonal directions. This is the reason for an increase in the steel strains of flexural bars when the panel is loaded in direct tension only (Fig. 5.3(c)). The second phenomenon is the weakening of the bond strength due to the widening of the longitudinal splitting cracks. In other words, a crack that is along the reinforcing bar can damage the bond strength especially when it becomes wider under transverse loading.

The abovementioned effect of longitudinal splitting cracks can also be explained with the aid of Fig. 5.4. This figure shows typical results of steel strains for flexural reinforcing bars in Panel B. Interestingly, the steel strain in the flexural reinforcing bar F3T is higher than those of other flexural reinforcing bars at the same distance to the nearest flexural crack. A closer look at the crack pattern of this panel (Fig. 5.1(b)) reveals that a direct tension crack is formed along this reinforcing bar on the axis F3. This crack behaves as a longitudinal splitting crack around the reinforcing bar F3T, as a result of which the bond strength is extremely damaged for this bar.

A similar behaviour is observed in the steel strain results of panel C. The steel strain readings of the gauge D3T at the 3rd stage is shown in Fig. 5.5. It can be seen that this strain is excessively increasing, despite the fact that the direct tension load is kept constant at about 600 *kN* while the bending load is increased. This behaviour is again confirms the bond damage induced by the widening of the splitting cracks in a two-way loading system. This effect must be considered in the crack prediction of two-way loaded elements.

Typical results of concrete strains are given in Fig. 5.6. These results are useful to detect the instant of crack initiation. Whenever a crack crosses a concrete strain gauge, an abrupt increase can be observed in the readings of that gauge.

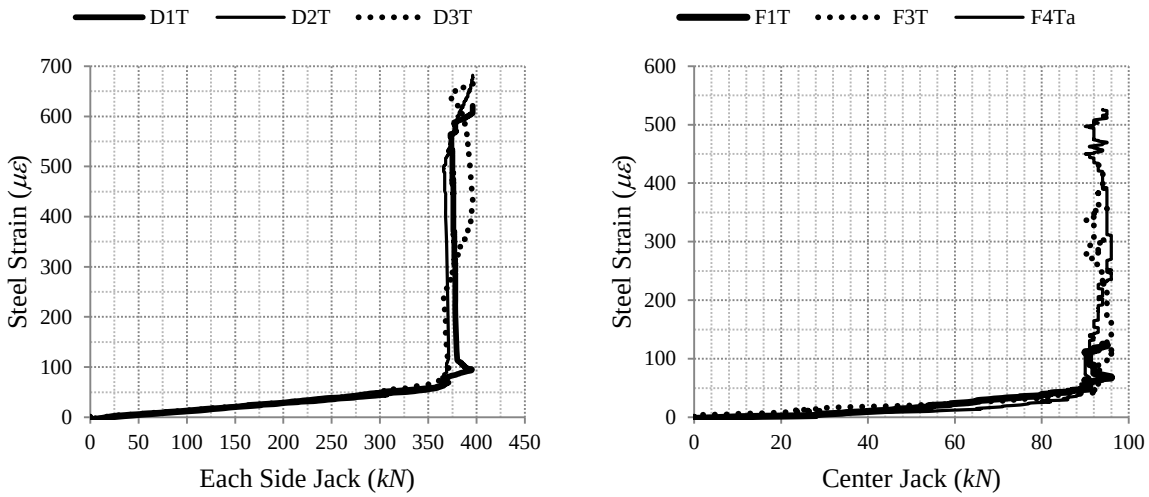

(a)

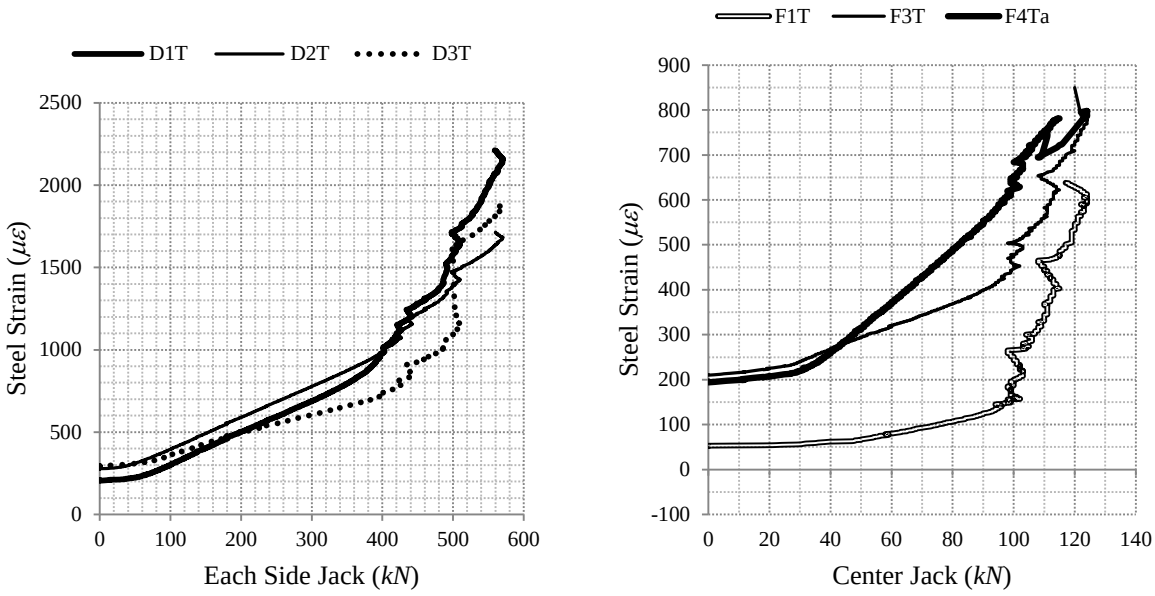

(b)

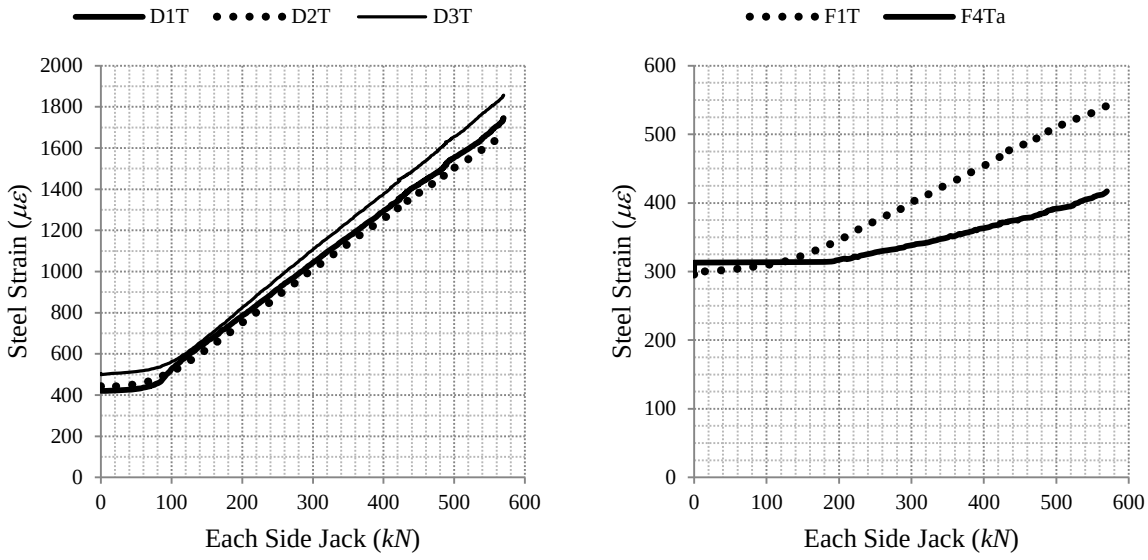

(c)

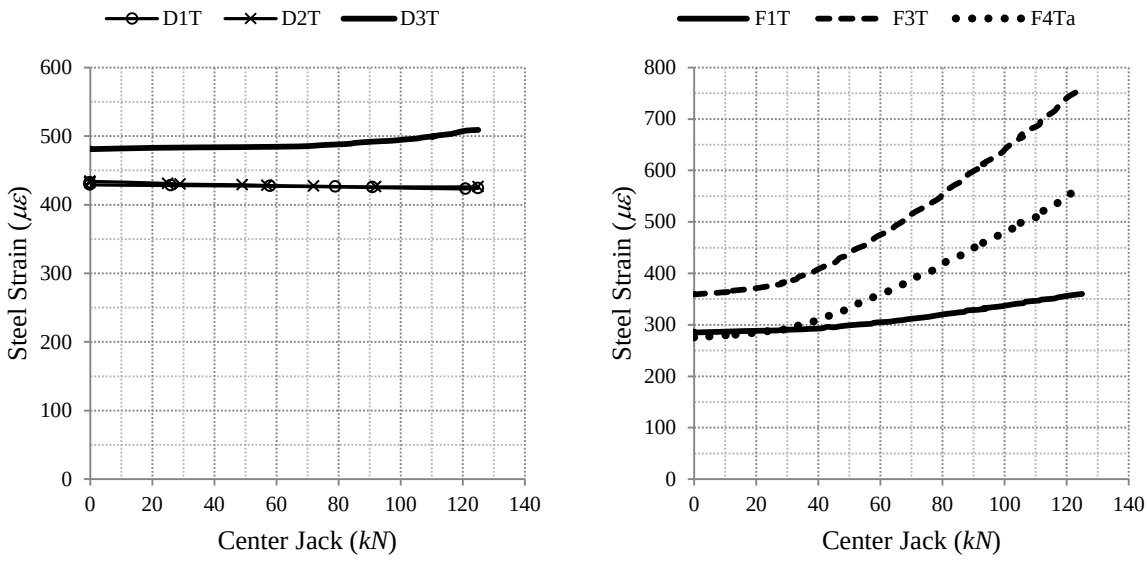

(d)

Fig. 5.3 Typical steel strains in panel A, a) 1st stage, b) 2nd stage, c) one-way tension, d) one-way bending

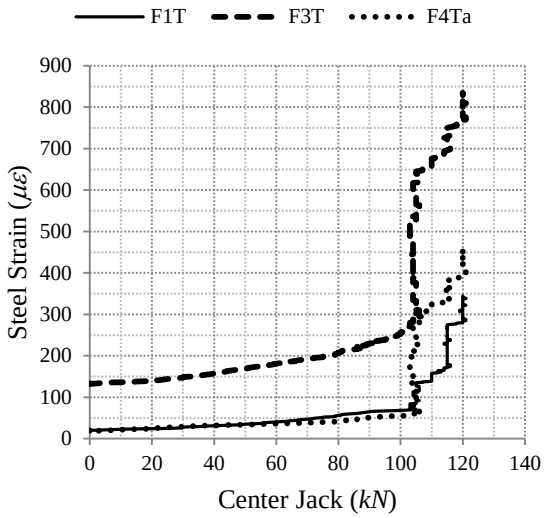

Fig. 5.4 Typical steel strains of flexural reinforcing bars in panel B, 2nd stage

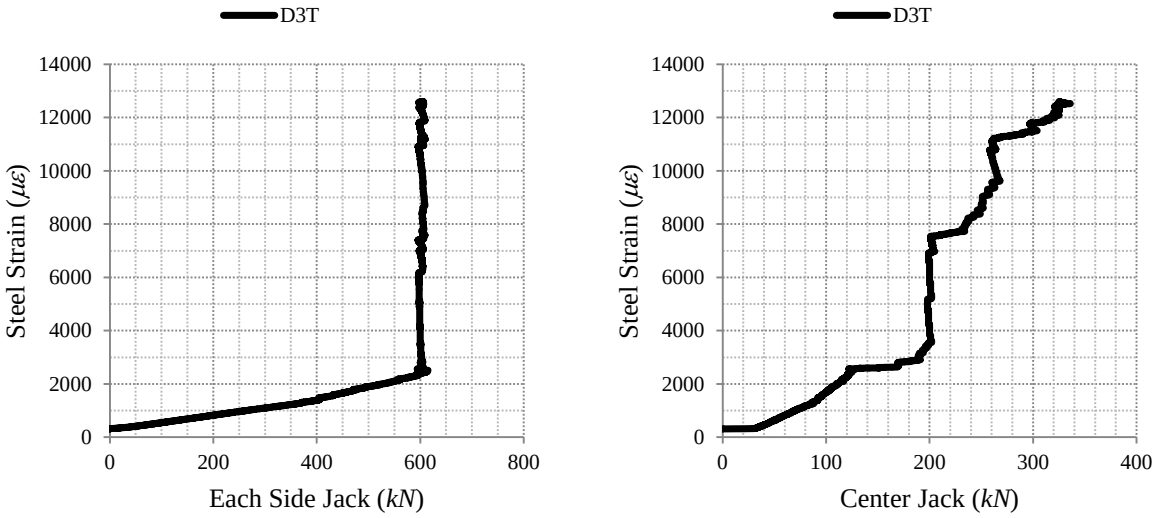

Fig. 5.5 Typical steel strains in panel C, 3rd stage

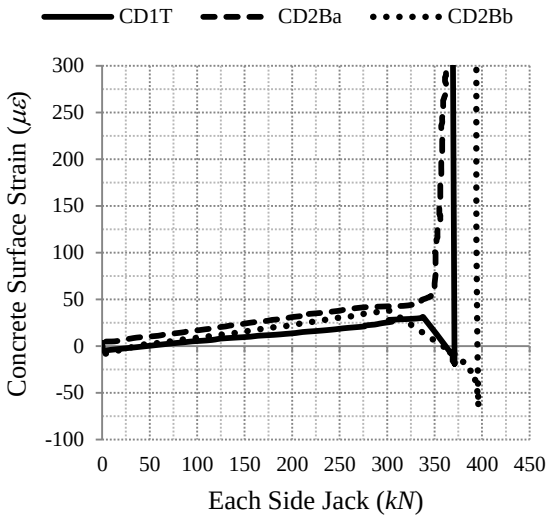

Fig. 5.6 Typical concrete strains (panel A, 1st stage)

5.6 Total Elongation

The collected data from the LVDT displacement transducers on panel B and C are presented in Section A.2. These results for panel C are also given here in Fig. 5.7 for easy reference. This LVDT shows the total elongation of panel along the direct tension axis. The formation of a crack will introduce a sudden increase in the readings of this sensor. It can be seen that a residual elongation remains in the panel even after complete unloading. This residual elongation is due to the combined effect of two phenomena. One phenomenon is the presence of residual crack widths due to irreversible bond-slip and irregularities inside crack surfaces, and the other reason is the presence of the residual strain in the concrete due to micro-cracking. This residual deformation is more significant when the new cracks are formed or the load is increased to a new level (Fig. 5.7 (a), and (e)) and is much smaller for repeated loading to the same previous highest load level (Fig. 5.7 (b), (c), (d), and (f)).

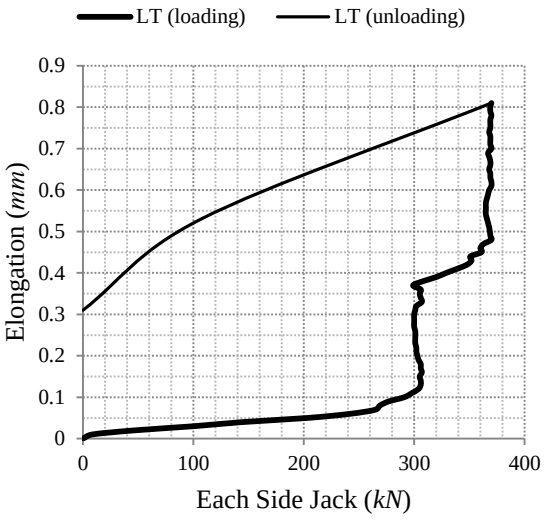
LT (loading)
LT (unloading)
Elongation (mm)
Each Side Jack (kN)
0
0.1
0.2
0.3
0.4
0.5
0.6
0.7
0.8
0.9
0
100
200
300
400

(a)

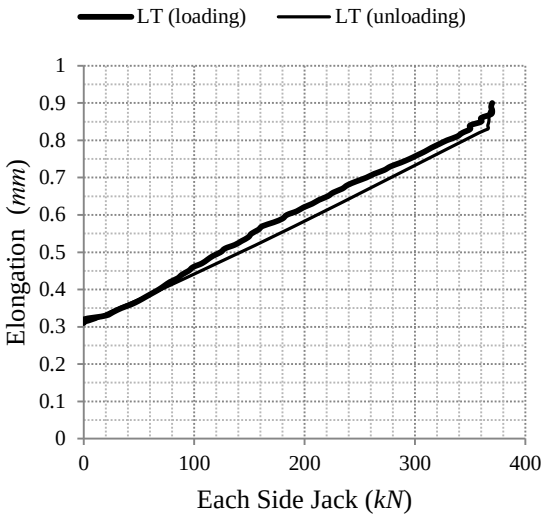
LT (loading)
LT (unloading)
Elongation (mm)
Each Side Jack (kN)
0
0.1
0.2
0.3
0.4
0.5
0.6
0.7
0.8
0.9
1
0
100
200
300
400

(b)

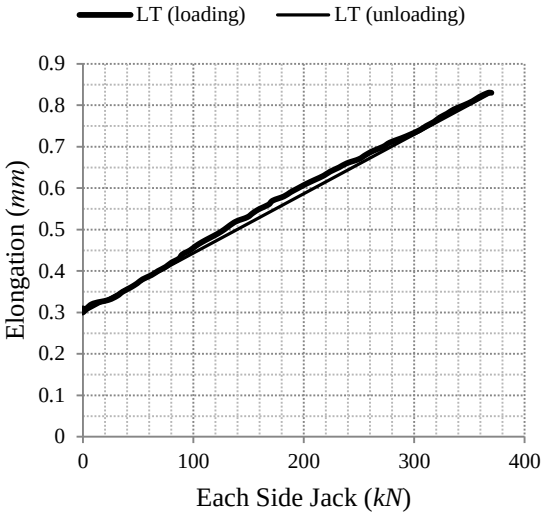
LT (loading)
LT (unloading)
Elongation (mm)
Each Side Jack (kN)
0
0.1
0.2
0.3
0.4
0.5
0.6
0.7
0.8
0.9
0
100
200
300
400

(c)

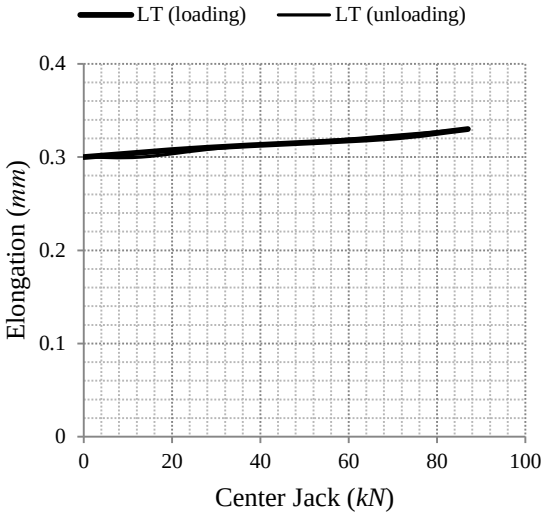
LT (loading)
LT (unloading)
Elongation (mm)
Center Jack (kN)
0
0.1
0.2
0.3
0.4
0
20
40
60
80
100

(d)

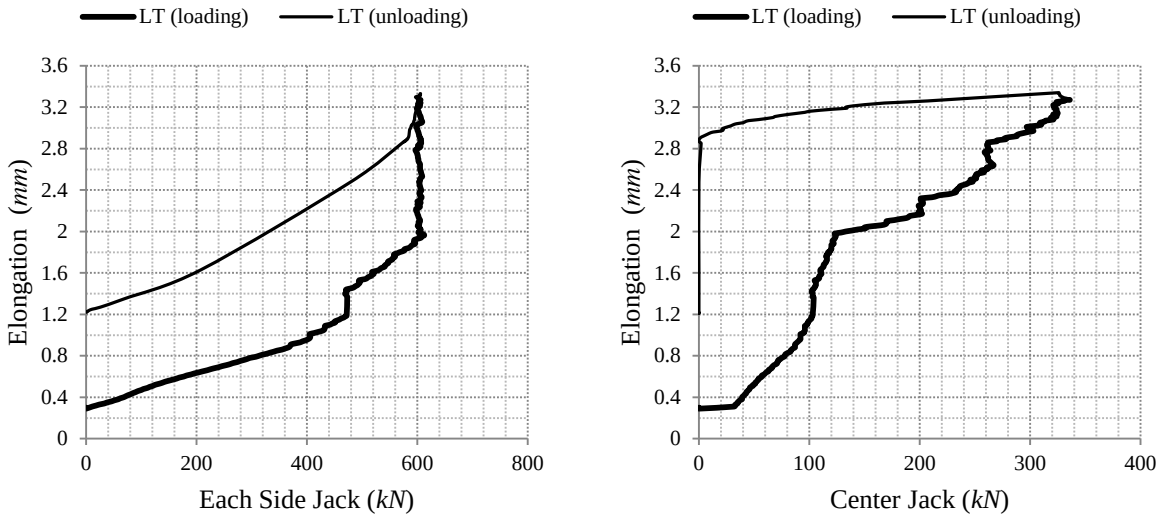

(e)

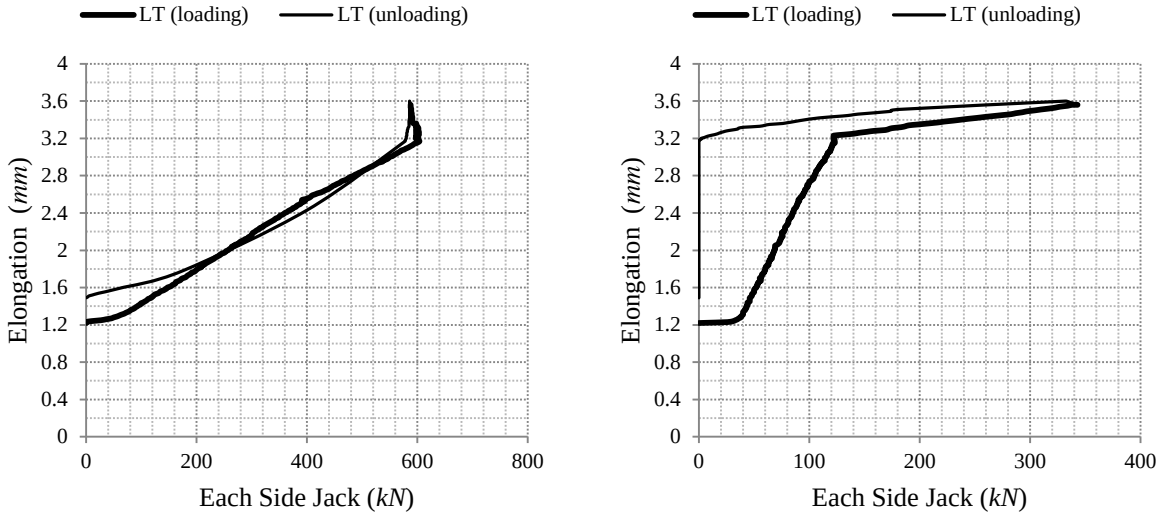

(f)

Fig. 5.7 Total elongation of panel C (LVDT LT), a) 1st stage, b) 2nd stage, c) one-way tension, d) one-way bending, e) 3rd stage, f) 4th stage

5.7 Crack Widths

The collected data from crack displacement transducers at different testing stages of all panels are presented in Section A.3. Typical results for crack widths in panel A are shown in Fig. 5.8. It can be noted that the residual crack widths are added at the beginning of each testing stage. Generally, it can be observed that the width of cracks at top surface is wider under two-way loading conditions (Fig. 5.8(a)) than under one-way loading condition (Fig. 5.8(b) and (c)). The widest crack under two-way loading is an inclined crack labelled as crack C. The two-way nature of this crack can be confirmed seeing that this crack is widening under both one-way tension and one-way bending conditions. Orthogonal flexural cracks, such as cracks E and H in Fig. 5.8(b), do not show any significant change under one-way tension loading. Likewise, orthogonal direct tension cracks, such as cracks A, G, A_b, and B_b in Fig. 5.8(c), do not show any significant change under one-way bending.

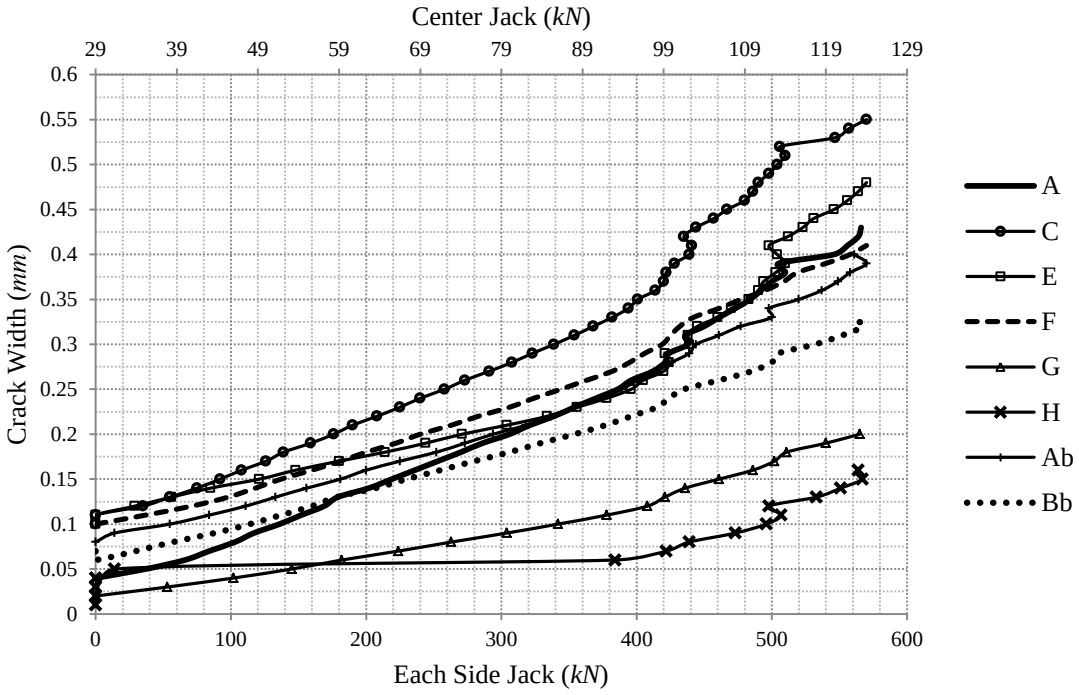

(a)

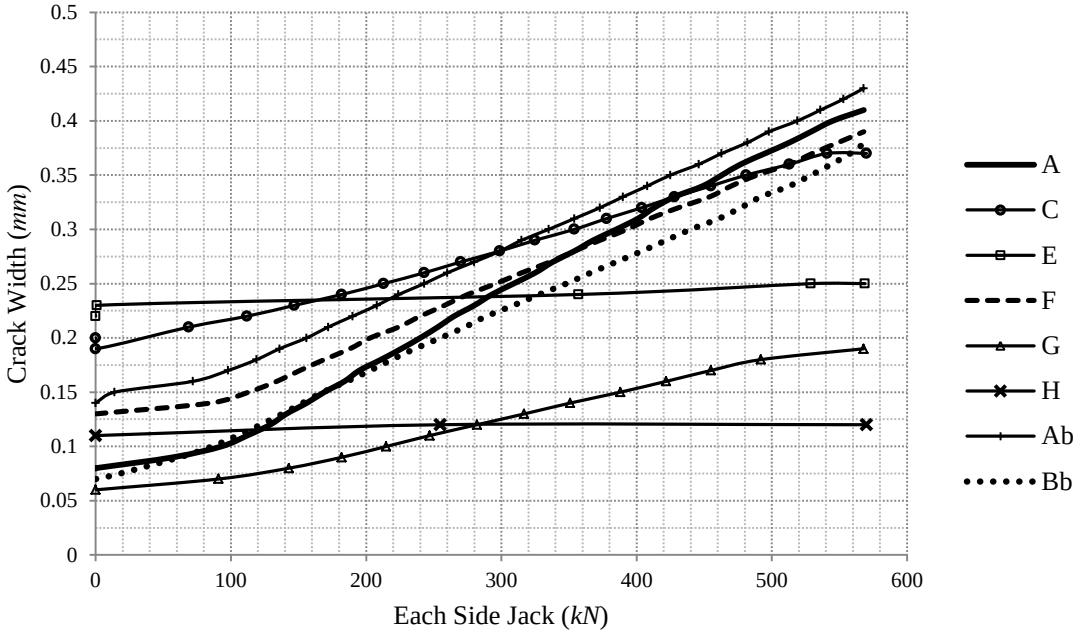

(b)

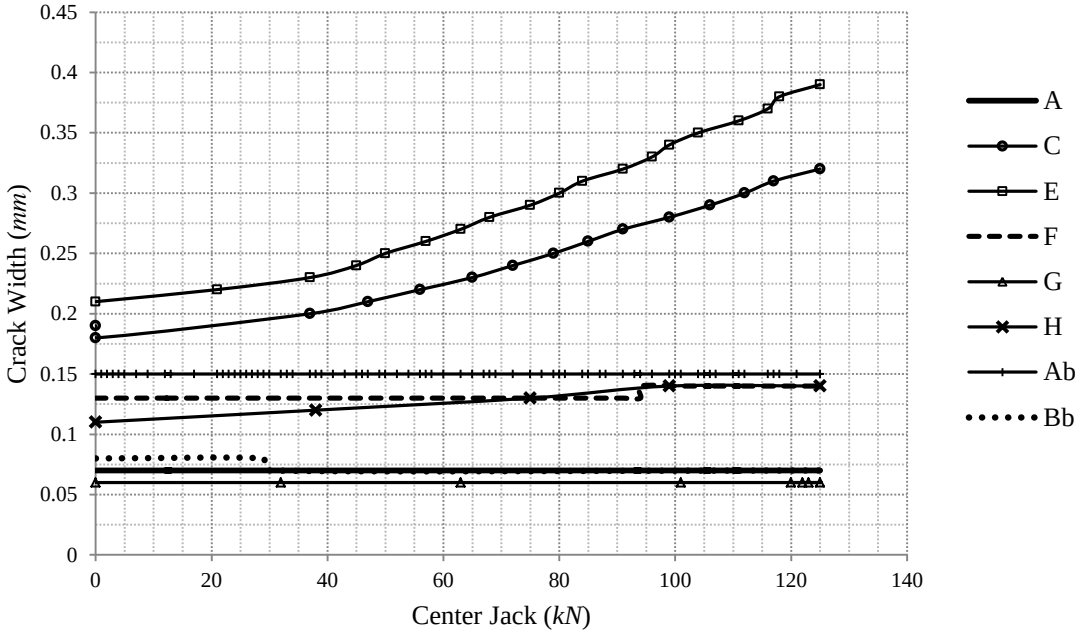

(c)

Fig. 5.8 Typical crack widths in panel A, a) 2nd stage, b) one-way tension, c) one-way bending

Some results for crack widths in panel B are given in Fig. 5.9. In the 2nd stage (Fig. 5.9(a)), the width of the direct tension crack A is suddenly increased by about 0.1 *mm* while the direct

tension load is kept constant at 372 *kN* for each side jack while the center jack is increased to 105 *kN*. This can be explained by looking at the crack pattern of panel B at 2nd stage (Fig. 5.1(b) 2nd stage). It can be seen that flexural cracks are newly formed at this loading step. These cracks can damage the bond strength of direct tension bars, and hence induce an increase in the width of direct tension cracks. Looking at the crack widths in the beginning of the 5th stage (Fig. 5.9(b)), it can be noted that large residual crack widths remain in panel after yielding of reinforcing bars in the previous stage. This demonstrates an extreme irreversible damage to the serviceability of a structure if the reinforcement yields.

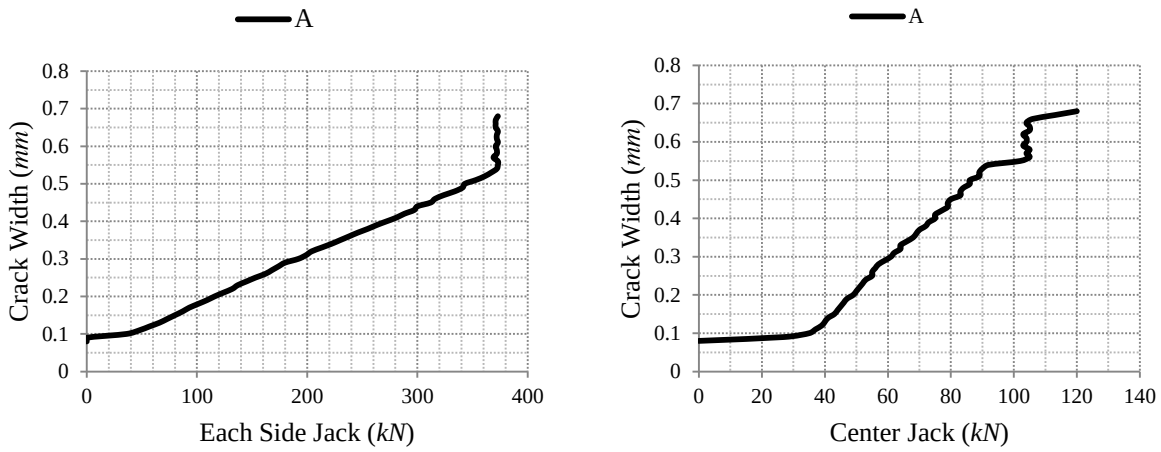

(a)

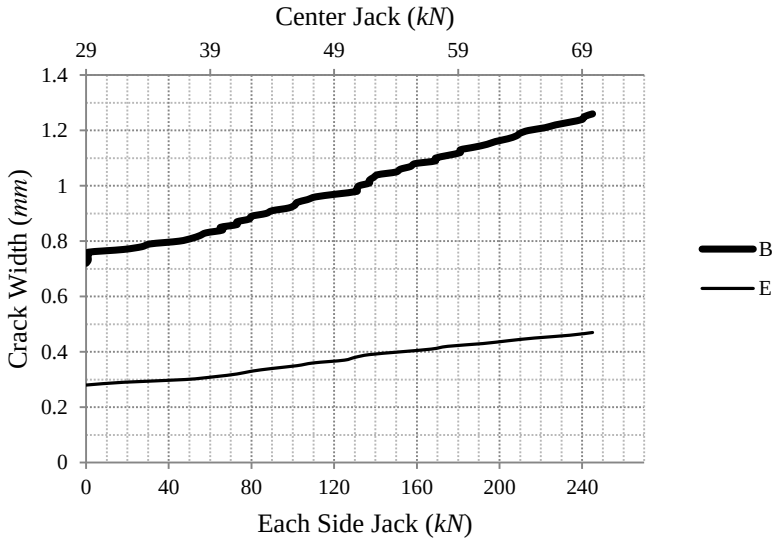

(b)

Fig. 5.9 Typial crack widths in panel B, a) 2nd stage, b) 5th stage

5.8 Leakage Observations

The mounting location of the chamber for each panel is depicted in Fig. 5.10. Also in this figure, the testing stage at which the leakage test is performed is indicated for each panel. No leakage is observed through flexural cracks. This is due to the presence of a compression zone in the depth of a flexural crack. On the other hand, orthogonal and inclined direct tension cracks penetrate the full depth of the panel, which provides an opening for water to leak. The observations for the leakage tests are summarized in Table 5.2. The rate of leakage is visually scaled for comparative purposes of this study only. It can be seen that the leakage is started as soon as the crack is exposed to the pressurized water without any loading of the specimen. This is due to the fact that residual crack widths always remain in an unloaded panel from the previous testing stage. Also, the leakage rate is observed to be dependent on the crack width gradient. In other words, the width of a crack at both top and bottom surfaces of panel can affect the leakage rate. This means an inclined crack that is wider at top surface than an orthogonal crack may not necessarily have a higher leakage rate due to its smaller crack width at the bottom surface. The leakage rate can be regarded as negligible if both top and bottom crack widths are limited to 0.1 *mm* as seen in panel A. The leakage rate may also be reduced over time for this range of crack widths due to autogenous healing.

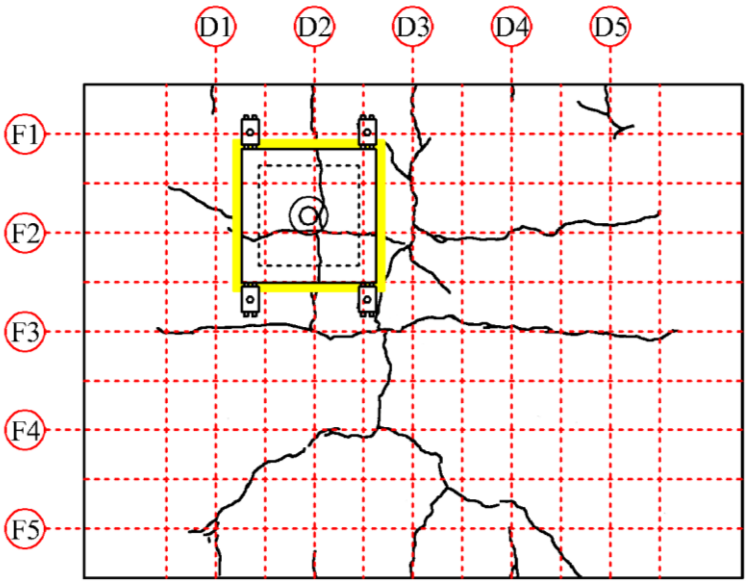

Panel A (2nd Stage)

(a)

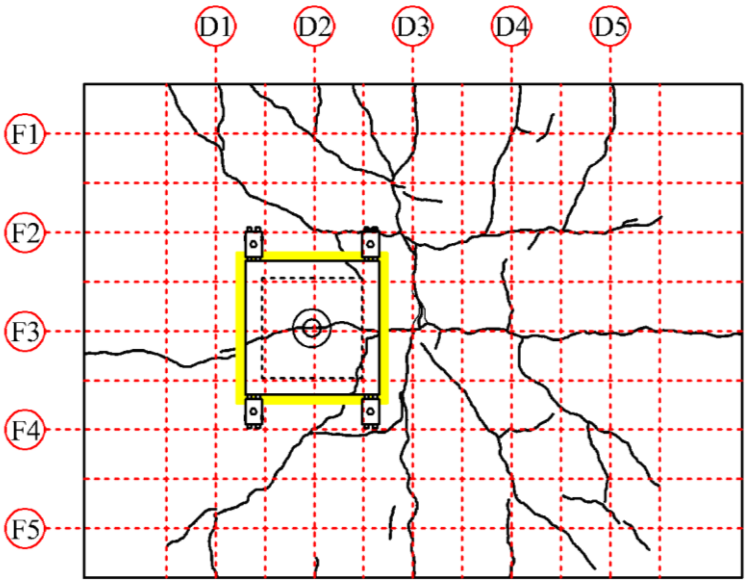

Panel B (5th Stage)

(b)

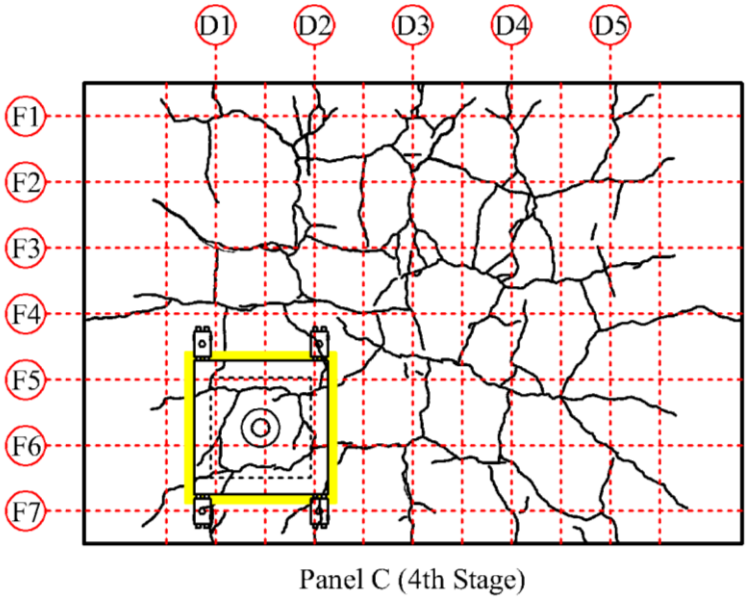

Panel C (4th Stage)

(c)

Fig. 5.10 Mounting locations of water pressure chamber, a) panel A, b) panel B, c) panel C

Table 5.2 Results of leakage tests

Panel	Test Stage	Crack Label @ Top Surface	Crack Label @ Bottom Surface	Each Side Jack Load (*kN*)	Crack Width (*mm*) @ Top Surface	Crack Width (*mm*) @ Bottom Surface	Leakage Observation	Approx. Flow Rate (*drops/sec*)
A	2nd	F	A_b	0	0.10	0.08	wet	
				180	0.17	0.15	slow dripping	5
				350	0.25	0.23	fast dripping	20
				400	0.28	0.26	very fast dripping	25 to 30
B	5th	A	A_b	0	0.19	0.09	very slow dripping	1
				120	0.36	0.09	slow dripping	5
				190	0.51	0.11	fast dripping	20
				220	0.57	0.13	very fast dripping	25 to 30
C	4th	E	A_b	0	0.52	0.06	very slow dripping	0.5
				100	0.64	0.06	very slow dripping	1
				160	0.71	0.06	slow dripping	5
				340	0.93	0.13	fast dripping	20
				400	1.01	0.15	very fast dripping	25 to 30
				490	1.09	0.19	continuous	

5.9 Discussions of Test Results

The results of three experimental tests reported earlier in this Chapter are examined further in this Section. A number of new findings are drawn from this study that can help to better understand and predict the cracking behaviour of two-way loaded panels.

5.9.1 Effect of bar spacing

The crack patterns of panels A and C are compared with each other in Fig. 5.11. Both panels have the same reinforcement ratio in both orthogonal directions. The differences are the bar size and the spacing of the flexural reinforcing bars, which are smaller in panel C (No. 15 at 200 *mm*) as compared to panel A (No. 20 at 300 *mm*). The minimum and the maximum spacings of direct tension cracks along D axes (D2, D3, and D4) observed at two steel stress levels in the direct reinforcing bars, i.e., at service ($0.6f_y$) and at yield (f_y), are measured and shown for each panel. Based on the theory of one-way cracking, it is expected that the two panels have the same

spacing of cracks under a one-way tension loading along D axis. This is because of their similar reinforcement ratio and layout in the direction of D axis. However, for two-way loading condition the spacing of cracks is observed to be generally smaller for panel C as compared to panel A. This is due to a smaller spacing of the flexural reinforcing bars in panel C. This demonstrates how the bar spacing in one direction can affect the crack spacing in the other direction. This phenomenon can be explained by the presence of splitting tensile stresses in a two-way loading system. Clearly, the one-way cracking theory fails to capture this behaviour.

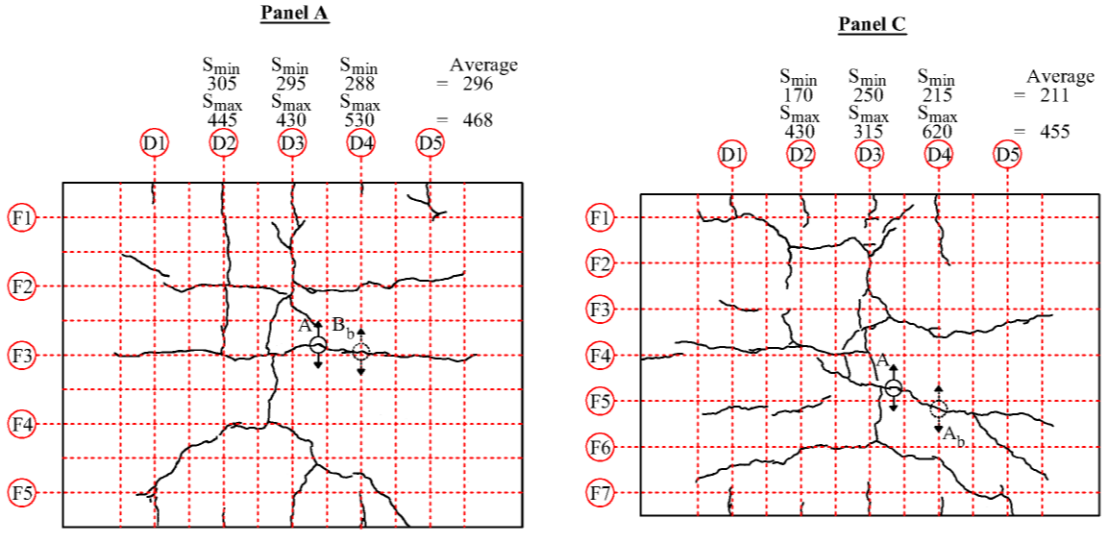

(a)

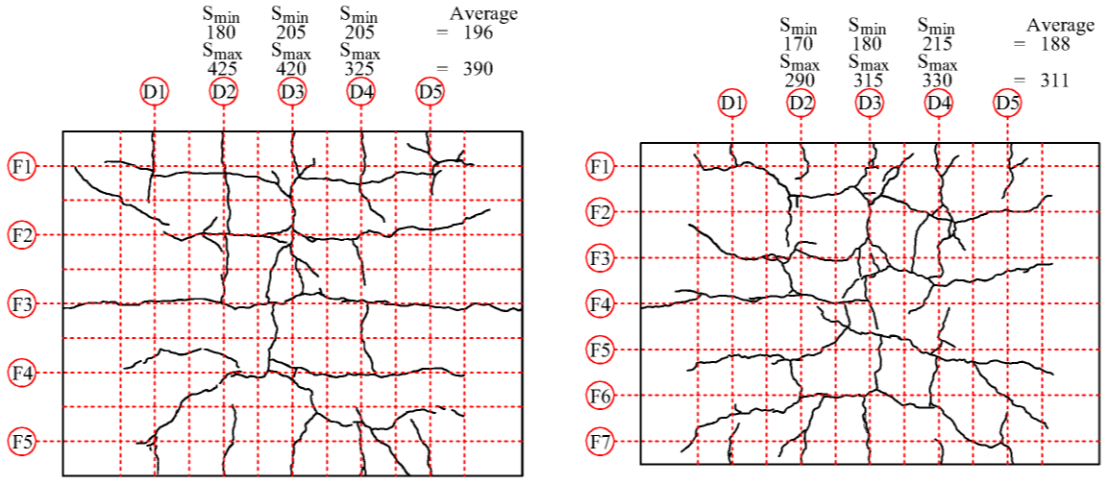

(b)

Fig. 5.11 Comparison of crack spacing between panels A and C at different steel stresses of direct reinforcing bars, a) at service $0.6f_y$, b) at yield f_y

5.9.2 Effect of reinforcement ratio

The crack patterns of panels A and B at the yield level of reinforcing bars in both orthogonal directions are compared with each other in Fig. 5.12. These two panels are completely identical except the reinforcement ratio, which is smaller in panel B (0.005) as compared to panel A (0.008). Besides the spacing of cracks, which is larger for panel B as expected, it is clear that a higher number of cracks form at an inclined angle in panel B than in panel A. This means that the reinforcement ratio not only can affect the crack spacing and the crack width, but also, it can affect the inclination of cracks.

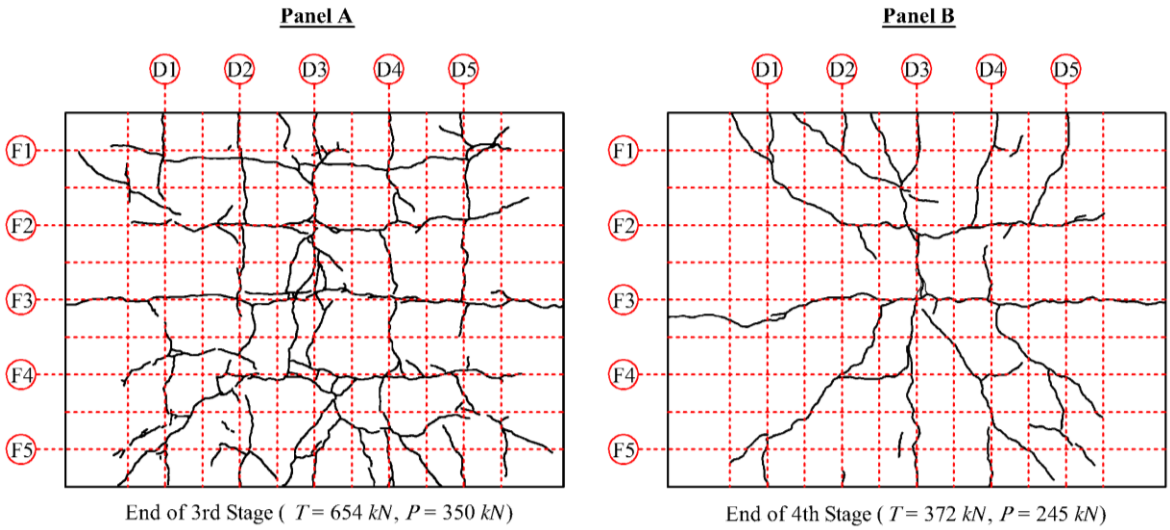

Fig. 5.12 Comparison of crack patterns for panels A and B at ultimate

5.9.3 Effect of concrete cover to bar diameter ratio

The concrete cover to bar diameter ratio (c_c/d_b) is higher in panel B (3.9 for direct tension reinforcement, and 2.9 for flexural reinforcement) than in panel A (3.1 for direct tension reinforcement, and 2.1 for flexural reinforcement). Beside the effect of reinforcement ratio explained in the previous Section, this factor can also affect the chance of inclined cracking. As it is shown in Fig. 5.12, the inclined cracking is more noticeable in panel B than in panel A. This can be partly due to the fact that, splitting tensile stresses are lower in panel B than in panel A

due to higher c_c/d_b in this panel. This can reduce the chance of orthogonal cracking along the reinforcing bars.

The same effect can also be confirmed by comparing the crack patterns of panel C and panel A, as shown in Fig. 5.11. The inclination of direct tension cracks is more noticeable in panel C than in panel A. The c_c/d_b ratio for flexural reinforcement is 2.8 in panel C, which is higher than in panel A (2.1). Therefore, smaller splitting tensile stresses are generated by flexural reinforcing bars in panel C, and hence, the chance of inclined cracking is higher for direct tension cracks in this panel.

5.9.4 Crack width gradient of inclined cracks

Under the two-way loading condition considered in this study, the width of a primary direct tension crack at top surface of the panel is wider for a crack that has some inclination than a primary orthogonal crack. However, the crack width at the bottom surface is smaller for an inclined direct tension crack than for an orthogonal direct tension crack. The crack width differences of inclined and orthogonal direct tension cracks at top and bottom surfaces are shown in Fig. 5.13. The width of an orthogonal direct tension crack in panel A is compared with that of an inclined direct tension crack in panel C at top and bottom surfaces of the panel. These cracks can be seen in Fig. 5.11(a). It can be seen that the inclined crack has a much higher gradient through the depth of the panel than that of the orthogonal crack. However, the average crack width through the depth is almost in the same range for the two types of cracks. This behaviour can reduce the rate of leakage through a full-depth inclined direct tension crack, as will be seen later.

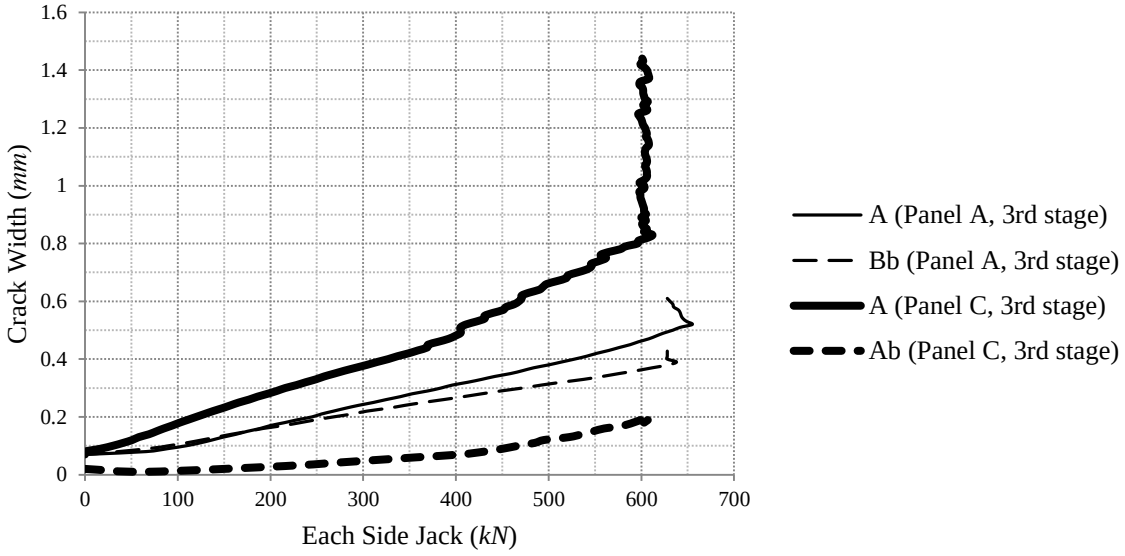

Fig. 5.13 Comparison of crack widths for inclined and orthogonal direct tension cracks

5.9.5 Residual crack width

The variation of the width of the crack A in panel C throughout successive loading and unloading stages is shown in Fig. 5.14. It can be seen that once a crack is formed a residual crack width always remains in place even after complete unloading. The residual crack width is pronounced in the unloading of the 1st stage in which the crack is initiated and in the 3rd stage in which the loading level is far exceeded the loading level of the preceding stage (2nd stage). This phenomenon can also be confirmed by looking at the elongation of panel C throughout the same loading stages as shown in Fig. 5.15. The residual deformation after unloading can be seen in the readings of LVDT LT in panel C. These residual deformations consist of mainly the residual width of primary cracks, and also, to a lesser extent, the residual concrete strains caused by micro-cracking.

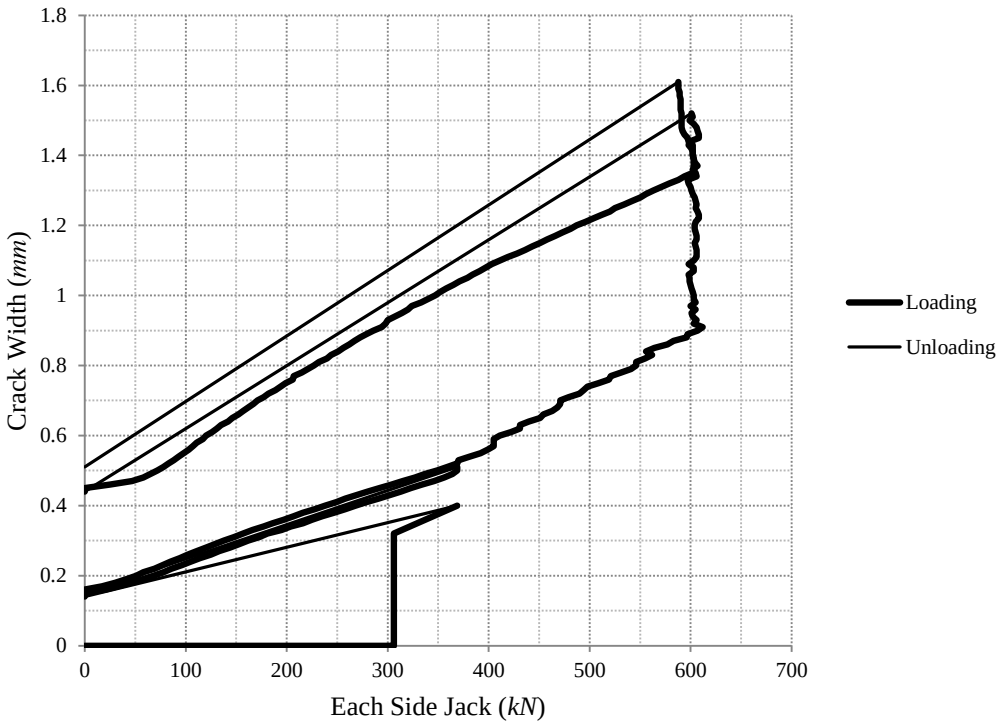

Fig. 5.14 Crack width variation of crack A in panel C throughout loading and unloading stages

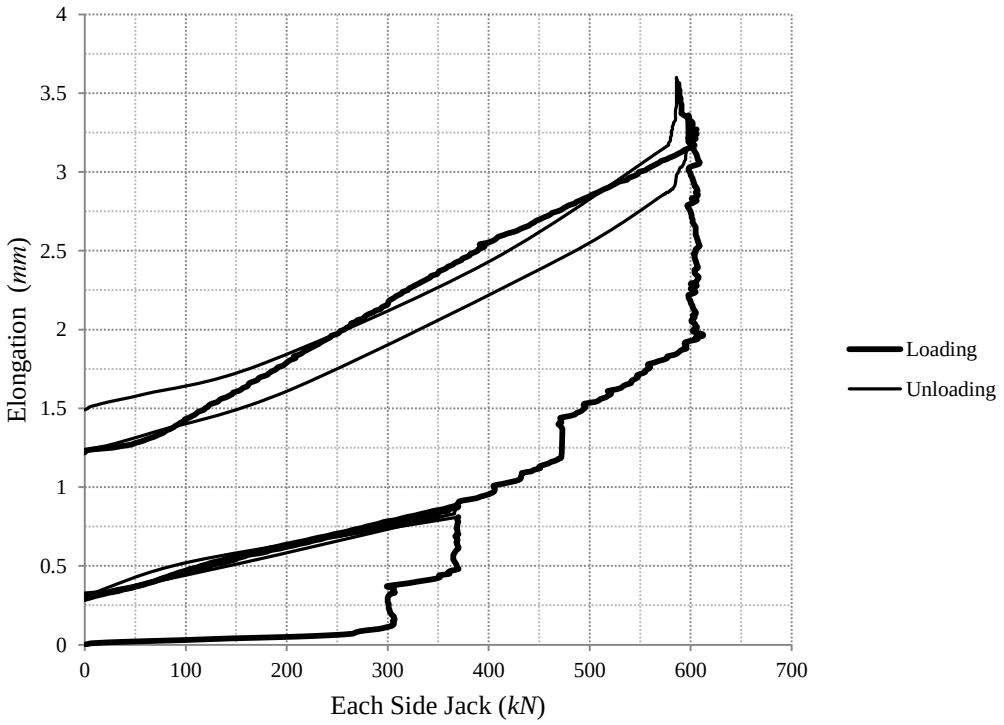

Fig. 5.15 Elongation of panel C (LVDT LT) throughout loading and unloading stages

5.9.6 Repeated loading effect

The width of the crack A in panel C during the three stages of two-way loading is shown in Fig. 5.16(a). It can be seen that the first time reloading of the panel C (2nd stage) after its initial cracking in the 1st stage causes an increase in the width of the crack A by an amount close to 0.1 *mm*. However, the second time repeated loading (3rd stage) does not considerably increase the crack width. This behaviour can also be confirmed in the readings of LVDT LT for panel C, shown in Fig. 5.16(b). This means a crack can become wider when it is subjected to a repeated loading, especially for the first cycle.

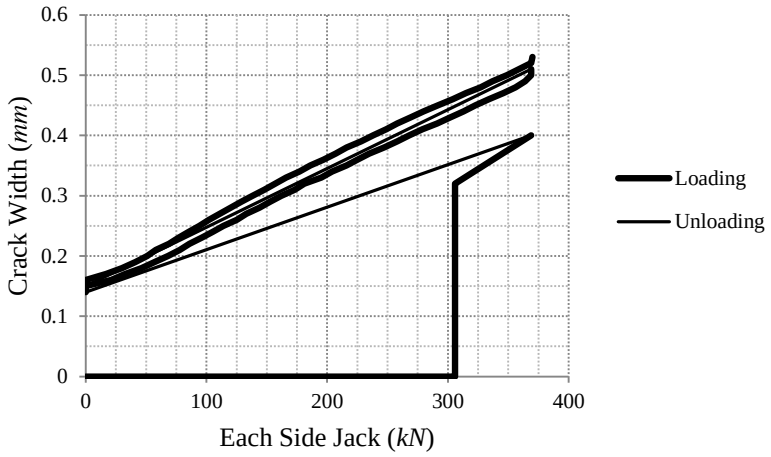

(a)

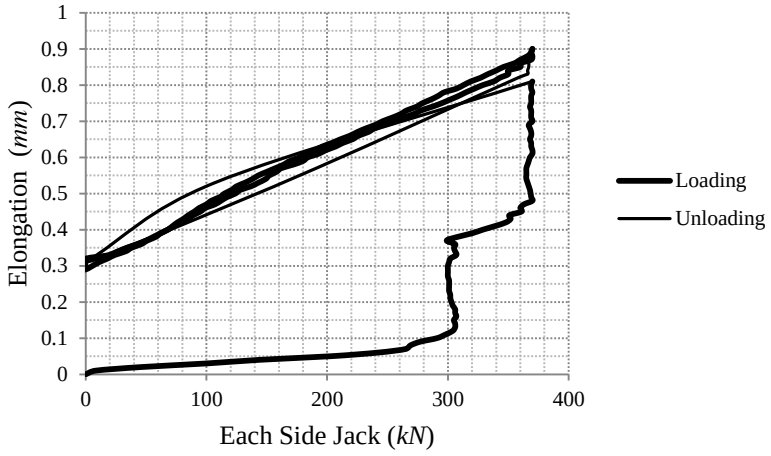

(b)

Fig. 5.16 Effect of repeated loading in panel C, a) width of crack A, b) LVDT LT

5.9.7 Stiffness reduction

The formation of any crack in a two-way structural system can damage the stiffness of the structure in all arbitrary directions. This effect becomes more evident as the inclination of the crack increases with respect to the considered axis of stiffness. As an example, the first crack in panel C is considered, as shown in Fig. 5.17(a). This crack has a slight degree of inclination with respect to the flexural axis F. The formation of this crack not only can damage the stiffness along the direct tension axis D, but also, it can decrease the stiffness along the flexural axis F. This effect can be confirmed by looking at the steel strain of flexural reinforcing bars in Fig. 5.17(b). The formation of this crack causes a jump in the steel strain readings of all flexural reinforcing bars. This is more obvious in the steel strain of reinforcing bar F4T for which the crack line is closely intersected with the strain gauge.

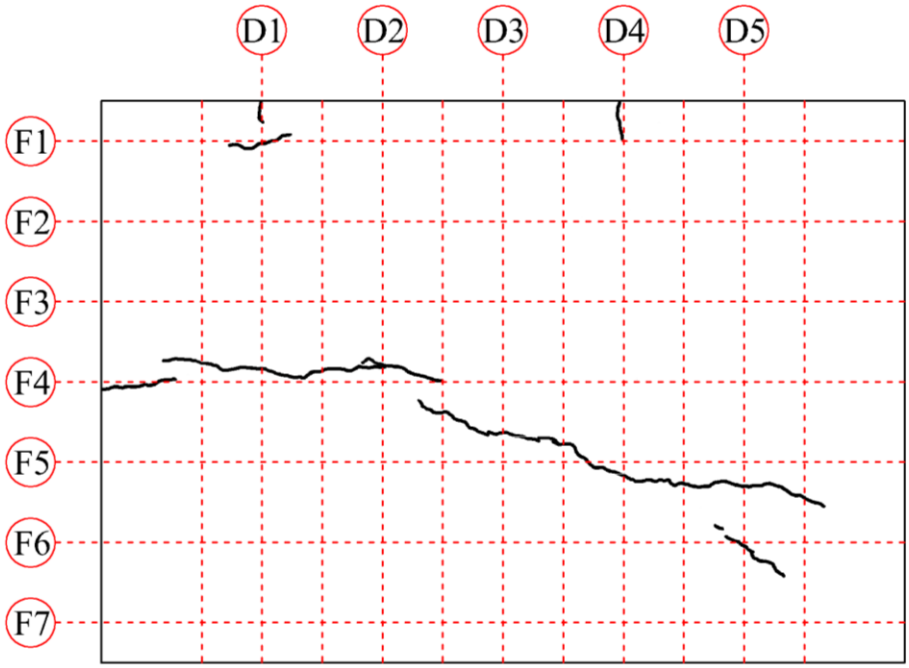

(a)

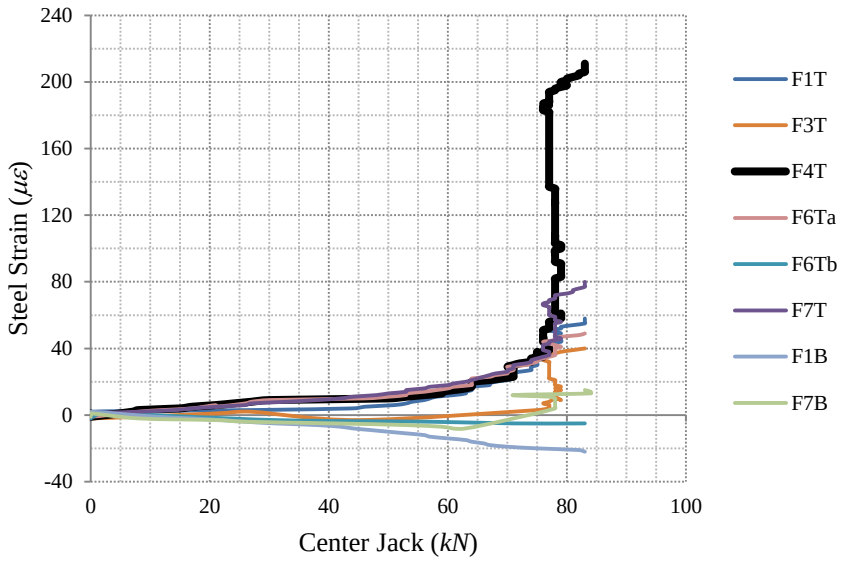

(b)

Fig. 5.17 Effect of cracking on structural stiffness, a) first crack in panel C, b) steel strains of flexural reinforcing bars up to the formation of first crack

The aforementioned effect of inclined cracking on the two-way structural stiffness can also be explained with the aid of panel B at the 4th stage of testing. While the direct tension load is kept constant at about 370 *kN* on each side jack (Fig. 5.18(a)), the continuation of the flexural loading causes an increase in the steel strains of the direct reinforcing bars (Fig. 5.18 (b) and (c)). This is due to the formation of new inclined cracks. This means the formation of inclined cracks can affect the structural stiffness in both orthogonal directions.

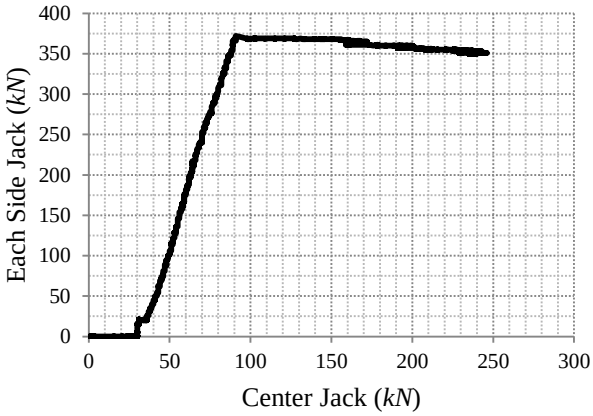

(a)

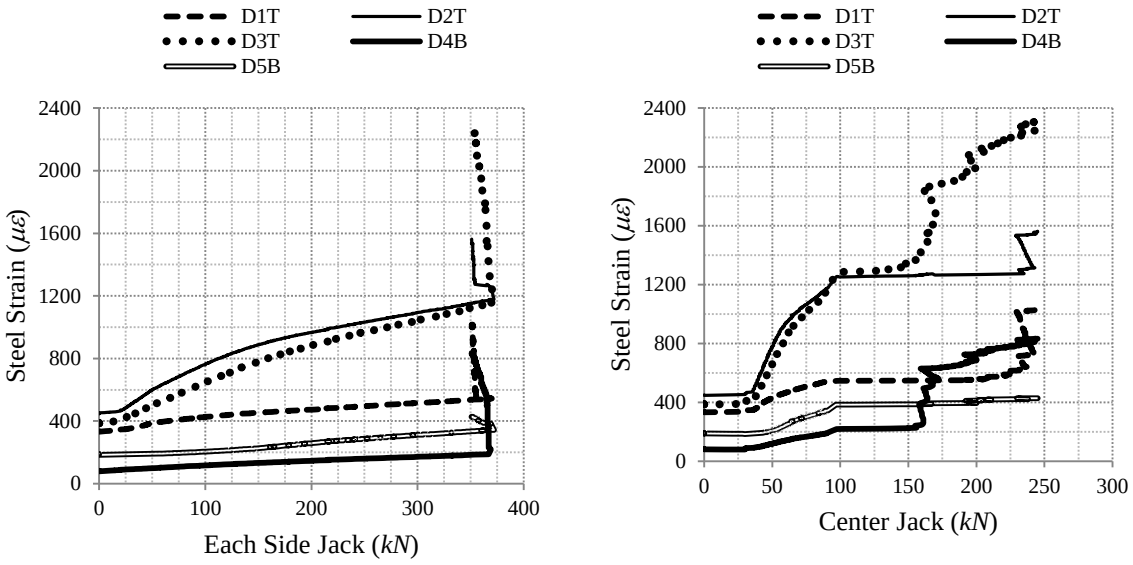

(b)

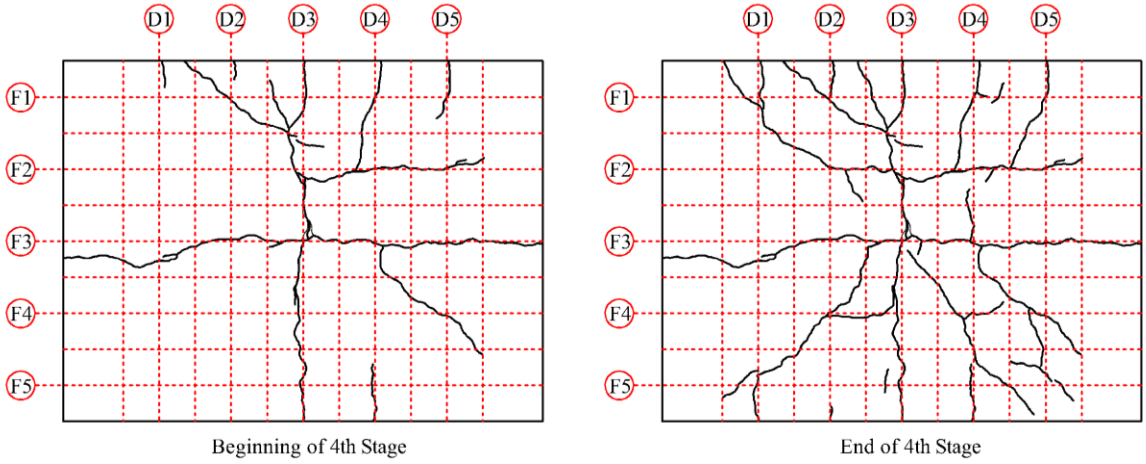

(c)

Fig. 5.18 Effect of inclined cracking, panel B at 4th stage of testing, a) loading plan, b) steel strains of direct reinforcing bars vs. each side jack or vs. center jack, c) crack patterns at beginning and at end of 4th stage

5.9.8 Behaviour of inclined cracks

To further investigate the characteristics of inclined cracking, an inclined crack in panel A, namely, crack C is considered, as shown in Fig. 5.19(a). The width of this crack under two-way (2nd stage) and one-way (one-way tension and one-way bending) loadings are given in Fig.

5.19(b). It can be seen that the crack C is widening under both one-way and two-way loading conditions. However, the width of this crack is smaller when the panel is loaded in one-way tension or one-way bending, than when it is loaded in two-way. This means that the width of an inclined crack under two-way loading is dependent on the level of loading in both orthogonal directions. Therefore, the theory of one-way cracking is not capable of predicting the width of an inclined crack under a two-way loading condition.

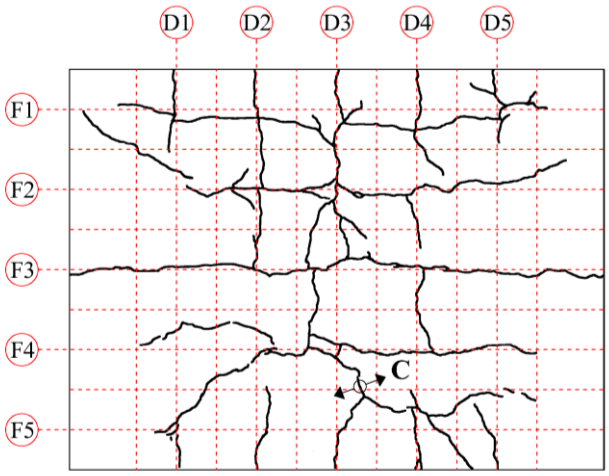

(a)

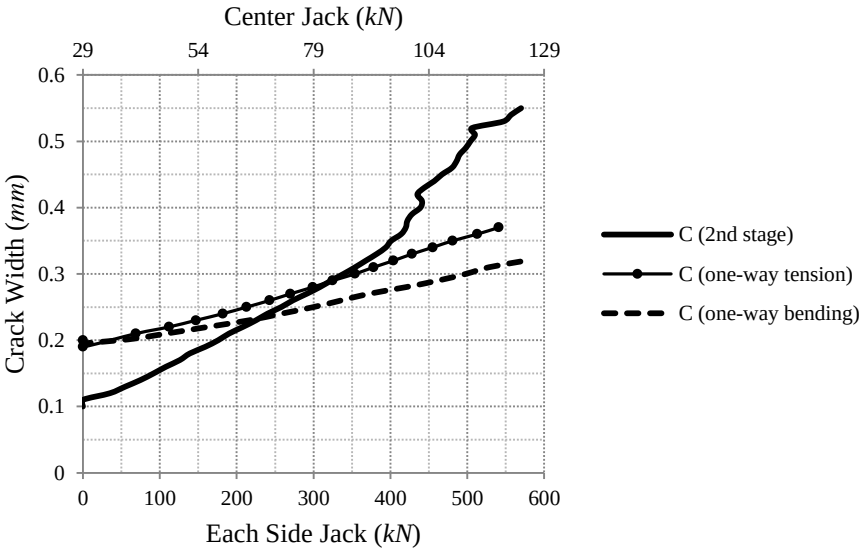

(b)

Fig. 5.19 Behaviour of an inclined crack, a) crack C in panel A, a) width of crack C under one-way and two-way loading conditions

5.9.9 Bond strength reduction

Another important experimental observation is an extreme damage to the bond strength that occurs in a two-way system. This effect can be explained for panel B in Fig. 5.20. The crack patterns and the steel strains of flexural reinforcing bars, namely, F3T, F4Ta, and F5T are shown at 1st and 2nd stages of testing in Fig. 5.20 (a) and (b), respectively. While all three steel strain gauges are at the same distance to the crack formed along the D3 axis, F3T shows a higher strain value than the other two gauges. This is an indication of a damage to the bond strength around the reinforcing bar F3T caused by the formation of a longitudinal crack along the F3 axis.

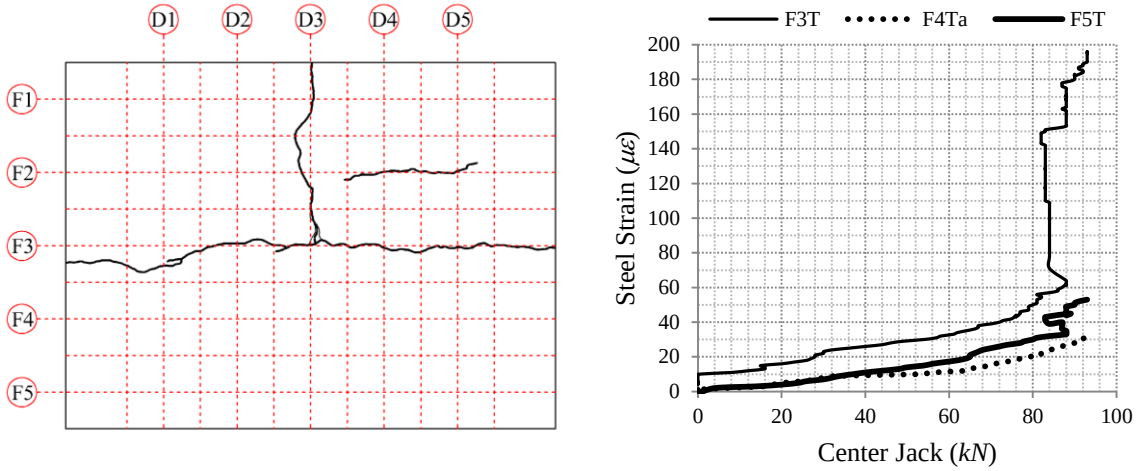

(a)

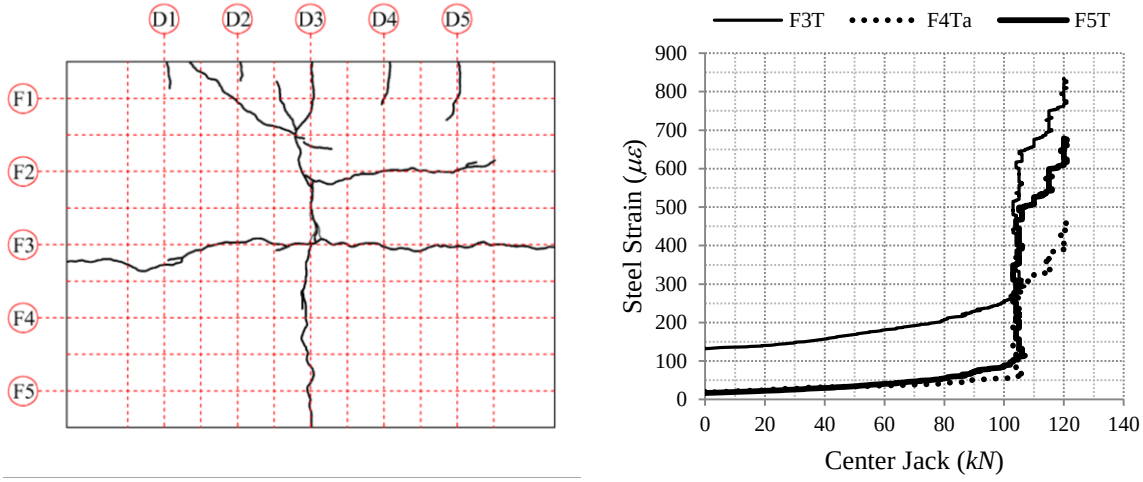

(b)

Fig. 5.20 Bond strength damage in two-way systems, crack patterns and steel strain of flexural reinforcing bars in panel B, a) 1st stage, b) 2nd stage

The aforementioned bond strength damage phenomenon can also be explained in a different way. For the fact that the most flexural cracks penetrate partly through the depth of the panel, the bond strength of the bottom layer of direct reinforcing bars is less affected by these cracks than that of the top layer. This effect is revealed by looking at the steel strains of top and bottom layers of direct reinforcing bars in all three tested panels in the stage of one-way tension, as shown in Fig. 5.21. It is obvious that the steel strains of the bottom layer of reinforcing bars are generally lower than those of the top layer.

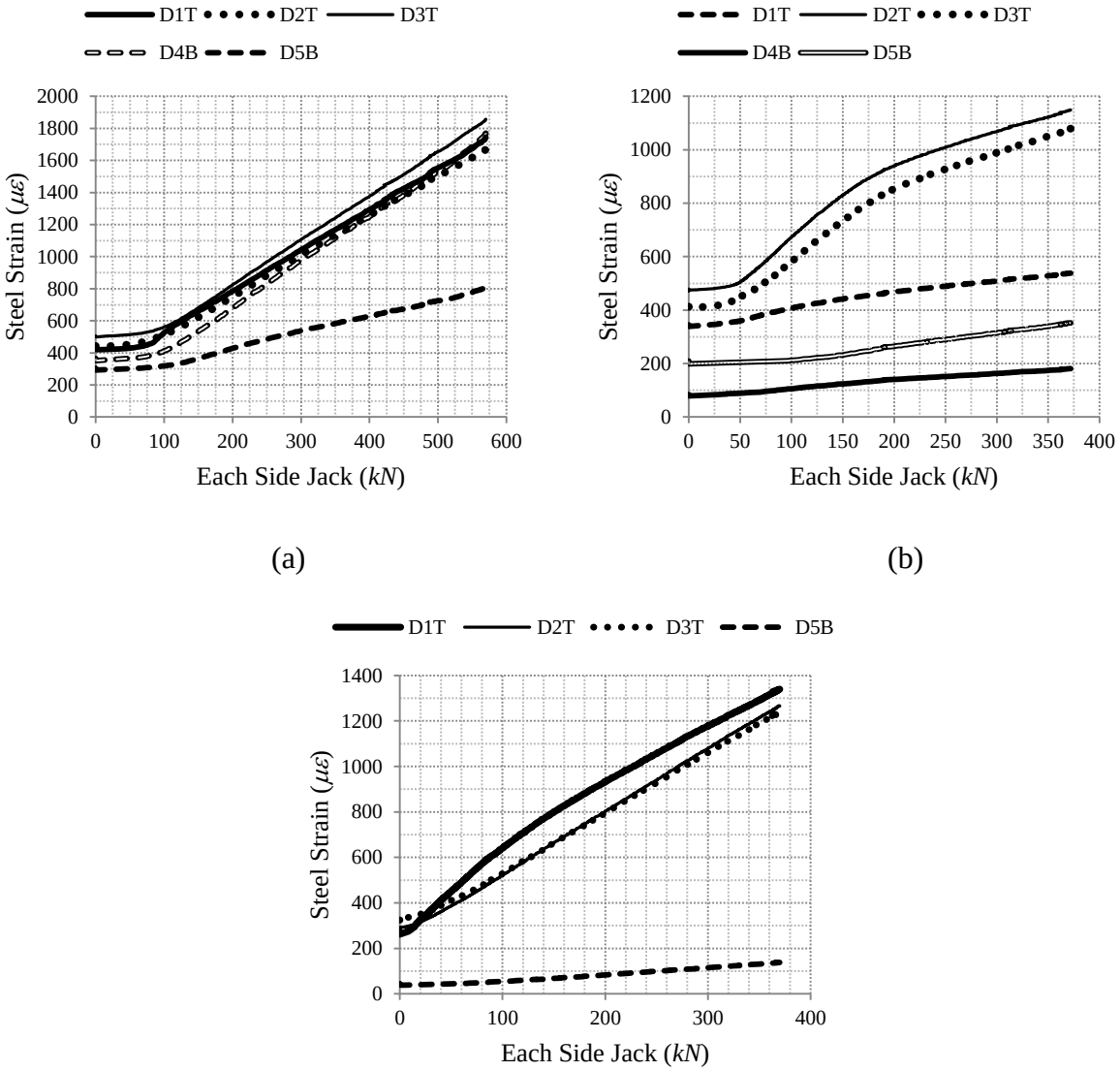

Fig. 5.21 Steel strains of top and bottom direct reinforcing bars under one-way tension, a) panel A, b) panel B, c) panel C

5.10 Summary

The results of three experiments described in the previous Chapter are presented in this Chapter. This experimental data can be used as a reference for benchmarking the analytical model of a two-way panel. Analysis of these experimental results has resulted in a number of new findings. These findings are briefly pointed out in the following,

- The crack patterns mainly reflect the shape of the reinforcement mesh. This is primarily due to the presence of splitting tensile stresses generated by radial bond forces. Therefore, the spacing of cracks in a two-way panel has a close relationship with the spacing of reinforcing bars in both orthogonal directions.

- A few cracks may always form at some inclination to the axes of orthogonal reinforcing bars. The possibility of inclined cracking is closely related to the two-way loading ratio, the reinforcement ratio, the clear cover to bar diameter ratio, and the bar spacing. The inclined cracking is more probable for the two-way loading ratios closer to 1, the reinforcement ratios less than 0.005, and the clear cover to bar diameter ratios more than 2.5. The effect of bar spacing is more complex. It seems there exists a range of bar spacings within which the chance of inclined cracking is reduced.

- The rate of leakage through a full-depth crack depends on the crack width gradient rather than just the maximum crack width at one side of the panel. Also, the compression zone that exists at the section of a flexural crack can prevent the water leakage through this type of cracks.

- The inclined cracks have a much higher gradient through the depth than direct tension cracks for a two-way loading condition that has a bending moment in at least one of the orthogonal directions. This would suggest a reduced water leakage through this type of cracks.

- Once a crack is formed a residual crack width remains in place even after complete unloading. The residual crack width increases by raising the peak level of loading. Also, some residual strains always exist in the tensioned concrete due to micro-cracking.

- The width of a crack can increase under repeated loading. This increase is observed to be much more significant at the first reloading stage of the tested panels in a range of 0.1 *mm*.

- The stiffness of a two-way panel along any arbitrary axis is reduced by the formation of a crack with any arbitrary orientation to that axis.

- The width of an inclined crack depends on the loading in both orthogonal directions.

- The bond strength is reduced in a two-way panel due to orthogonal cracking along the reinforcing bars. The damaging effect of these cracks on the bond strength is similar to the damaging effect of a longitudinal splitting crack along a reinforcing bar on the bond strength of that bar.

CHAPTER 6

ANALYTICAL MODELING OF TWO-WAY CRACKS

6.1 Introduction

The experimental study explained in the previous Chapter has revealed a number of behavioural differences between one-way and two-way cracking systems. This makes the theory of one-way cracking inefficient in predicting all aspects of two-way cracking behaviour. Therefore, attempts are made in this Chapter to develop a new analytical model that is more relevant for predicting the cracking of a two-way system. The FE model, which has been developed in Chapter 3, is also used here to help calculating various parameters involved in the analytical model. The newly developed analytical model can be used as a basis for crack control of two-way elements.

6.2 Cracking Load based on One-Way Theory

In most design practices, the prediction of initial cracking load is commonly simplified with the assumption of one-way loading condition. The scale of error accompanied with such a simplification is investigated by comparing the one-way predicted values of the initial cracking load with the experimental data for the tested panels in Chapter 5. The properties of concrete and steel for the three tested panels are given in Table 6.1.

Table 6.1 Properties of concrete and steel for three tested panels

Panel	f_{cm} (*MPa*)	γ_c (kg/m^3)	E_c (*MPa*) ACI209R	E_c (*MPa*) CEB	E_c (*MPa*) Assumed	f_{ck} (*MPa*)	$f_{sp,mean}$ (*MPa*)
A	41.9	2300	30702	34661	34000	33.9	3.3
B	46.0	2300	32169	35757	35000	38	3.1
C	37.4	2300	29007	33373	33000	29.4	3.1
			Eq. 3.17	Eq. 3.14		Eq. 3.16	

Panel	f_{ct} (*MPa*) ACI209R	f_{ct} (*MPa*) CEB	f_{ct} (*MPa*) 0.9f_{sp}	f_{ct} (*MPa*) Assumed	$f_{r,mean}$ (*MPa*)	E_s (*GPa*)	α_e
A	2.14	3.16	2.97	2.97	5.4	200	5.9
B	2.24	3.41	2.79	2.79	5.2	200	5.7
C	2.02	2.87	2.79	2.79	4.6	200	6.1
	Eq. 3.18	Eq. 3.15					

The calculations of the cracking loads of direct tension and flexural cracks for panel A with the assumption of one-way loading is as follows,

$$\begin{aligned} T_r &= \left[bh + (\alpha_e - 1)A_s\right] f_{ct} \\ &= \left[3 \times 300 \times 250 + (5.9 - 1) \times 6 \times 300\right] \\ &\quad \times \frac{10}{6} \times 2.97 \times 10^{-3} = 1157 \quad kN \end{aligned} \tag{6.1}$$

$$\begin{aligned} P_r &= \left[\frac{bh^3}{12} + (\alpha_e - 1)A_s y_{st}^{\ 2}\right] \times f_r \times \frac{2}{0.5l \times y_t} + s.w. \\ &= \left[\frac{1500 \times 250^3}{12} + 2 \times (5.9 - 1) \times 5 \times 300 \times 75^2\right] \\ &\quad \times 5.4 \times \frac{2}{0.5 \times 1800 \times 125} \times 10^{-3} + 29 = 224 \quad kN \end{aligned} \tag{6.2}$$

where T_r = stabilized cracking load of direct tension cracks (total of side jack loads) (*kN*); P_r = stabilized cracking load of flexural cracks (center jack) (*kN*); b = section width (*mm*); h = section height (*mm*); α_e = modular ratio; A_s = area of steel in tension (*mm*^{2}); f_{ct} = tensile strength of concrete (MPa); y_{st} = distance from neutral axis to the level of tensile reinforcement (*mm*); f_r = modulus of rupture (*MPa*); l = span length in flexural direction (mm); y_t = distance from neutral axis to tensile fibre (*mm*); and *s.w.* = self weight (*kN*).

These calculations are repeated for all three tested panels and summarized in Table 6.2. The comparison with experimental results shows significant discrepancies in ranges of 50 to 80% and 100 to 145% for direct tension and flexural cracks, respectively. Aside from possible errors in the estimated tensile strength of concrete, one major contributing factor to such a large discrepancy can be the effect of splitting tensile stresses inherent to a two-way loading system, which is ignored in one-way cracking calculations. Interestingly, the higher error in the predicted flexural cracking loads is expected due to higher splitting tensile stresses existing in the flexural sections. This is because the stress in the direct tension reinforcing bars is higher than in the flexural reinforcing bars at the instant of cracking.

Table 6.2 Comparison of one-way predicted cracking load and experimental data

	Stabilized Cracking Load (kN)					
	Direct Tension Crack (T_r)			Flexural Crack (P_r)		
Panel	Experiment	One-way Prediciton	Error (%)	Experiment	One-way Prediction	Error (%)
A	756	1157	53	92	224	144
B	708 to 744	1073	44 to 51	88 to 105	214	104 to 143
C	612 to 738	1089	48 to 78	86	184	114

6.3 Effect of Concrete Shrinkage

Concrete undergoes continuous volumetric contraction from the time it is cast. This time dependent strain is called shrinkage, which can be categorized into three main types of plastic, drying, and chemical. The plastic shrinkage takes place at the early setting process of concrete at which the concrete is still in a plastic state. This shrinkage is attributed to the capillary tension of the pore water, and happens when the rate of water loss due to evaporation at the concrete surface is higher than the rate of bleeding water. The plastic shrinkage is prevented during the experiment by keeping the concrete surface moistened for the first week after casting. The drying shrinkage is mainly due to the loss of capillary water in the hardened concrete over time. The chemical shrinkage is the volume reduction associated with the reaction between cement and water in the hydrating cement paste. The total shrinkage usually refers to the sum of drying and

chemical shrinkage strains. The total shrinkage strain increases over time at a decreasing rate until it reaches to its maximum at infinity.

When a concrete element is unrestrained under shrinkage, the concrete can freely move and adjust itself to the new length without the creation of any tensile stress. However, some degree of restraint always exists for a reinforced concrete element. This restraint can be categorized into two types, i.e., internal and external. The internal restraint arises from the presence of the reinforcement inside the concrete, while the external restraint is caused by the external supports. Both of these restraints can resist the free contraction of concrete, which, in turn, will generate tensile stresses in the concrete. For externally restrained members, these tensile stresses can be high enough on their own to reach the tensile strength of concrete and cause the formation of cracks. For internally restrained members, the shrinkage tensile stresses will combine with the existing tensile stresses, and hence, will reduce the cracking load. This effect can be accountable for a part of errors in Table 6.2, as the internally restraint shrinkage is not considered in the calculations of the cracking load. This effect is investigated through a FE parametric study in the following sections.

Beside the effect of restrained shrinkage strains on raising the tensile stresses in the concrete and reducing the cracking load, the shrinkage strain can increase the width of existing cracks. This effect is also explained in the following sections.

The shrinkage may also affect the bond strength over time. The internal restraint is higher in concrete closer to the reinforcing bar. Therefore, if the shrinkage strain increases above 100 $\mu\varepsilon$, it is probable that micro-cracks develop in concrete near the reinforcing bar affecting the bond strength. That may be the reason of the bond damage observed in the long-term tests by Gilbert (2005).

6.3.1 Calculation of total shrinkage strain

The recommendations of CEB MC90 (1990) for the calculation of the total shrinkage strain are adopted here, as follows,

$$\varepsilon_{cs}(t,t_s) = \varepsilon_{cso}\beta_s(t-t_s) \tag{6.3}$$

where $\varepsilon_{cs}(t,t_s)$ = total shrinkage strain at time t; ε_{cso} = notional shrinkage coefficient; β_s = coefficient to describe the development of shrinkage with time; t = age of concrete (*days*); and t_s = age of concrete at the beginning of shrinkage (*days*).

The notional shrinkage coefficient can be calculated as,

$$\varepsilon_{cso} = \varepsilon_s(f_{cm})\beta_{RH} \tag{6.4}$$

in which,

$$\varepsilon_s(f_{cm}) = \left[160 + 10\beta_{sc}\left(9 - f_{cm}/f_{cmo}\right)\right]\times 10^{-6} \tag{6.5}$$

$$\begin{aligned} \beta_{RH} &= -1.55\beta_{sRH} \rightarrow 40\% \le RH < 99\% \\ \beta_{RH} &= +0.25 \rightarrow RH \ge 99\% \end{aligned} \tag{6.6}$$

$$\beta_{sRH} = 1 - \left(\frac{RH}{RH_o}\right)^3 \tag{6.7}$$

where f_{cm} = mean compressive strength of concrete at the age of 28 days (*MPa*); f_{cmo} = 10 *MPa*; β_{sc} = coefficient related to the type of cement (4 for slowly hardening cements SL, 5 for normal or rapid hardening cements N and R, and 8 for rapid hardening high strength cements RS); RH = relative humidity of the ambient atmosphere (%); RH_o = 100%.

The development of shrinkage in Eq. 6.3 can be calculated as,

$$\beta_s(t-t_s) = \left[\frac{(t-t_s)/t_1}{350(h_n/h_o)^2 + (t-t_s)/t_1}\right]^{0.5} \tag{6.8}$$

in which,

$$h_n = 2A_c / u \tag{6.9}$$

where t_1 = 1 *day*; h_o = 100 *mm*; h_n = notional size of member (*mm*); A_c = cross-sectional area; and u = perimeter of the member in contact with atmosphere.

Using the above equations, the total shrinkage strain is calculated for the three tested panels at the day of testing and presented in Table 6.3. Because of the fact that all the panels are cured on site, the shrinkage of hardened concrete starts few hours after the casting.

Table 6.3 Total shrinkage strains for three tested panels

Panel	t (days)	t_s (days)	A_c (mm^2)	u (mm)	h (mm)	$\beta_s(t-t_s)$	RH (%)	β_{sc}	f_{cm} (MPa)	ε_{cso} ($\mu\varepsilon$)	$\varepsilon_{cs}(t,t_s)$ ($\mu\varepsilon$)
A	116	0	375000	3500	214	0.259	50	5	41.9	-543	-141
B	73	0	375000	3500	214	0.208	50	5	46.0	-515	-107
C	63	0	350000	3300	212	0.196	50	5	37.4	-574	-113

6.3.2 FE parametric study of internally restrained shrinkage

To investigate the tensile stresses caused by the internally restraint shrinkage, a FE parametric study is conducted. The material properties of concrete and steel in the FE model are chosen to be similar to those of panel A, as given in Table 6.4. A concentrically reinforced cylindrical tension tie member is selected for modeling. This structure is modeled with axisymmetric elements, as shown in Fig. 6.1(a). The modelling technique is the same as that introduced in Chapter 3 with the bond layer model and the explicit dynamic solution technique. The shrinkage strain is introduced to the model with an equivalent temperature change. The deformed shape after shrinkage is shown in Fig. 6.1(b).

Table 6.4 Concrete and steel properties in FE model of internally restrained shrinkage

E_s (GPa)	ν_s	$a_{s,max}$ (mm)	α_F	f_c' (MPa)	E_c (MPa)	f_{ct} (MPa)	ν_c	G_f (CEB) ($N.mm/mm^2$)	Post-Cracking Curve (CEB) w (mm)	Post-Cracking Curve (CEB) σ_{ct} (MPa)	Concrete Compressive Curve Total Strain ($\mu\varepsilon$)	Concrete Compressive Curve Inelastic Strain ($\mu\varepsilon$)	Concrete Compressive Curve Stress (MPa)
200	0.3	20	6.5	41.9	34000	2.97	0.2	0.068	0	2.97	0	0	0
									0.02	0.45	441	0	15
									0.15	0	2200	968	41.9

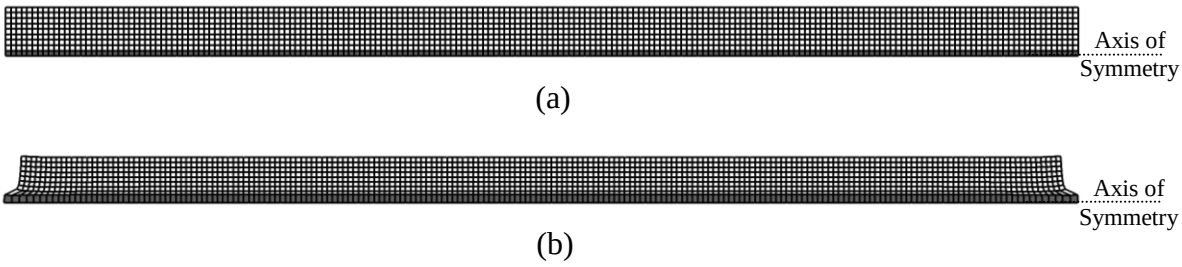

Fig. 6.1 FE model for investigation of internally restrained shrinkage, a) undeformed shape, b) deformed shape

The results of parametric study are shown in Fig. 6.2. These results show the tensile stresses developed in an externally unrestrained circular tie member due to internally restrained shrinkage strain. The total shrinkage strain of 50 $\mu\varepsilon$ is applied to tie members with various clear concrete covers. It can be seen that concrete tensile stresses due to internally restrained shrinkage can rise up to about 12% of f_{ct} for small concrete covers. Therefore, the errors in the prediction of initial cracking loads in Table 6.2 can be partly due to these shrinkage stresses ignored in the calculations. Taking to account that for the tested panels the size of effective tension area of concrete around each reinforcing bar is on average 300 by 125 *mm*, the equivalent concrete cover would be at least $4d_b$. This means the error in the prediction of initial cracking load caused by ignoring shrinkage strain of 50 to 100 $\mu\varepsilon$ would be in the range of 5 to 10%, which is still far from the 53 and 144% errors in panel A. A major portion of these errors is attributed to the presence of splitting tensile stresses ignored in one-way formulas as will be confirmed later. It must also be noted that only a part of shrinkage strain that is happening after the hardening of the bond can contribute to the internally restrained shrinkage strains. For the tested panels, on

average the shrinkage strain during the first two days after casting may be considered free to slip, which is about 20 $\mu\varepsilon$.

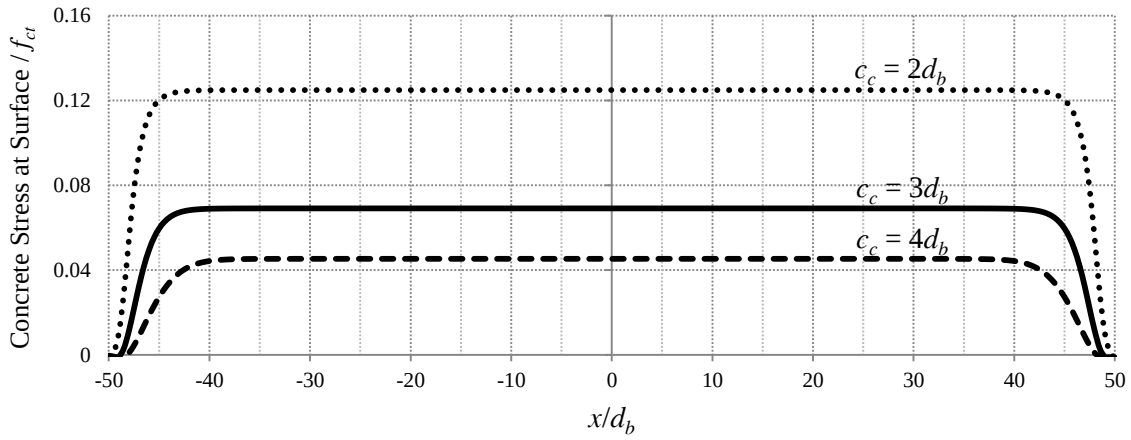

Fig. 6.2 Internally restrained shrinkage stresses for a cylindrical tension tie member with various concrete covers (shrinkage strain = 50 $\mu\varepsilon$)

6.3.3 Effect of shrinkage on crack width

The shrinkage strain can directly increase the width of existing cracks. The effect of shrinkage on the crack width is different in externally restrained and unrestrained members. The contribution of the shrinkage strain on the crack width in an externally unrestrained member is illustrated in Fig. 6.3. It can be seen that only a part of total shrinkage strain, i.e., the unrestrained shrinkage strain after the bond hardening, can contribute to the crack width. For simplicity, a conservative approach for design purposes is to consider the total shrinkage strain as a contributing strain to the crack width. In this way, the product of the total shrinkage strain and the crack spacing is the shrinkage crack width and must be added to the crack width equation. For instance, by conservatively ignoring the effect of Δ_c and Δ_{sho}, the maximum contribution of shrinkage to the crack width would be 0.04 *mm* for a total shrinkage strain of 140 $\mu\varepsilon$ and a crack spacing of 300 *mm* ($140\times10^{-6}\times300mm$).

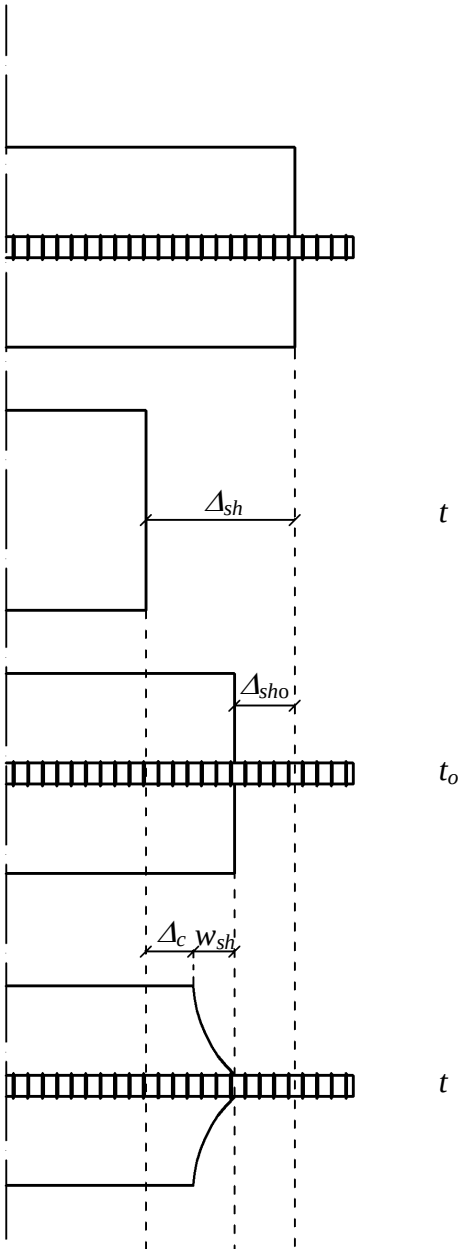

Δ_{sh} : total free shrinkage displacement at time t
Δ_{sho} : shrinkage displacement prior to bond hardening
Δ_c : internally restraint shrinkage displacement at concrete surface
w_{sh} : the contribution of shrinkage to the crack width at surface at time t

Fig. 6.3 Contribution of shrinkage to the crack width for externally unrestrained RC member

For externally restrained structure, shrinkage can contribute to the crack width in two ways. One is the same as the abovementioned effect of the unrestrained shrinkage through shortening of the concrete between cracks, with only difference that the shrinkage before hardening of the bond

can also affect the crack width. Another one is by increasing the strain in the steel reinforcing bar at the crack. Therefore, this additional strain in the steel must be added to the crack width equations. However, if the total shrinkage strain is conservatively used in the crack width equation, this effect of shrinkage on the steel strains should not be added to the steel strains.

6.4 Parametric Study of Splitting Tensile Stresses

As explained in Chapter 3, radial bond forces can develop around a reinforcing bar due to the presence of bar lugs. These radial bond forces are the reason for the creation of splitting tensile stresses. A good estimation of splitting tensile stresses is essential in the prediction of two-way cracks. Therefore, a parametric study is performed to calculate these stresses under various geometrical conditions. The specification of the FE model is shown in Fig. 6.4(a). The effects of clear concrete cover and the member length are considered in this study. The material properties of the steel and concrete are the same as those given in Table 6.4. The stress contours of splitting tensile stresses at various steel stresses are shown for a typical model in Fig. 6.4(b). The higher tensile stresses are shown in a darker color. It is clear that the splitting tensile stresses are concentrated in a conical region at two free ends of the tie member.

The variation of splitting tensile stresses over the depth of concrete cover at section A-A in Fig. 6.4(b) is presented in Fig. 6.5 for various concrete covers. It is clear that the splitting tensile stresses increase with increasing steel stresses. Also, it can be seen that the average splitting tensile stresses are higher for smaller concrete covers.

The variation of splitting tensile stresses along the longitudinal axis at section B-B in Fig. 6.4(b) is shown in Fig. 6.6 and Fig. 6.7 for various concrete covers and for various lengths of the tie member, respectively. It can be seen that, regardless of the size of the concrete cover and the length of the tie member, a region with a length of approximately $l/3$ from the free end of the tie member is influenced by the splitting tensile stresses.

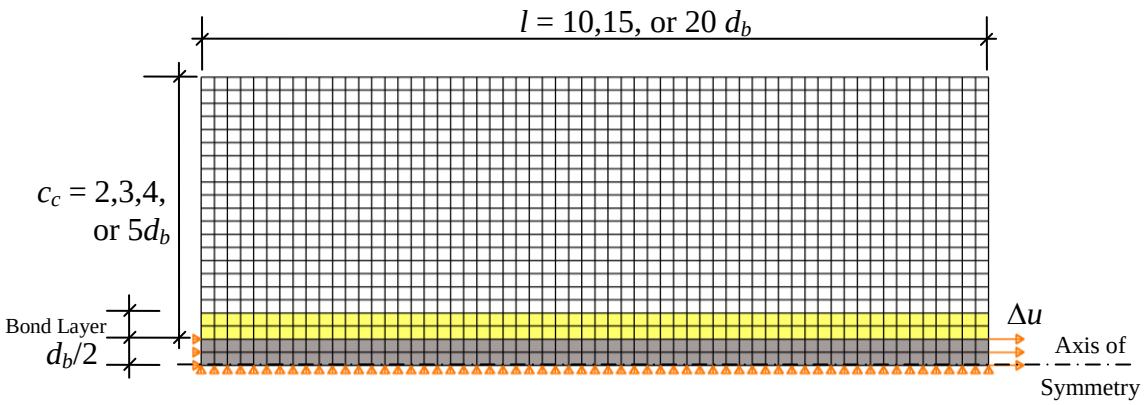

(a)

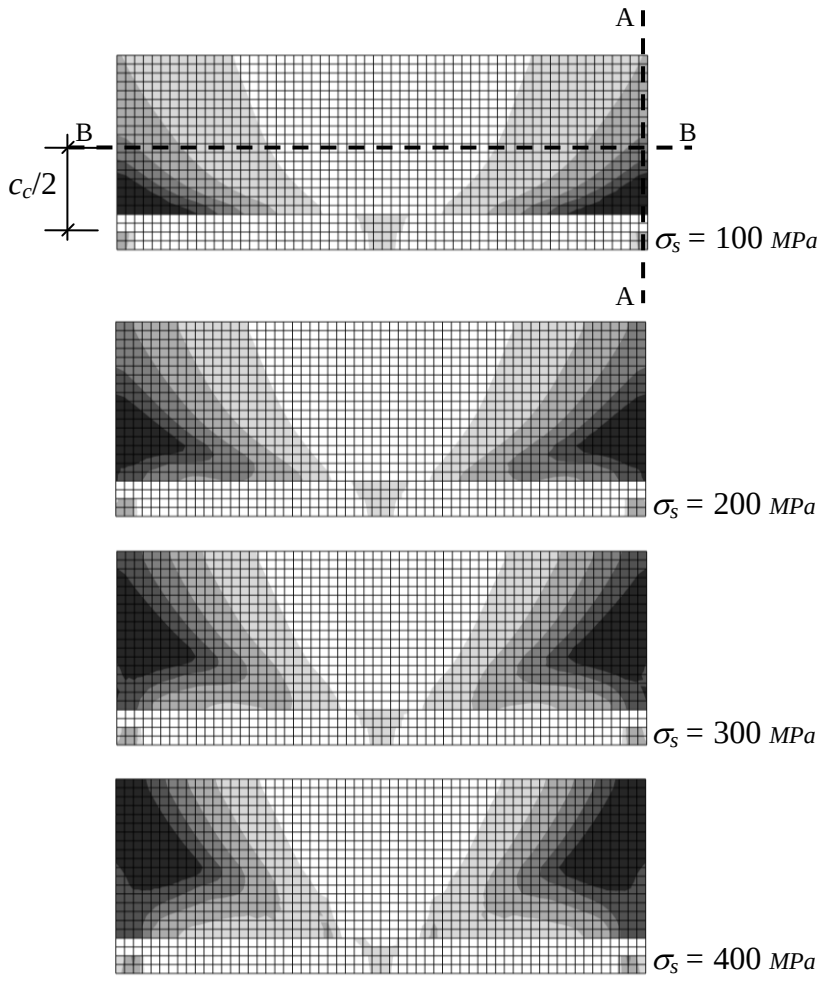

(b)

Fig. 6.4 Investigation of splitting tensile stresses, a) FE model specifications, b) splitting tensile stresses contour (c_c = 5d_b , l = 15 d_b) (higher tensile stresses shown in a darker color)

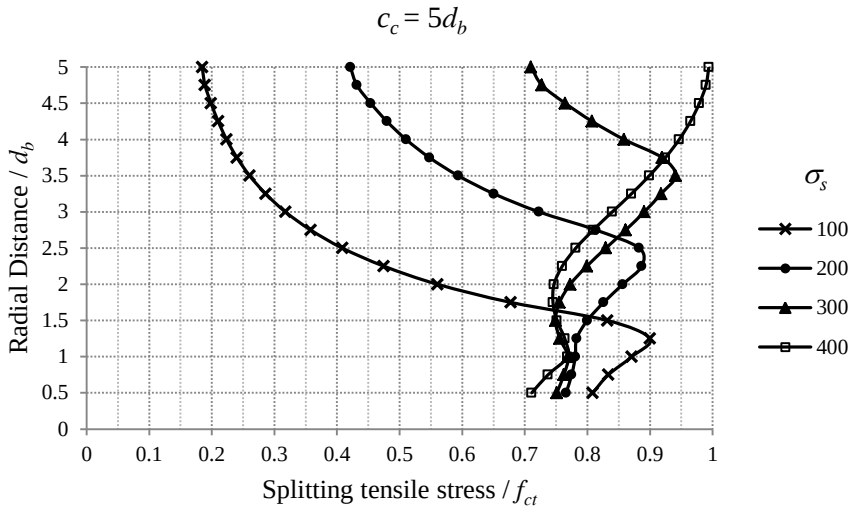
$c_c = 5d_b$
Radial Distance / d_b
Splitting tensile stress / f_{ct}
σ_s
100
200
300
400

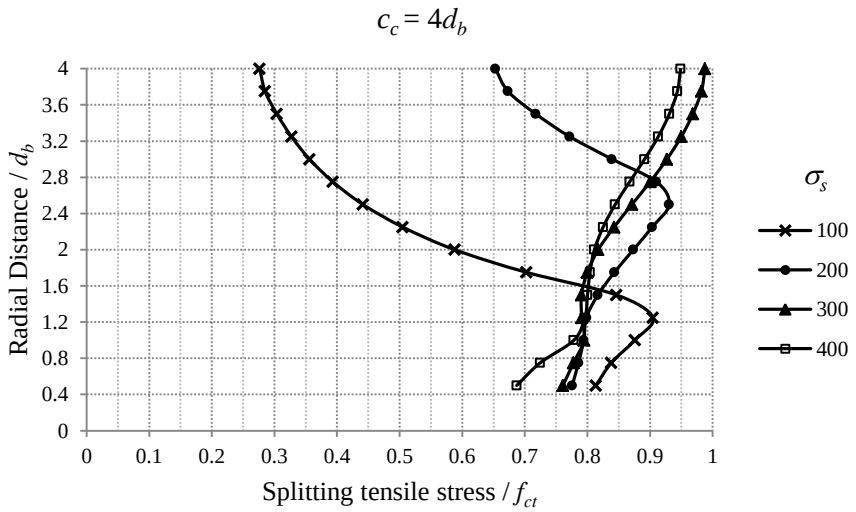
$c_c = 4d_b$
Radial Distance / d_b
Splitting tensile stress / f_{ct}
σ_s
100
200
300
400

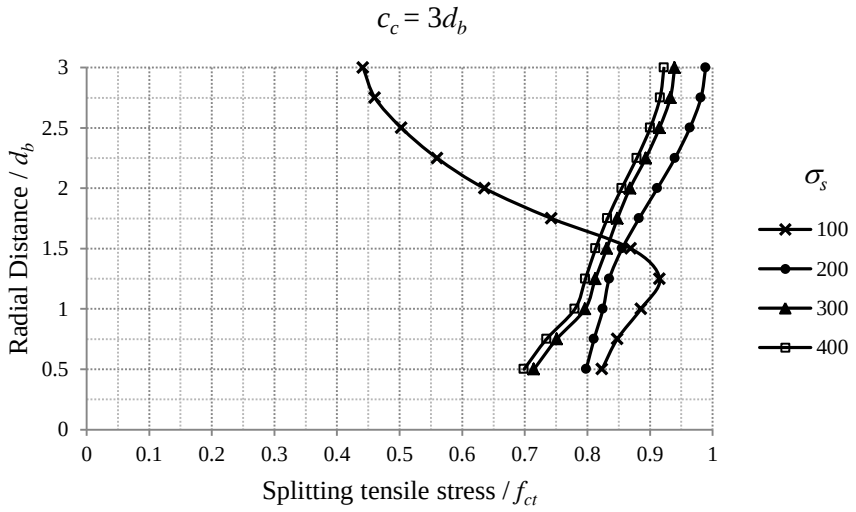
$c_c = 3d_b$
Radial Distance / d_b
Splitting tensile stress / f_{ct}
σ_s
100
200
300
400

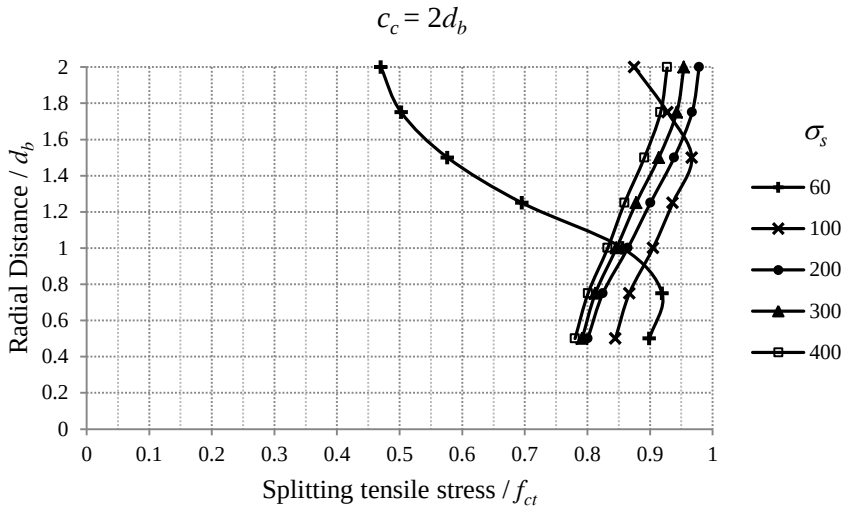

Fig. 6.5 Splitting tensile stresses at section A-A in Fig. 6.4(b) for various concrete covers (l = 15 d_b)

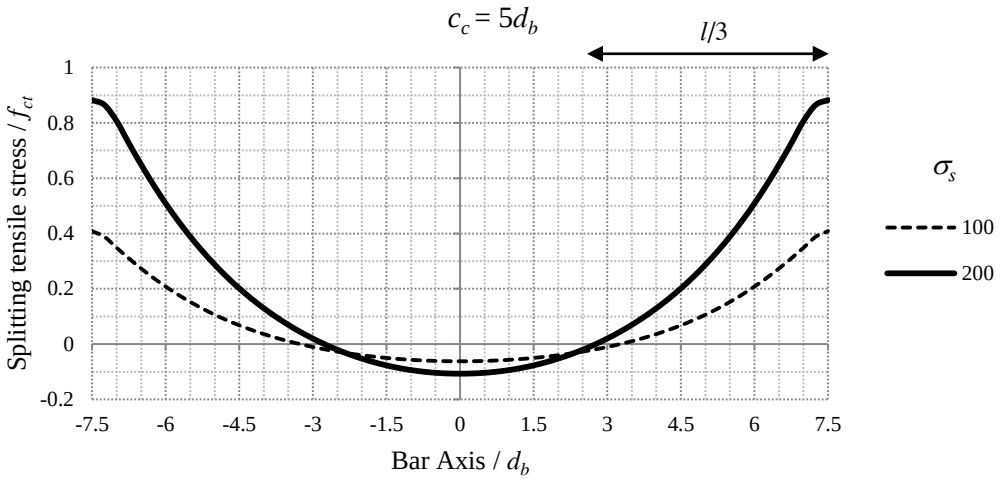

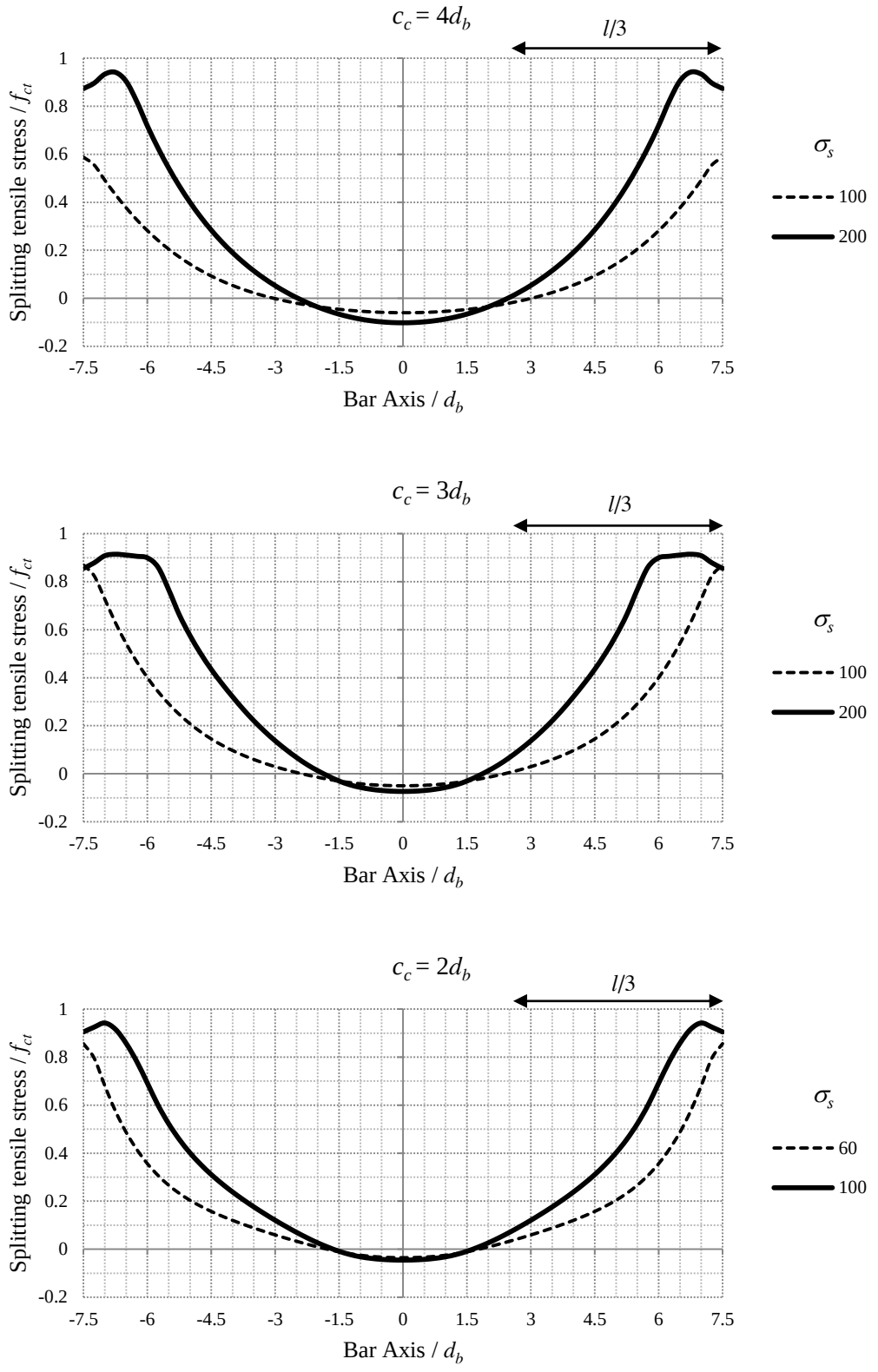

Fig. 6.6 Splitting tensile stresses at section B-B in Fig. 6.4(b) for various concrete covers (l = 15 d_b)

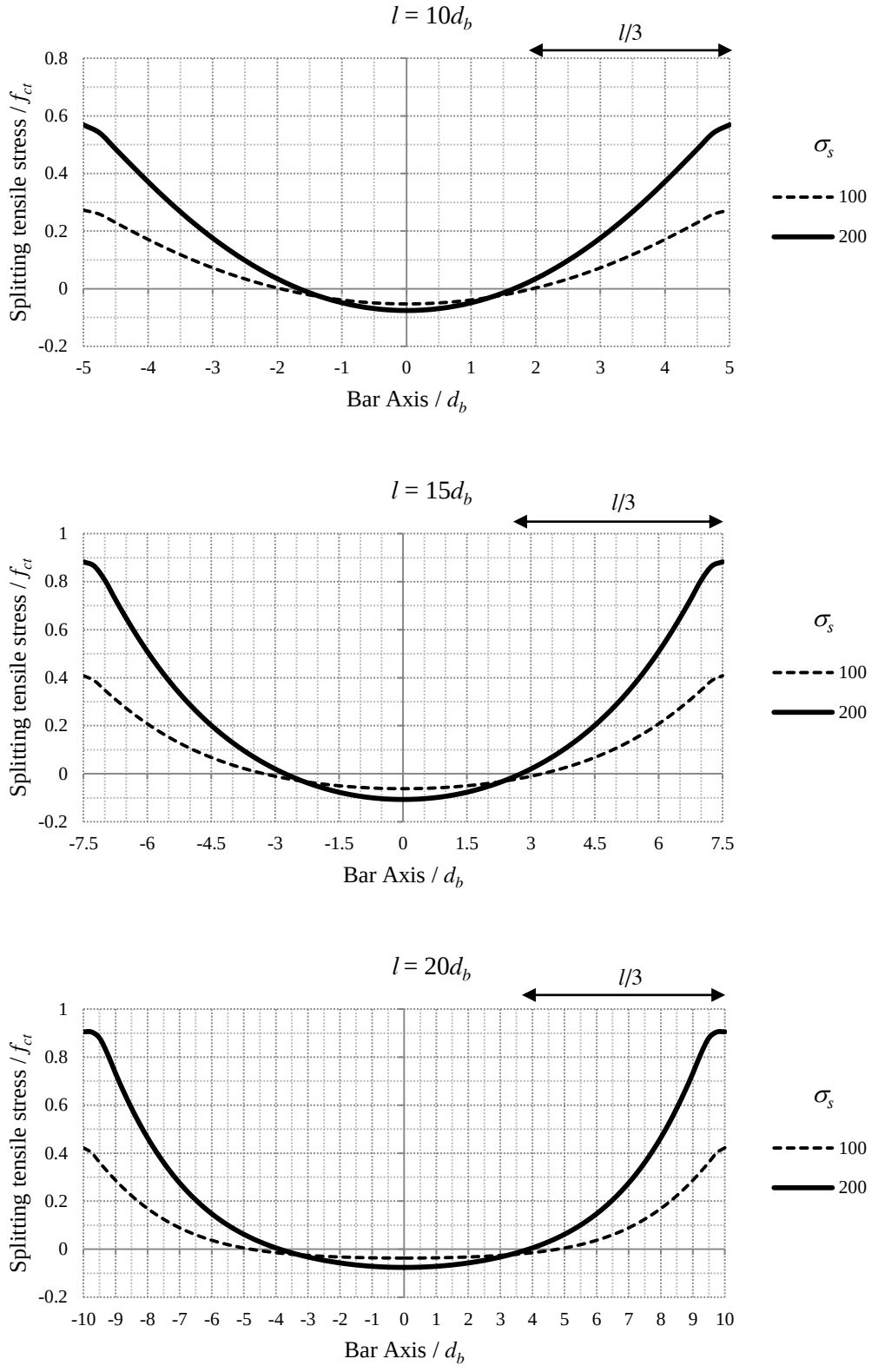

Fig. 6.7 Splitting tensile stresses at section B-B in Fig. 6.4(b) for various lengths of tie member ($c_c = 5d_b$)

The average of splitting tensile stresses in the influenced end region (l/3 from each free end) is computed and shown in Fig. 6.8 for various concrete covers and lengths of tie member. In the calculation of these average stresses, the splitting tensile stress for the cracked elements in the influenced end region is taken equal to the tensile strength of concrete. It can be seen that the effect of the length of the tie member on the average splitting tensile stresses is insignificant and can be ignored for all practice purposes. Therefore, the average splitting tensile stresses in the influenced end region are calculated for various concrete covers based on the model with the tie element length of $10d_b$ and presented in Table 6.5. These results are also presented graphically in Fig. 6.9, which can be used for design purposes.

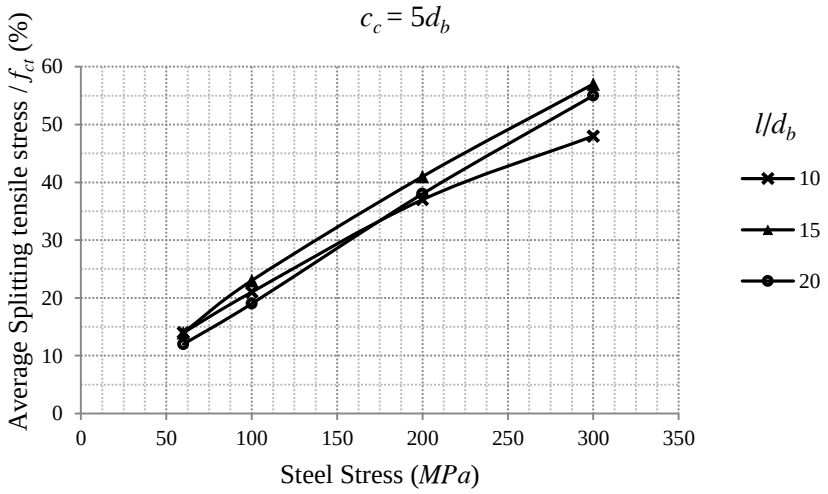

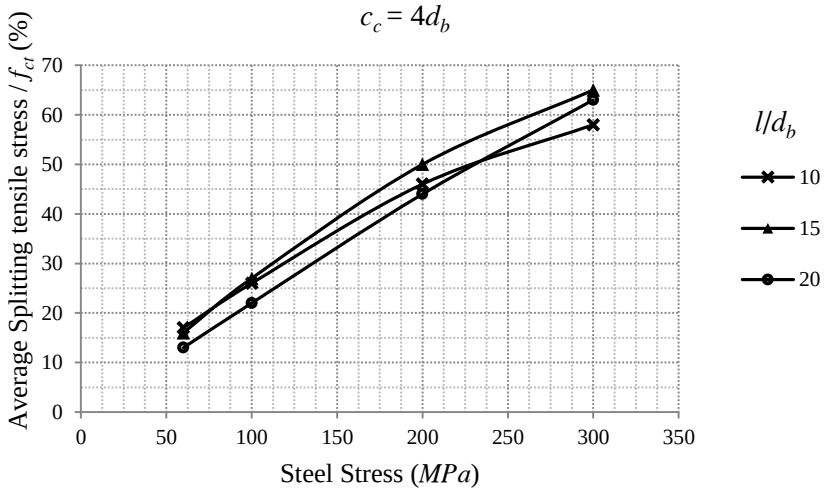

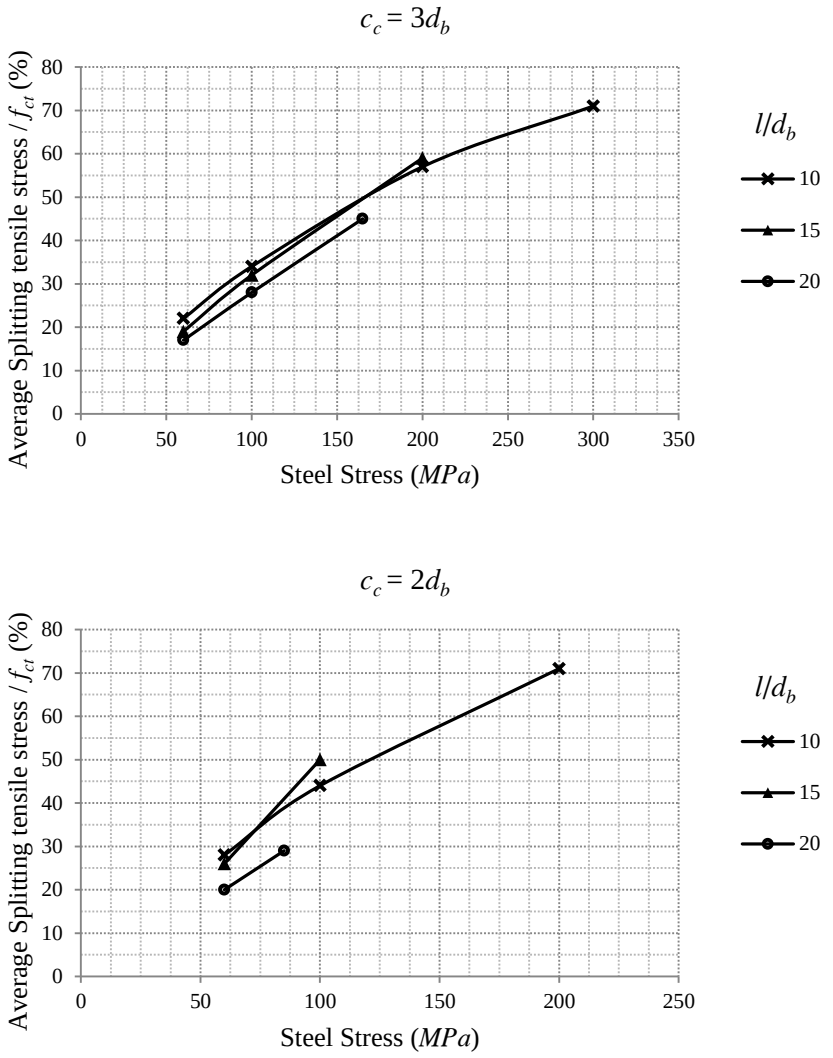

Fig. 6.8 Average splitting tensile stress in influenced end region (*l*/3 from each free end) for various concrete covers and lengths of tie member

Table 6.5 Average splitting tensile stresses in the influenced end region (*l*/3 from each free end) for various concrete covers

	$\sigma_{sp,ave}/f_{ct}$ (%)			
	σ_s (*MPa*)			
c_c/d_b	60	100	200	300
2	28	44	71	
3	22	34	57	71
4	17	26	46	58
5	14	21	37	48

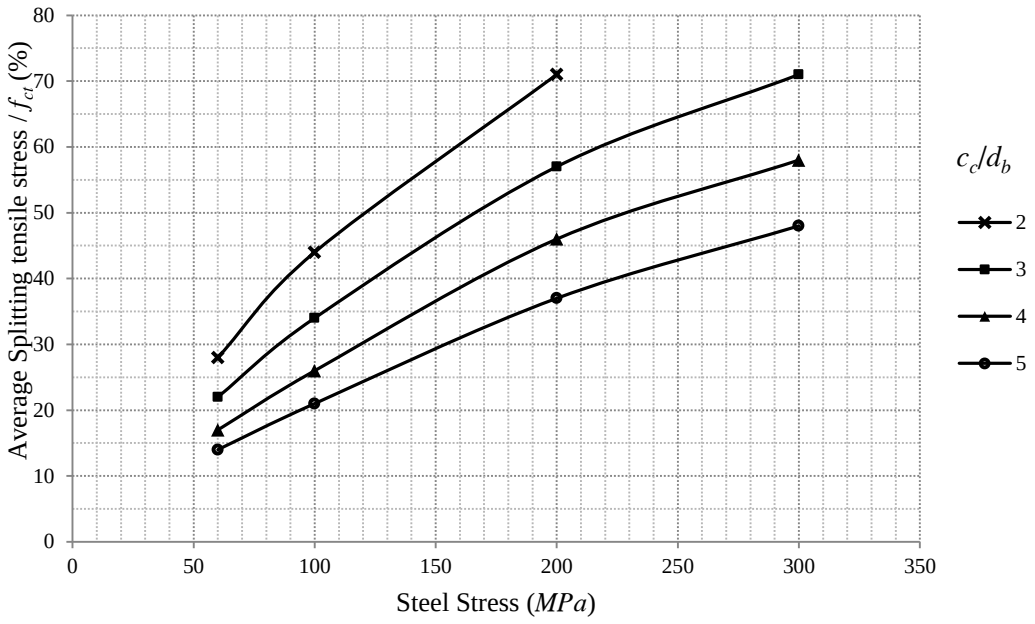

Fig. 6.9 Average splitting tensile stress in the influenced end region (l/3 from each free end) for various concrete covers

5.5 Effect of Longitudinal Splitting Cracks on Bond Strength

As explained in the previous Chapter, a significant reduction of bond strength is observed in the results of the two-way cracking experiments. This reduction is due to the formation of splitting cracks along the axis of reinforcing bars in a two-way loaded system. The reduction of bond strength would result in a higher bond-slip and a wider crack width. To further investigate this phenomenon, a FE parametric study is performed. A prismatic RC tie member is considered as shown in Fig. 6.10(a). Only one-eighth of the tie member, shown in a shaded color, is modeled due to symmetry. The boundary conditions and the meshing of the FE model without and with the longitudinal splitting crack are shown in Fig. 6.10 (a) and (b), respectively. The only difference between these two models is the boundary condition, which is left free to move on one side in Fig. 6.10(c) to simulate the presence of a longitudinal splitting crack. The same modeling technique as in the previous section is used in this model with the only difference of using three dimensional solid elements in this model. The material properties of the steel and concrete are the same as those given in Table 6.4.

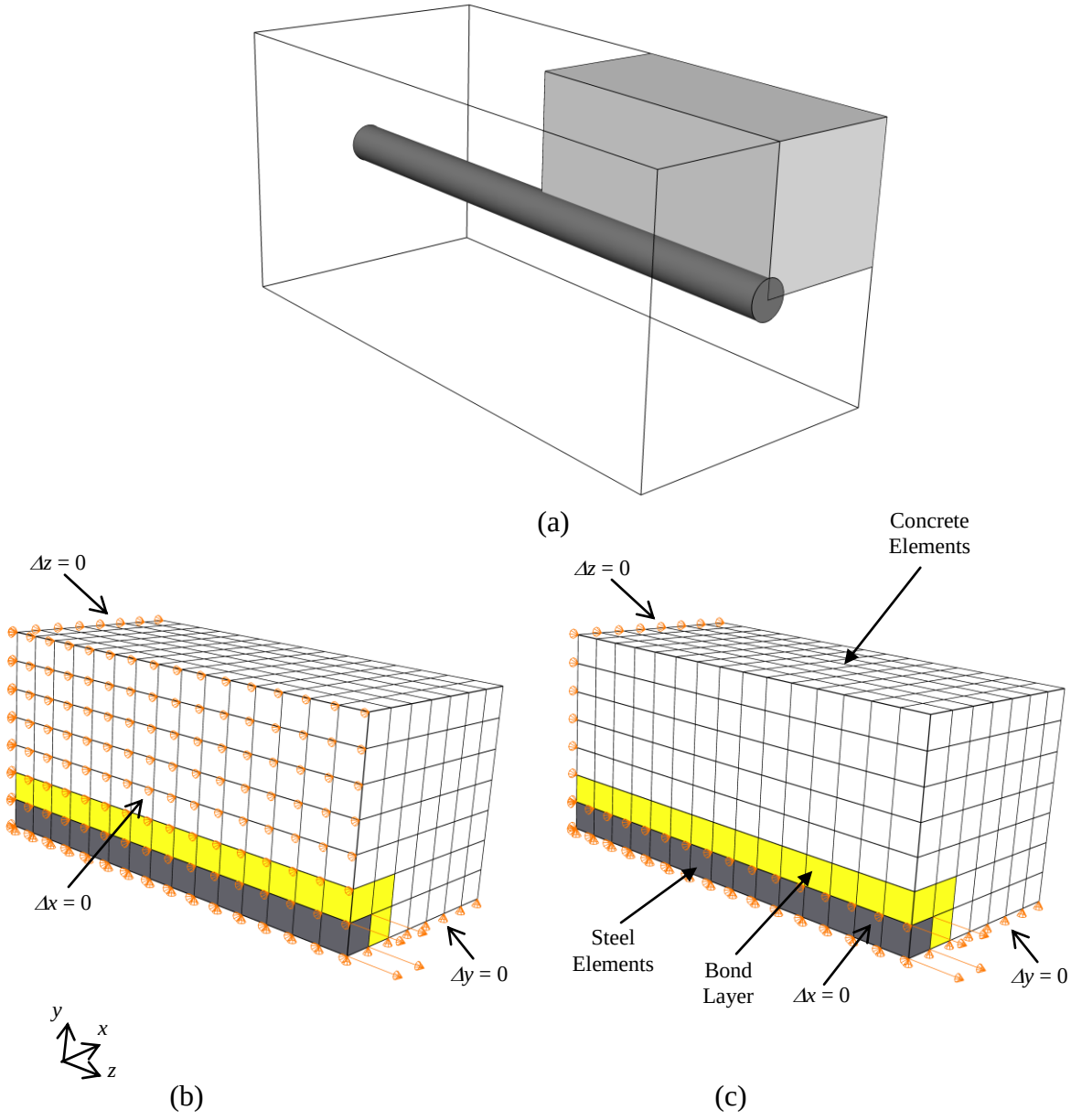

Fig. 6.10 Investigating the effect of longitudinal splitting crack on bond strength, a) prismatic tie member, b) FE model without longitudinal crack, c) FE model with longitudinal crack

In this model, the circular section of the reinforcing bar is approximated with an enclosing square section. For this reason, the modulus of elasticity of steel is modified based on the following equation to make up for the difference in the sectional area without changing the size of the square section,

$$E_{s,eq} = \frac{A_{s,cicular}}{A_{s,square}} E_{s,actual} \tag{6.10}$$

Hence, the actual steel stresses are calculated from the results of the FE model based on either of the following equations,

$$\sigma_{s,actual} = E_{s,actual} \varepsilon_{s,\mathrm{model}} \tag{6.11}$$

$$\sigma_{s,actual} = \frac{A_{s,square}}{A_{s,circular}} \sigma_{s,\mathrm{model}} \tag{6.12}$$

The results of FE analysis for a typical model are shown in Fig. 6.11. Looking at the variation of steel stresses along the bar axis at service load levels, shown in Fig. 6.11(a), it is clear that these stresses are higher for the model with the longitudinal splitting crack. The shear bond stresses are calculated from the variation of steel stresses based on the following equation,

$$\tau_t = \frac{A_s \Delta\sigma}{p_s \Delta x} \tag{6.13}$$

where τ_t = shear bond stress (MPa); A_s = cross sectional area of steel reinforcing bar (mm^2); p_s = perimeter of the cross section of steel reinforcing bar (mm); Δx = finite length of steel reinforcing bar (mm); and $\Delta\sigma$ = variation of steel stress over the length Δx (MPa).

The calculated shear bond stresses for the FE model is shown in Fig. 6.11(b). As expected, the shear bond stresses are significantly reduced for the FE model with the longitudinal splitting crack. The peak shear bond stress reduction factor due to the longitudinal splitting crack (α_{sp}) is defined as,

$$\alpha_{sp} = \frac{\tau_{tp,sp}}{\tau_{tp}} \tag{6.14}$$

where $\tau_{tp,sp}$ = peak shear bond stress in a tie member with longitudinal splitting crack; and τ_{tp} = peak shear bond stress in a tie member without longitudinal splitting crack.

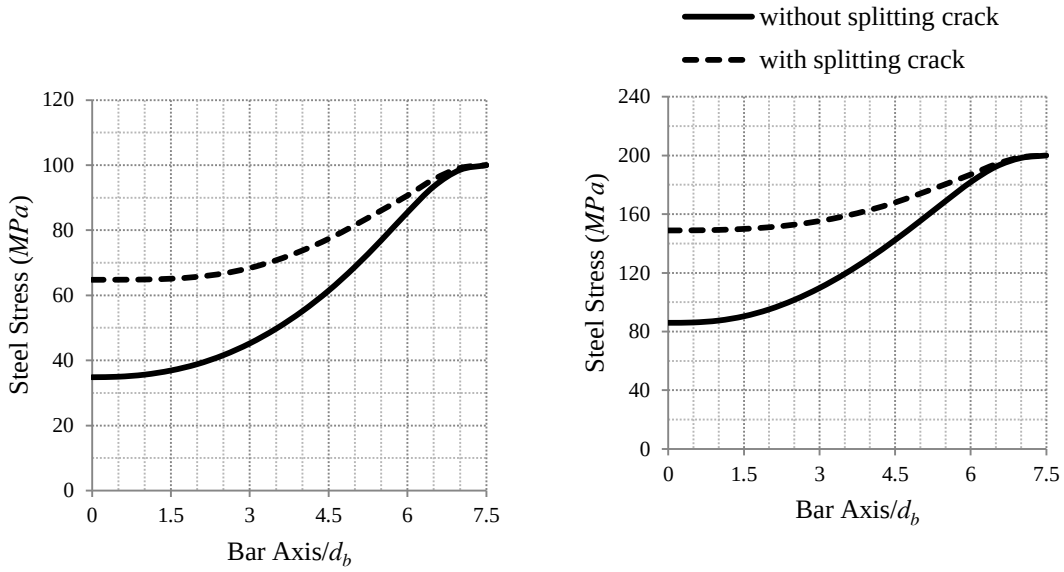

(a)

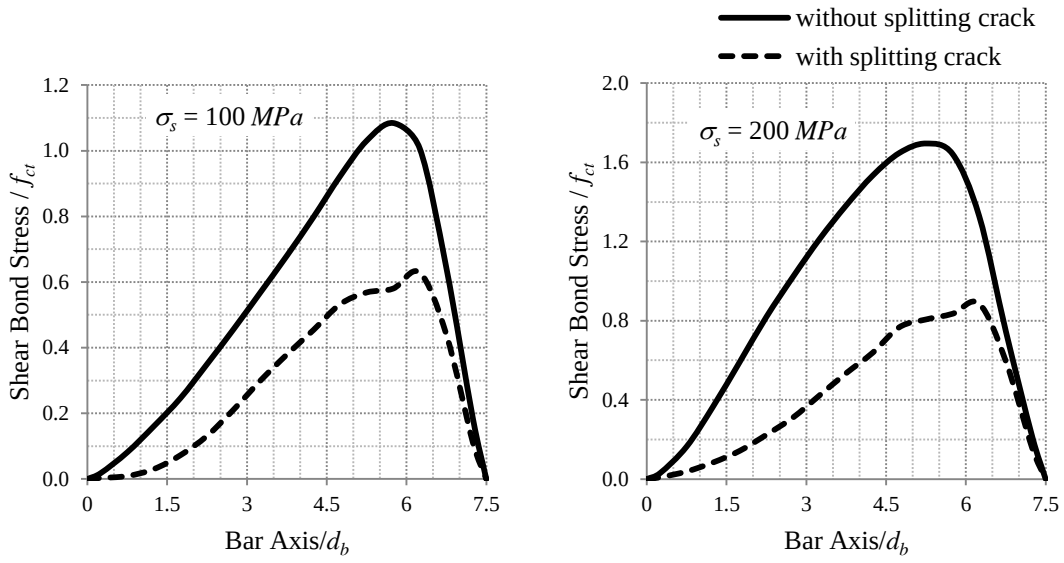

(b)

Fig. 6.11 Effect of longitudinal splitting crack on bond stresses, results of FE model ($c_c = 3d_b$), a) variation of steel stress along the bar axis, b) variation of bond stress along the bar axis

The FE analysis is repeated for several prismatic tie members with various concrete covers and total lengths. The results of the peak bond stress reduction factor are summarized in Table 6.6. Generally, the peak bond stress reduction factor is higher for larger concrete covers and smaller lengths of tie member. The sensitivity to the length of tie member is only observed in the model with the longitudinal splitting crack. Based on these FE results, the peak bond stress reduction factor is on average 55% at the service load level. This value will be used in the proposed model for the prediction of two-way cracking.

Table 6.6 Peak bond stress reduction factor, results of FE parametric analysis for the effect of longitudinal splitting cracks

		$\tau_{tp,sp}/\tau_{tp}$ (%)	
		σ_s (*MPa*)	
c_c/d_b	l/d_b	100	200
2	15	45	60
3	15	58	52
4	15	67	57
4	30	49	46
5	30	58	55

6.6 Calculation of the Steel Strain

One of the main parameters in any crack prediction model is the steel strain at the crack. The crack width is directly proportional to this parameter, and hence, its proper estimation is of great importance for an accurate calculation of the crack width. The steel strain at the crack ($\varepsilon_{s,cr}$) for direct tension cracks in the tested panels can be calculated by the following equation,

$$\varepsilon_{s,cr} = \frac{T}{E_s A_s} = \frac{2T'}{E_s A_s} \tag{6.15}$$

where E_s = modulus of elasticity of steel (*MPa*); A_s = area of steel in tension (mm^2); T = direct tension load (total of side jack loads) (*N*); and T' = direct tension load (each side jack load) (*N*).

For flexural cracks, the maximum steel strain occurs at the mid-span of the panel, which corresponds to the maximum crack width. This strain can be calculated as,

$$\varepsilon_{s,cr} = \frac{\sigma_{s,cr}}{E_s} = \frac{\alpha_e}{E_s} \cdot \frac{M_{\max} y_{st}}{I_{cr,tr}} = \frac{\alpha_e}{E_s} \cdot \frac{M_{\max}\left(d - kd\right)}{I_{cr,tr}} \tag{6.16}$$

where $\sigma_{s,cr}$ = steel stress at the crack (*MPa*); α_e = modular ratio (E_s/E_c); M_{max} = maximum bending moment at mid-span (*N.mm*); y_{st} = distance from neutral axis to the level of tensile reinforcement; $I_{cr,tr}$ = moment of inertia of the transformed cracked section (mm^4); d = effective depth of tensile reinforcement (*mm*); and kd = depth of neutral axis (*mm*).

The maximum bending moment can be calculated from,

$$M_{\max} = \left(\frac{P - s.w.}{2}\right) \times \frac{l_F}{2} = \left(\frac{P - 29000}{2}\right) \times \frac{1800}{2} = 450\left(P - 29000\right) \tag{6.17}$$

where P = center jack load (*N*); *s.w.* = self-weight of panel And attached equipments (*N*); and l_F = span length in flexural direction (*mm*).

The moment of inertia of the transformed cracked section ($I_{cr,tr}$) in Eq. 6.16 can be calculated by,

$$I_{cr,tr} = \frac{b\left(kd\right)^3}{12} + bkd\left(\frac{kd}{2}\right)^2 + \alpha_e A_s \left(d - kd\right)^2 \tag{6.18}$$

where b = section width (*mm*); and A_s = area of steel in tension (mm^2).

As the neutral axis is very close to the bottom layer of reinforcing bars, the effect of these bars are ignored in Eq. 6.18 for simplicity.

The calculated steel strains based on Eqs. 6.15 and 6.16 are summarized in Table 6.7. These calculated steel strains are compared with the experimental data in Fig. 6.12. The estimated strains are in a good range of the experimental data prior to the yield of the steel. It must be

noted that the estimated strains correspond to the monotonic loading condition, and hence, the residual strains due to the repeated loading in the experiments would result in strains higher than the estimated data at the beginning of each loading stage. This deviation would reduce as the load increases to its previously reached maximum level.

It must also be noted that the estimated steel strains correspond to the maximum steel strains at the crack, and hence, most of the experimental data are lower than the estimated strains depending on the distance of the strain gauge to the location of the crack. However, for some of the strain gauges, in spite of a distance between these strain gauges and the location of the cracks, the strain readings are close to the maximum estimated strains. As explained before, this can be an indication of an extreme damage to the bond strength due to the formation of longitudinal splitting cracks in a two-way system.

Table 6.7 Calculation of steel strains at the crack for tested panels

			Direct Tension Cracks	
Panel	E_s (GPa)	A_s (mm^2)	$\varepsilon_{s,cr}$ ($\mu\varepsilon$)	
A	200	3000	$3.33\times10^{-3}T'$	
B	200	2000	$5.00\times10^{-3}T'$	
C	200	3000	$3.33\times10^{-3}T'$	

				Flexural Cracks			
Panel	α_e	b (per bar) (mm)	A_s (per bar) (mm^2)	d (mm)	kd (mm)	$I_{cr,tr}$ (per bar) (mm^4)	$\varepsilon_{s,cr}$ ($\mu\varepsilon$)
A	5.9	300	300	200	43	51448930	$8.08\times10^{-3}P$ -234
B	5.7	300	200	196	35	33911495	$12.21\times10^{-3}P$ -354
C	6.1	200	200	198	43	34420776	$8.76\times10^{-3}P$ -254

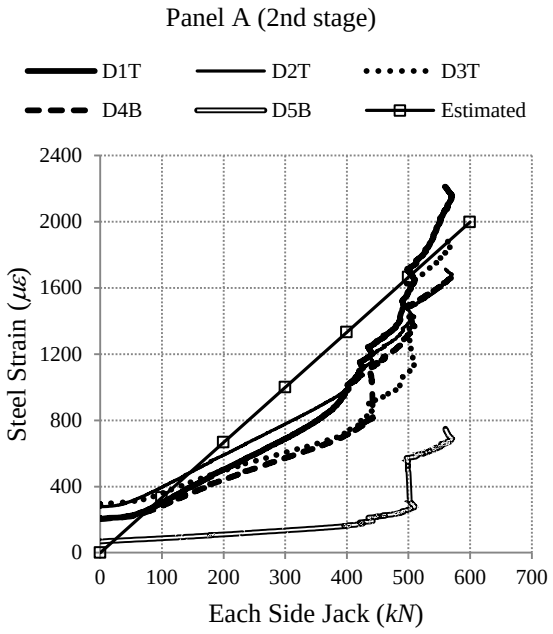
Panel A (2nd stage)
D1T
D2T
D3T
D4B
D5B
Estimated
Steel Strain (με)
Each Side Jack (kN)

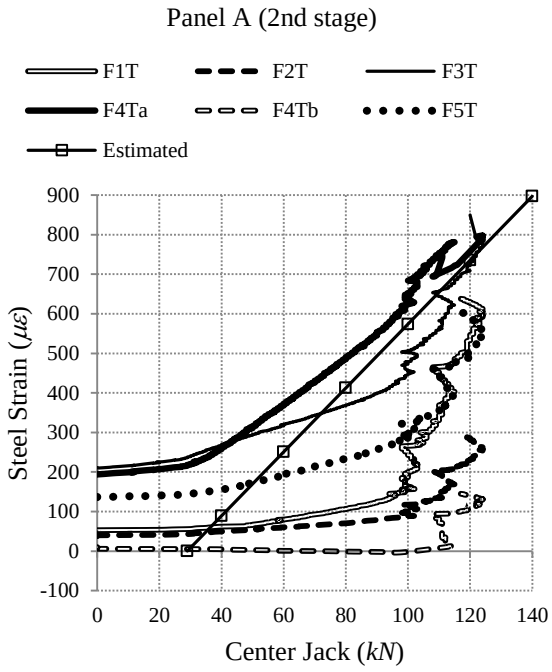
Panel A (2nd stage)
F1T
F2T
F3T
F4Ta
F4Tb
F5T
Estimated
Steel Strain (με)
Center Jack (kN)

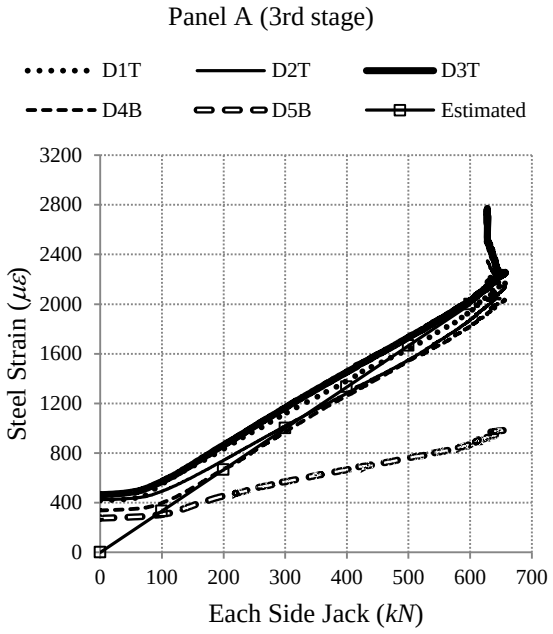
Panel A (3rd stage)
D1T
D2T
D3T
D4B
D5B
Estimated
Steel Strain (με)
Each Side Jack (kN)

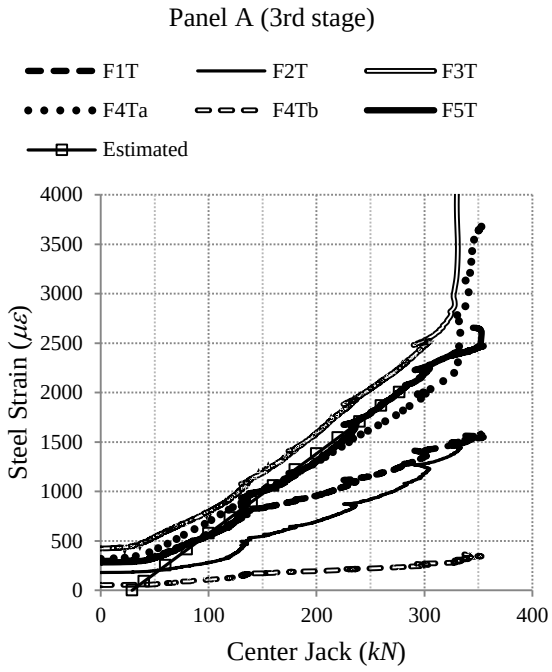
Panel A (3rd stage)
F1T
F2T
F3T
F4Ta
F4Tb
F5T
Estimated
Steel Strain (με)
Center Jack (kN)

(a)

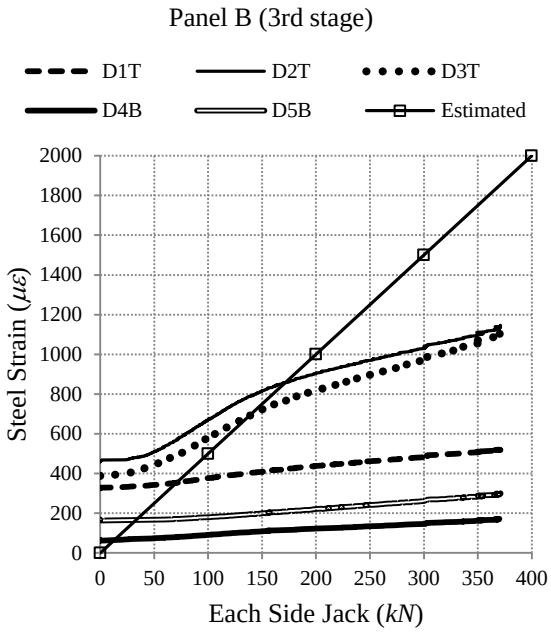
Panel B (3rd stage)
D1T
D2T
D3T
D4B
D5B
Estimated
Steel Strain (με)
Each Side Jack (kN)

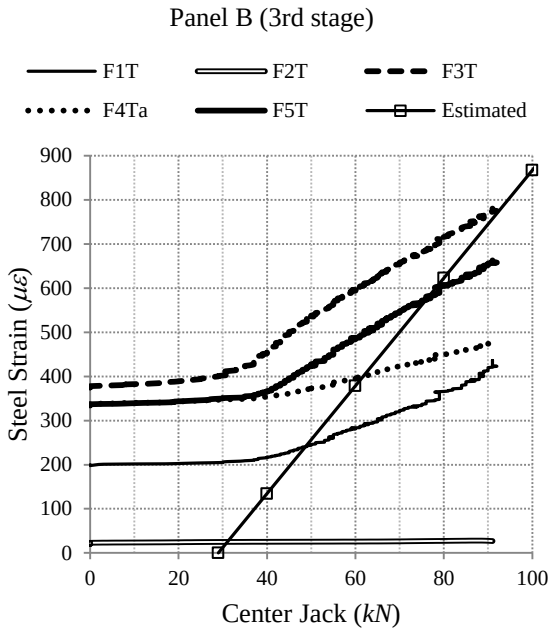
Panel B (3rd stage)
F1T
F2T
F3T
F4Ta
F5T
Estimated
Steel Strain (με)
Center Jack (kN)

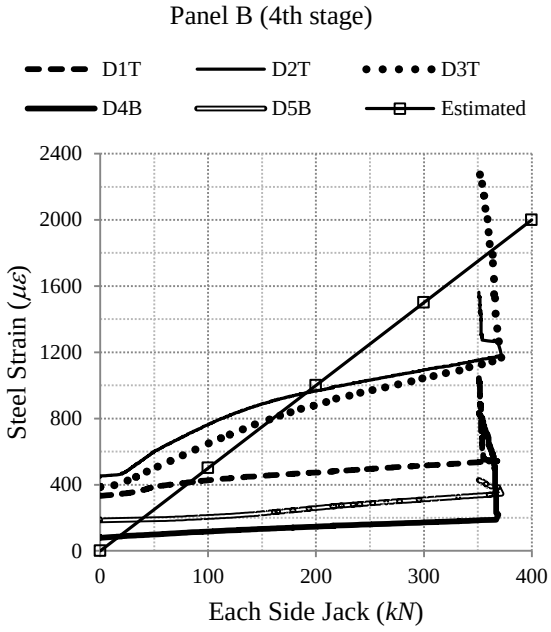
Panel B (4th stage)
D1T
D2T
D3T
D4B
D5B
Estimated
Steel Strain (με)
Each Side Jack (kN)

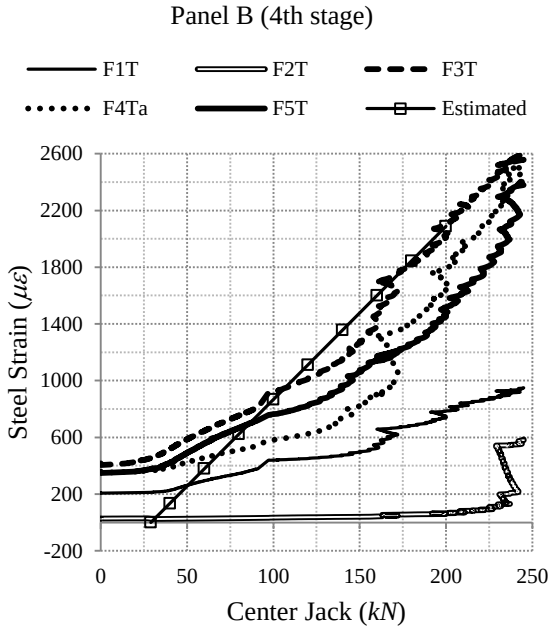
Panel B (4th stage)
F1T
F2T
F3T
F4Ta
F5T
Estimated
Steel Strain (με)
Center Jack (kN)

(b)

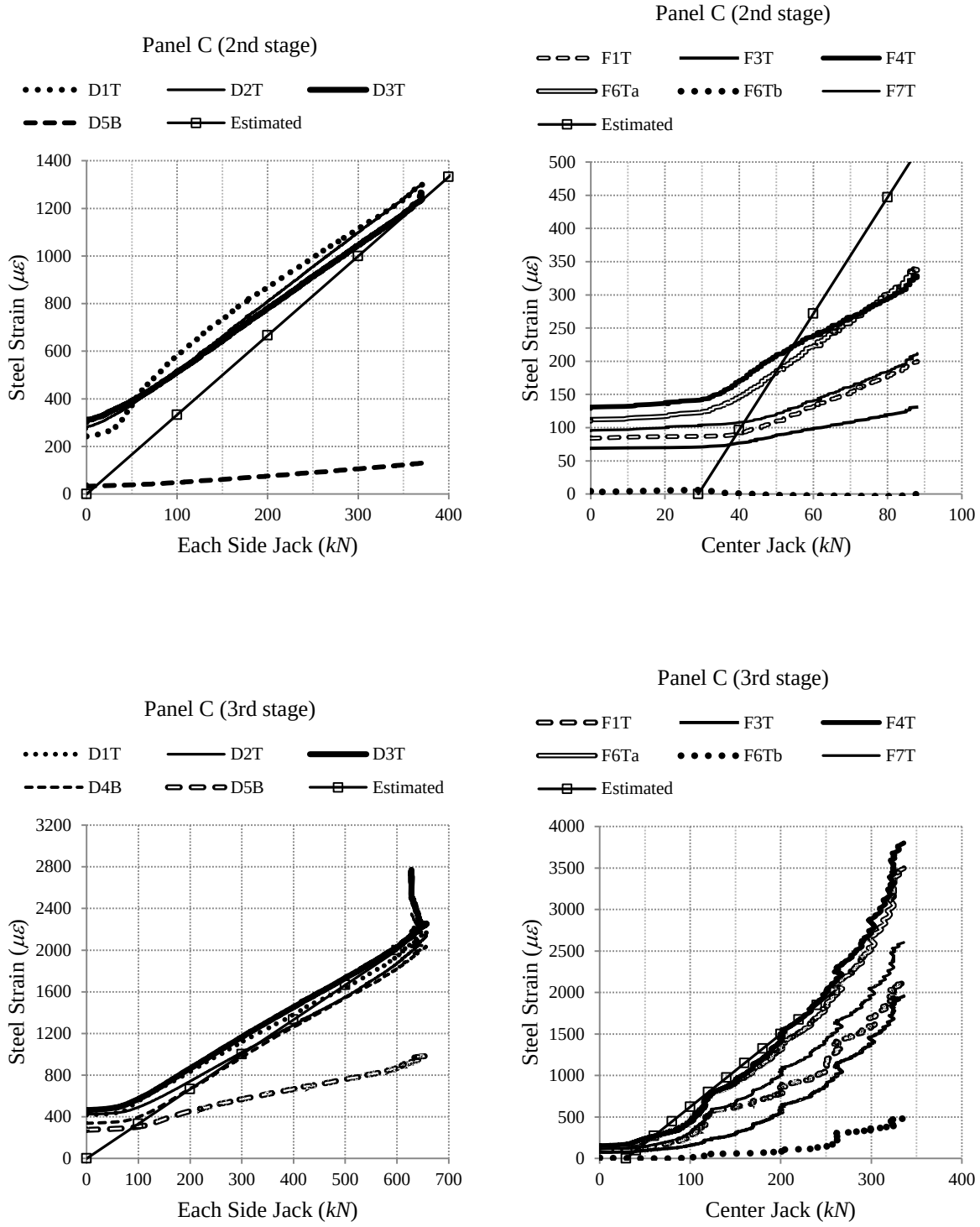

(c)

Fig. 6.12 Comparison of estimated steel strains at the crack and experimental data, a) panel A, b) panel B, c) panel C

6.7 Proposed Crack Prediction Model for Two-Way Loaded Panels

As it is shown earlier in this study, the cracking behaviour of two-way panels is significantly different than that of one-way members. This implies the inadequacy of one-way cracking models for the prediction of cracking in two-way panels. As a result, using the information presented thus far in this study, a new set of equations is proposed for the prediction of orthogonal cracking in two-way panels. These models are presented in the following sections.

6.7.1 Stabilized cracking load

As it is shown in section 6.2, the cracking load in a two-way panel cannot be accurately determined by the one-way cracking models. This inaccuracy can be due to a number of reasons. The main reason is the effect of splitting tensile stresses in reducing the cracking load. Also, the internally restrained shrinkage stresses to some extent can influence the cracking load. Furthermore, improper determination of the effective tension area of concrete can affect the final predictions. In view of this, a new formulation is recommended in which the effect of all various influential parameters is included. For the calculation of the cracking load, the cracks are assumed to form at the location of transverse reinforcement due to a higher stress concentration at these locations. Accordingly, the cracking load can be calculated by,

$$N_{rx} = \left(f_{ctm}(t) - \beta_{spy}\sigma_{spy} - \sigma_{csx} \right) A_{c,efx} \left(1 + \alpha_e \rho_{s,efx} \right) \qquad (6.19)$$

where N_{rx} = stabilized cracking load for cracks normal to direction x (N); $f_{ctm}(t)$ = mean tensile strength of concrete at time t (MPa), β_{spy} = a factor accounting for the average splitting tensile stresses over the effective tension area caused by reinforcement in direction y, σ_{spy} = average splitting tensile stress in the effective end region caused by reinforcement in direction y (MPa), σ_{csx} = concrete tensile stress in direction x due to internally restrained shrinkage (MPa), $A_{c,efx}$ = effective tension area of concrete for the section normal to direction x (mm^2), α_e = modular ratio (E_s/E_c), and $\rho_{s,efx}$ = effective reinforcement ratio in direction x.

In the preceding and all the subsequent equations, the cracking is predicted for cracks that form normal to direction *x*. For the prediction of cracks normal to direction *y*, all the subscripts *x* and *y* must be replaced with each other. The directions *x* and *y* and the corresponding bar diameter and bar spacing designations are depicted in Fig. 6.13. The direction *x* is arbitrarily one of the two orthogonal bar directions.

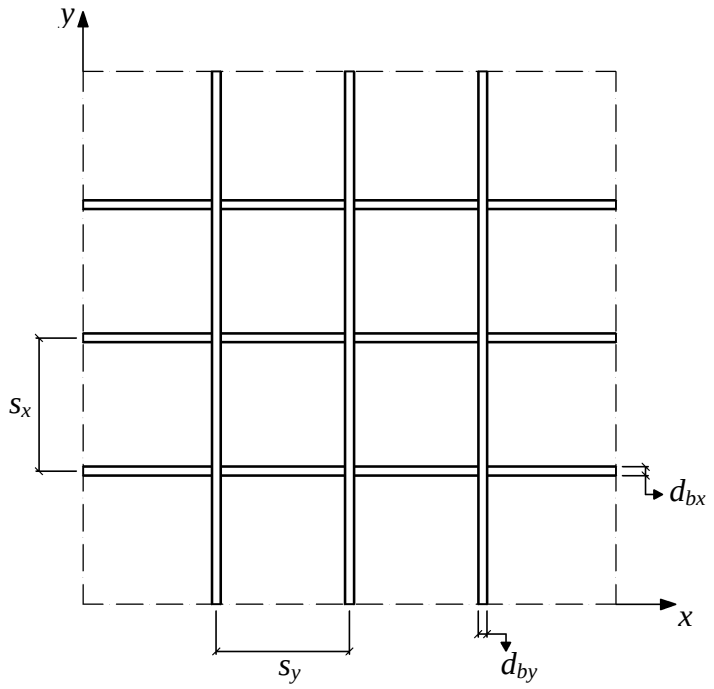

Fig. 6.13 Bar spacing and bar diameter designations

The effective tension area of concrete $A_{c,efx}$ in Eq. 6.19 can be calculated as,

$$A_{c,efx\,(\text{per bar})} = \left(d_{t,efx} - d_{by}\right)s_x \tag{6.20}$$

where $d_{t,efx}$ = depth of effective tension area of concrete (*mm*); d_{by} = diameter of the reinforcing bar in direction *y* (*mm*); and s_x = spacing of reinforcing bars in direction *x* (*mm*).

The depth of effective tension area of concrete $d_{t,efx}$ (previously described in Fig. 2.3) can be calculated as follows,

$$d_{t,efx} = \begin{cases} \text{lesser of } \left(2.5d_{cx}\,,\, 0.5h\right) & \text{for direct tension cracks} \\ k'_{tx}\left(d_x - kd_x\right) + d_{cx} & \text{for flexural cracks} \end{cases} \tag{6.21}$$

where d_{cx} = concrete cover to the center of reinforcing bar in direction x (mm); h = section depth (mm); d_x = effective depth of reinforcement in direction x (mm); kd_x = depth of neutral axis for the section normal to direction x (mm); and k'_{tx} = new factor of effective tension area for the section normal to direction x (based on Fig. 3.40).

In determination of k'_{tx} based on Fig. 3.40 the reinforcement ratio in direction x, ρ_{sx}, can be calculated as,

$$\rho_{sx} = \frac{A_{sx\,(\text{per bar})}}{s_x d_x} = \frac{\frac{1}{4}\pi d_{bx}^2}{s_x d_x} \tag{6.22}$$

where A_{sx} = area of tension reinforcement in direction x (mm^2).

The effective reinforcement ratio $\rho_{s,efx}$ in Eq. 6.19 can be calculated as,

$$\rho_{s,efx} = \frac{A_{sx\,(\text{per bar})}}{A_{c,efx\,(\text{per bar})}} = \frac{\frac{1}{4}\pi d_{bx}^2}{\left(d_{t,efx} - d_{by}\right)s_x} \tag{6.23}$$

Based on the parametric studies presented in section 6.4, the value of the factor β_{spy} in Eq. 6.19 is approximated by the following expression,

$$\beta_{spy} \cong \frac{2}{3} \times \frac{2c_{cy}}{d_{t,efx}} \le \frac{2}{3} \tag{6.24}$$

where c_{cy} = clear concrete cover to the reinforcing bar in direction y (mm).

The average splitting tensile stress in the influenced end region σ_{spy} in Eq. 6.19 can be determined from Fig. 6.9 based on the following definition,

$$\sigma_{spy} = f(f_{ct}, c_{cy}/d_{by}, \sigma_{sy,crx}) \tag{6.25}$$

where $\sigma_{sy,crx}$ = tensile stress in reinforcement in direction *y* when cracking occurs normal to direction *x* (*MPa*).

The concrete stress due to internally restrained shrinkage σ_{csx} in Eq. 6.19 is determined based on the following equation,

$$\sigma_{csx} = \frac{-\varepsilon_{cs}}{50\times10^{-6}}\sigma_{csox} \tag{6.26}$$

where ε_{cs} = total shrinkage strain at the time of cracking (negative value); σ_{csox} = concrete stress in direction *x* due to internally restrained shrinkage based on a total shrinkage strain of 50 $\mu\varepsilon$ (*MPa*).

The base shrinkage induced stress σ_{csox} can be found from Fig. 6.2 based on the following equation,

$$\sigma_{csox} = f(c_{c,eqx}/d_{bx}, \varepsilon_{cso} = 50\times10^{-6}) \tag{6.27}$$

in which,

$$c_{c,eqx} = \sqrt{\frac{s_x d_{t,efx}}{\pi}} - \frac{d_{bx}}{2} \tag{6.28}$$

where $c_{c,eqx}$ = equivalent clear concrete cover to the reinforcing bar in direction *x* (*mm*); and ε_{cso} = base total shrinkage strain.

6.7.2 Minimum and maximum crack spacings

The prediction of the crack spacing in a two-way system is not as straightforward as in a one-way system. A new theory is proposed here for determination of the crack spacing in a two-way system. The minimum crack spacing in a two-way system for cracks normal to one of the main orthogonal axes, axis *x* in this case, is illustrated in Fig. 6.14. The minimum possible crack spacing S^{II}_{minx} is the transfer length needed for the concrete stresses at the location of the transverse reinforcement to reach the tensile strength of concrete. The concrete tensile stress at this section is a combination of bond transferred stresses, splitting tensile stresses, and internally restrained shrinkage stresses. Therefore,

$$\frac{\alpha_{sp}\beta_b\tau_{tpx}S^{II}_{\min x}\pi d_{bx}}{\left(d_{t,efx}-d_{by}\right)s_x}+\beta_{spy}\sigma_{spy}+\sigma_{csx}=f_{ctm}\longrightarrow$$

$$S^{II}_{\min x}=\frac{\left(d_{t,efx}-d_{by}\right)s_x}{\alpha_{sp}\beta_b\tau_{tpx}\pi d_{bx}}\left(f_{ctm}-\beta_{spy}\sigma_{spy}-\sigma_{csx}\right) \tag{6.29}$$

where S^{II}_{minx} = minimum crack spacing for cracks normal to direction *x* under two-way loading condition (*mm*); α_{sp} = peak shear bond stress reduction factor due to splitting crack (taken as 1 for estimation of crack spacing); β_b = average bond stress factor (taken as 0.5); and τ_{tpx} = peak bond stress for reinforcement in direction *x* (*MPa*).

The bond stress reduction factor α_{sp} is assumed to be 1 for estimation of the crack spacing. This is because the splitting cracks are not yet formed in the establishing phase of the crack spacing. The average bond stress factor is assumed to be 0.5 based on the Eq. 3.10. The peak bond stress τ_{tpx} can be determined from Fig. 3.32 based on the following equation,

$$\tau_{tpx}=f\left(f_{ct},c_{c,eqx}/d_{bx},\sigma_{sr2x}\right) \tag{6.30}$$

in which,

$$\sigma_{sr2x} = \frac{N_{rx}}{A_{sx}} \tag{6.31}$$

where σ_{sr2x} = steel stress at crack at cracking load level for reinforcement in direction x (*MPa*).

The calculation of the minimum crack spacing for cracks normal to direction x assuming one-way loading condition, $S^{\mathrm{I}}_{\mathrm{min}x}$, shown in Fig. 6.14, is also needed for determination of the maximum crack spacing. This can be achieved by eliminating the effect of the transverse reinforcement in Eq. 6.29 as follows,

$$S^{\mathrm{I}}_{\mathrm{min}\,x} = \frac{d_{t,efx} s_x}{\alpha_{sp} \beta_b \tau_{tpx} \pi d_{bx}} \left(f_{ctm} - \sigma_{csx} \right) \tag{6.32}$$

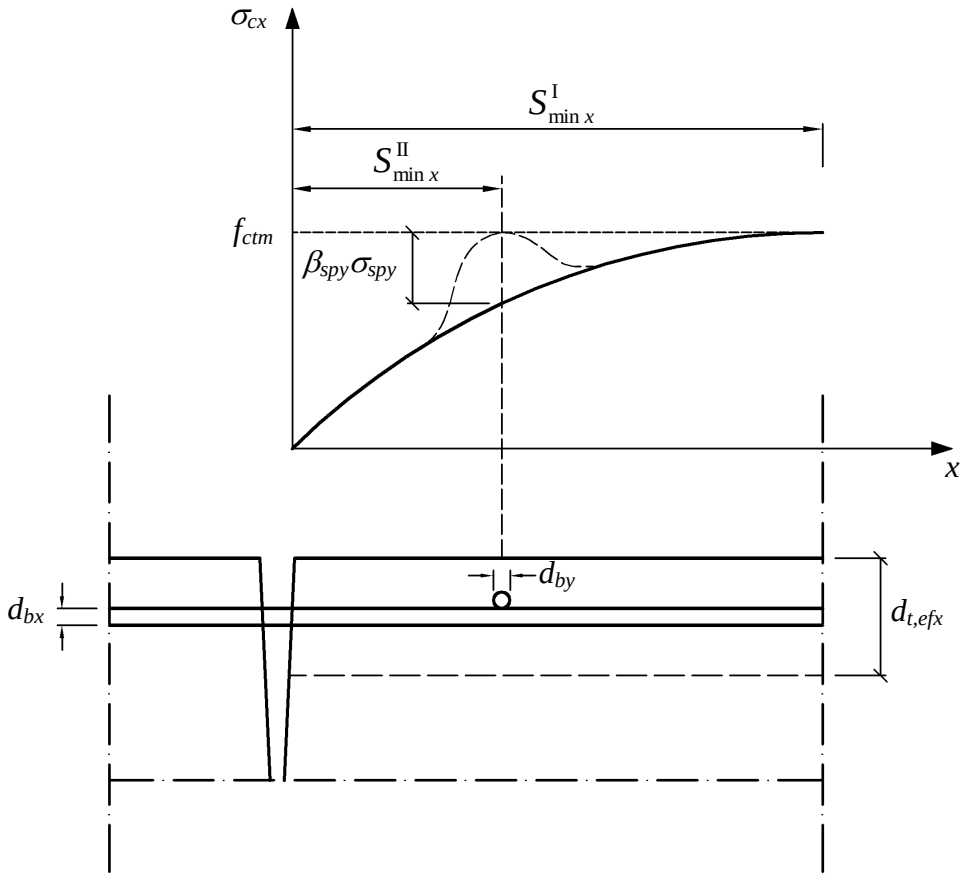

Fig. 6.14 Minimum crack spacing

The maximum crack spacing at stabilized cracking for cracks normal to direction x assuming one-way loading condition, S^{I}_{maxx}, can be twice the minimum crack spacing as follows,

$$S^{I}_{max\,x} = 2S^{I}_{min\,x} \tag{6.33}$$

A hypothesis for determination of the maximum crack spacing in a two-way system for cracks normal to one of the main orthogonal directions, direction x in this case, is depicted in Fig. 6.15. If two cracks form just a distance S^{II}_{maxx} apart, in a way that the section at the mid-way between these two cracks is away from the transverse reinforcement, no further cracking can happen in-between these two cracks. This is because in this case the transfer length is not long enough for the concrete tensile stresses to reach the tensile strength of concrete. Also, this spacing cannot be larger than the maximum crack spacing with the assumption of one-way loading condition at any circumstance. Therefore,

$$S^{II}_{max\,x} = \text{lesser of} \begin{cases} s_y + 2S^{II}_{min\,x} \\ S^{I}_{max\,x} \end{cases} \tag{6.34}$$

where S^{II}_{maxx} = maximum crack spacing at stabilized cracking for cracks normal to direction x under two-way loading condition (low probability) (*mm*); s_y = spacing of reinforcing bars in direction y (*mm*).

Although the abovementioned hypothesis is theoretically valid, such an arrangement of two consecutive cracks can be very rare. In this way, the role of transverse reinforcement is undermined. Therefore, the maximum crack spacing by Eq. 6.34 has a very low probability of occurrence. A higher probability of the maximum crack spacing corresponds with a case in which at least one of the consecutive cracks is at the location of the transverse reinforcement. In this case, the maximum crack spacing is the summation of the spacing of the transverse reinforcing bars and the minimum crack spacing. This maximum crack spacing should not be taken lesser than twice the minimum crack spacing under two-way loading condition and greater than the maximum crack spacing with the assumption of one-way loading condition. Therefore,

$$S^{\text{II}}_{\max x} = \text{larger of} \begin{cases} s_y + S^{\text{II}}_{\min x} \\ 2S^{\text{II}}_{\min x} \end{cases} < S^{\text{I}}_{\max x} \tag{6.35}$$

where $S^{\text{II}}_{\max x}$ = maximum crack spacing at stabilized cracking for cracks normal to direction x under two-way loading condition (high probability) (*mm*).

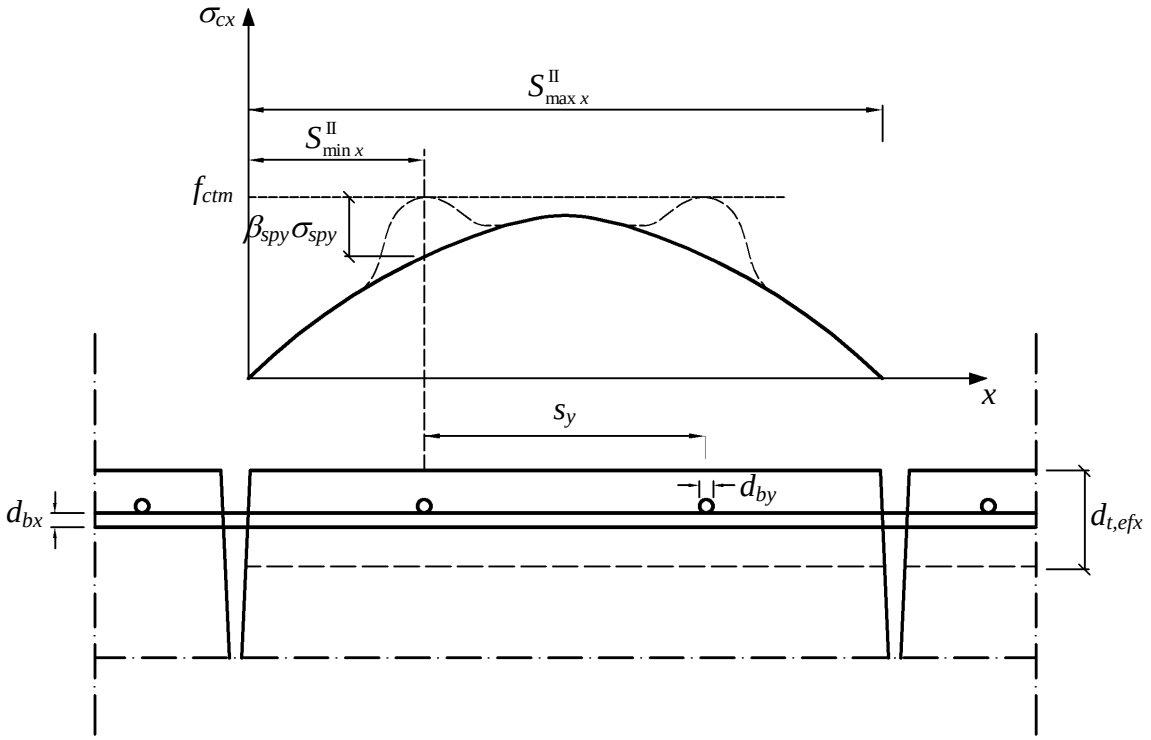

Fig. 6.15 Maximum crack spacing

6.7.3 Maximum crack width

A modified version of Eq. 2.10 is recommended for determination of the maximum crack width. The new equation gives the maximum crack width for loading and reloading of a stabilized cracking system. The resulting crack widths can be conservatively used as the basis of crack control in pre-stabilized cracking system as well. Accordingly,

$$w_{\max x} = \beta_{gx} S^{\text{II}}_{\max x} \left(\varepsilon_{smx} - \varepsilon_{cmx} - \varepsilon_{cs} \right) \tag{6.36}$$

where w_{maxx} = maximum crack width at stabilized cracking for cracks normal to direction x (mm); ε_{smx} = average steel strain within S^{II}_{maxx} for reinforcement in direction x; ε_{cmx} = average concrete strain within S^{II}_{maxx} in direction x; and β_{gx} = crack width gradient factor for cracks normal to direction x.

The crack width gradient factor β_{gx} can be found by,

$$\beta_{gx} = \begin{cases} \dfrac{h - kd_x}{d_x - kd_x} & \text{Flexural cracks} \\ 1 & \text{Direct Tension Cracks} \end{cases} \tag{6.37}$$

The average steel strain ε_{smx} can be calculated from,

$$\varepsilon_{smx} = \varepsilon_{s2x} - \beta_e(\Delta\varepsilon_{sx}) \tag{6.38}$$

where ε_{s2x} = steel strain at crack for reinforcement in direction x; β_e = empirical factor to assess average strain within S^{II}_{maxx} (taken as 0.6 according to section 3.9.2); $\Delta\varepsilon_{sx}$ = total variation of steel strain over transfer length $S^{II}_{maxx}/2$ for reinforcement in direction x.

The total variation of steel strain $\Delta\varepsilon_{sx}$ is estimated by,

$$\Delta\varepsilon_{sx} = \varepsilon_{s2x} - \varepsilon_{sEx} = \frac{\sigma_{s2x} - \sigma_{sEx}}{E_s} = \frac{1}{E_s} \cdot \frac{\alpha_{sp}\beta_b\tau_{tpx}\frac{1}{2}S^{II}_{max\,x}\pi d_{bx}}{\frac{1}{4}\pi d_{bx}^2}$$

$$\rightarrow \Delta\varepsilon_{sx} = \frac{2\alpha_{sp}\beta_b\tau_{tpx}S^{II}_{max\,x}}{E_s d_{bx}} \tag{6.39}$$

where α_{sp} = peak shear bond stress reduction factor due to splitting crack (taken as 0.55 for estimation of the crack width based on the analysis presented in Section 6.5)

In determination of the peak shear bond stress, it must be noted that,

$$\begin{cases} N_{sdx} = 0 \rightarrow \tau_{tpx} = 0 \\ N_{sdx} \geq N_{rx} \rightarrow \tau_{tpx} = f\left(f_{ct}, c_{c,eqx} / d_{bx}, \sigma_{sr2x}\right) \quad \text{from Fig. 3.32} \end{cases} \tag{6.40}$$

where N_{sdx} = tensile force in steel in direction x at crack (kN).

The average concrete strain ε_{cmx} can be calculated as,

$$\varepsilon_{cmx} = \beta_e \varepsilon_{cEx} = \beta_e \frac{\sigma_{cEx}}{E_c} = \beta_e \frac{\alpha_e}{E_s} \cdot \frac{\alpha_{sp}\beta_b \tau_{tpx} \frac{1}{2} S^{\text{II}}_{\max x} \pi d_{bx}}{A_{c,efx(\text{per bar})}} = \beta_e \frac{\alpha_e}{E_s} \cdot \frac{\alpha_{sp}\beta_b \tau_{tpx} \frac{1}{2} S^{\text{II}}_{\max x} \pi d_{bx}}{\frac{1}{4}\pi d_{bx}^2 / \rho_{s,efx}}$$

$$\rightarrow \varepsilon_{cmx} = \beta_e \alpha_e \rho_{s,efx} \Delta\varepsilon_{sx} < \beta_e \varepsilon_{ct} \tag{6.41}$$

where ε_{cEx} = concrete strain at the point of zero slip in direction x; and σ_{cEx} = concrete stress at the point of zero slip in direction x (MPa).

Using Eqs. 6.38 and 6.41, the difference of steel and concrete strains can be written as,

$$\varepsilon_{smx} - \varepsilon_{cmx} = \varepsilon_{s2x} - \beta_e\left(\Delta\varepsilon_{sx}\right) - \beta_e \alpha_e \rho_{s,efx} \Delta\varepsilon_{sx}$$

$$\rightarrow \varepsilon_{smx} - \varepsilon_{cmx} = \varepsilon_{s2x} - \beta_e \Delta\varepsilon_{sx}\left(1 + \alpha_e \rho_{s,efx}\right) \tag{6.42}$$

Substituting Eq. 5.42 into Eq. 5.36 gives,

$$w_{\max x} = \beta_{gx} S^{\text{II}}_{\max x}\left(\varepsilon_{s2x} - \beta_e \Delta\varepsilon_{sx}\left(1 + \alpha_e \rho_{s,efx}\right) - \varepsilon_{cs}\right) \tag{6.43}$$

The $\Delta\varepsilon_{sx}$ can be found from Eq. 6.39.

6.7.4 Verification of the proposed model

To verify the aforementioned proposed model for the prediction of cracking in two-way panels, this model is applied to the tested panels and the results are compared with the experimental data, as follows,

Stabilized cracking load

The stabilized cracking load is calculated for the tested panels using Eq. 6.19. These calculations along with the experimental data are summarized in Table 6.8. Comparing the predicted and the experimental cracking loads, it can be seen that these values are in a good agreement with each other. The excessive errors observed in the one-way cracking model (Table 6.2) are successfully eliminated in the proposed method.

Table 6.8 Calculation of stabilized cracking load for tested panels based on proposed model

Panel	f_{ctm} (MPa)	α_e	ε_{cs} ($\mu\varepsilon$)	d_{bx} (mm)	d_{by} (mm)	c_{cx} (mm)	c_{cy} (mm)	s_x (mm)	s_y (mm)	$\sigma_{sx,cry}$ (MPa)	$\sigma_{sy,crx}$ (MPa)
A	2.97	5.9	-141	19.5	19.5	60	40	300	300	250	100
B	2.79	5.7	-107	16.0	16.0	62	46	300	300	370	150
C	2.79	6.1	-113	19.5	16.0	60	44	300	200	250	100

Panel	σ_{spx}/f_{ct} (%)	σ_{spx} (MPa)	σ_{spy}/f_{ct} (%)	σ_{spy} (MPa)	$d_{t,efx}$ (mm)	ρ_{sy}	k'_{ty}	d_y (mm)	kd_y (mm)	$d_{t,efy}$ (mm)
A	65	1.93	45	1.34	125	0.0050	0.34	200	43	103
B	65	1.81	45	1.26	125	0.0034	0.21	196	35	88
C	65	1.81	35	0.98	125	0.0051	0.34	198	43	105

Panel	β_{spx}	β_{spy}	$A_{c,efx}$ (per bar) (mm^2)	$A_{c,efy}$ (per bar) (mm^2)	$c_{c,eqx}$ (mm)	$c_{c,eqy}$ (mm)	σ_{csox} (MPa)	σ_{csoy} (MPa)	σ_{csx} (MPa)	σ_{csy} (MPa)
A	0.67	0.43	31650	25091	100	90	0.10	0.12	0.28	0.34
B	0.67	0.49	32700	21542	101	84	0.10	0.10	0.21	0.21
C	0.67	0.47	32700	17019	100	74	0.10	0.12	0.23	0.27

Panel	N_{rx} (per bar) (kN)	T_r (kN)	N_{ry} (per bar) (kN)	P_r (kN)	Experiment T_r (kN)	Experiment P_r (kN)	Error (%) for T_r	Error (%) for P_r
A	71	707	36	103	756	92	-7	12
B	66	662	31	92	708 to 744	88 to 105	-7 to -11	5 to -12
C	73	726	24	97	612 to 738	86	19 to -2	13

Minimum and maximum crack spacings

The proposed model for calculation of the crack spacing explained in Section 6.7.2 is also applied to the tested panels. The results are summarized in Table 6.9. The theoretical results are generally in an acceptable range of the experimental results. It must be noted that the experimental results are the minimum and the maximum observed spacings of cracks and they do not represent the absolute minimum and maximum possible crack spacings. Therefore, these observed results are expected to be within the range of the theoretical minimum and maximum crack spacings. This criterion is met for all the calculated spacings, except a marginal disagreement for one case in panel B pertaining to the maximum spacing of the direct tension cracks. This small discrepancy is quite acceptable for such a limited test data.

Table 6.9 Calculation of maximum spacing of cracks at stabilized cracking for tested panels based on proposed model

Panel	α_{sp}	β_b	σ_{sr2x} (MPa)	σ_{sr2y} (MPa)	$c_{c,eqx}/d_{bx}$ (mm)	$c_{c,eqy}/d_{by}$ (mm)	τ_{tpx}/f_{ct}	τ_{tpy}/f_{ct}	τ_{tpx} (MPa)	τ_{tpy} (MPa)	S^{II}_{minx} (mm)	S^{II}_{miny} (mm)
A	1	0.5	236	120	5.1	4.6	3.4	2.1	10.10	6.24	217	177
B	1	0.5	331	155	6.3	5.2	4.3	2.5	12.00	6.98	212	168
C	1	0.5	242	120	5.1	4.6	3.4	2.1	9.49	5.86	237	152

					Low Probability		High Probability		Experiment @ D3 axis			
Panel	S^{I}_{minx} (mm)	S^{I}_{miny} (mm)	S^{I}_{maxx} (mm)	S^{I}_{maxy} (mm)	S^{II}_{maxx} (mm)	S^{II}_{maxy} (mm)	S^{II}_{maxx} (mm)	S^{II}_{maxy} (mm)	S^{II}_{minx} (mm)	S^{II}_{miny} (mm)	S^{II}_{maxx} (mm)	S^{II}_{maxy} (mm)
A	326	426	652	852.9	652	733.07	517	477	295	200	430	414
B	320	387	641	774.3	641	724.48	512	468	260	270	750	540
C	331	358	662	716.4	662	716.36	474	452	250	300	315	350

Minimum and maximum crack widths

Equation 6.43 is applied to the tested panels for determination of the maximum crack width and the results are summarized in Table 6.10. The predicted crack widths of this model will be compared with the experimental data in Section 6.8.6.

Table 6.10 Calculation of maximum crack width for tested panels based on proposed model

Direct Tension Cracks

Panel	β_{qx}	S^{II}_{maxx} (mm)	N_{rx} (per bar) (kN)	T_r (kN)	σ_{sr2x} (MPa)	$c_{c,eqx}/d_{bx}$ (mm)	τ_{tpx}/f_{ct}	τ_{tpx} (MPa)	β_e	α_{sp}	β_b	d_{bx} (mm)
A	1	517	71	353	236	5.1	3.4	10.10	0.6	0.55	0.5	19.5
B	1	512	66	331	331	6.3	4.3	12.00	0.6	0.55	0.5	16.0
C	1	474	73	363	242	5.1	3.4	9.49	0.6	0.55	0.5	19.5

Panel	E_c (MPa)	E_s (GPa)	$\Delta\varepsilon_{sx}$ ($\mu\varepsilon$)	$A_{c,efx}$ (per bar) (mm^2)	$\rho_{s,efx}$	α_e	ε_{cmx} ($\mu\varepsilon$)	$\beta_e\varepsilon_{ct}$ ($\mu\varepsilon$)	ε_{cs} ($\mu\varepsilon$)	w_{maxx} ($N_{sd}=0$) (mm)	w_{maxx} ($N_{sd}=N_{rx}$) (mm)
A	34000	200	736	31650	0.0094	5.9	24	52	-141	0.07	0.44
B	35000	200	1056	32700	0.0061	5.7	22	48	-107	0.06	0.57
C	33000	200	634	32700	0.0091	6.1	21	51	-113	0.05	0.44

Flexural Cracks

Panel	β_{qy}	S^{II}_{maxy} (mm)	N_{ry} (per bar) (kN)	P_r (kN)	σ_{sr2y} (MPa)	$c_{c,eqy}/d_{by}$ (mm)	τ_{tpy}/f_{ct}	τ_{tpy} (MPa)	β_e	α_{sp}	β_b	d_{by} (mm)
A	1.32	477	36	103	120	4.6	2.1	6.24	0.6	0.55	0.5	19.5
B	1.34	468	31	92	155	5.2	2.5	6.98	0.6	0.55	0.5	16.0
C	1.34	452	24	97	120	4.6	2.1	5.86	0.6	0.55	0.5	16.0

Panel	E_c (MPa)	E_s (GPa)	$\Delta\varepsilon_{sy}$ ($\mu\varepsilon$)	$A_{c,efy}$ (per bar) (mm^2)	$\rho_{s,efy}$	α_e	ε_{cmy} ($\mu\varepsilon$)	$\beta_e\varepsilon_{ct}$ ($\mu\varepsilon$)	ε_{cs} ($\mu\varepsilon$)	w_{maxy} ($N_{sd}=0$) (mm)	w_{maxy} ($N_{sd}=N_{ry}$) (mm)
A	34000	200	419	25091	0.0119	5.9	18	52	-141	0.09	0.30
B	35000	200	561	21542	0.0093	5.7	18	48	-107	0.07	0.33
C	33000	200	455	17019	0.0118	6.1	20	51	-113	0.07	0.25

6.8 Comparison of Various Crack Prediction Models

In this section, the accuracy of several well-known crack prediction models in predicting the cracking behaviour of a two-way system is investigated. Most of these models, which are introduced in Chapter 2, are the basis for the crack control recommendations of various design codes. All of these models are applied to the tested panels and their results are compared with the experimental data. The results of the proposed model for the maximum crack width, calculated in the previous section, are also included for comparison.

6.8.1 CEB MC90 model

The maximum crack spacing for the tested panels is calculated based on the Eq. 2.9 recommended by CEB MC90 (1990). The effective tension area of concrete ($A_{c,ef}$) in this equation is calculated according to Fig. 2.3 and Eq. 2.3 for direct tension and flexural cracks. These calculations are summarized in Table 6.11. Also shown in this Table, the CEB predicted values are compared with the experimental observations. The CEB model overestimates the maximum crack spacing for direct tension cracks. This is mainly because the splitting tensile stresses are not considered in the formulations. It is also clear that the one-way formula could not reflect the effect of different reinforcing bar spacings in panels A and C. This shows the incapability of the one-way formulation in the prediction of two-way cracks. Additionally, the CEB model underestimates the maximum crack spacing for flexural cracks. This seems to be caused by an underestimation of the effective tension area of concrete for flexural cracks.

Table 6.11 Maximum crack spacing, comparison of CEB model and experimental data

	Direct Tension Cracks					Flexural Cracks							
	CEB			Experiment		CEB						Experiment	
Panel	ϕ_s (mm)	$A_{c,ef}$ (per bar) (mm^2)	S_{max} (mm)	S_{max} (@D3 Axis) (mm)	Error (%)	ϕ_s (mm)	d (mm)	kd (mm)	$d_{t,ef}$ (mm)	$A_{c,ef}$ (per bar) (mm^2)	S_{max} (mm)	S_{max} (@D3 Axis) (mm)	Error (%)
A	19.5	37500	677	430	57	19.5	200	43	69	20702	374	414	-10
B	16.0	37500	833	750	11	16.0	196	35	72	21498	478	540	-12
C	19.5	37500	677	315	115	16.0	198	43	69	13780	306	350	-13

The crack widths are calculated based on the Eq. 2.10. These calculations are summarized in Fig. 6.12 for the direct tension and flexural cracks. Repeated loading condition is assumed in these calculations. One obvious error in the Eq. 2.10 is that the shrinkage strain is multiplied by the transfer length ($l_{s,max}$) instead of the crack spacing. The transfer length changes from a zero value at the beginning of the loading to its maximum value at the stabilized cracking load, which is the maximum crack spacing. Therefore, at the pre-stabilized cracking stage the effect of shrinkage strain is underestimated due to smaller values of the transfer length. The predicted crack widths of this model will be compared with the experimental data in Section 6.8.6.

Table 6.12 Crack width calculations based on CEB MC90 model

Direct Tension Cracks

Panel	ϕ_s (mm)	ε_{cs} ($\mu\varepsilon$)	ε_{s2} ($\mu\varepsilon$)	f_{ctm} (mm)	$A_{c,ef}$ (per bar) (mm^2)	α_e	$\rho_{s,ef}$	N_r (per bar) (kN)	T'_r (kN)
A	19.5	-141	$3.33\times10^{-3}T'$	2.97	37500	5.9	0.008	117	583
B	16.0	-107	$5.00\times10^{-3}T'$	2.79	37500	5.7	0.005	108	539
C	19.5	-113	$3.33\times10^{-3}T'$	2.79	37500	6.1	0.008	110	548

	pre-stabilized (repeated loading)				post-stabilized (repeated loading)				
Panel	τ_{bk} (MPa)	$l_{s,max}$ (mm)	β_e	w_k (mm)	τ_{bk} (MPa)	$l_{s,max}$ (mm)	ε_{sr2} ($\mu\varepsilon$)	β_e	w_k (mm)
A	4.01	$1.54\times10^{-3}T'$	0.6	$2.05\times10^{-12}T'^2+2.17\times10^{-7}T'$	5.35	677	1944	0.38	$2.25\times10^{-6}T'-0.40$
B	3.77	$2.06\times10^{-3}T'$	0.6	$4.12\times10^{-12}T'^2+2.21\times10^{-7}T'$	5.02	833	2695	0.38	$4.17\times10^{-6}T'-0.76$
C	3.77	$1.64\times10^{-3}T'$	0.6	$2.18\times10^{-12}T'^2+1.85\times10^{-7}T'$	5.02	677	1828	0.38	$2.25\times10^{-6}T'-0.39$
	$T' < T'_r$			$T' < T'_r$	$T' > T'_r$				$T' > T'_r$

Flexural Cracks

Panel	ϕ_s (mm)	ε_{cs} ($\mu\varepsilon$)	ε_{s2} ($\mu\varepsilon$)	f_{ctm} (mm)	$A_{c,ef}$ (per bar) (mm^2)	α_e	$\rho_{s,ef}$	N_r (per bar)	P_r (kN)
A	19.5	-141	$8.08\times10^{-3}P-234$	2.97	20702	5.9	0.0145	67	167
B	16.0	-107	$12.21\times10^{-3}P-354$	2.79	21498	5.7	0.009	63	158
C	16.0	-113	$8.76\times10^{-3}P-254$	2.79	13780	6.1	0.0145	42	148

	pre-stabilized (repeated loading)				post-stabilized (repeated loading)				
Panel	τ_{bk} (MPa)	$l_{s,max}$ (mm)	β_e	w_k (mm)	τ_{bk} (MPa)	$l_{s,max}$ (mm)	ε_{sr2} ($\mu\varepsilon$)	β_e	w_k (mm)
A	4.01	$3.62\times10^{-3}P-105$	0.6	$1.17\times10^{-11}P^2-1.68\times10^{-7}P$	5.35	374	1112	0.38	$3.02\times10^{-6}P-0.19$
B	3.77	$4.92\times10^{-3}P-143$	0.6	$2.40\times10^{-11}P^2-8.67\times10^{-7}P$	5.02	478	1579	0.38	$5.83\times10^{-6}P-0.40$
C	3.77	$3.42\times10^{-3}P-99$	0.6	$1.20\times10^{-11}P^2-3.10\times10^{-7}P$	5.02	306	1046	0.38	$2.68\times10^{-6}P-0.17$
	$P < P_r$			$P < P_r$	$P > P_r$				$P > P_r$

6.8.2 BS 8007-1987 model

The recommendations of the BS 8007 Code (1987) is explained in Section 2.4. Based on this Code, crack control can be achieved by either limiting the steel stress or limiting the directly calculated crack width. In the former approach the limiting stress is generalized for all types of structural geometries, reinforcement layouts and loading conditions. This method by itself cannot be a proper solution for crack control as it fails to consider the effect of other influential parameters, such as, concrete cover, loading condition, bar spacing, shrinkage strain, etc. Here,

the accuracy of the second approach is investigated. Hence, the crack widths are calculated based on the Eqs. 2.14 and 2.17 for the flexural and direct tension cracks, respectively. These calculations are summarized in Table 6.13. The predicted crack widths of this model will be compared with the experimental data in Section 6.8.6.

Table 6.13 Crack width calculations based on BS 8007-1987 Code

	Direct Tension Cracks			
Panel	a_{cr} (mm)	ε_1 ($\varepsilon_{s,cr}$) ($\mu\varepsilon$)	ε_2 ($\mu\varepsilon$)	w (mm)
A	60	$3.33\times10^{-3}T'$	833	$0.60\times10^{-6}T'$-0.15
B	62	$5.00\times10^{-3}T'$	1250	$0.93\times10^{-6}T'$-0.23
C	60	$3.33\times10^{-3}T'$	833	$0.60\times10^{-6}T'$-0.15

	Flexural Cracks								
Panel	β_g	a_{cr} (mm)	c_{min} (mm)	kd (mm)	$I_{cr,tr}$ (per bar) (mm^4)	$\varepsilon_{s,cr}$ ($\mu\varepsilon$)	ε_1 ($\mu\varepsilon$)	ε_2 ($\mu\varepsilon$)	w (mm)
A	1.32	40	40	43	51448930	$8.08\times10^{-3}P$-234	$1.07\times10^{-2}P$-309	455	$1.28\times10^{-6}P$-0.09
B	1.34	46	46	35	33911495	$12.21\times10^{-3}P$-354	$1.63\times10^{-2}P$-473	718	$2.25\times10^{-6}P$-0.16
C	1.34	44	44	43	34420776	$8.76\times10^{-3}P$-254	$1.17\times10^{-2}P$-339	460	$1.54\times10^{-6}P$-0.11

6.8.3 Gergely-Lutz model

The Gergely-Lutz (1968) model is one of the most widely used crack prediction models in various design codes, including, ACI318-95 (1995), CSA A23.3-04 (2004), ACI 350-01 (2001), and an alternative method in ACI 350-06 (2006). This model has been developed based on the statistical analysis of a large number of test results from different sources. The model is only aimed to predict flexural cracks. The inapplicability of this model to direct tension cracks is a major drawback in design recommendations that are solely created based on this model. The Gergely-Lutz equation, Eq. 2.21, is applied to the tested panels and the results are summarized in Table 6.14. The predicted crack widths of this model will be compared with the experimental data in Section 6.8.6.

Table 6.14 Crack width calculations based on Gergely-Lutz model

	Flexural Cracks				
Panel	β_g	d_c (mm)	A_e (mm^2)	$f_{s,cr}$ (MPa)	$w_{t,max}$ (mm)
A	1.32	50	30000	$1.62\times10^{-3}P$-46.8	$2.68\times10^{-6}P$-0.08
B	1.34	54	32400	$2.44\times10^{-3}P$-70.8	$4.32\times10^{-6}P$-0.13
C	1.34	52	20800	$1.75\times10^{-3}P$-50.8	$2.64\times10^{-6}P$-0.08

6.8.4 Frosch and ACI 350 models

The Frosch (1999) model is the basis for the new method of crack control in the ACI350-06 (2006). This model and the approach of ACI 350-06 are explained in Section 2.4. The predicted crack widths for the tested panels based on the Eq. 2.22 are given in Table 6.15. The ACI 350-06 new method of crack control is also applied to the tested panels the results of which are presented in Table 6.16. Accordingly, the limiting steel stresses are calculated for both one-way and two-way structural conditions based on the Eq. 2.24. Interestingly, the limiting steel stresses are higher in a two-way flexural member than in a one-way flexural member. This implies that the cracking is less critical in a two-way member than in a one-way member. The basis for such an approach is not clearly explained in the Code. Another major shortcoming of the ACI 350-06 Code is that it does not provide any crack controlling method for direct tension cracks. The predicted crack widths of this model will be compared with the experimental data in Section 6.8.6.

Table 6.15 Crack width calculations based on Frosch model

	Flexural Cracks				
Panel	β_g	d_c (mm)	s (mm)	$f_{s,cr}$ (MPa)	$w_{t,max}$ (mm)
A	1.32	50	300	$1.62\times10^{-3}P$-46.8	$3.38\times10^{-6}P$-0.10
B	1.34	54	300	$2.44\times10^{-3}P$-70.8	$5.19\times10^{-6}P$-0.15
C	1.34	52	200	$1.75\times10^{-3}P$-50.8	$2.64\times10^{-6}P$-0.08

Table 6.16 Limiting steel stresses based on ACI 350-06

	Flexural Cracks (severe exposure)				
Panel	β_g	s (mm)	d_b (mm)	$f_{s,max}$ (one-way) (MPa)	$f_{s,max}$ (two-way) (MPa)
A	1.32	300	19.5	115	140
B	1.34	300	16.0	115	140
C	1.34	200	16.0	147	147

6.8.5 Nawy model

The Nawy's equation is one of the few available models for the prediction of two-way flexural cracks. This model is explained in Section 2.5. Although this model is not quite appropriately calibrated for normally reinforced concrete panels, the model is used here to make useful comparisons. Therefore, the Eq. 2.26 is applied to the tested panels and the predicted maximum crack widths of flexural cracks are summarized in Table 6.17. The panel is assumed to be simply supported on 4 edges under a concentrated load for determination of the fracture coefficient K in Table 2.1. The predicted crack widths of this model will be compared with the experimental data in Section 6.8.6.

Table 6.17 Crack width calculations based on Nawy model

	Flexural Cracks							
Panel	β	s_1 (mm)	s_2 (mm)	d_c (mm)	d_{b1} (mm)	K ($\times 10^{-6}$) (mm^2/N)	$f_{s,cr}$ (MPa)	$w_{t,max}$ (mm)
A	1.32	300	300	50	19.5	3.0	$1.62\times10^{-3}P$-46.8	$4.99\times10^{-6}P$-0.14
B	1.34	300	300	54	16.0	3.0	$2.44\times10^{-3}P$-70.8	$8.73\times10^{-6}P$-0.25
C	1.34	200	300	52	16.0	3.0	$1.75\times10^{-3}P$-50.8	$5.02\times10^{-6}P$-0.15

6.8.6 Comparison of theoretical and experimental crack widths

The predicted crack widths calculated in the previous sections are compared with the experimental observations in Fig. 6.16. The comparison is made at the early testing stages to limit the effect of repeated loading. The cracks are categorized into two types of direct tension

and flexural cracks depending on their primary behaviour. The widths of direct tension and flexural cracks are compared with their corresponding crack models. Looking at the results of the direct tension cracks in Fig. 6.16 (a), it can be seen that the BS 8007-1987 method largely underestimates the crack widths. This may be due to the underestimation of the crack spacing and the overestimation of the concrete tension stiffening in this model. The predicted crack widths of the CEB MC90 model have a different trend than the experimental crack widths. This is because this model in its original form predicts the crack widths in the crack formation phase at pre-stabilized cracking stage, which is clearly not suitable for design purposes. A model based on the reloading of a stabilized cracking system is safely conservative for design purposes. Also, the CEB MC90 model does not properly consider the effect of shrinkage strains on the crack width at the beginning of the loading. The results of the CEB MC90 model tend to approach the experimental results as the load approaches the stabilized cracking load. However, as shown previously, the predicted stabilized cracking load of the CEB MC90 model is not reliable for the two-way systems. The proposed model suitably captures the maximum observed crack widths at loads up to the stabilized cracking load. It must be noted that, while the width of the crack A in panel B is lower than the predicted values in the 2nd stage of testing, the width of this crack is slightly underestimated in the 3rd stage. This is partly due to the effect of repeated loading, and also, due to an uncommonly large spacing of this crack, as it has been previously explained in the calculations of the crack spacing.

Looking at the results of the flexural cracks in Fig. 6.16 (b), it can again be seen that the BS 8007-1987 model gives significantly underestimated crack widths. The CEB MC90 model also makes crack width predictions un-conservatively lower than the experimental results. The Gergely-Lutz and the Frosch model yield similar results especially for panel C in which the spacing of flexural bars are smaller. Such a similarity is expected for the tested panels in which the clear concrete covers are smaller than 50 *mm*. The maximum allowed steel stress line of the ACI 350-06 intersects the Frosch predictions at crack widths of about 0.3 *mm* for panels A and B and 0.22 *mm* for panel C. This shows that larger crack widths are allowed for panels A and B with absolutely no justification. Such a discrepancy originates from the recommended permissible steel stress of 140 *MPa* for two-way members. Also, the Frosch model underestimates the crack widths in panel A. The Nawy model shows a different trend than the

experimental results. This model yields crack widths that are much higher than those of all other models, and the experimental results of the panels B and C. The Nawy model is developed based on the experimental data of two-way flexural slabs, and hence, it appears to be inappropriate for the two-way loading condition used in this study. The results of the proposed model suitably encompass the maximum observed crack widths up to the stabilized cracking load for all panels.

Overall, it can be concluded that the proposed model is accurate in predicting the maximum crack width under two-way loading condition. Although only one unique combination of direct tension and flexural loading is investigated, the applicability of the proposed model can be easily extended to any combination of two-way loading.

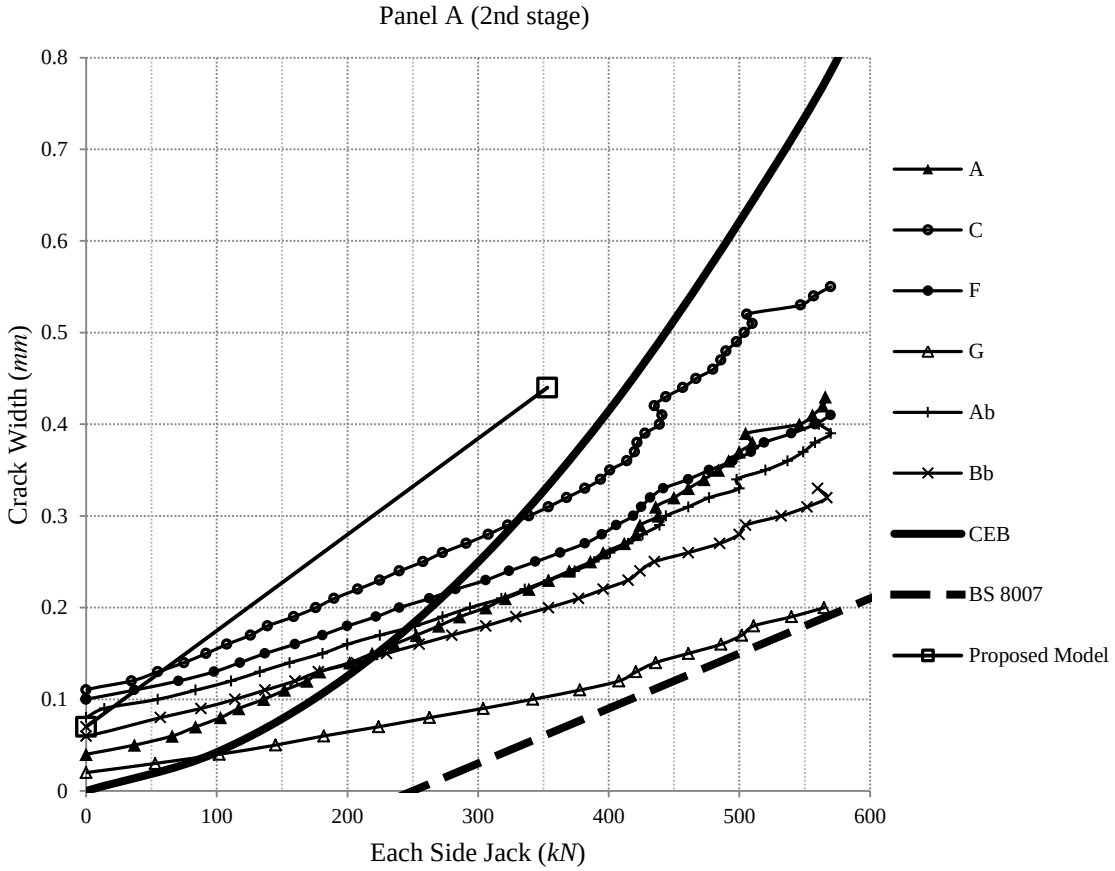

Panel B (2nd stage)

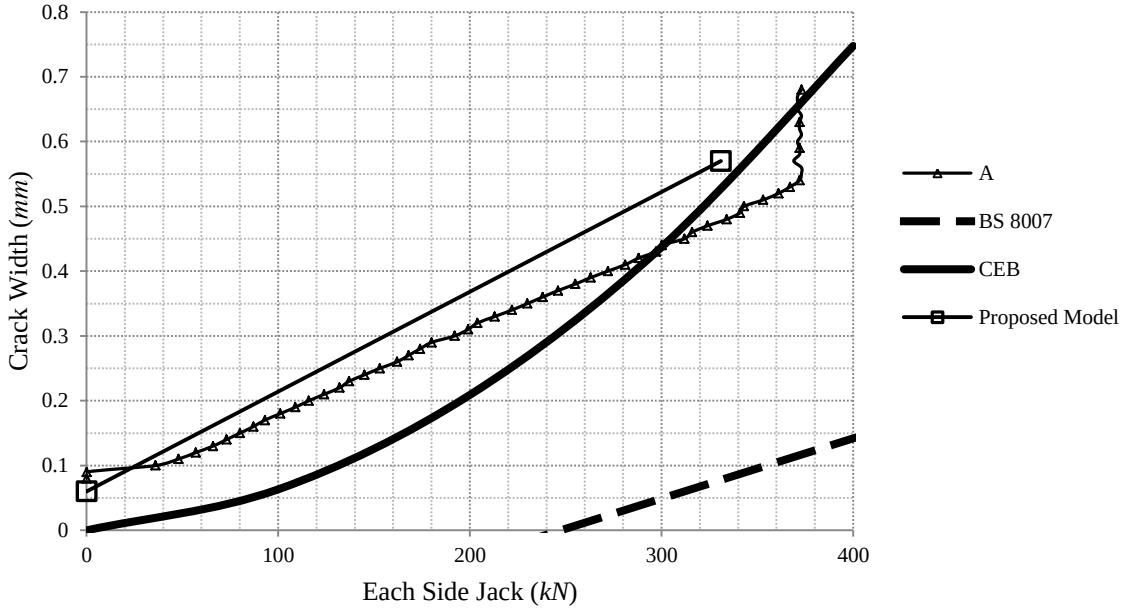

Panel B (3rd stage)

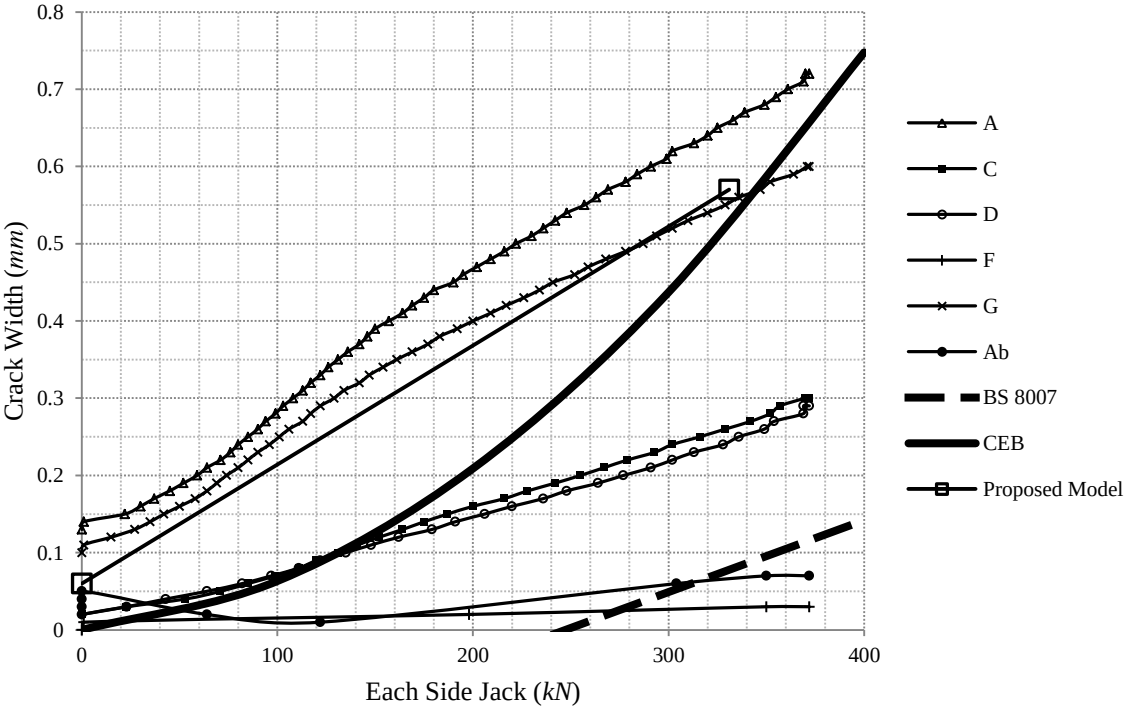

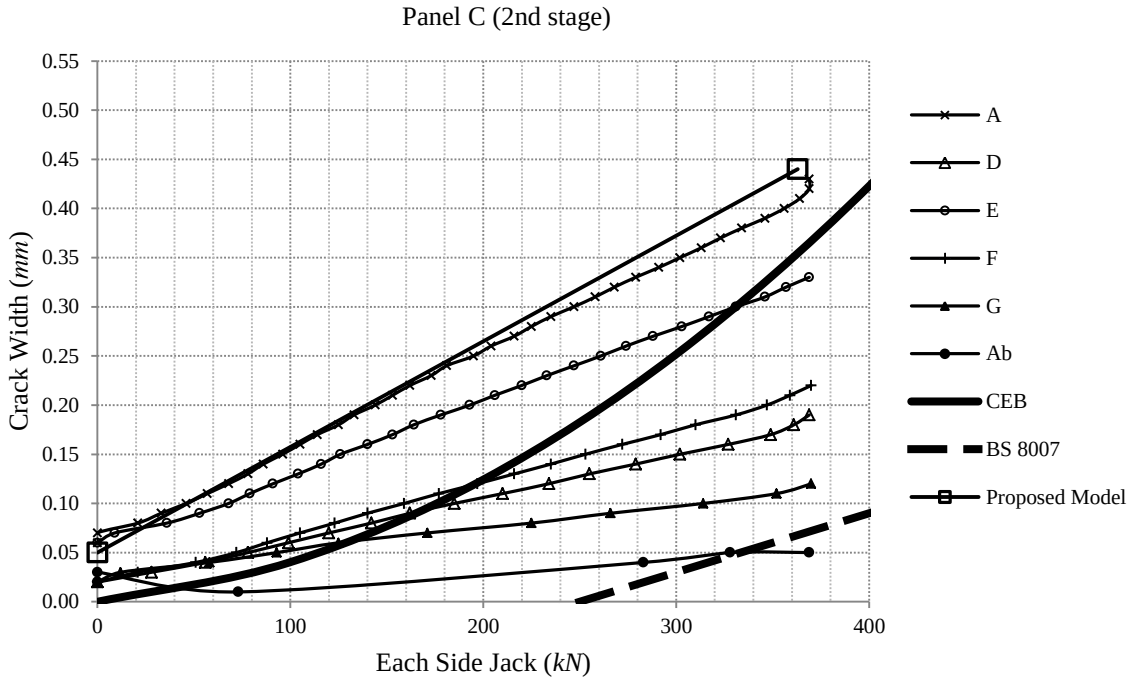
Panel C (2nd stage)
Crack Width (mm)
Each Side Jack (kN)
0.00
0.05
0.10
0.15
0.20
0.25
0.30
0.35
0.40
0.45
0.50
0.55
0
100
200
300
400
A
D
E
F
G
Ab
CEB
BS 8007
Proposed Model

(a)

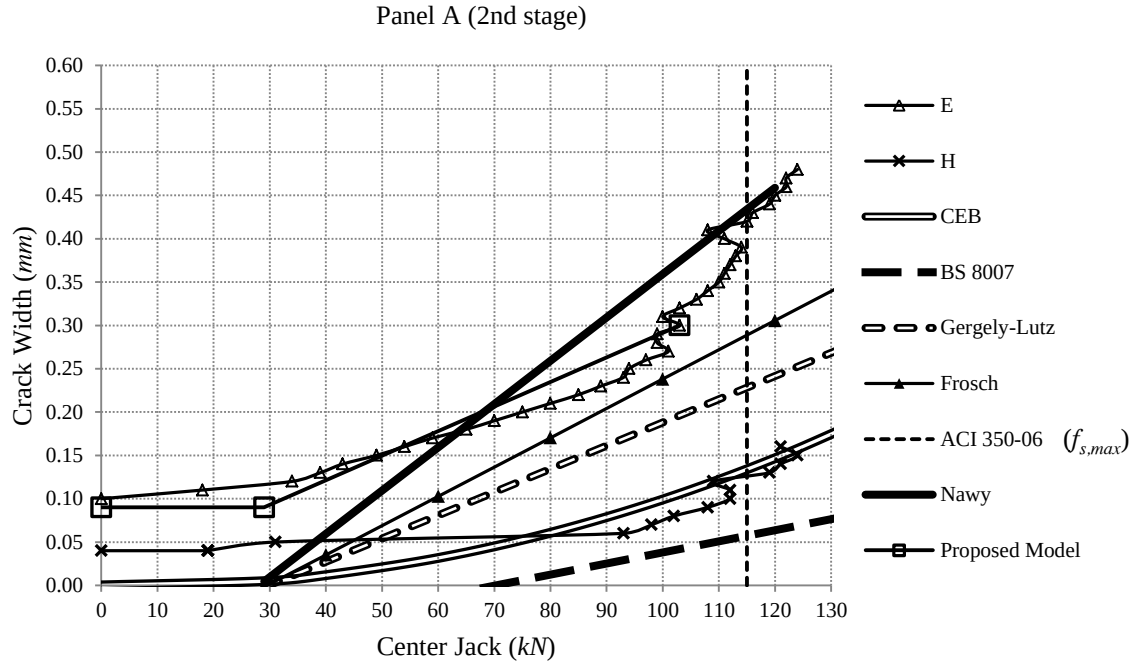
Panel A (2nd stage)
Crack Width (mm)
Center Jack (kN)
0.00
0.05
0.10
0.15
0.20
0.25
0.30
0.35
0.40
0.45
0.50
0.55
0.60
0
10
20
30
40
50
60
70
80
90
100
110
120
130
E
H
CEB
BS 8007
Gergely-Lutz
Frosch
ACI 350-06 (f_s,max)
Nawy
Proposed Model

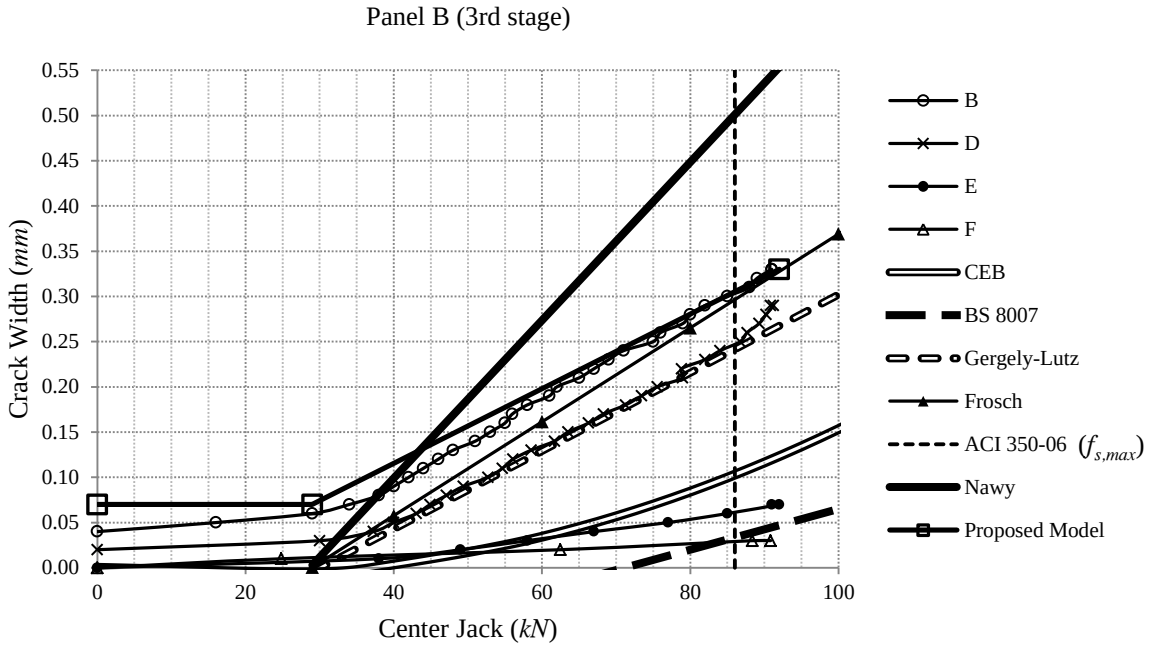

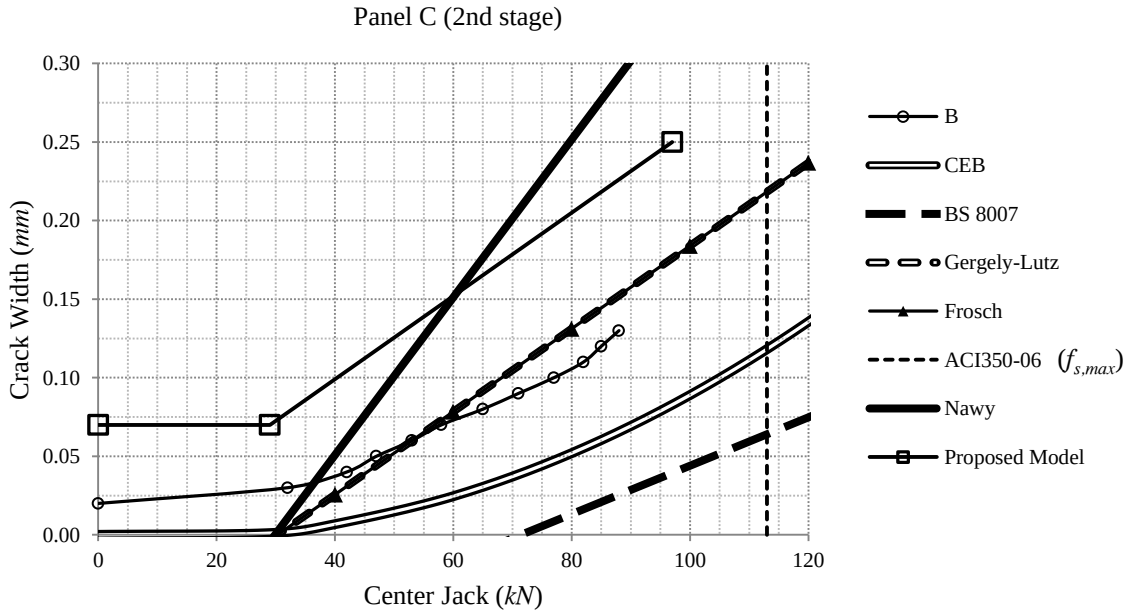

(b)

Fig. 6.16 Comparison of predicted crack widths and experimental data, a) direct tension cracks, b) flexural cracks

6.9 Summary

A new analytical model is developed in this Chapter to predict the cracking behaviour of two-way panels. For this purpose, first the internally restrained shrinkage stresses due to the presence of the longitudinal reinforcement and the splitting tensile stresses produced by the transverse reinforcement are determined through FE parametric studies. Then, the effect of the longitudinal splitting crack on reducing the peak bond stress is investigated through another FE parametric study. A reduction factor of 55% on average is accepted for this parameter at the service load level. All the new findings are incorporated in one comprehensive crack prediction model, which is capable of predicting the cracking load, the maximum and the minimum spacing of cracks, and the maximum crack width. The accuracy of this model along with other models available in the literature is examined using the experimental data of the tested panels in this study. It is found that the one-way cracking theories are invalid for prediction of the cracking load and the crack spacing of the two-way systems. Also, these one-way cracking models, which are the basis for the crack control recommendations of various design codes, underestimate the crack widths of two-way systems. On the other hand, it is shown that the proposed model can successfully provide an accurate estimation of the cracking load, the minimum and the maximum spacing of cracks, and the maximum crack width for the two-way cracking experimental tests. The proposed method can easily be used to generate simplified design guidelines for crack control of two-way panels.

CHAPTER 7

CONCLUSIONS

7.1 Summary

A study is performed with an ultimate goal of developing an analytical model to predict the cracking of a two-way structural panel. For this purpose, first the cracking of a one-way member is closely investigated. Following a discussion on the underlying physics for the one-way cracking phenomenon, two main parameters, namely, the bond stress and the effective tension area of concrete are selected for further investigation using the FE technique. A non-linear FE model based on a damaged plasticity model for concrete with various post-cracking models, and an explicit dynamic or a static Riks solution technique is introduced. The validity of this model is verified using an experimental data from a test performed by Kankam (1997). The explicit dynamic solution technique is found to be the preferred technique due to its higher accuracy within a short processing time. To improve the accuracy of this model, attention is given to the actual bond mechanism between the reinforcing bar and the surrounding concrete. Based on a theory of the bond mechanism, three different bond modeling techniques, namely, perfect bond, diagonal link elements, and bond layer models are introduced and incorporated into the FE model. Based on a comparison with the experimental data, the bond layer model is chosen among other techniques for its simplicity and reasonable accuracy in predicting both shear and radial bond stresses. The newly developed FE model is also validated using the experimental data of a test performed by Tammo and Thelandersson (2009).

Based on the results of the FE analysis, a bilinear curve is suggested for approximating the shear bond stresses. A parametric study is performed using the validated FE model to find the

correlation between the peak shear bond stress and other parameters, including, clear concrete cover, tensile strength of concrete, diameter of the reinforcing bar, steel stress and confinement condition. The effective tension area of concrete in flexural members is also investigated through another FE parametric study. A new factor, which is independent of the clear concrete cover, is recommended for determination of the depth of the effective tension area. The variation of this factor with the reinforcement ratio is obtained.

In the next step, an experimental investigation is conducted on the cracking behaviour of two-way loaded RC panels. Three different medium-scale RC panels that represent a segment of the wall of a liquid containing tank are built to consider the effect of the reinforcement ratio and the bar spacing. These panels are tested under a two-way loading condition that resembles the internal forces of the actual structure. Accordingly, the panels are loaded simultaneously in direct tension in one direction and the bending moment in the other direction perpendicular to the first one. A unique test setup is designed for this purpose. These tests are performed in several stages of one-way and two-way loading cycles. Also, the extent of water leakage through these panels is examined by exposing a few selected cracks to pressurized water. The collected data from these tests include concrete properties, applied loads, strain of steel reinforcing bars, strain at the concrete surface, elongation of the panel, crack pattern, crack width, and water leakage observations. Further analysis of these results has revealed a number of new findings that can improve the understanding of the two-way cracking phenomenon.

In the final step, a new analytical model is developed to predict the cracking behaviour of a two-way panel. To achieve this, first the concrete tensile stresses due to internally restrained shrinkage and splitting tensile stresses caused by radial bond stresses of transverse reinforcement are determined through FE parametric studies. Then, in another FE parametric study the effect of a longitudinal splitting crack on the peak shear bond stress is investigated. All the new findings achieved in this study are incorporated in one comprehensive crack prediction model, which is capable of predicting the cracking load, the maximum and the minimum spacing of cracks, and the maximum crack width. The accuracy of this model is examined using the experimental data of the tested panels in this study. It is shown that unlike other models available in the literature

the proposed model can successfully provide an accurate estimation of the cracking behaviour of a two-way system.

7.2 Outcomes and Conclusions

The cracking behaviour of reinforced concrete panels is investigated both analytically and experimentally. As a result, several improvements in the understanding of both one-way and two-way cracking phenomena are achieved throughout this study. The main outcomes of this research are highlighted as follows,

FE analysis of cracking in one-way members

- A sensitivity analysis is performed on a FE model, which makes use of a damaged plasticity model for concrete. The effect of various parameters, including, solution technique, post-cracking curve of concrete, number of time increments, mesh size, and tensile strength of concrete are investigated.

- It is found that for the same level of accuracy the dynamic explicit formulation is a more time-efficient solution technique than the static Riks formulation to predict the highly non-linear tensile cracking behaviour of concrete.

- Three different approaches for modeling the bond behaviour are introduced and compared with each other, namely, the perfect bond, the diagonal link element, and the bond layer models. It is found that the perfect bond model underestimates the amount of bond-slip due to an underestimated angle of the bond force relative to the bar axis. This problem is alleviated in the other two bond models in which the radial bond stress, and hence, the angle of the bond force is larger. This is in agreement with the hypothesis that bond-slip mainly occurs due to micro-cracking at the interface of the concrete and steel, and also, the bond forces mainly transfer from the steel to the concrete through diagonal compression struts.

- Based on the FE analysis, a bi-linear curve is proposed for approximation of the distribution of the shear bond stress. The location of the peak shear bond stress is found to be biased toward the location of the nearest crack.

- The peak shear bond stress is determined through a FE parametric study. The parameters considered are clear concrete cover, bar diameter, tensile strength of concrete, steel stress, and confinement condition.

- A new factor, which is independent of the clear concrete cover, unlike other conventional factors, is proposed for determination of the depth of effective tension area of concrete in flexural members. The values of this factor are determined based on a FE parametric study.

Experimental investigation of cracking in two-way panels

- A significant source of experimental data is produced on the two-way cracking phenomenon. The cracking behaviour of three medium-scale two-way panels is experimentally investigated. The collected data from these tests include concrete properties, applied loads, strain of steel reinforcing bars, strain at the concrete surface, elongation of the panel, crack pattern, crack width, and water leakage observations.

- The cracking load of a two-way panel is found to be much lower than the predicted values using the one-way cracking theory. This is due to the presence of the splitting tensile stresses caused by the transverse reinforcement.

- The crack patterns found to be mainly a reflection of the shape of the reinforcement mesh. This is primarily due to the presence of splitting tensile stresses generated by radial bond forces. Therefore, the spacing of cracks in a two-way panel has a close relationship with the spacing of reinforcing bars in both orthogonal directions.

- A few cracks may always form at some inclination to the axes of orthogonal reinforcing bars. The possibility of inclined cracking is closely related to the two-way loading ratio, the reinforcement ratio, the clear cover to bar diameter ratio, and the bar

spacing. The inclined cracking is more probable for the two-way loading ratios closer to 1, the reinforcement ratios less than 0.005, and the clear cover to bar diameter ratios more than 2.5. The effect of bar spacing is more complex. It seems a range of bar spacings exists within which the chance of inclined cracking is reduced.

- The rate of leakage through a full-depth crack depends on the crack width gradient rather than just the maximum crack width at one side of the panel. Also, the compression zone that exists at the section of a flexural crack can prevent the water leakage.

- The inclined cracks have a much higher gradient through the depth than direct tension cracks for a two-way loading condition that has a bending moment in at least one of the orthogonal directions. This would suggest a reduced water leakage through this type of cracks.

- Once a crack is formed, a residual crack width remains in place even after complete unloading. The residual crack width increases by raising the maximum level of loading. Also, some residual strains always exist in the tensioned concrete due to micro-cracking.

- The width of a crack can increase under repeated loading. This increase is much more significant at the first cycle in a range of 0.1 *mm*.

- The stiffness of a two-way panel along any arbitrary axis is reduced by the formation of a crack with any arbitrary orientation to that axis.

- The width of an inclined crack depends on the loading in both orthogonal directions.

- The bond strength is greatly reduced in a two-way panel due to orthogonal cracking along the reinforcing bars, which has an effect similar to longitudinal splitting cracks for these reinforcing bars.

Analytical investigation of cracking in two-way panels

- The one-way cracking theories are invalid for prediction of the cracking behaviour of a two-way system. These models significantly underestimate the cracking load and overestimate the crack spacing. Also, these one-way cracking models, which are the basis for the crack control recommendations of various design codes, underestimate the crack widths of two-way systems.

- The two-way flexural cracking model proposed by Nawy is found to overestimate the maximum crack width of the tested panels at the service load levels. This model may only be applicable to two-way flexural slabs.

- Recommendations are made for determination of the concrete tensile stresses due to the internally restrained shrinkage and the splitting tensile stresses caused by the radial bond stresses of transverse reinforcement through FE parametric studies.

- The effect of the longitudinal splitting crack on reducing the peak shear bond stress is investigated through a FE parametric study. A reduction factor of 55% on average is proposed for this parameter at the service load level.

- A new comprehensive analytical model is developed, which is capable of predicting the cracking load, the maximum and the minimum spacing of cracks, and the maximum crack width in a two-way panel.

- Unlike other models available in the literature the proposed model can successfully provide an accurate estimation of the cracking behaviour of a two-way system. The proposed method can easily be used to generate simplified design guidelines for the crack control of a two-way panel.

7.3 Recommendations for Future Research

The cracking of reinforced concrete is a very complex phenomenon in which a wide range of parameters are involved. Consideration of the effect of all these parameters in one study is just not feasible. The current study not only provides a number of advancements in the understanding of the cracking behaviour of one-way and two-way members, but it also offers reliable tools and new avenues for further investigations. The following are few suggestions for future research studies based on the findings of this research,

- The FE technique described in this study is successfully used for one-way loaded members. The application of this FE technique can be extended for direct modeling of a two-way loaded RC panel. A FE parametric study of such a two-way RC panel may reveal new aspects of two-way cracking behaviour.

- The suggested FE model can also be used in a parametric study of the effect of combined loading in a one-way member, meaning, combined tension, flexure, and shrinkage. The effective tension area of concrete under these loading conditions can also be investigated.

- This study is limited to externally unrestrained members. The cracking can be investigated in an externally restrained member using the suggested FE technique.

- The effect of external confining pressure on the bond stresses can be investigated through a FE parametric study.

- The effect of repeated loading on bond stress, and hence, the crack width at service load levels observed in this study can be the subject of further investigations.

- The number of experimental tests performed in this study is limited. These experiments can be repeated to investigate the effect of various two-way loading ratios, smaller bar spacings, higher reinforcement ratios, and larger clear concrete covers.

- The effect of long-term loading on the crack width can also be investigated.

- The effect of crack width and its gradient, and water pressure on the rate of water leakage through a full-depth crack needs further experimental investigations. The reduction in the rate of leakage over time for various crack widths can also be studied.

- The effect of the width of longitudinal splitting cracks on the bond stresses in a two-way panel requires further analytical and experimental investigations.

- The analytical model proposed in this study for the prediction of two-way cracking can be used as the basis for developing simple design guidelines for crack control of two-way panels. For this purpose, the model can either be used in a parametric study of two-way panels to produce simple design charts for determination of bar spacing and steel stress limits with a known maximum crack width, or a simplified form of this model can be directly used after making several conservative assumptions.

APPENDIX A

EXPERIMENTAL RESULTS

A.1 Steel and Concrete Strains

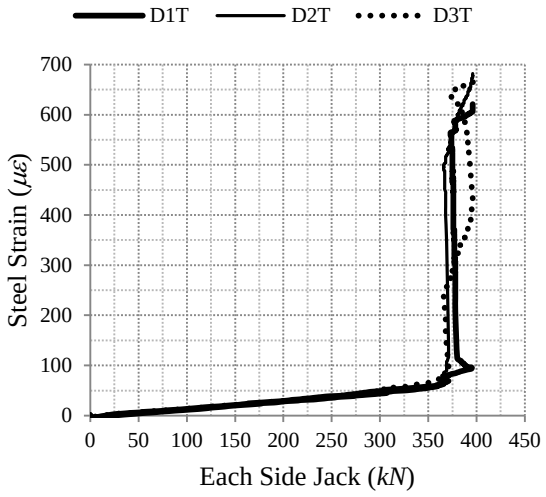

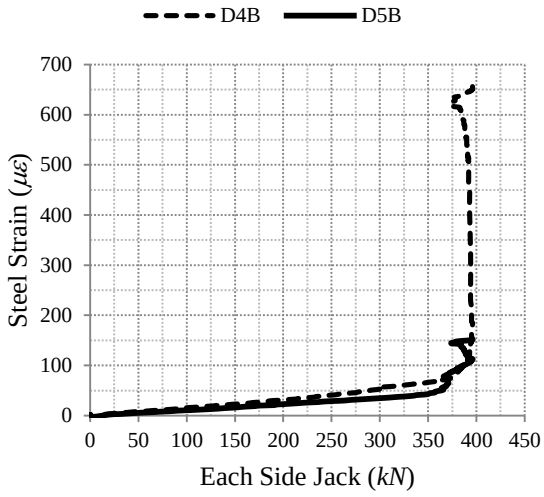

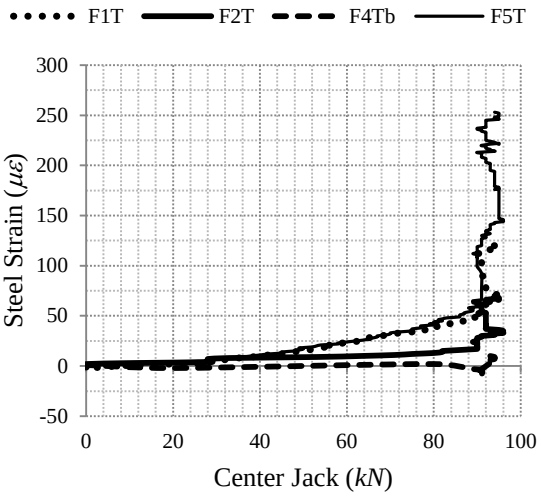

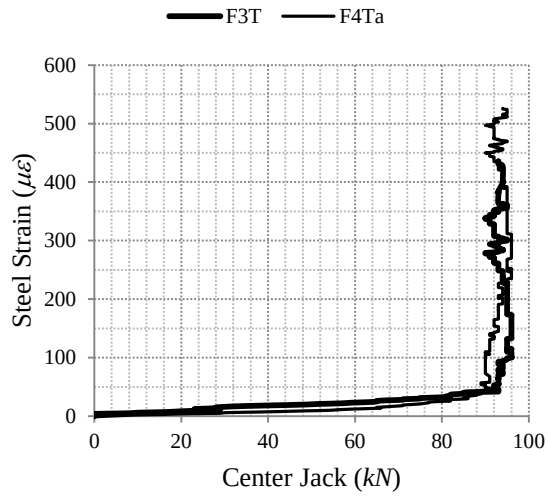

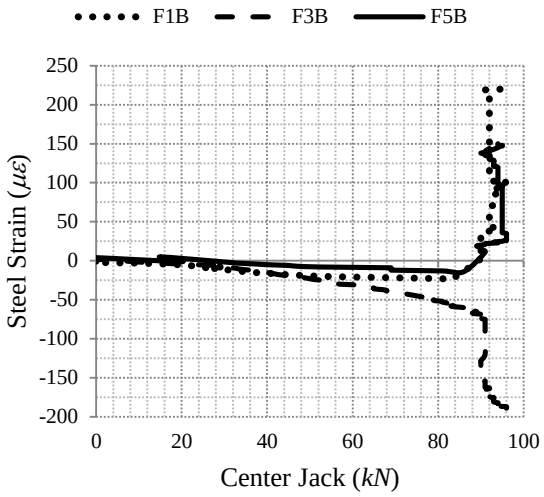
F1B
F3B
F5B
250
200
150
100
50
0
-50
-100
-150
-200
Steel Strain (με)
0
20
40
60
80
100
Center Jack (kN)

(a)

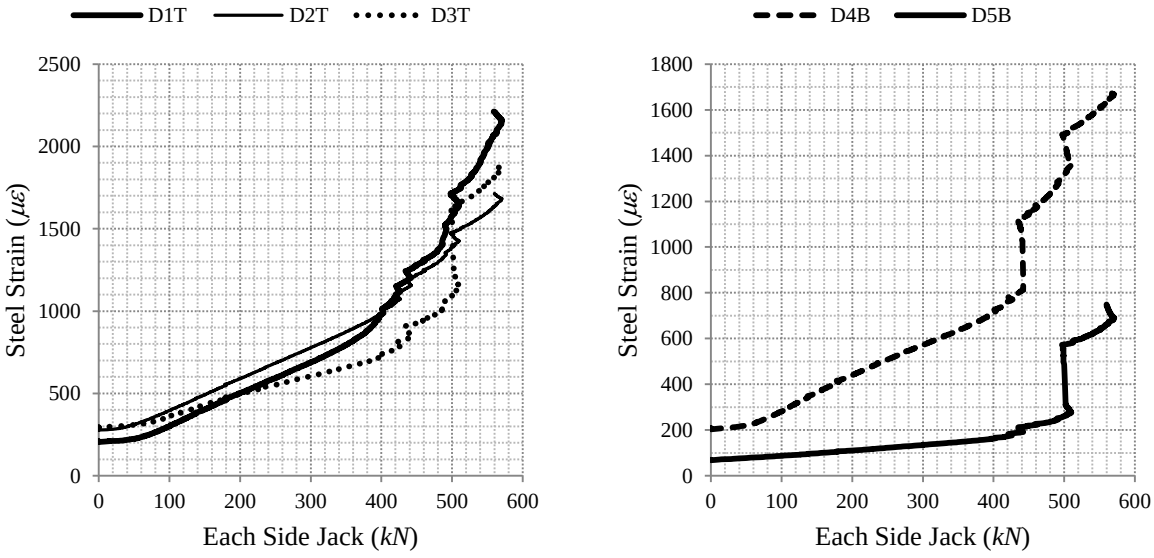
D1T
D2T
D3T
2500
2000
1500
1000
500
0
Steel Strain (με)
0
100
200
300
400
500
600
Each Side Jack (kN)
D4B
D5B
1800
1600
1400
1200
1000
800
600
400
200
0
Steel Strain (με)
0
100
200
300
400
500
600
Each Side Jack (kN)

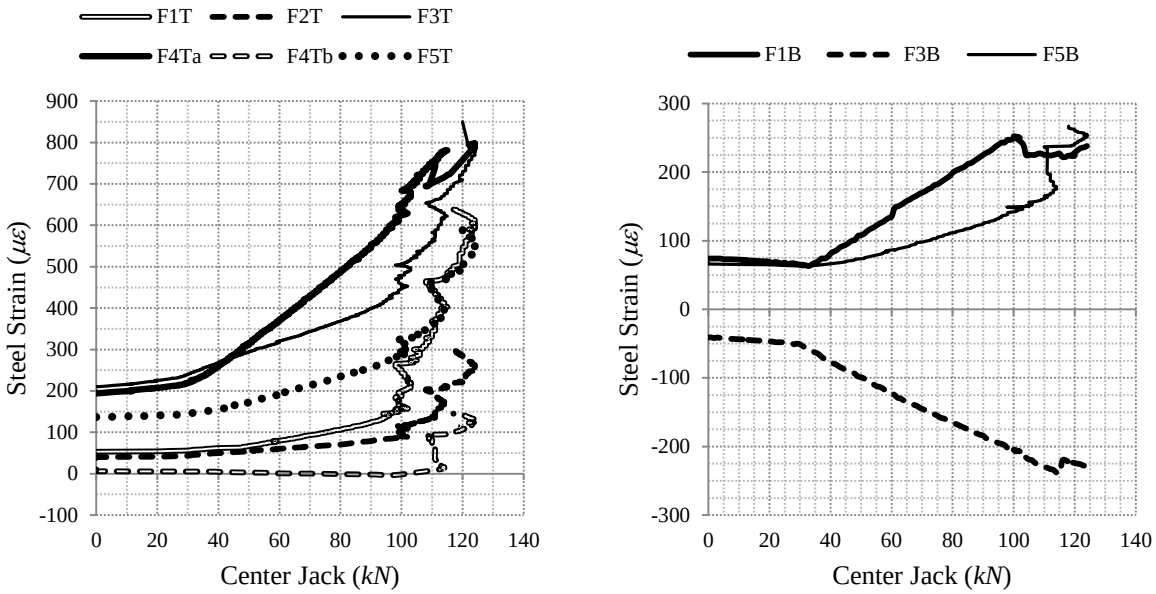
F1T
F2T
F3T
F4Ta
F4Tb
F5T
Steel Strain (με)
Center Jack (kN)
F1B
F3B
F5B
Steel Strain (με)
Center Jack (kN)

(b)

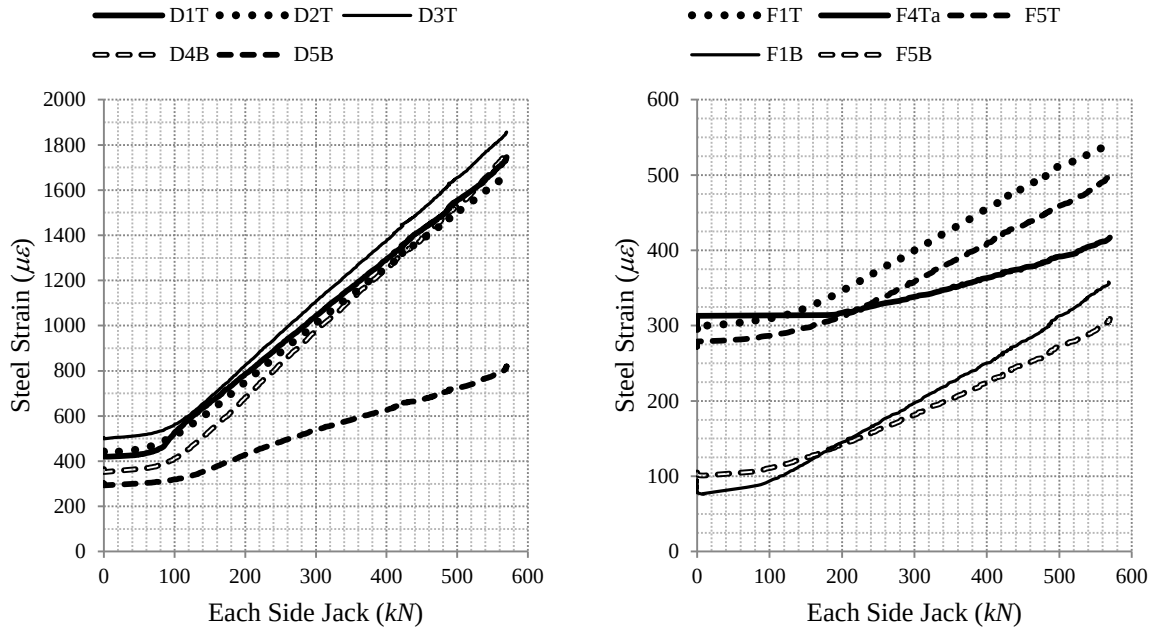
D1T
D2T
D3T
D4B
D5B
Steel Strain (με)
Each Side Jack (kN)
F1T
F4Ta
F5T
F1B
F5B
Steel Strain (με)
Each Side Jack (kN)

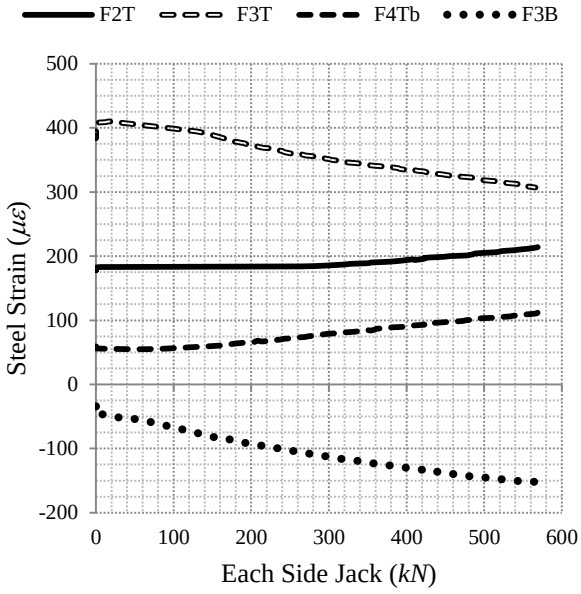
F2T
F3T
F4Tb
F3B
Steel Strain (με)
Each Side Jack (kN)

(c)

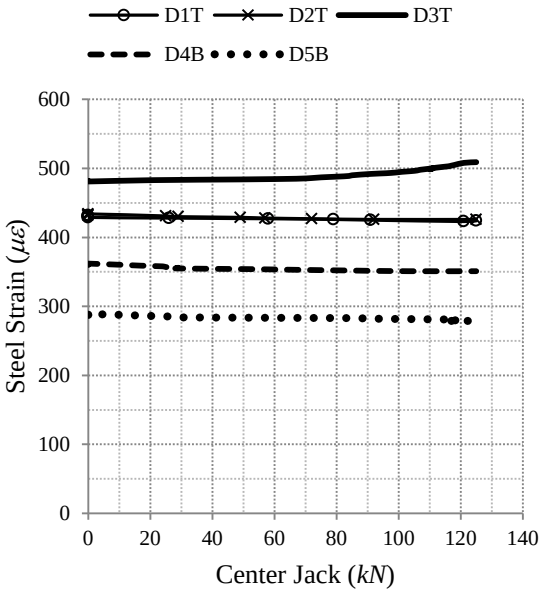
D1T
D2T
D3T
D4B
D5B
Steel Strain (με)
Center Jack (kN)

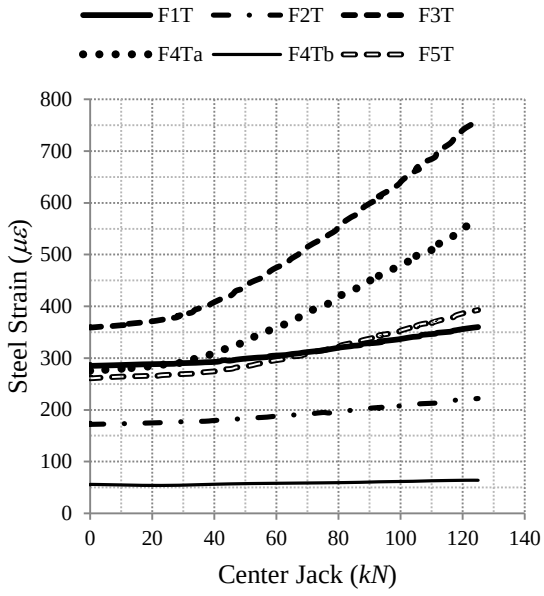
F1T
F2T
F3T
F4Ta
F4Tb
F5T
Steel Strain (με)
Center Jack (kN)

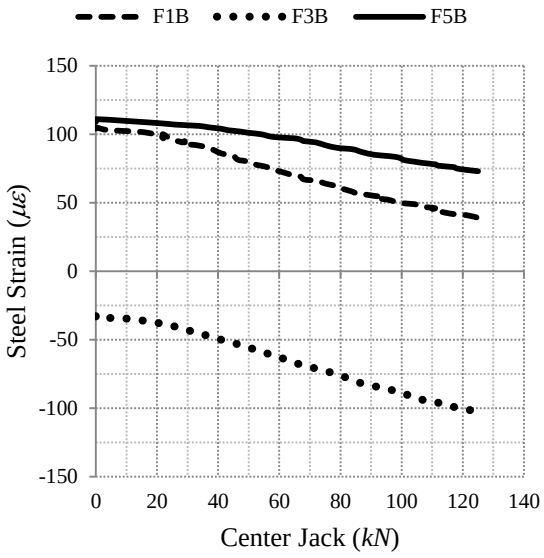
F1B
F3B
F5B
150
100
50
0
-50
-100
-150
0
20
40
60
80
100
120
140
Steel Strain (με)
Center Jack (kN)

(d)

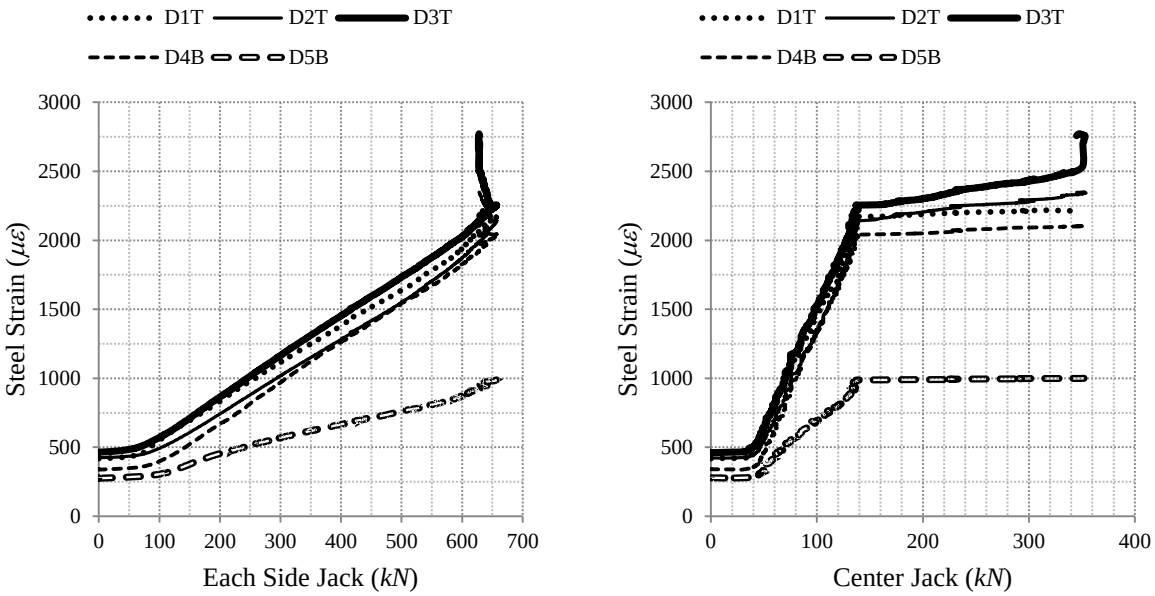
D1T
D2T
D3T
D4B
D5B
3000
2500
2000
1500
1000
500
0
0
100
200
300
400
500
600
700
Steel Strain (με)
Each Side Jack (kN)
D1T
D2T
D3T
D4B
D5B
3000
2500
2000
1500
1000
500
0
0
100
200
300
400
Steel Strain (με)
Center Jack (kN)

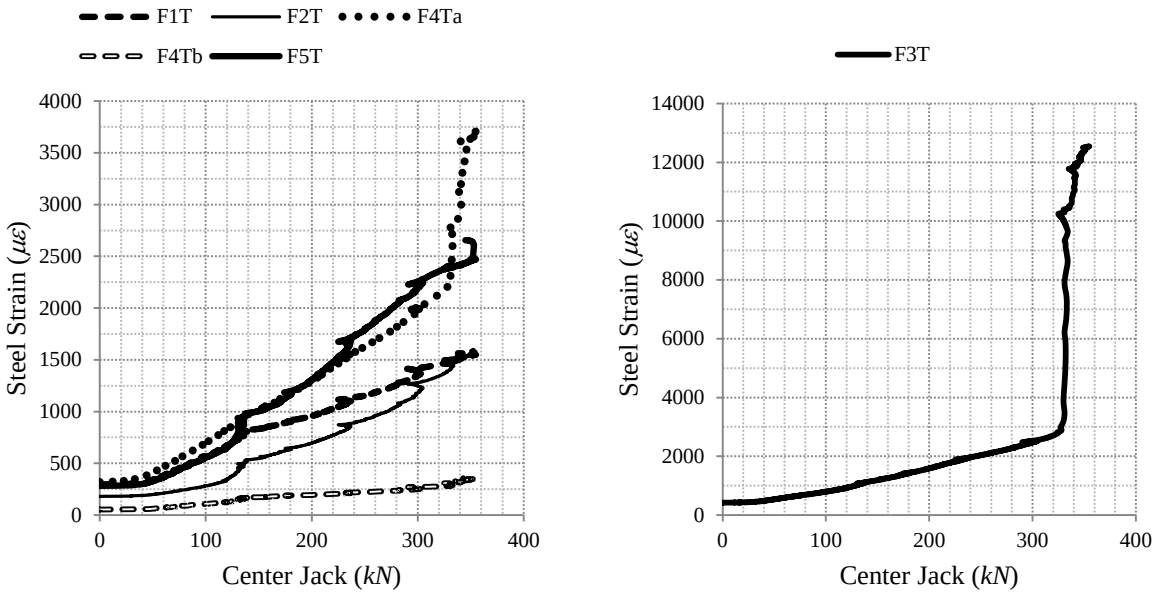

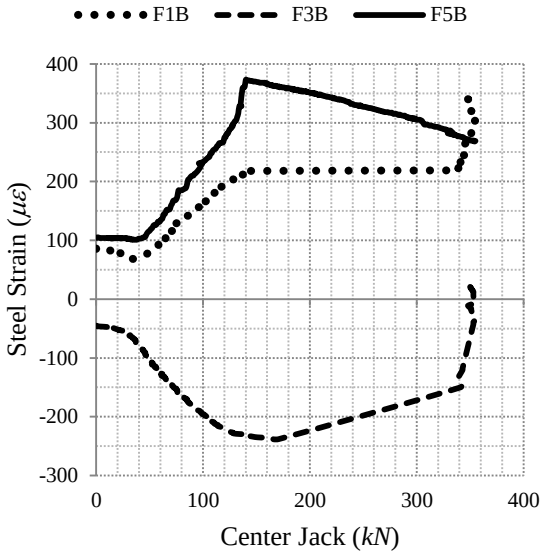

(e)

Fig. A.1 Steel strains in panel A, a) 1st stage, b) 2nd stage, c) one-way tension, d) one-way bending, e) 3rd stage

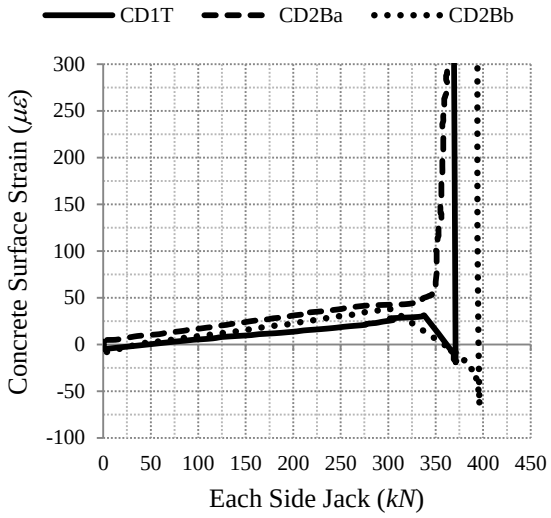
CD1T
CD2Ba
CD2Bb
Concrete Surface Strain ($\mu\varepsilon$)
300
250
200
150
100
50
0
-50
-100
0 50 100 150 200 250 300 350 400 450
Each Side Jack (kN)

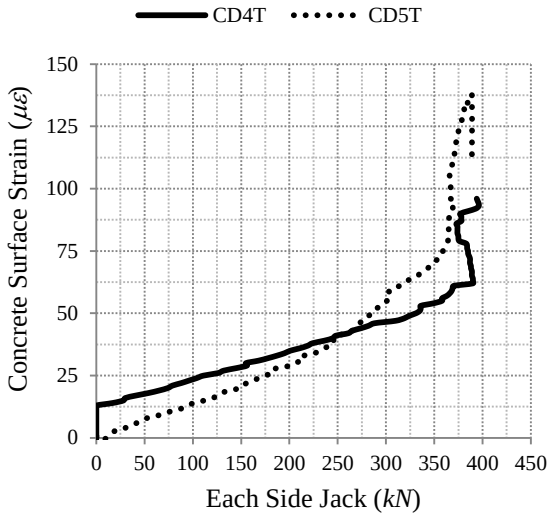
CD4T
CD5T
Concrete Surface Strain ($\mu\varepsilon$)
150
125
100
75
50
25
0
0 50 100 150 200 250 300 350 400 450
Each Side Jack (kN)

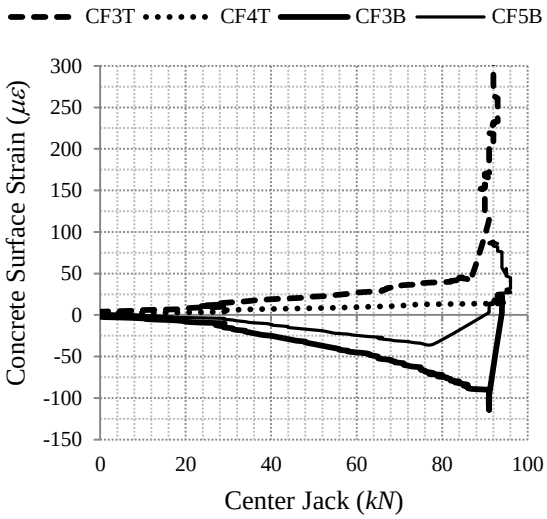
CF3T
CF4T
CF3B
CF5B
Concrete Surface Strain ($\mu\varepsilon$)
300
250
200
150
100
50
0
-50
-100
-150
0 20 40 60 80 100
Center Jack (kN)

(a)

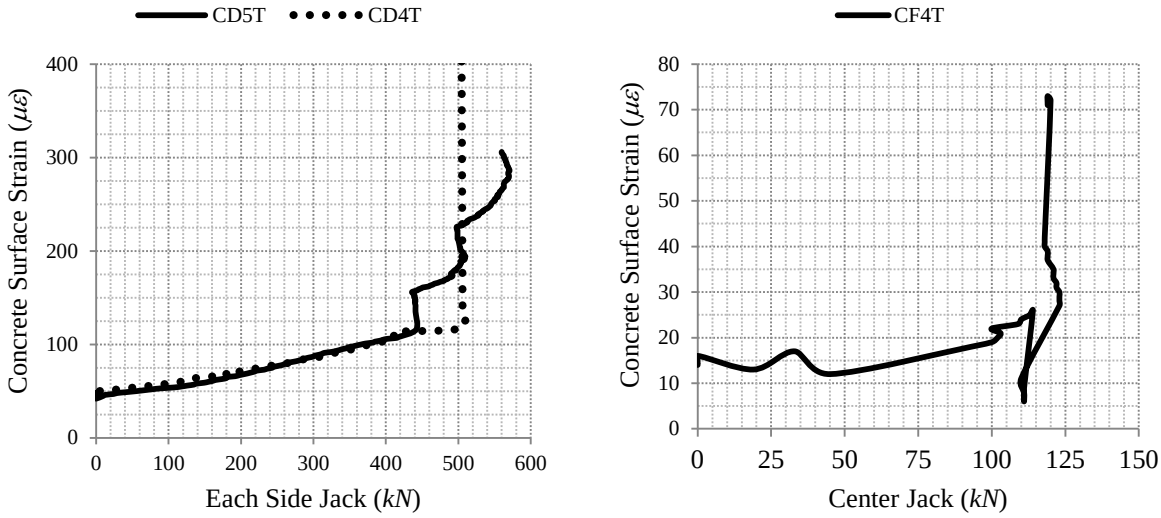
CD5T
CD4T
Concrete Surface Strain (με)
Each Side Jack (kN)
CF4T
Concrete Surface Strain (με)
Center Jack (kN)

(b)

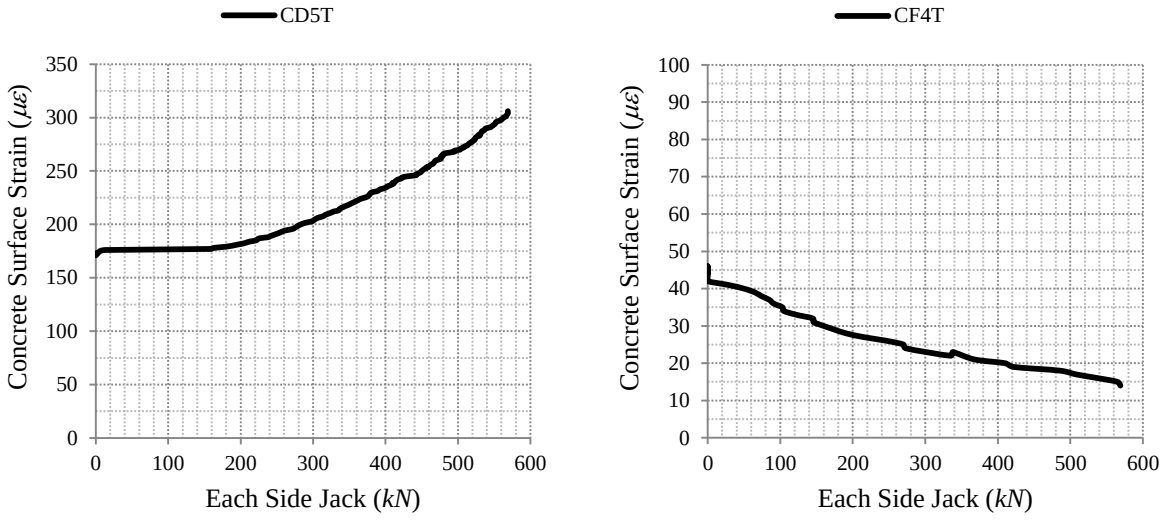
CD5T
Concrete Surface Strain (με)
Each Side Jack (kN)
CF4T
Concrete Surface Strain (με)
Each Side Jack (kN)

(c)

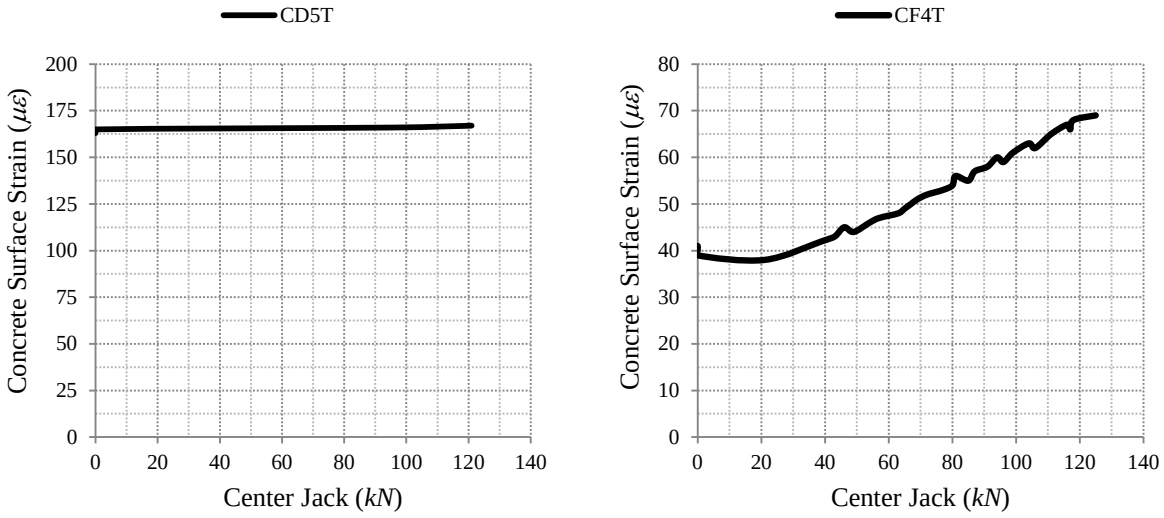

(d)

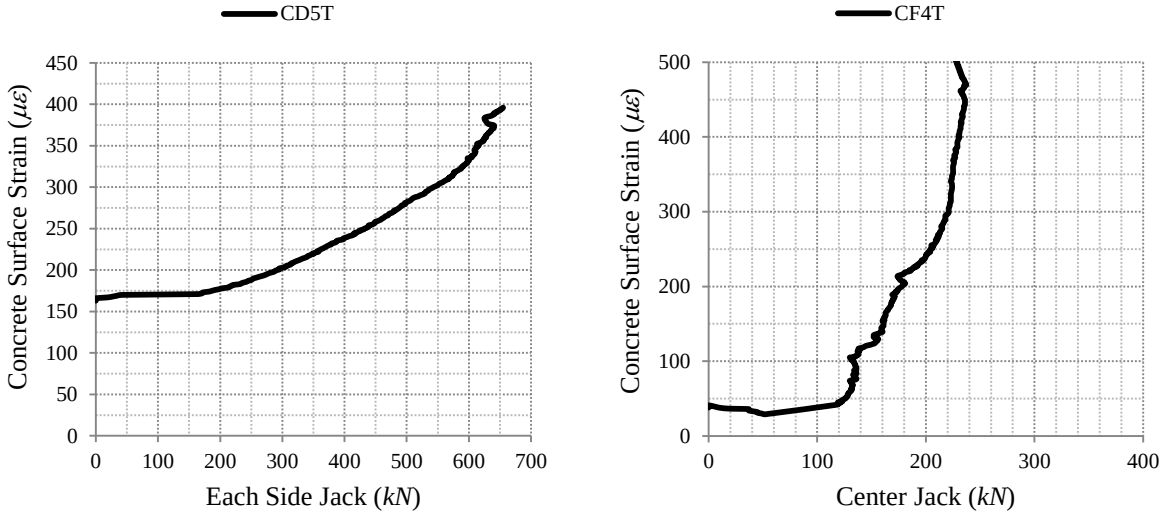

(e)

Fig. A.2 Concrete strains in panel A, a) 1st stage, b) 2nd stage, c) one-way tension, d) one-way bending, e) 3rd stage

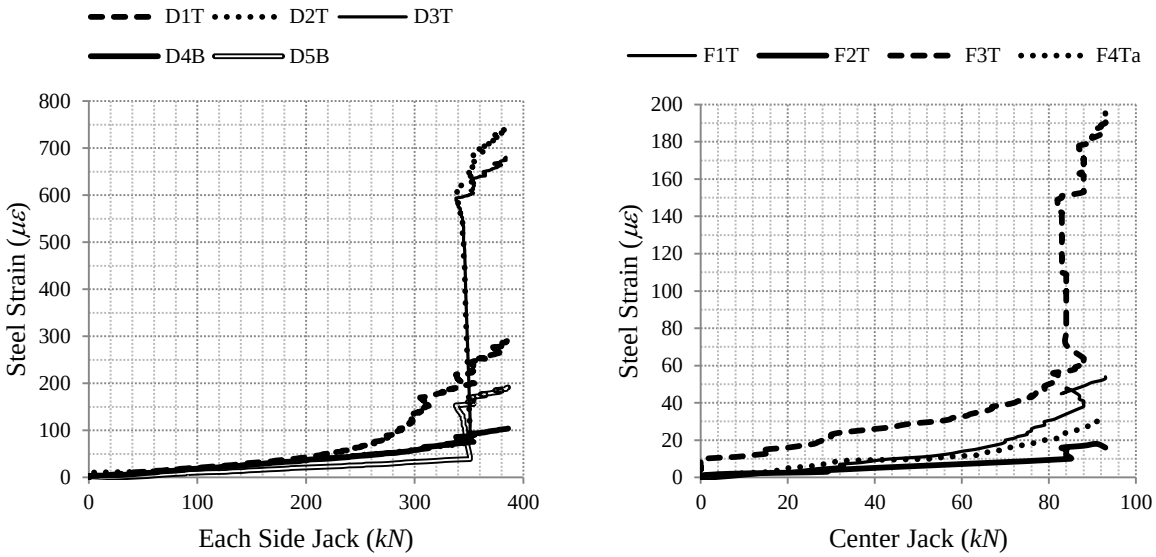
D1T
D2T
D3T
D4B
D5B
Steel Strain (με)
Each Side Jack (kN)
F1T
F2T
F3T
F4Ta
Steel Strain (με)
Center Jack (kN)

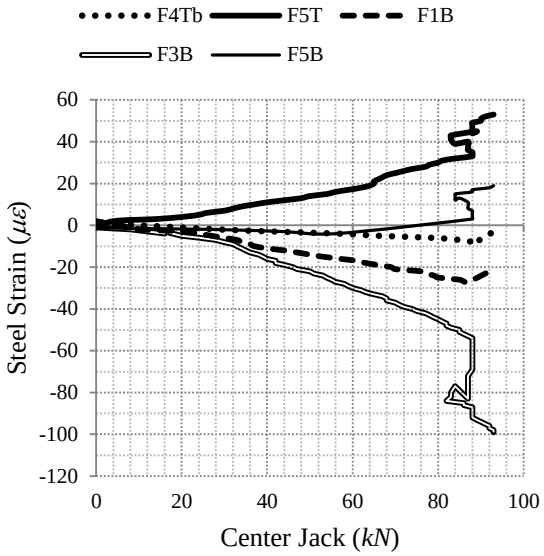
F4Tb
F5T
F1B
F3B
F5B
Steel Strain (με)
Center Jack (kN)

(a)

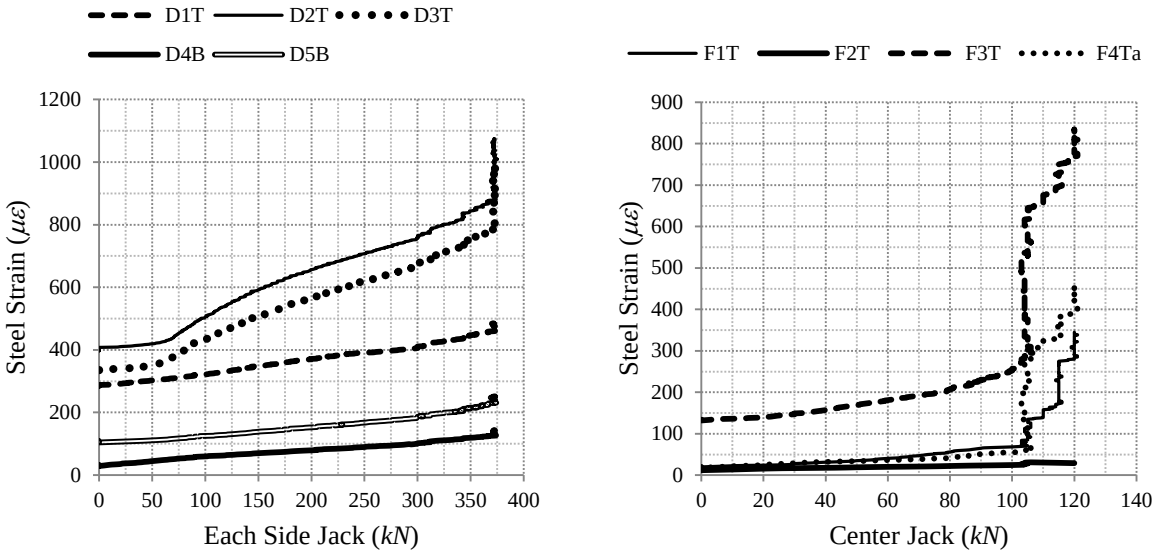
D1T
D2T
D3T
D4B
D5B
Steel Strain ($\mu\varepsilon$)
Each Side Jack (kN)
F1T
F2T
F3T
F4Ta
Steel Strain ($\mu\varepsilon$)
Center Jack (kN)

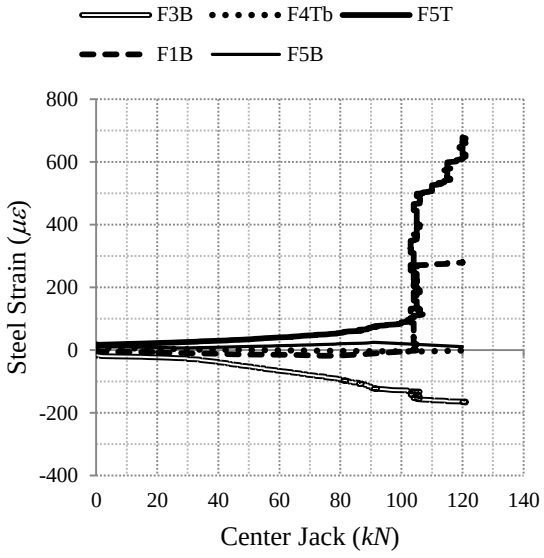
F3B
F4Tb
F5T
F1B
F5B
Steel Strain ($\mu\varepsilon$)
Center Jack (kN)

(b)

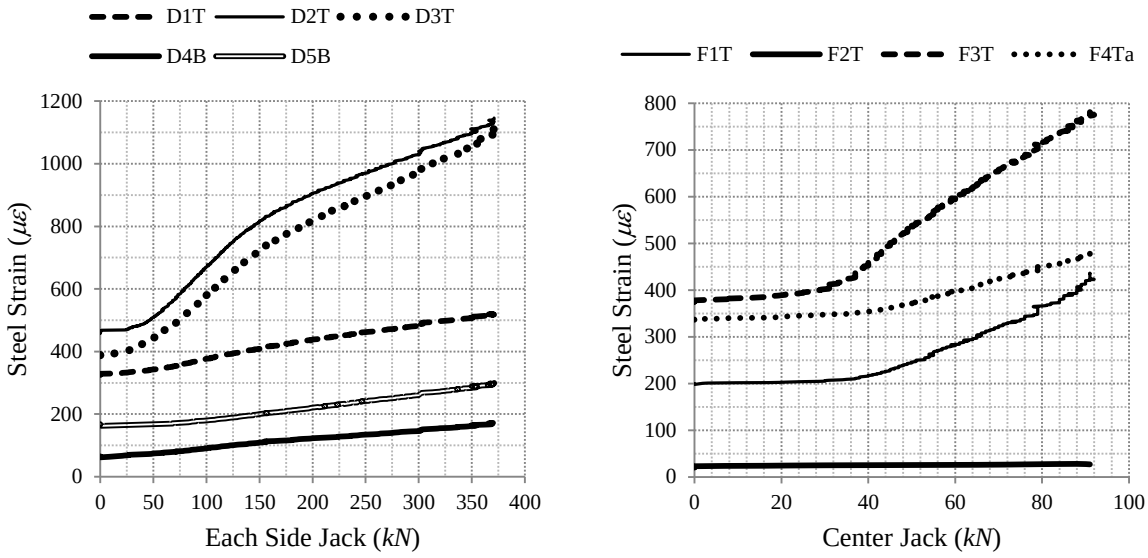
D1T
D2T
D3T
D4B
D5B
Steel Strain (με)
Each Side Jack (kN)
F1T
F2T
F3T
F4Ta
Steel Strain (με)
Center Jack (kN)

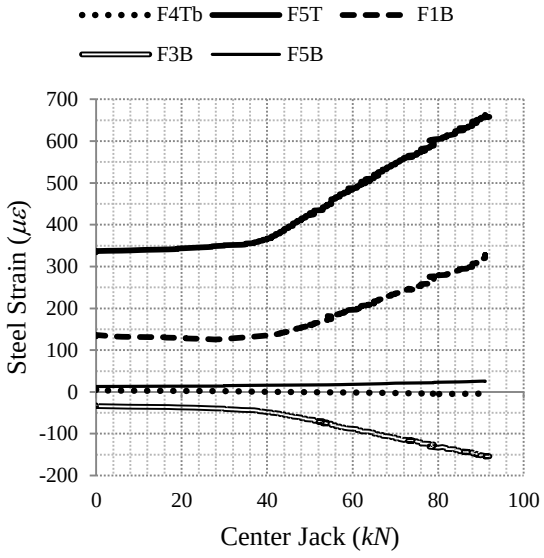
F4Tb
F5T
F1B
F3B
F5B
Steel Strain (με)
Center Jack (kN)

(c)

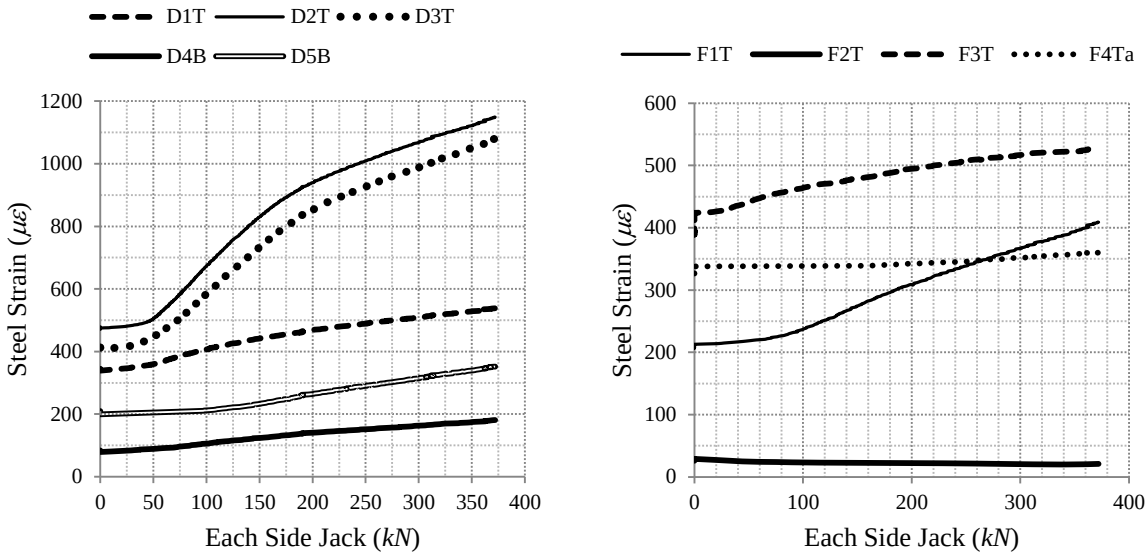
D1T
D2T
D3T
D4B
D5B
Steel Strain (με)
Each Side Jack (kN)
F1T
F2T
F3T
F4Ta
Steel Strain (με)
Each Side Jack (kN)

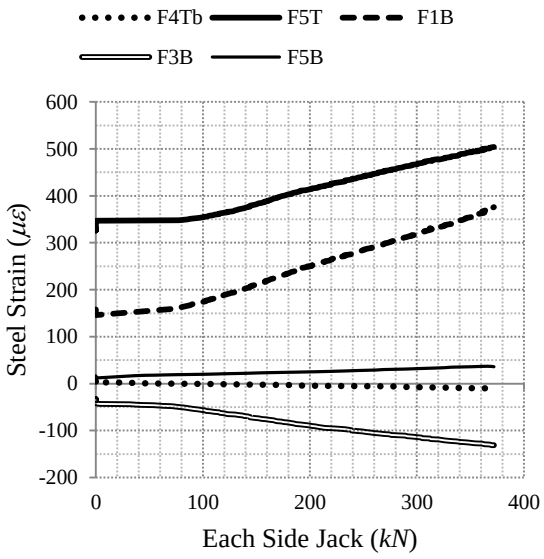
F4Tb
F5T
F1B
F3B
F5B
Steel Strain (με)
Each Side Jack (kN)

(d)

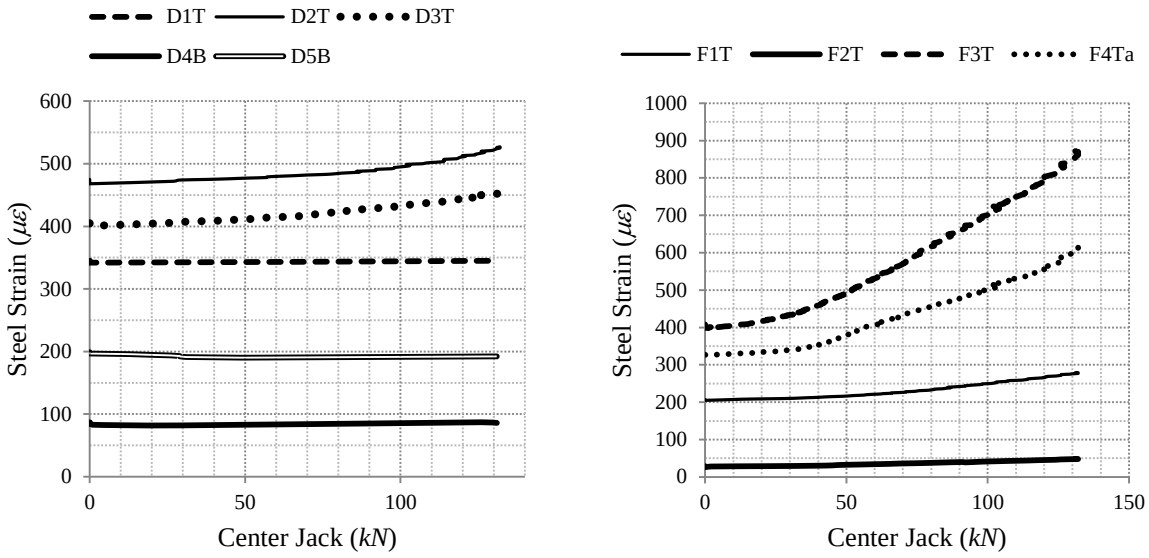
D1T
D2T
D3T
D4B
D5B
Steel Strain (με)
Center Jack (kN)
F1T
F2T
F3T
F4Ta
Steel Strain (με)
Center Jack (kN)

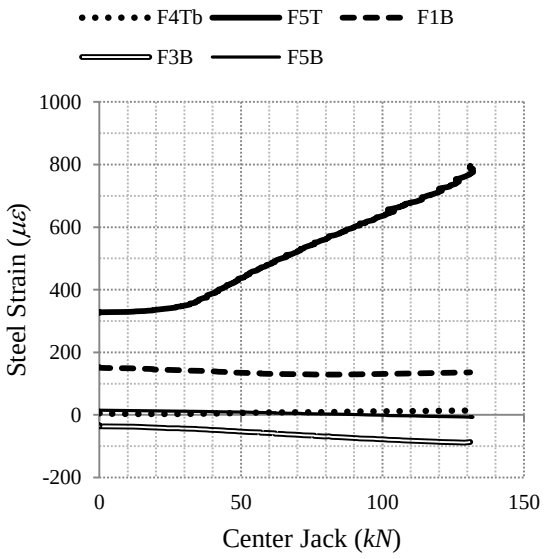
F4Tb
F5T
F1B
F3B
F5B
Steel Strain (με)
Center Jack (kN)

(e)

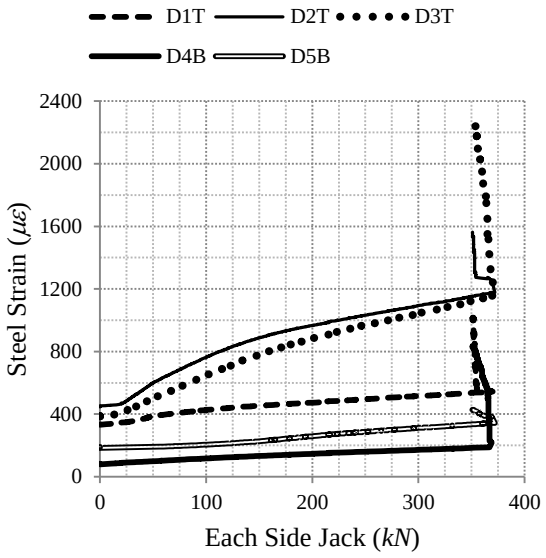
D1T
D2T
D3T
D4B
D5B
Steel Strain (με)
Each Side Jack (kN)

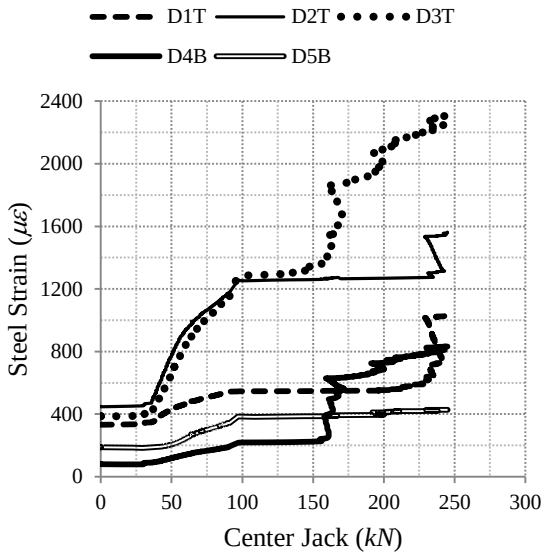
D1T
D2T
D3T
D4B
D5B
Steel Strain (με)
Center Jack (kN)

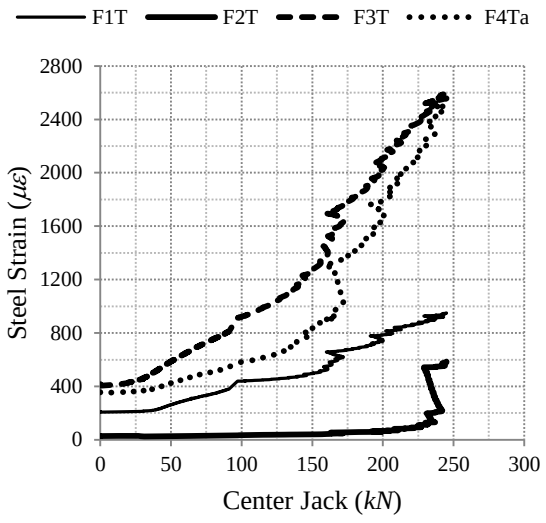
F1T
F2T
F3T
F4Ta
Steel Strain (με)
Center Jack (kN)

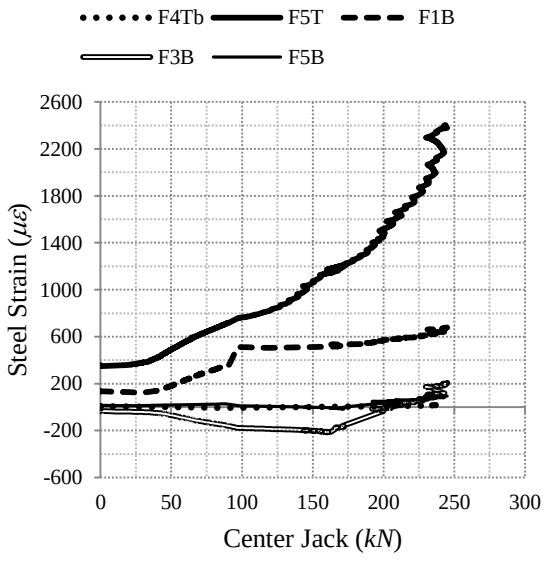
F4Tb
F5T
F1B
F3B
F5B
Steel Strain (με)
Center Jack (kN)

(f)

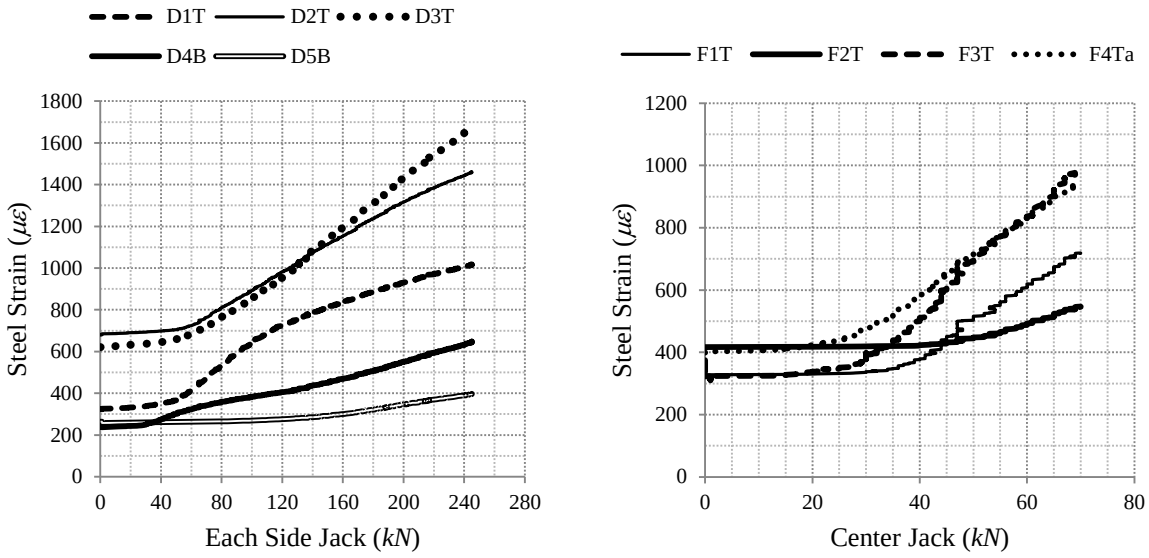

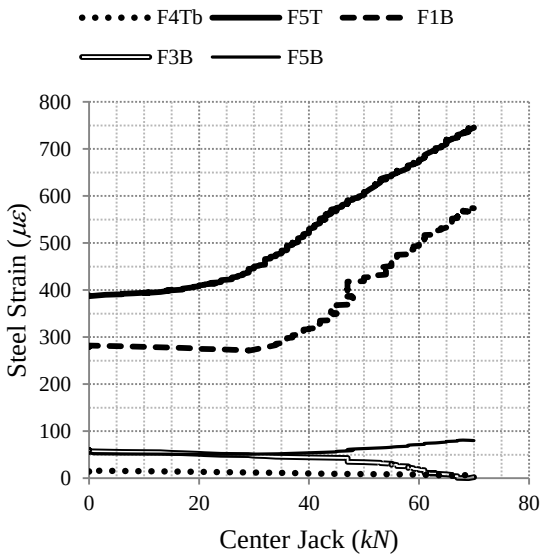

(g)

Fig. A.3 Steel strains in panel B, a) 1st stage, b) 2nd stage, c) 3rd stage, d) one-way tension, e) one-way bending, f) 4th stage, g) 5th stage

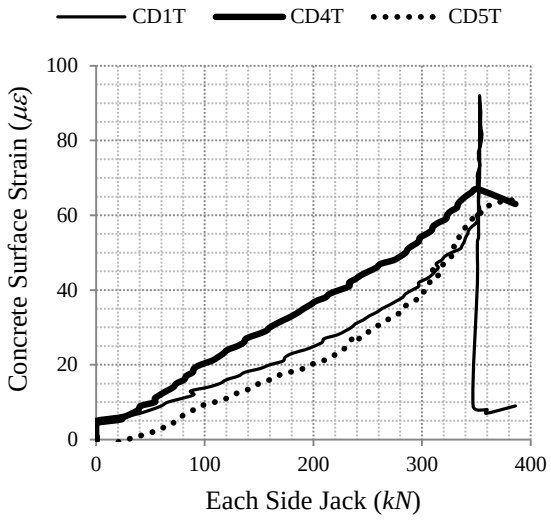
CD1T
CD4T
CD5T
Concrete Surface Strain (με)
Each Side Jack (kN)
0
20
40
60
80
100
0
100
200
300
400

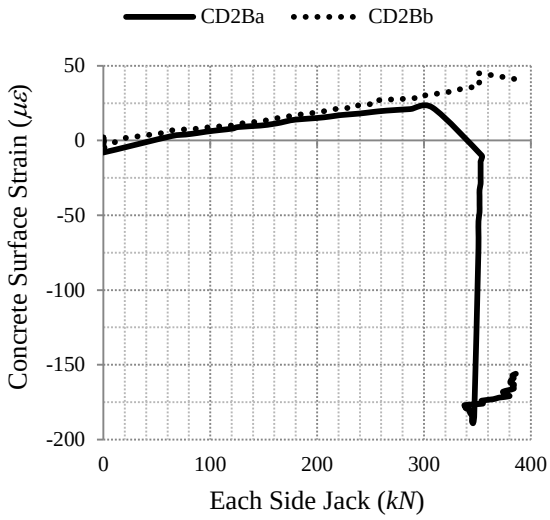
CD2Ba
CD2Bb
Concrete Surface Strain (με)
Each Side Jack (kN)
50
0
-50
-100
-150
-200
0
100
200
300
400

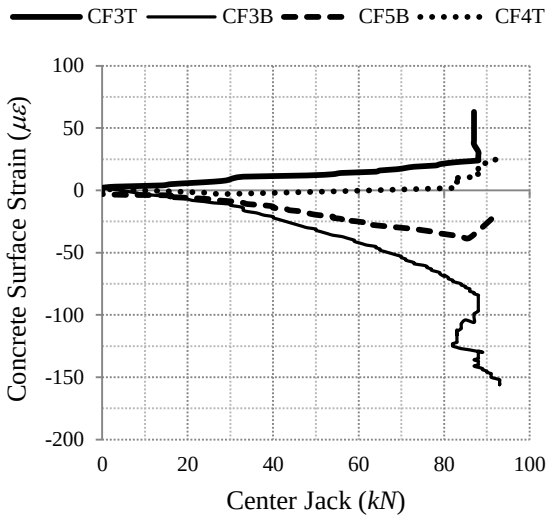
CF3T
CF3B
CF5B
CF4T
Concrete Surface Strain (με)
Center Jack (kN)
100
50
0
-50
-100
-150
-200
0
20
40
60
80
100

(a)

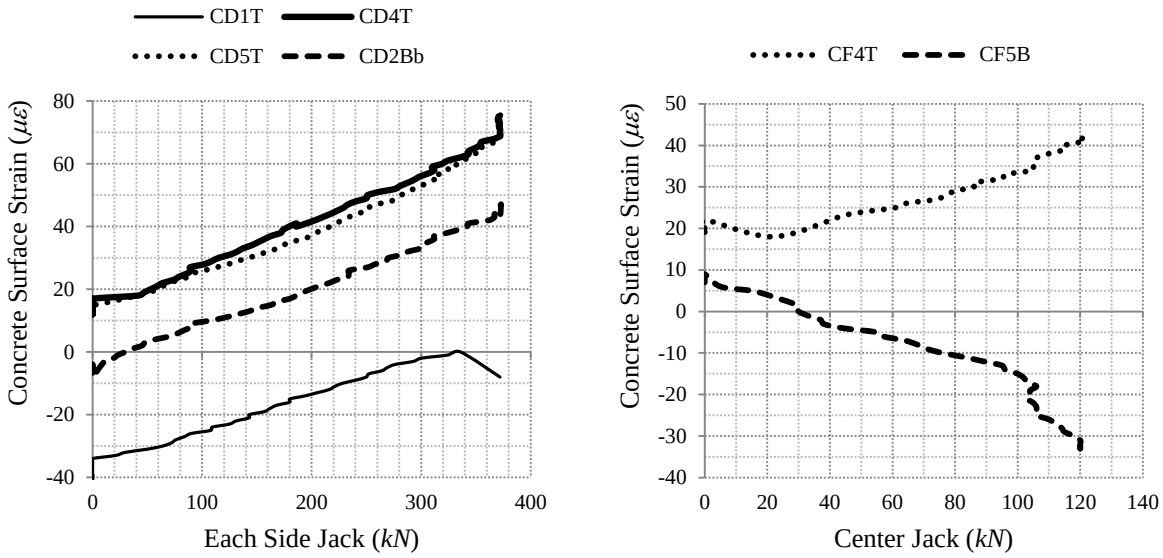
CD1T
CD4T
CD5T
CD2Bb
Concrete Surface Strain (με)
Each Side Jack (kN)
CF4T
CF5B
Concrete Surface Strain (με)
Center Jack (kN)

(b)

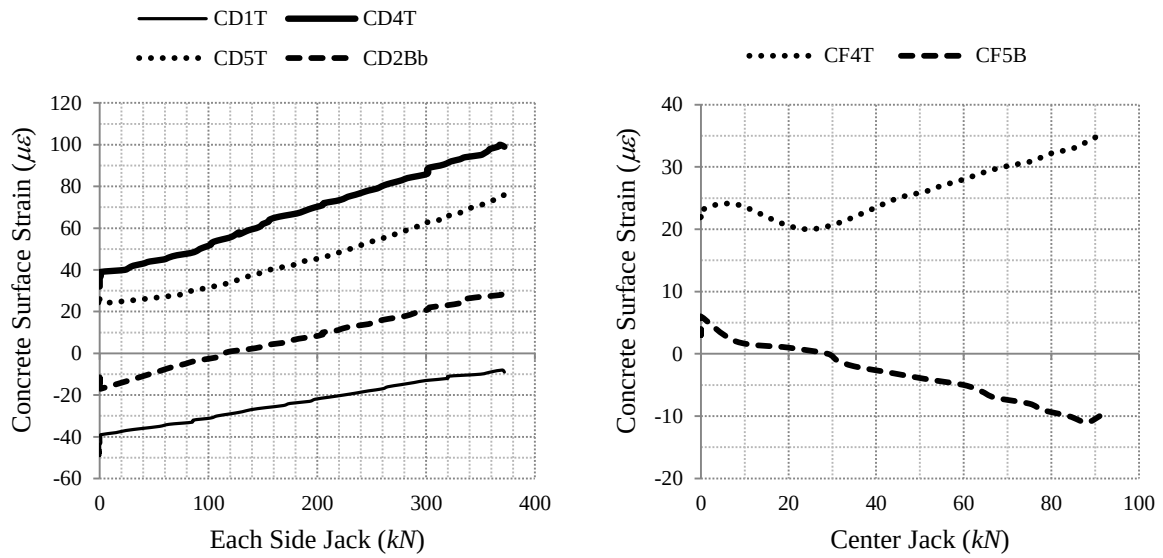
CD1T
CD4T
CD5T
CD2Bb
Concrete Surface Strain (με)
Each Side Jack (kN)
CF4T
CF5B
Concrete Surface Strain (με)
Center Jack (kN)

(c)

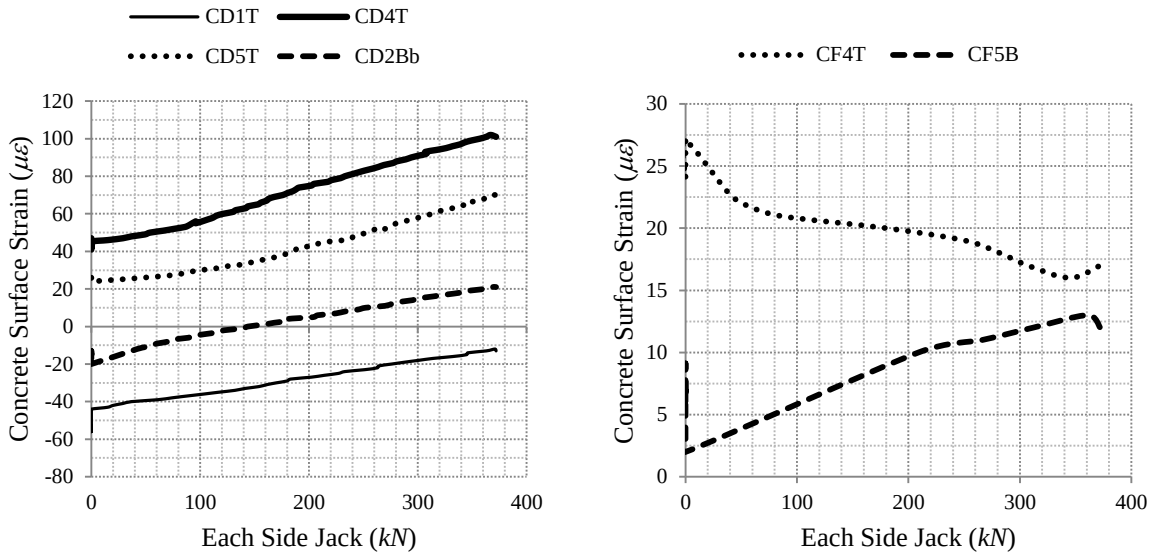
CD1T
CD4T
CD5T
CD2Bb
Concrete Surface Strain (με)
Each Side Jack (kN)
CF4T
CF5B
Concrete Surface Strain (με)
Each Side Jack (kN)

(d)

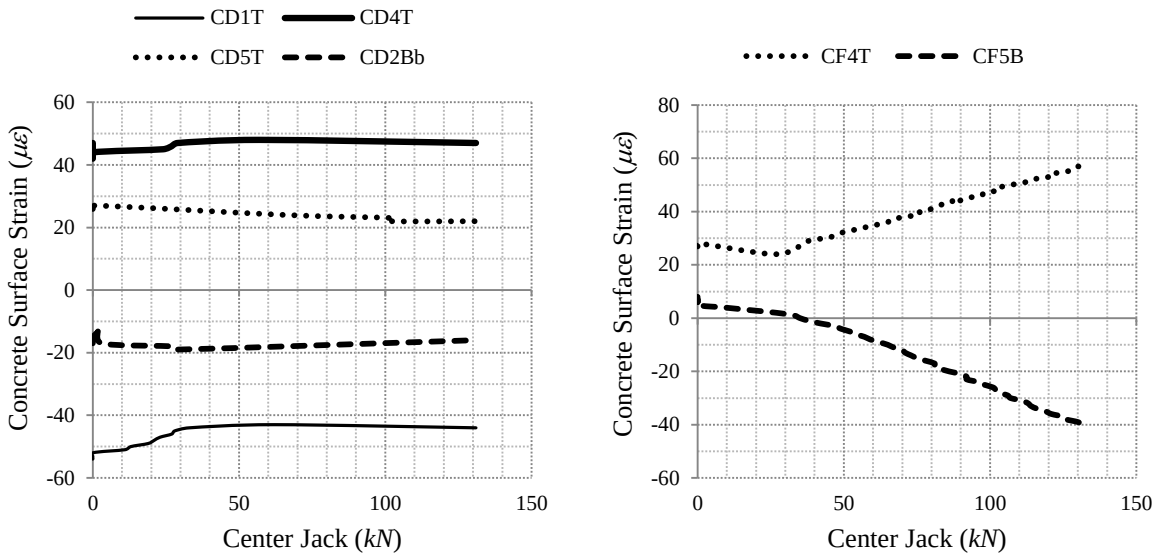
CD1T
CD4T
CD5T
CD2Bb
Concrete Surface Strain (με)
Center Jack (kN)
CF4T
CF5B
Concrete Surface Strain (με)
Center Jack (kN)

(e)

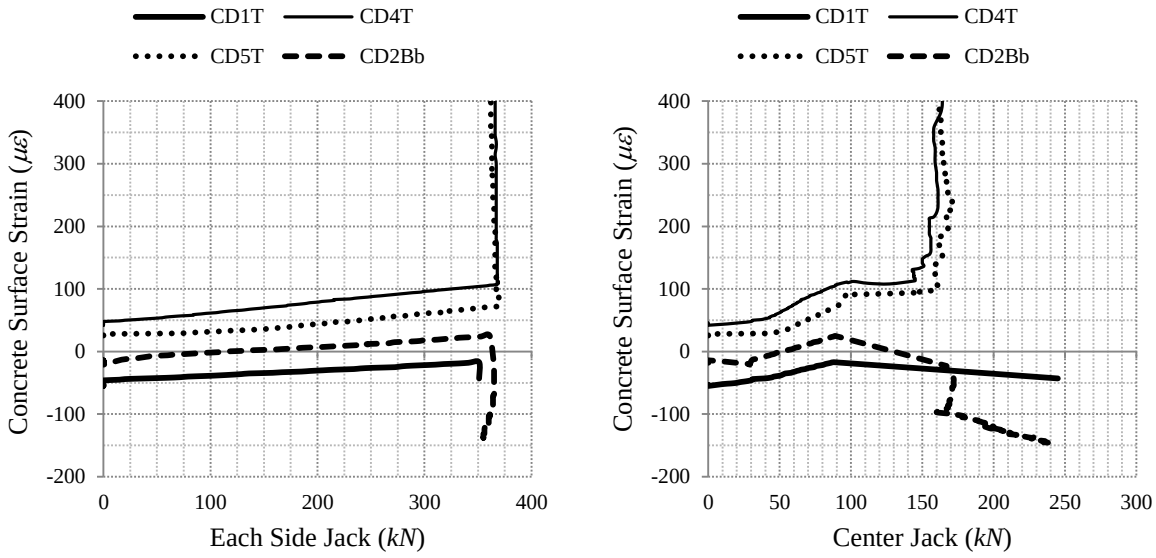
CD1T
CD4T
CD5T
CD2Bb
Concrete Surface Strain (με)
400
300
200
100
0
-100
-200
0
100
200
300
400
Each Side Jack (kN)
CD1T
CD4T
CD5T
CD2Bb
Concrete Surface Strain (με)
400
300
200
100
0
-100
-200
0
50
100
150
200
250
300
Center Jack (kN)

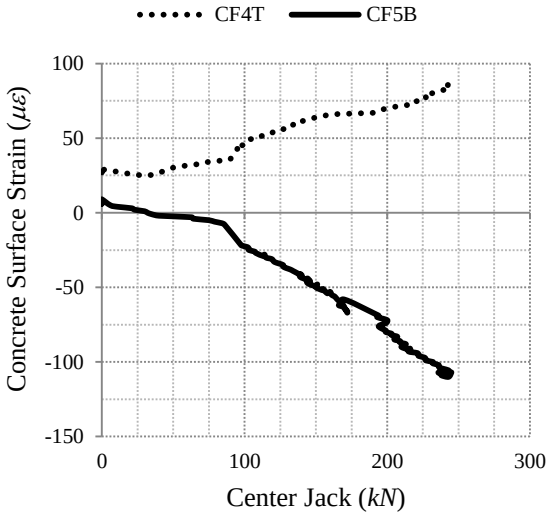
CF4T
CF5B
Concrete Surface Strain (με)
100
50
0
-50
-100
-150
0
100
200
300
Center Jack (kN)

(f)

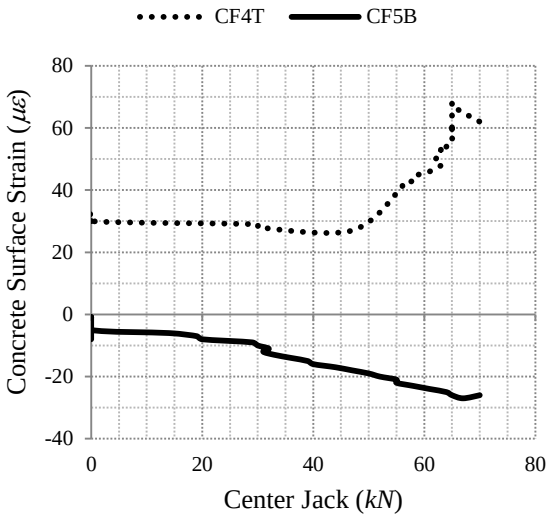

(g)

Fig. A.4 Concrete strains in panel B, a) 1st stage, b) 2nd stage, c) 3rd stage, d) one-way tension, e) one-way bending, f) 4th stage, g) 5th stage

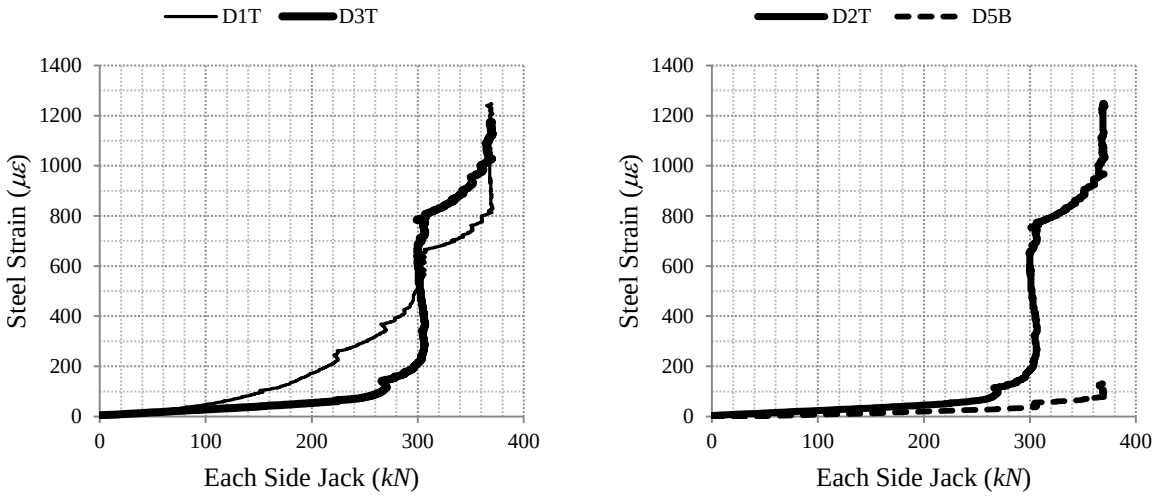

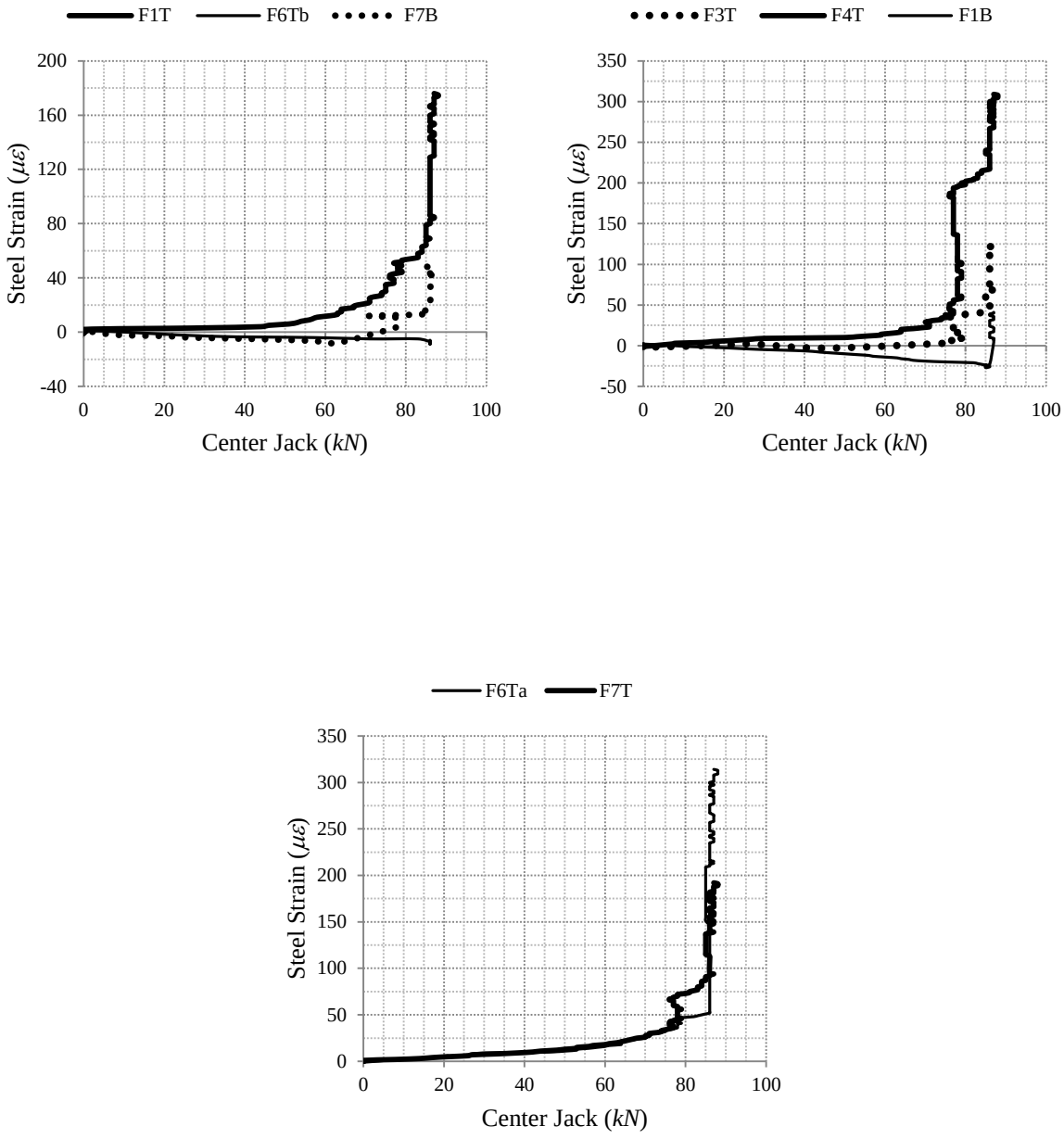
F1T
F6Tb
F7B
Steel Strain (με)
Center Jack (kN)
F3T
F4T
F1B
Steel Strain (με)
Center Jack (kN)
F6Ta
F7T
Steel Strain (με)
Center Jack (kN)

(a)

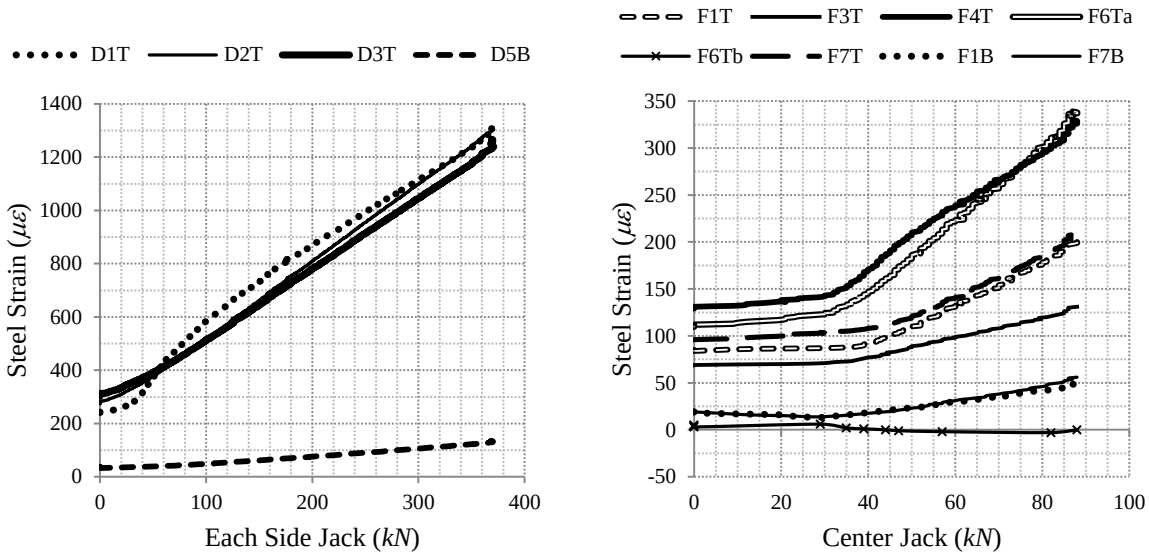
D1T
D2T
D3T
D5B
Steel Strain (με)
Each Side Jack (kN)
F1T
F3T
F4T
F6Ta
F6Tb
F7T
F1B
F7B
Steel Strain (με)
Center Jack (kN)

(b)

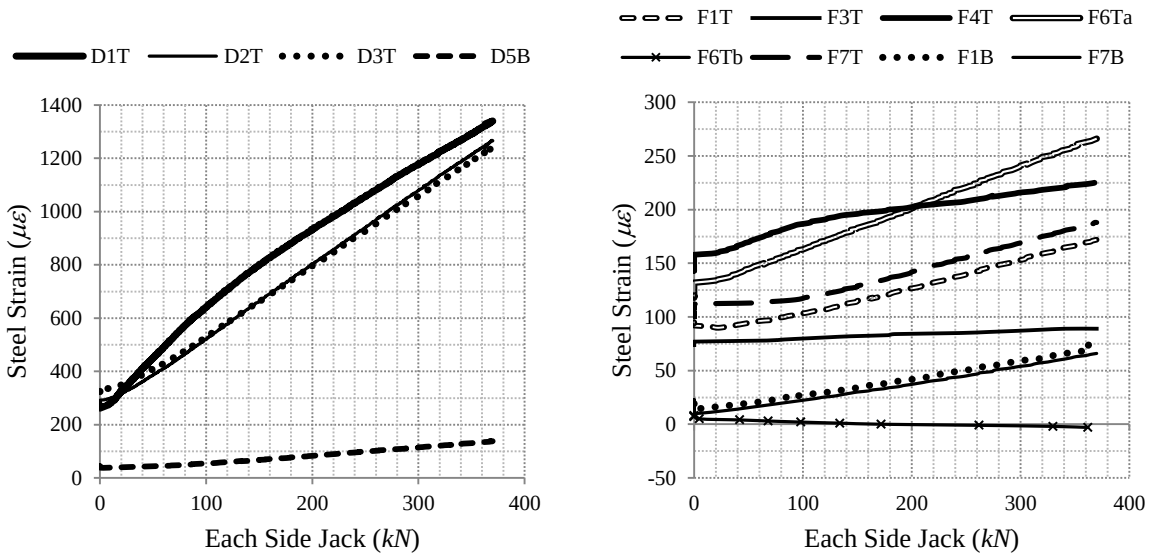
D1T
D2T
D3T
D5B
Steel Strain (με)
Each Side Jack (kN)
F1T
F3T
F4T
F6Ta
F6Tb
F7T
F1B
F7B
Steel Strain (με)
Each Side Jack (kN)

(c)

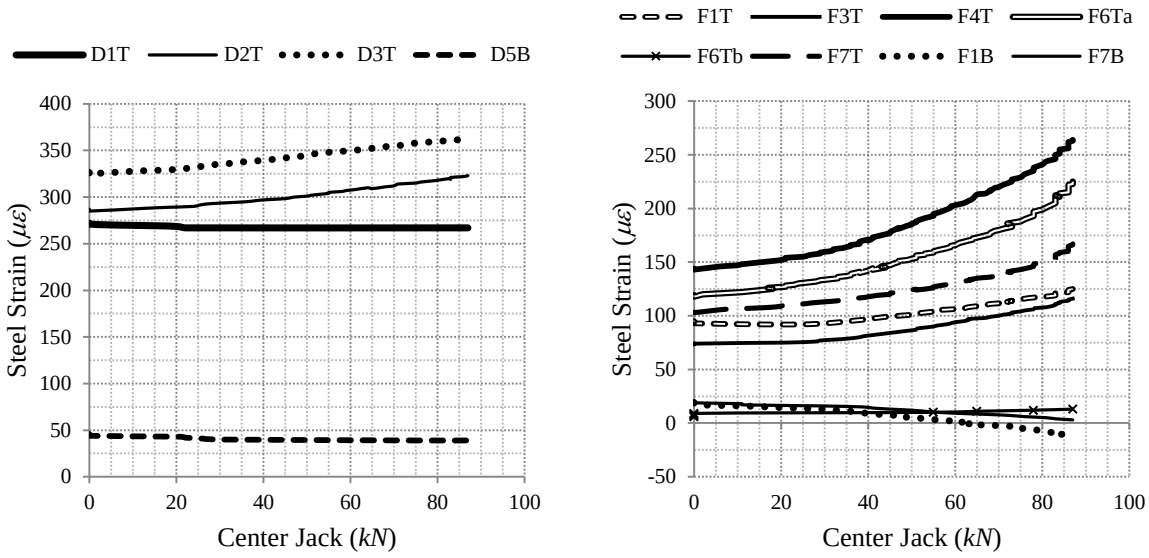
D1T
D2T
D3T
D5B
Steel Strain (με)
Center Jack (kN)
F1T
F3T
F4T
F6Ta
F6Tb
F7T
F1B
F7B
Steel Strain (με)
Center Jack (kN)

(d)

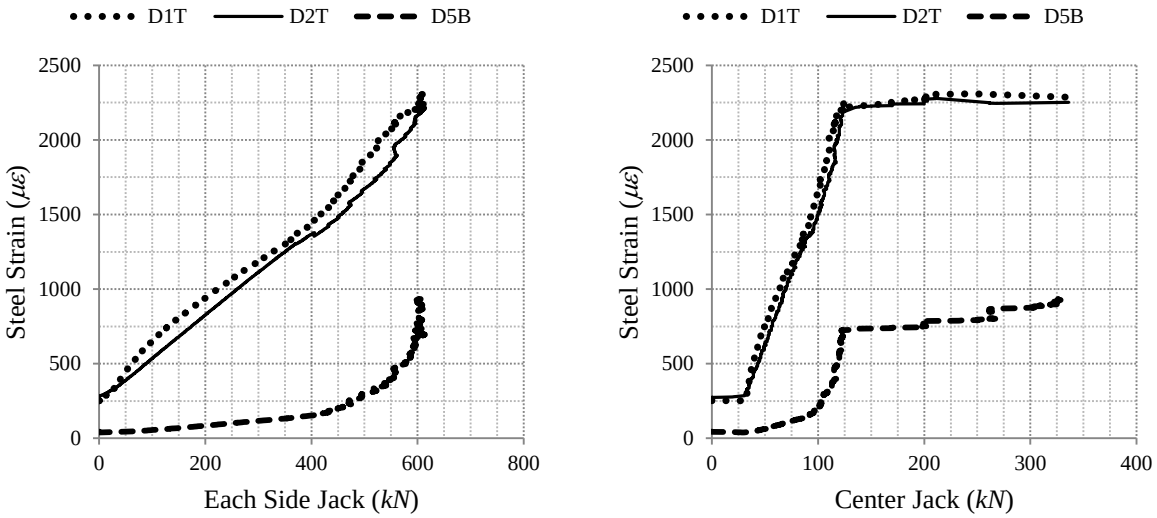
D1T
D2T
D5B
Steel Strain (με)
Each Side Jack (kN)
D1T
D2T
D5B
Steel Strain (με)
Center Jack (kN)

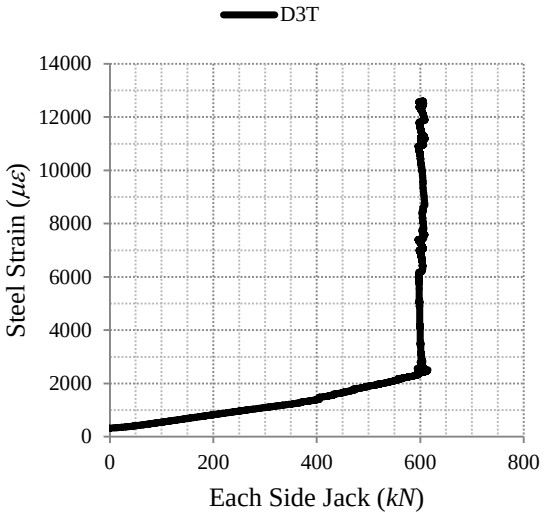
D3T
Steel Strain (με)
Each Side Jack (kN)

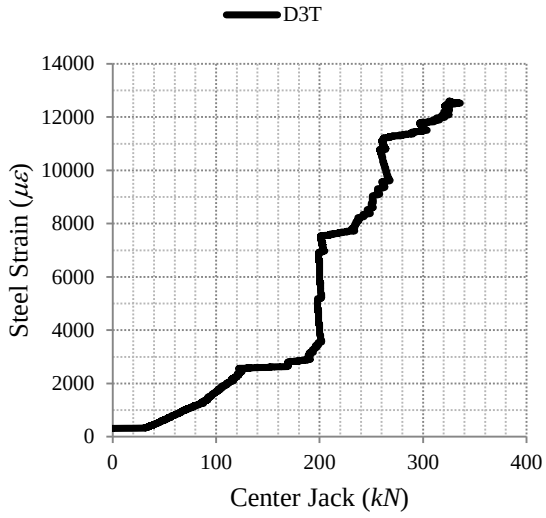
D3T
Steel Strain (με)
Center Jack (kN)

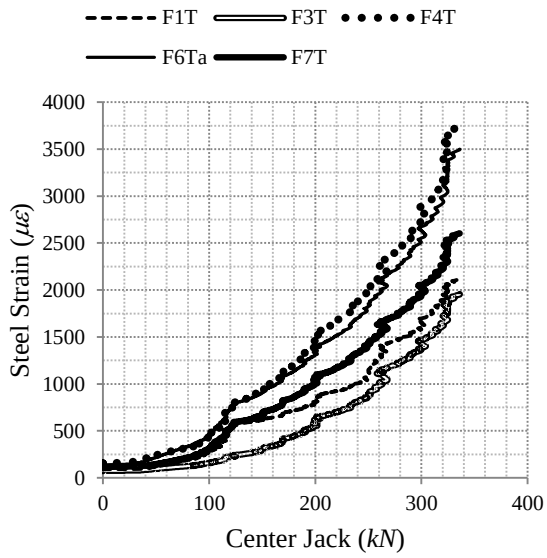
F1T
F3T
F4T
F6Ta
F7T
Steel Strain (με)
Center Jack (kN)

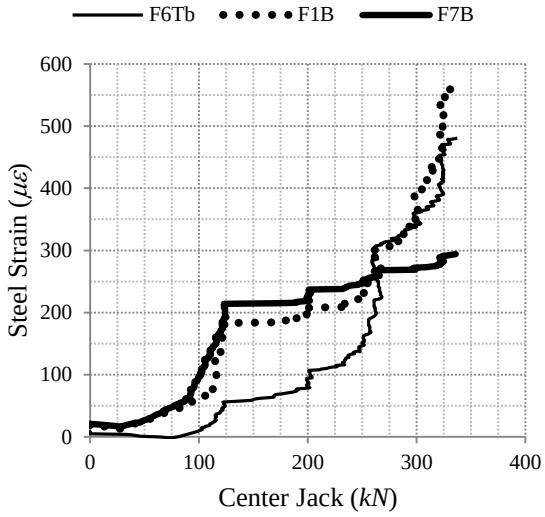
F6Tb
F1B
F7B
Steel Strain (με)
Center Jack (kN)

(e)

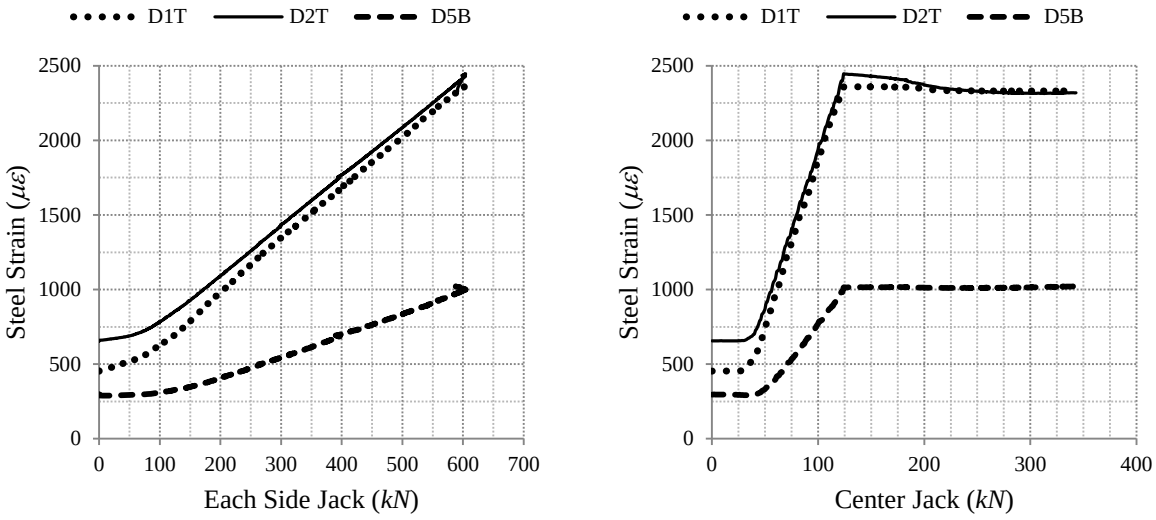

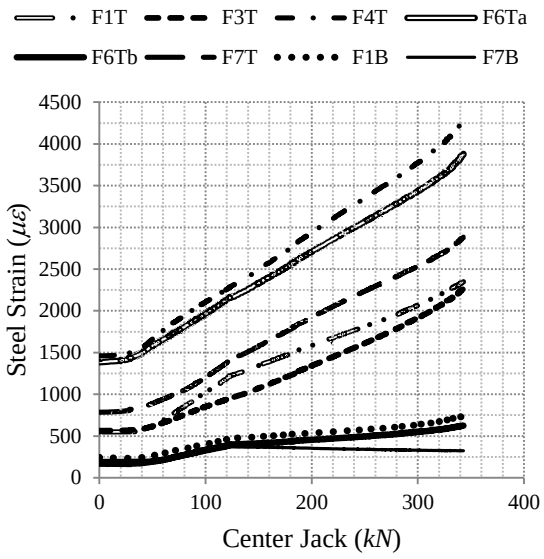

(f)

Fig. A.5 Steel strains in panel C, a) 1st stage, b) 2nd stage, c) one-way tension, d) one-way bending, e) 3rd stage, f) 4th stage

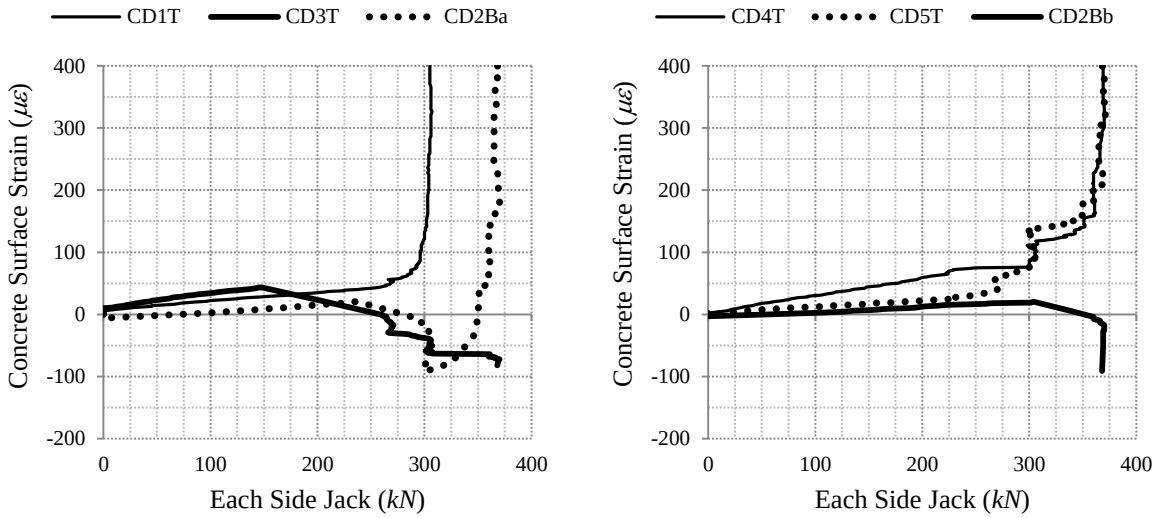
CD1T
CD3T
CD2Ba
CD4T
CD5T
CD2Bb
Concrete Surface Strain (με)
Each Side Jack (kN)
400
300
200
100
0
-100
-200
0
100
200
300
400

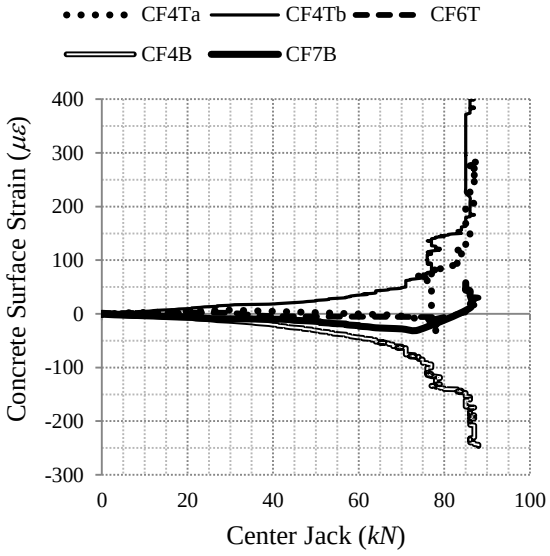
CF4Ta
CF4Tb
CF6T
CF4B
CF7B
Concrete Surface Strain (με)
Center Jack (kN)
400
300
200
100
0
-100
-200
-300
0
20
40
60
80
100

(a)

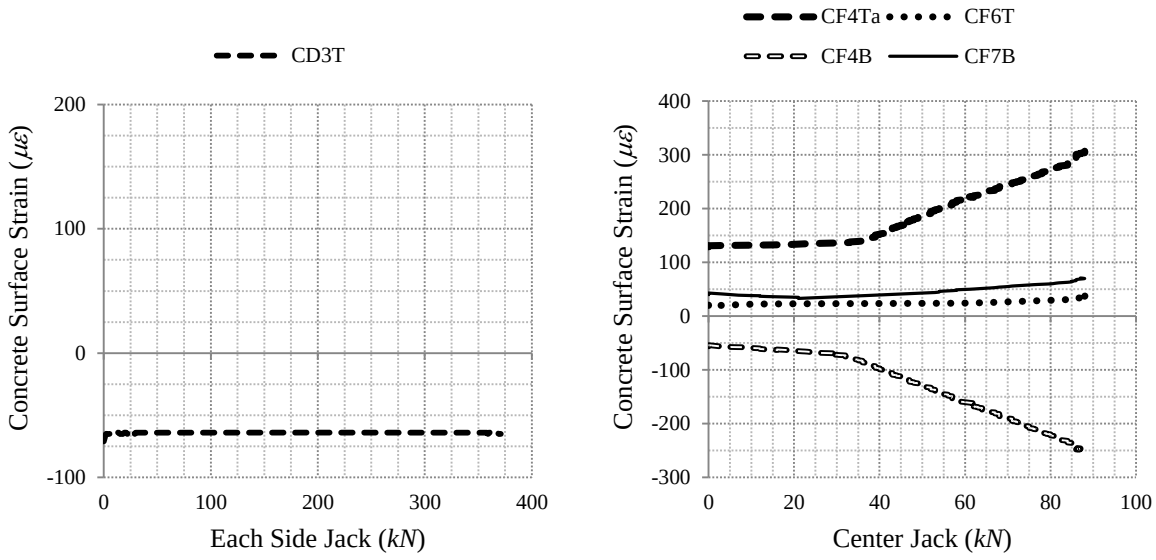
CD3T
CF4Ta
CF6T
CF4B
CF7B
Concrete Surface Strain (με)
Each Side Jack (kN)
Center Jack (kN)

(b)

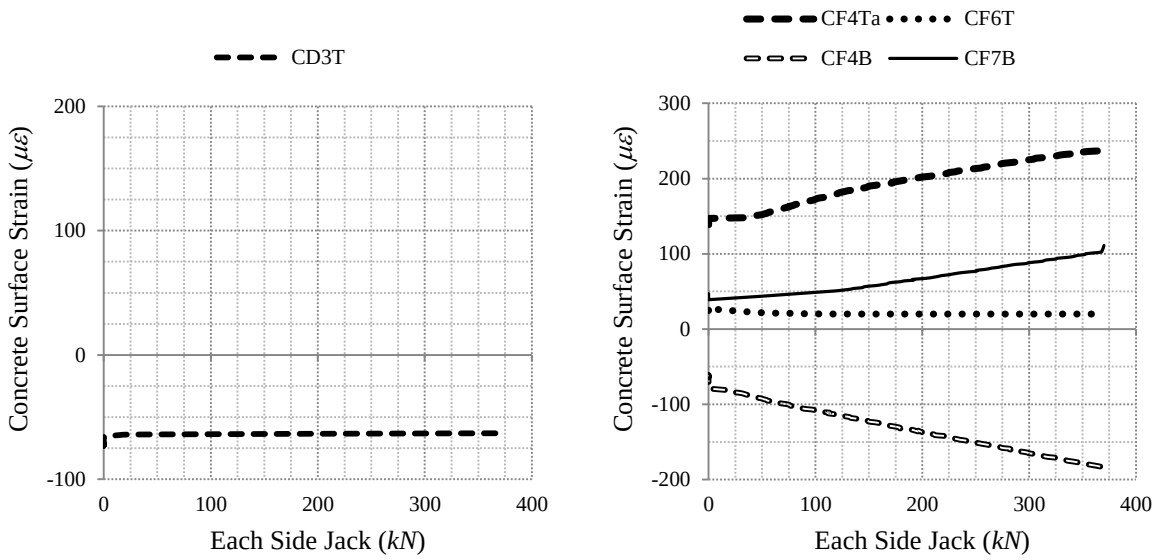
CD3T
CF4Ta
CF6T
CF4B
CF7B
Concrete Surface Strain (με)
Each Side Jack (kN)

(c)

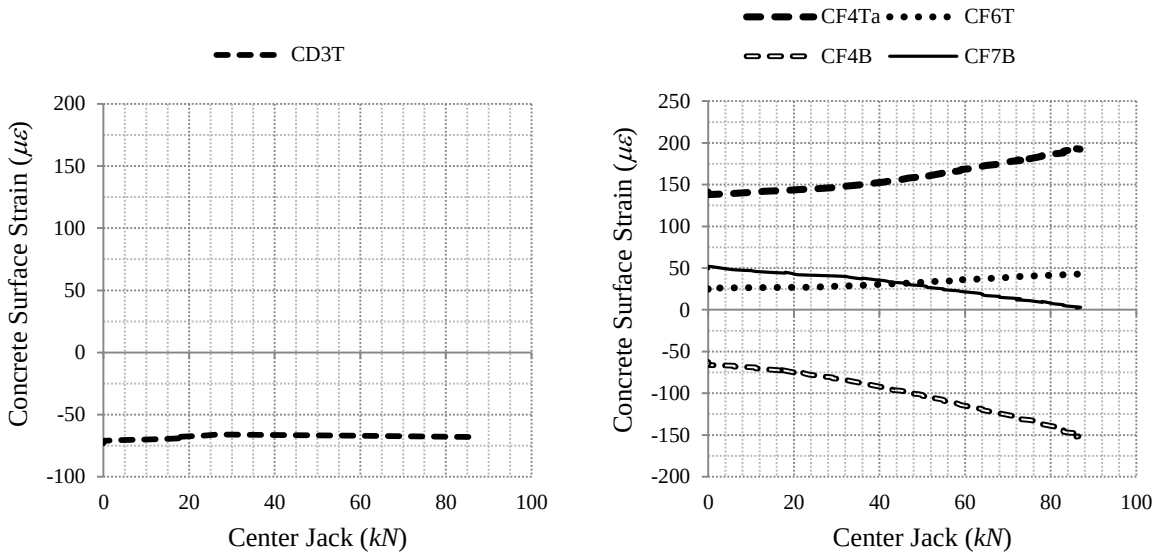

(d)

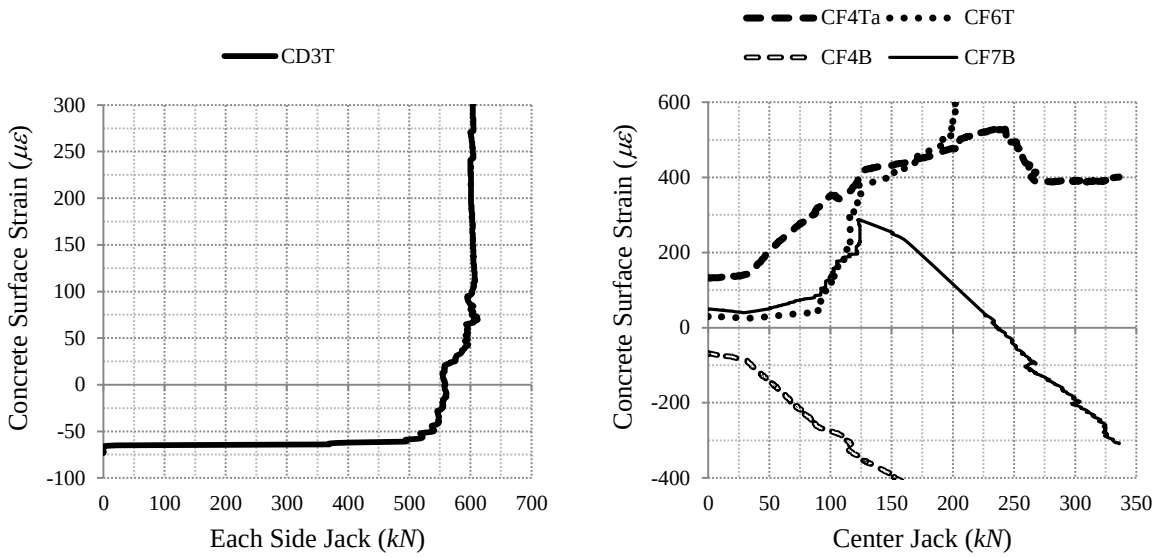

(e)

Fig. A.6 Concrete strains in panel C, a) 1st stage, b) 2nd stage, c) one-way tension, d) one-way bending, e) 3rd stage

A.2 Total Elongation

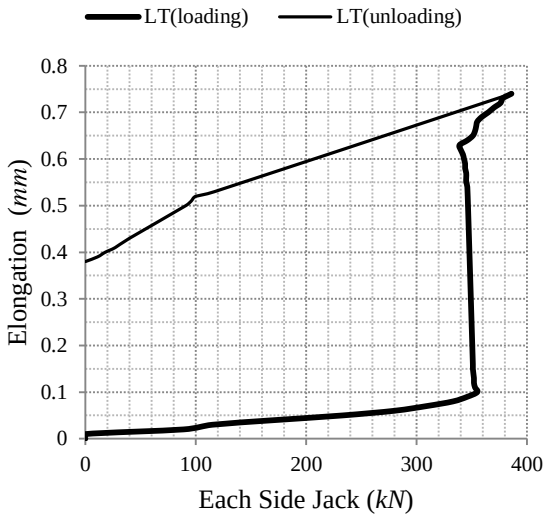

(a)

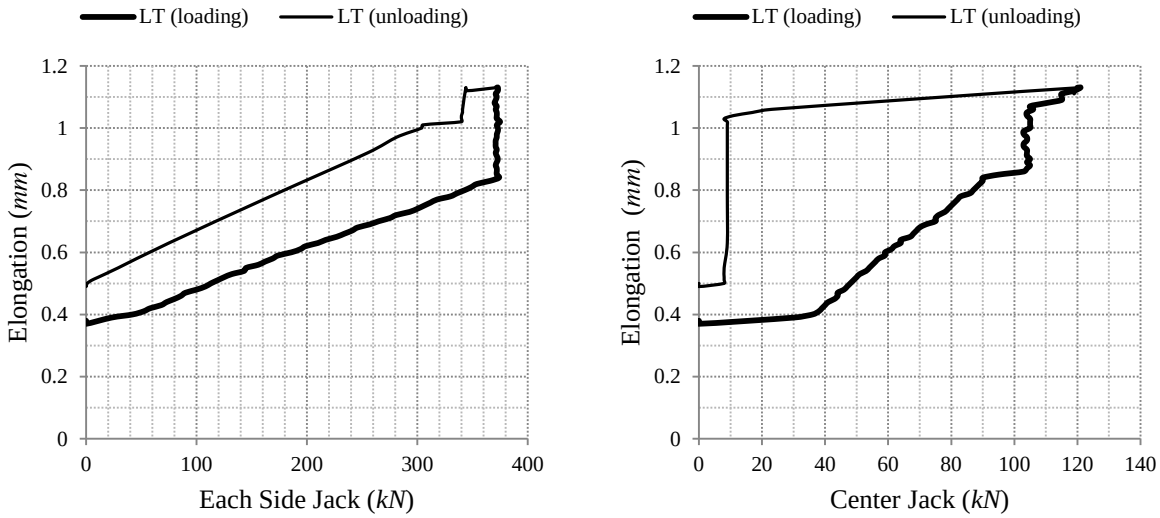

(b)

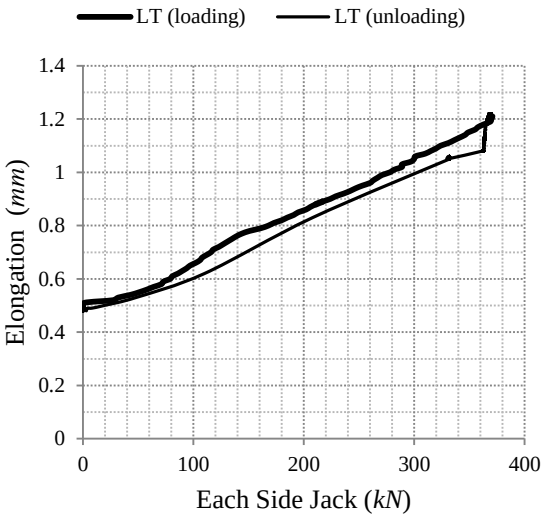
LT (loading)
LT (unloading)
Elongation (mm)
Each Side Jack (kN)
0
0.2
0.4
0.6
0.8
1
1.2
1.4
0
100
200
300
400

(c)

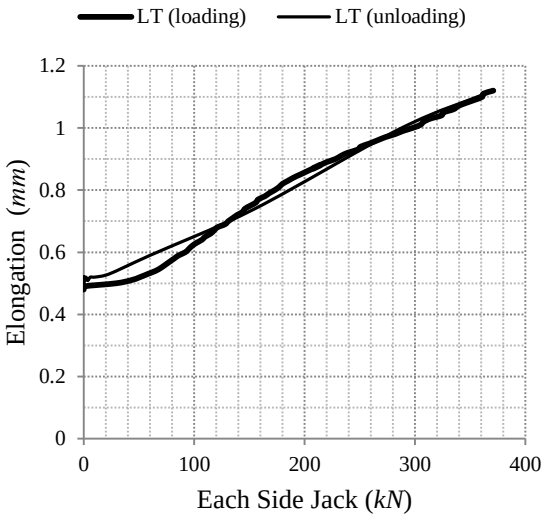
LT (loading)
LT (unloading)
Elongation (mm)
Each Side Jack (kN)
0
0.2
0.4
0.6
0.8
1
1.2
0
100
200
300
400

(d)

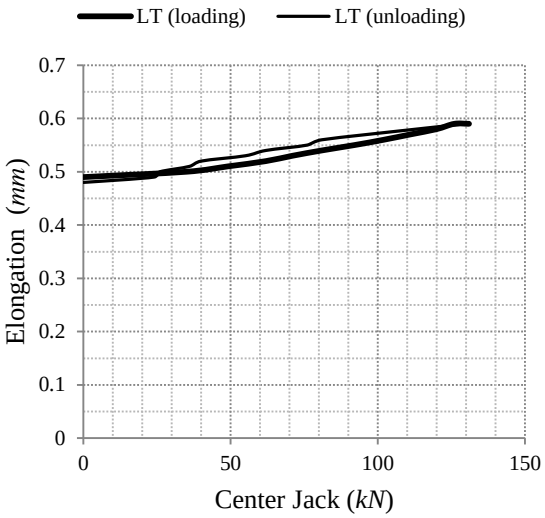
LT (loading)
LT (unloading)
Elongation (mm)
Center Jack (kN)
0
0.1
0.2
0.3
0.4
0.5
0.6
0.7
0
50
100
150

(e)

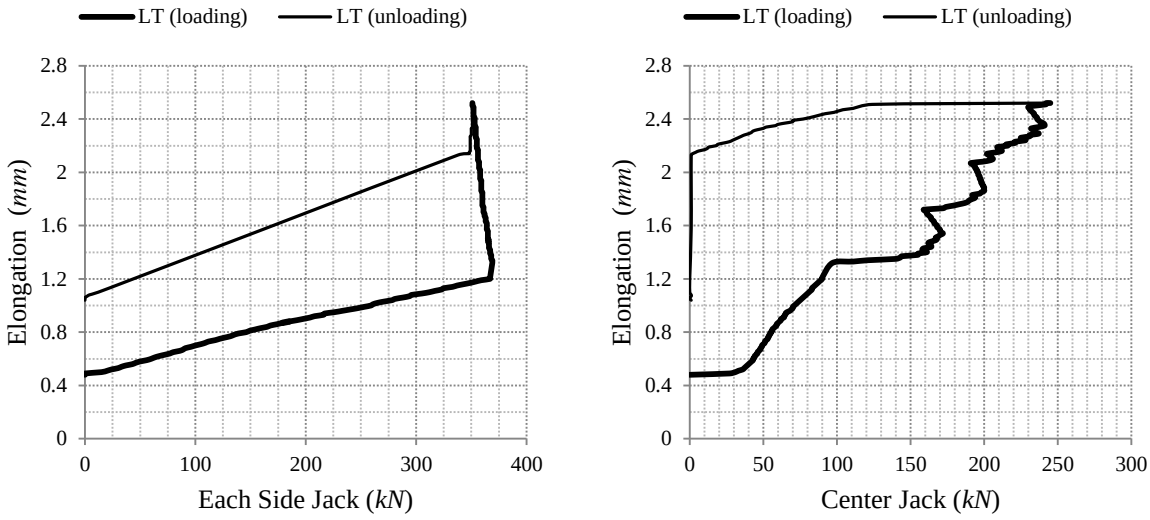

(f)

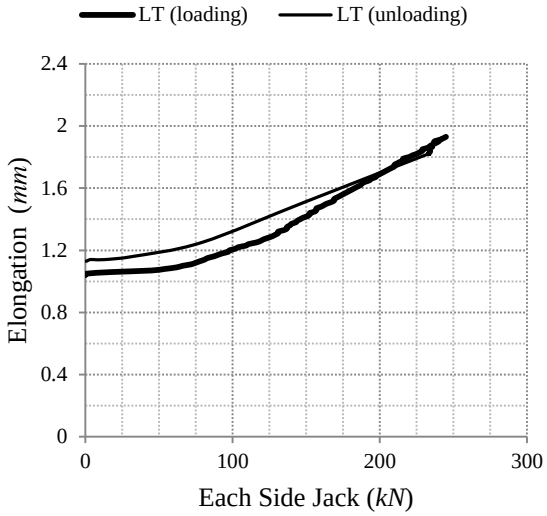

(g)

Fig. A.7 Total elongation of panel B (LVDT LT), a) 1st stage, b) 2nd stage, c) 3rd stage, d) one-way tension, e) one-way bending, f) 4th stage, g) 5th stage

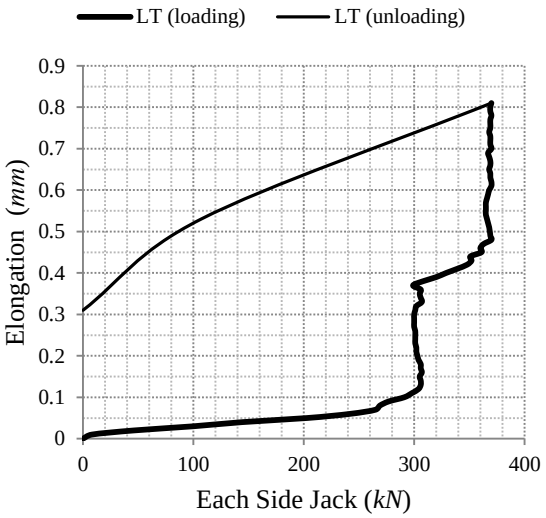
LT (loading)
LT (unloading)
Elongation (mm)
0
0.1
0.2
0.3
0.4
0.5
0.6
0.7
0.8
0.9
0
100
200
300
400
Each Side Jack (kN)

(a)

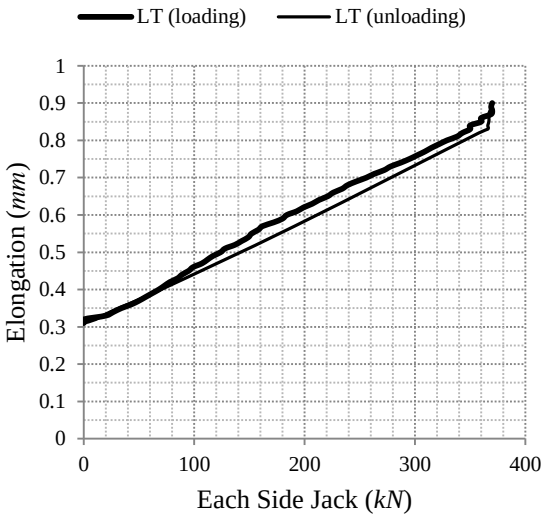
LT (loading)
LT (unloading)
Elongation (mm)
0
0.1
0.2
0.3
0.4
0.5
0.6
0.7
0.8
0.9
1
0
100
200
300
400
Each Side Jack (kN)

(b)

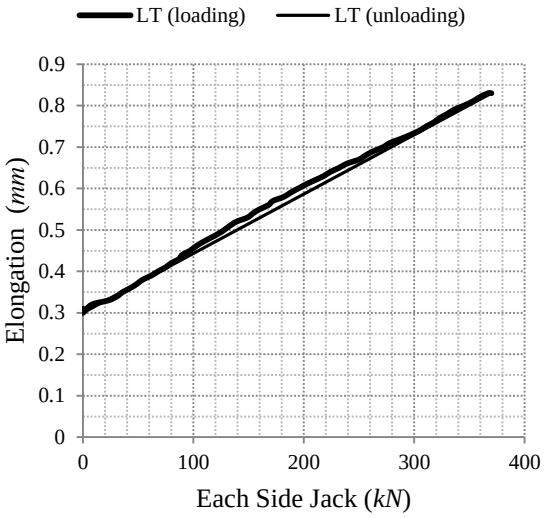
LT (loading)
LT (unloading)
Elongation (mm)
0
0.1
0.2
0.3
0.4
0.5
0.6
0.7
0.8
0.9
0
100
200
300
400
Each Side Jack (kN)

(c)

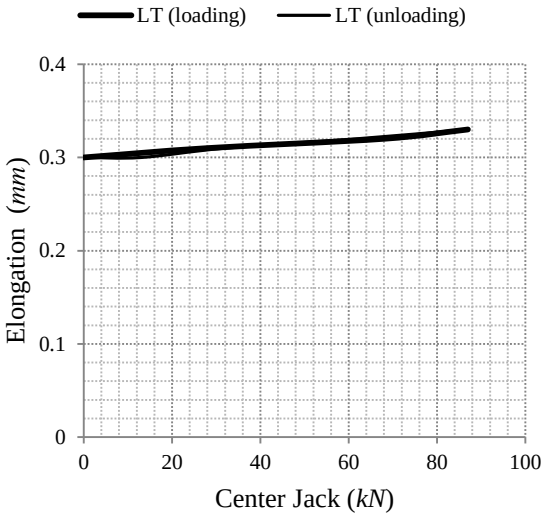
LT (loading)
LT (unloading)
Elongation (mm)
0
0.1
0.2
0.3
0.4
0
20
40
60
80
100
Center Jack (kN)

(d)

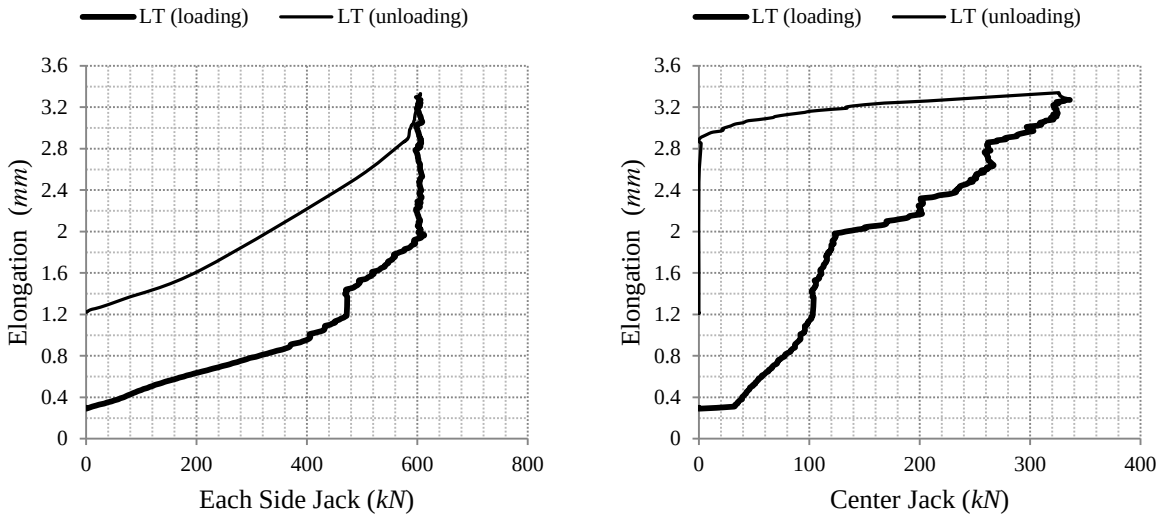

(e)

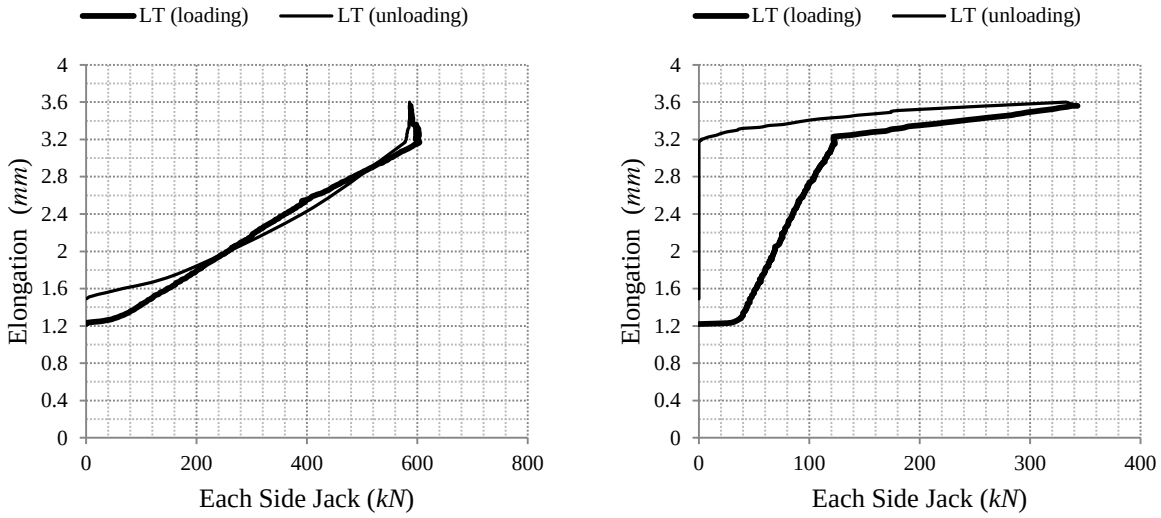

(f)

Fig. A.8 Total elongation of panel C (LVDT LT), a) 1st stage, b) 2nd stage, c) one-way tension, d) one-way bending, e) 3rd stage, f) 4th stage

A.3 Crack Widths

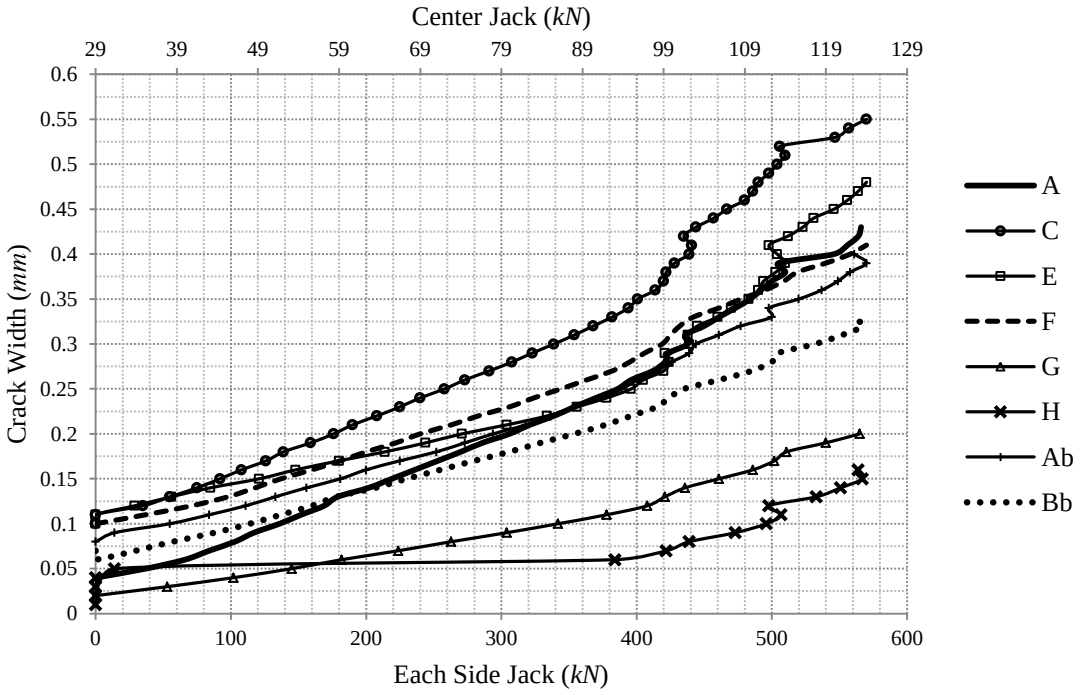

(a)

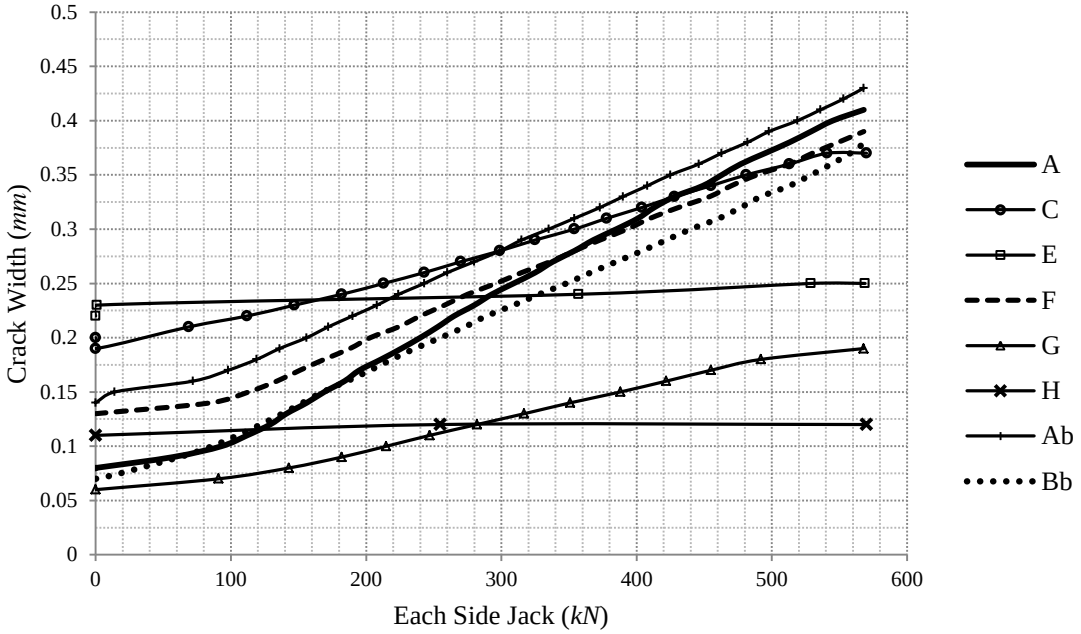

(b)

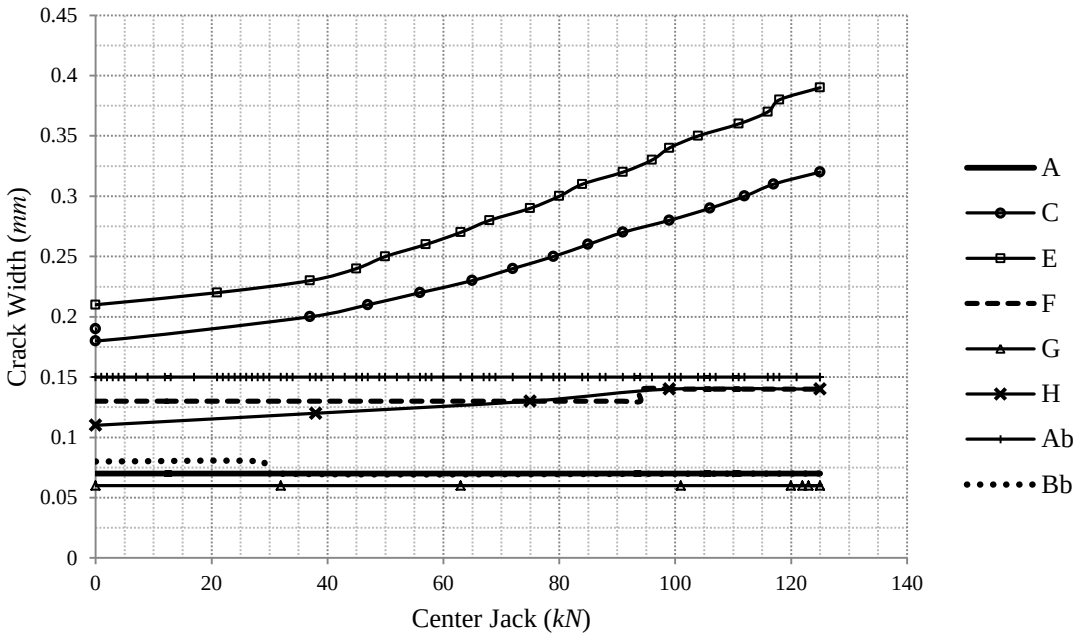
0.45
0.4
0.35
0.3
0.25
0.2
0.15
0.1
0.05
0
Crack Width (mm)
0
20
40
60
80
100
120
140
Center Jack (kN)
A
C
E
F
G
H
Ab
Bb

(c)

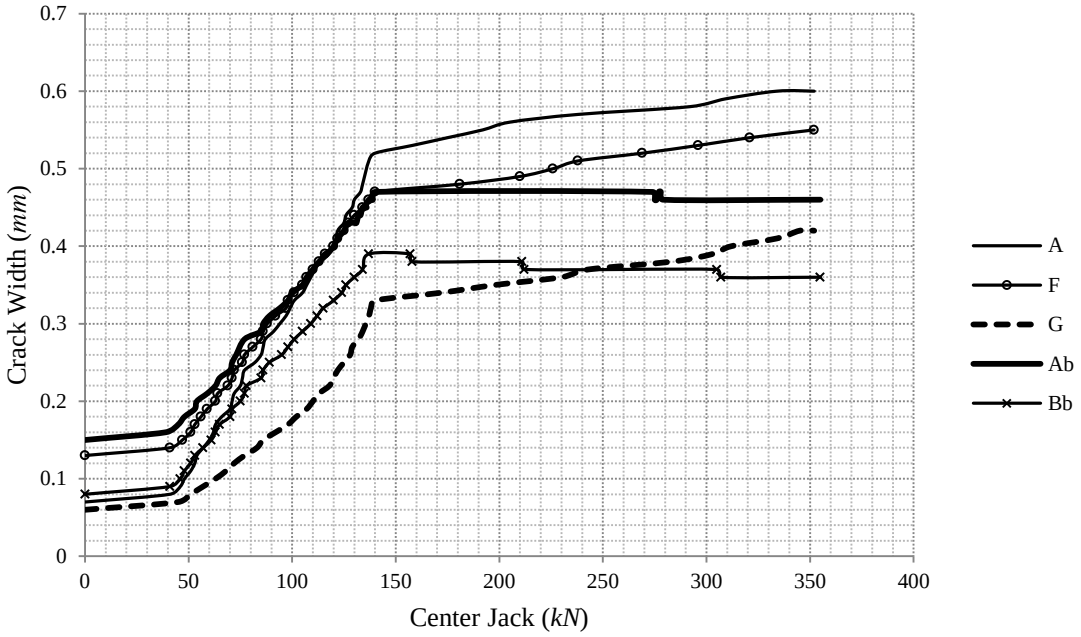
0.7
0.6
0.5
0.4
0.3
0.2
0.1
0
Crack Width (mm)
0
50
100
150
200
250
300
350
400
Center Jack (kN)
A
F
G
Ab
Bb

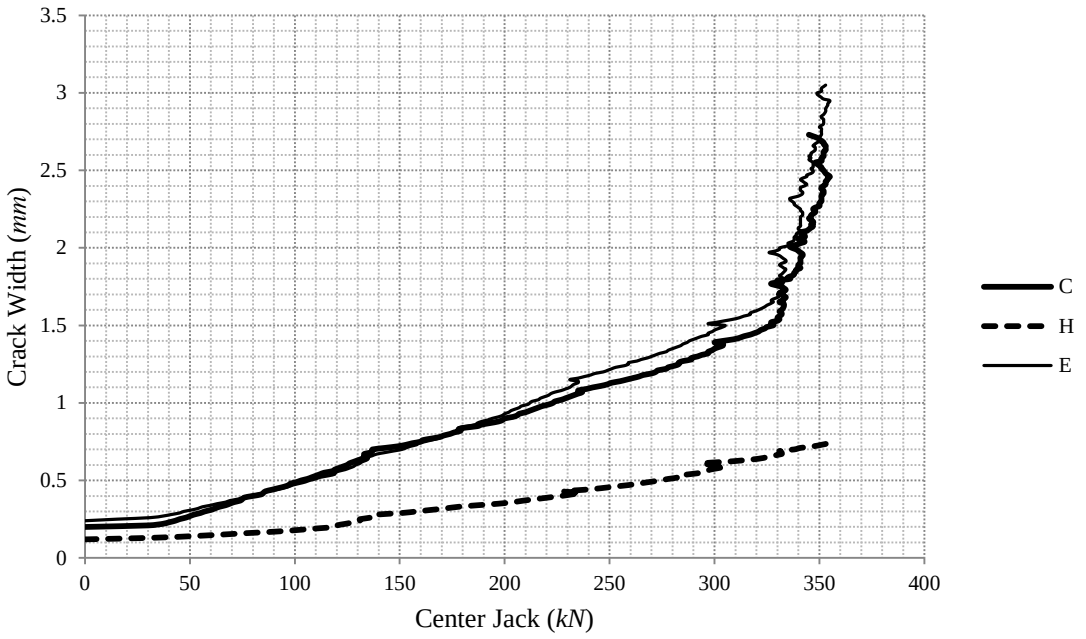

(d)

Fig. A.9 Crack widths in panel A, a) 2nd stage, b) one-way tension, c) one-way bending, d) 3rd stage

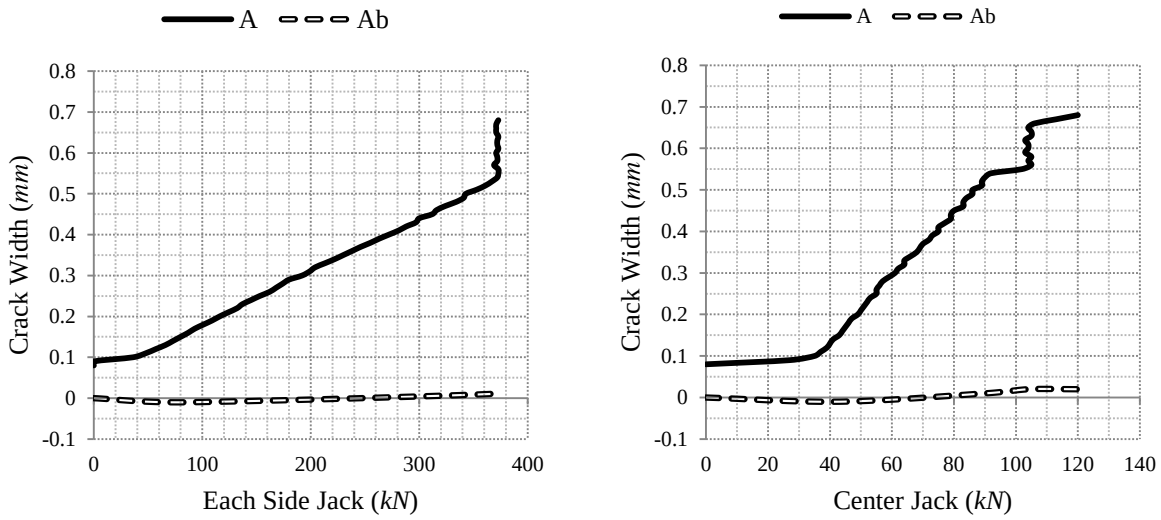

(a)

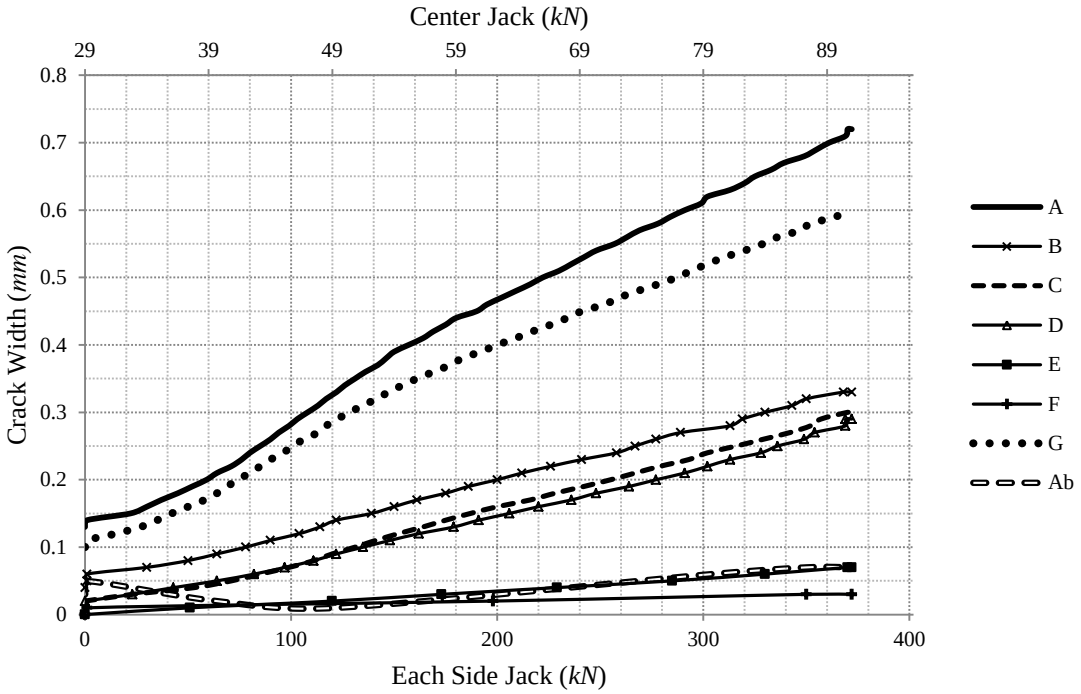
Center Jack (kN)
29
39
49
59
69
79
89
Crack Width (mm)
0.8
0.7
0.6
0.5
0.4
0.3
0.2
0.1
0
0
100
200
300
400
Each Side Jack (kN)
A
B
C
D
E
F
G
Ab

(b)

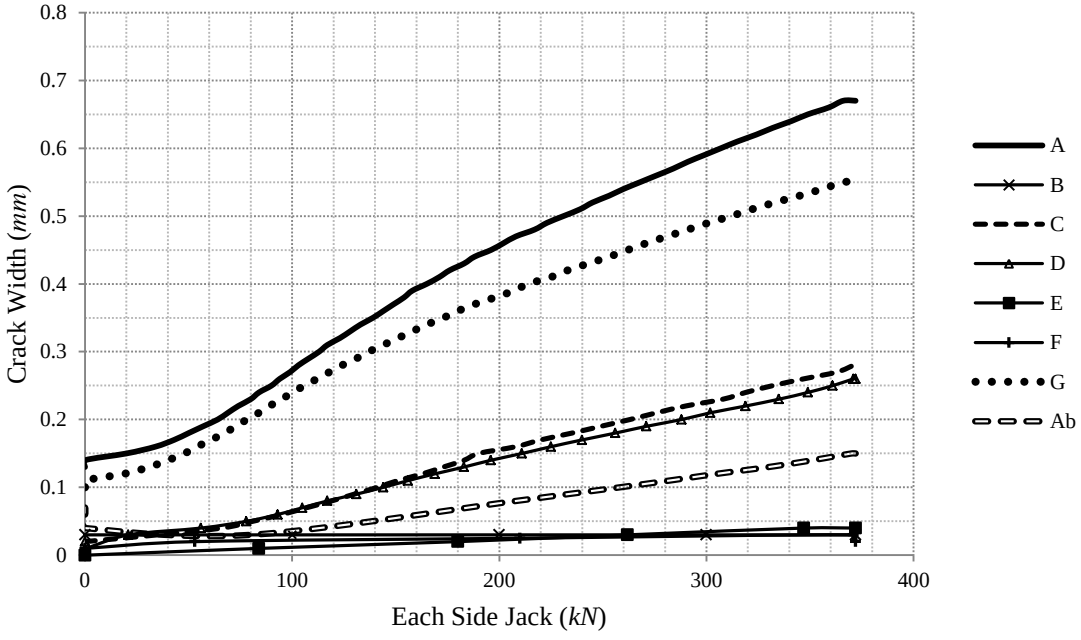
Crack Width (mm)
0.8
0.7
0.6
0.5
0.4
0.3
0.2
0.1
0
0
100
200
300
400
Each Side Jack (kN)
A
B
C
D
E
F
G
Ab

(c)

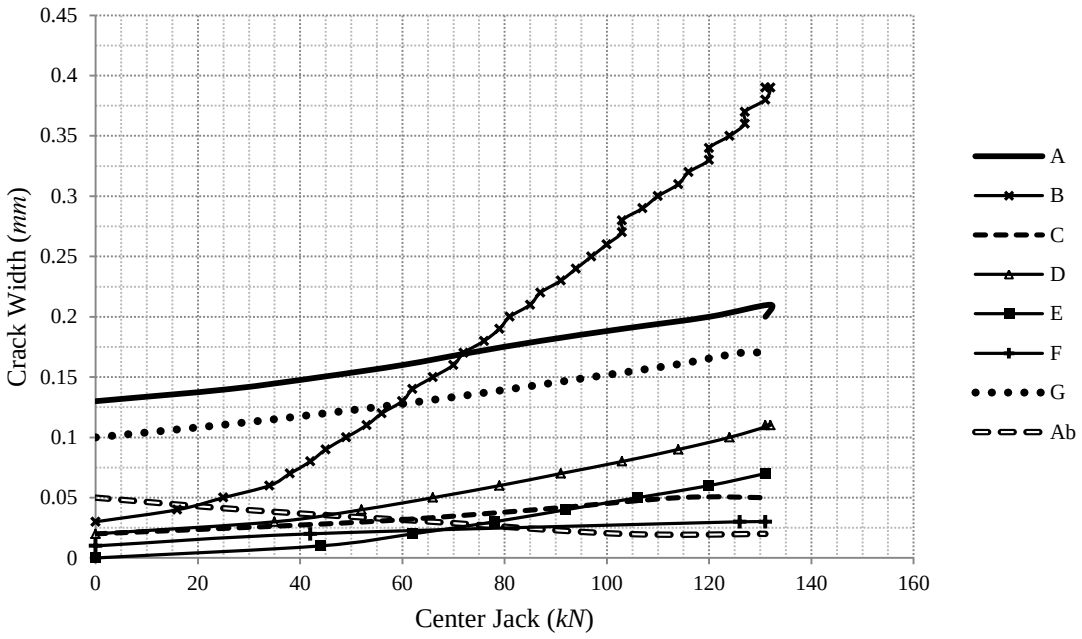
0.45
0.4
0.35
0.3
0.25
0.2
0.15
0.1
0.05
0
Crack Width (mm)
0
20
40
60
80
100
120
140
160
Center Jack (kN)
A
B
C
D
E
F
G
Ab

(d)

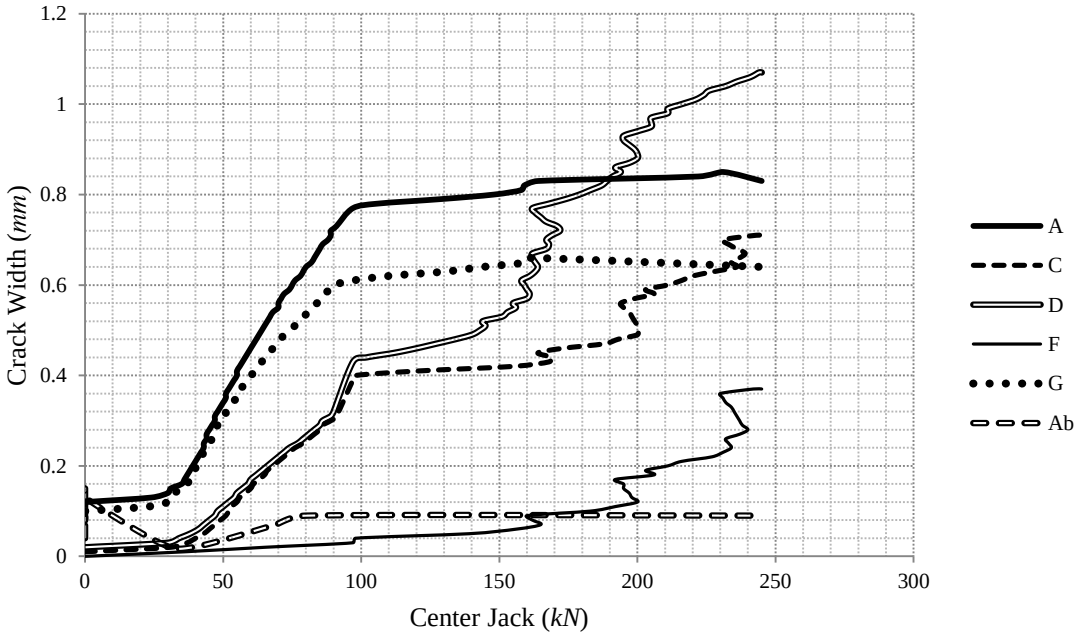
1.2
1
0.8
0.6
0.4
0.2
0
Crack Width (mm)
0
50
100
150
200
250
300
Center Jack (kN)
A
C
D
F
G
Ab

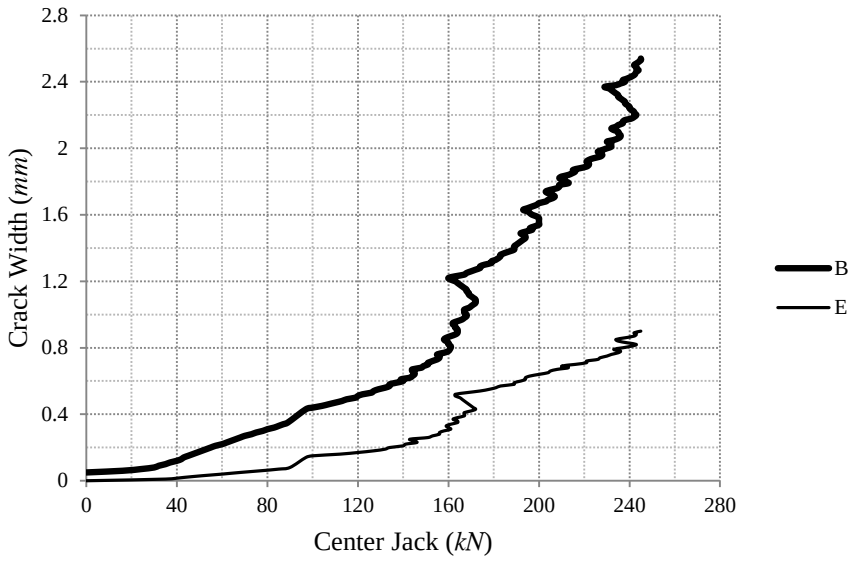
Crack Width (mm)
2.8
2.4
2
1.6
1.2
0.8
0.4
0
0
40
80
120
160
200
240
280
Center Jack (kN)
B
E

(e)

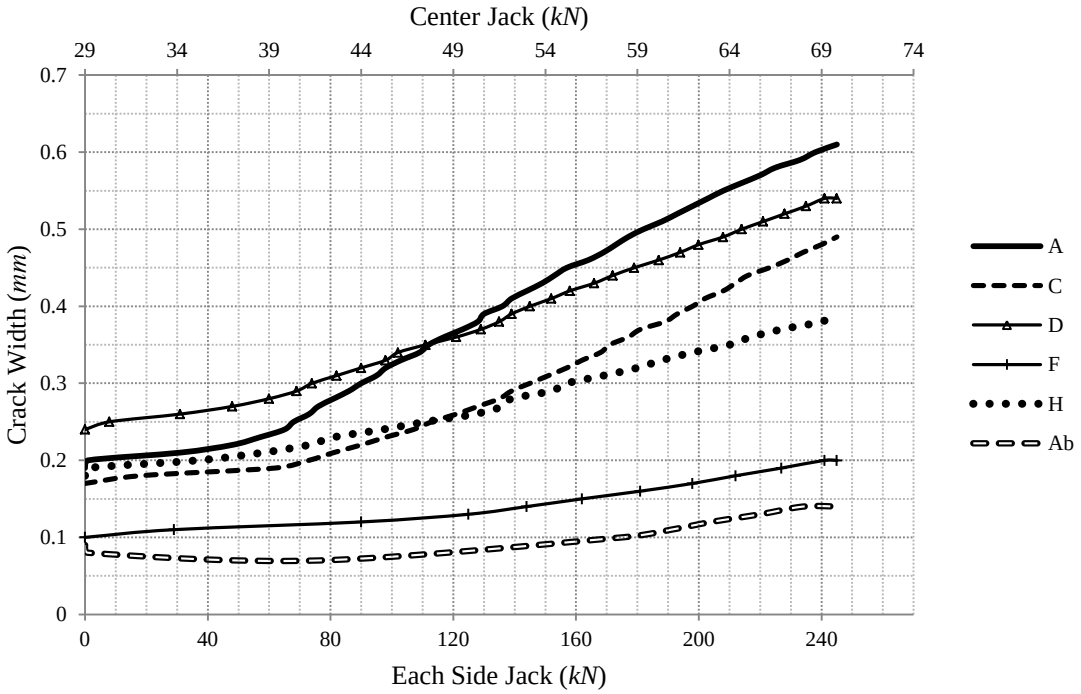
Center Jack (kN)
29
34
39
44
49
54
59
64
69
74
Crack Width (mm)
0.7
0.6
0.5
0.4
0.3
0.2
0.1
0
0
40
80
120
160
200
240
Each Side Jack (kN)
A
C
D
F
H
Ab

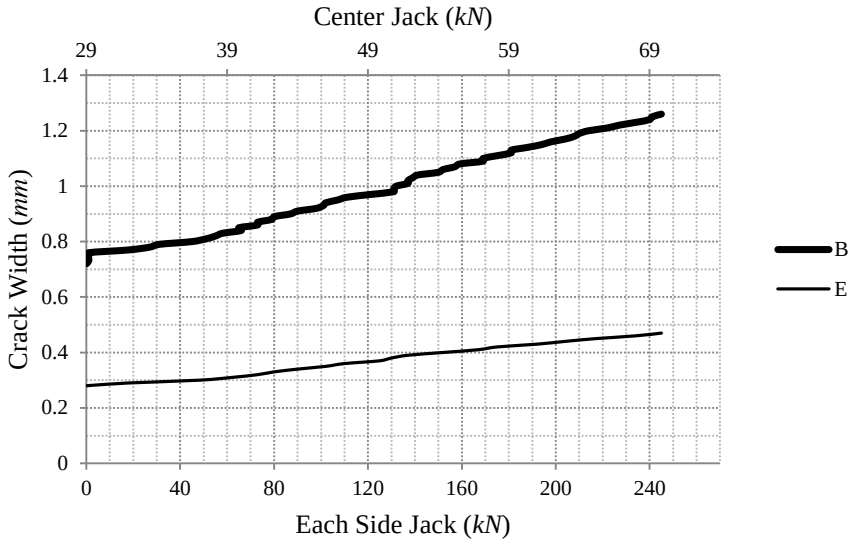

(f)

Fig. A.10 Crack widths in panel B, a) 2nd stage, b) 3rd stage, c) one-way tension, d) one-way bending, e) 4th stage, f) 5th stage

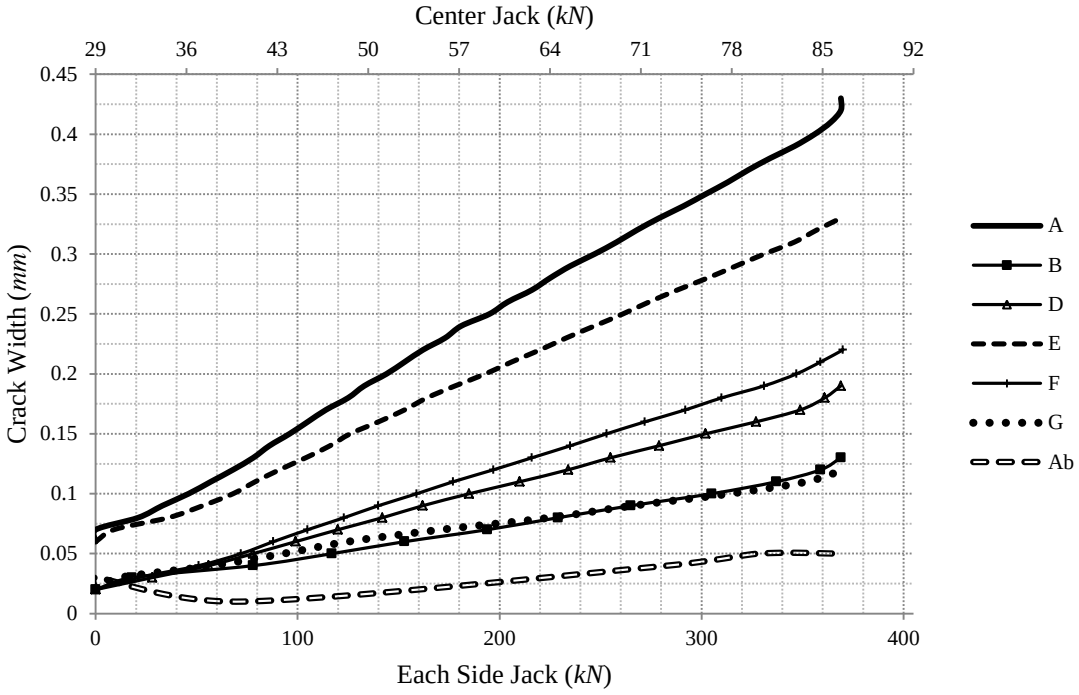

(a)

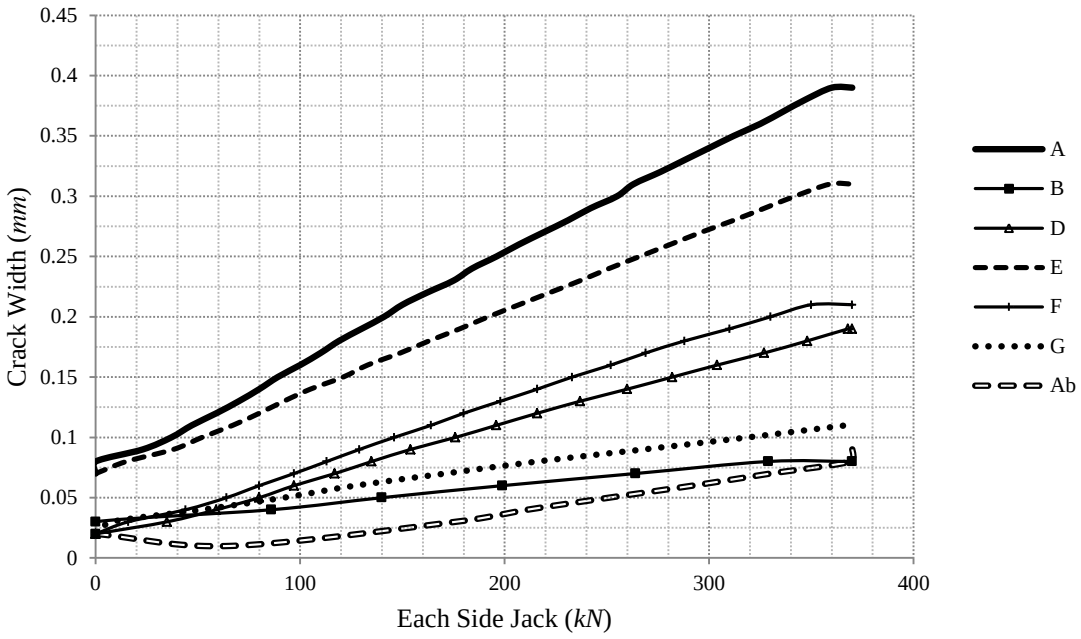
0.45
0.4
0.35
0.3
0.25
0.2
0.15
0.1
0.05
0
Crack Width (mm)
0
100
200
300
400
Each Side Jack (kN)
A
B
D
E
F
G
Ab

(b)

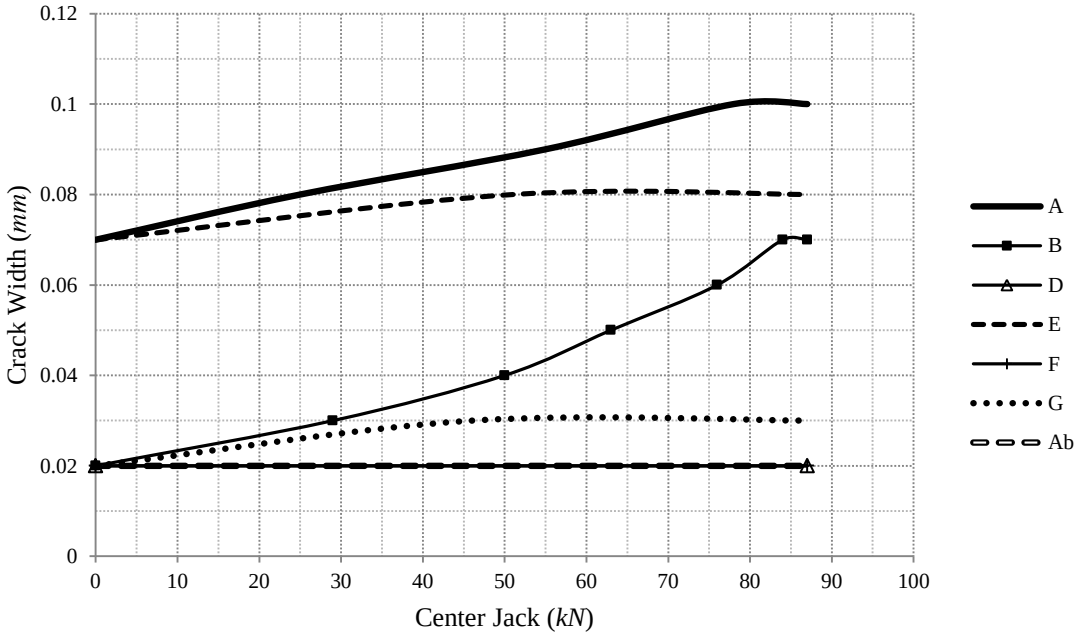
0.12
0.1
0.08
0.06
0.04
0.02
0
Crack Width (mm)
0
10
20
30
40
50
60
70
80
90
100
Center Jack (kN)
A
B
D
E
F
G
Ab

(c)

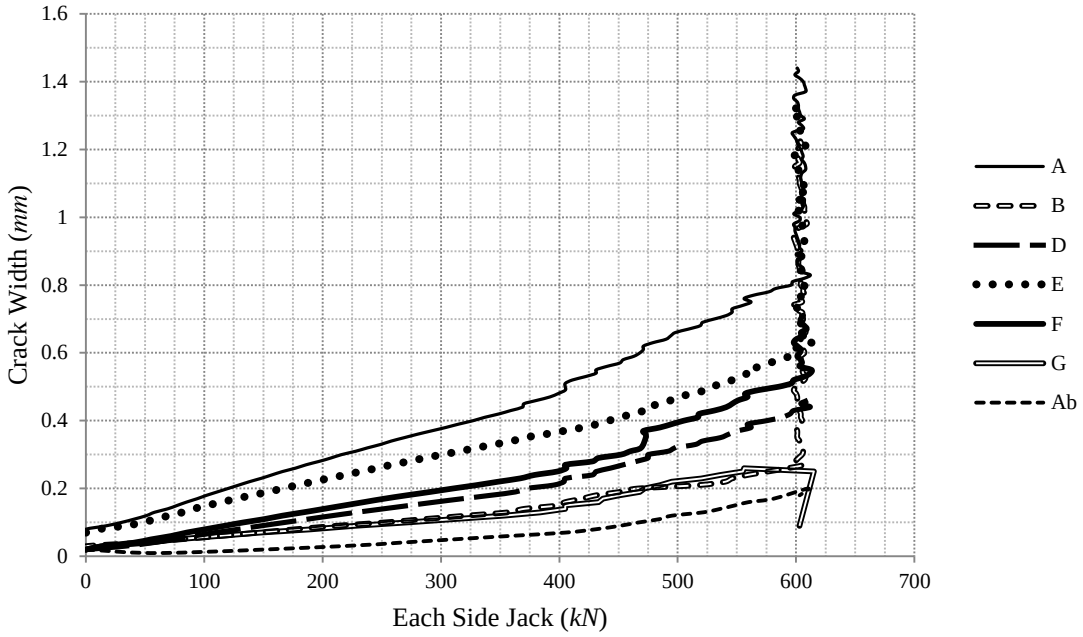
1.6
1.4
1.2
1
0.8
0.6
0.4
0.2
0
Crack Width (mm)
0
100
200
300
400
500
600
700
Each Side Jack (kN)
A
B
D
E
F
G
Ab

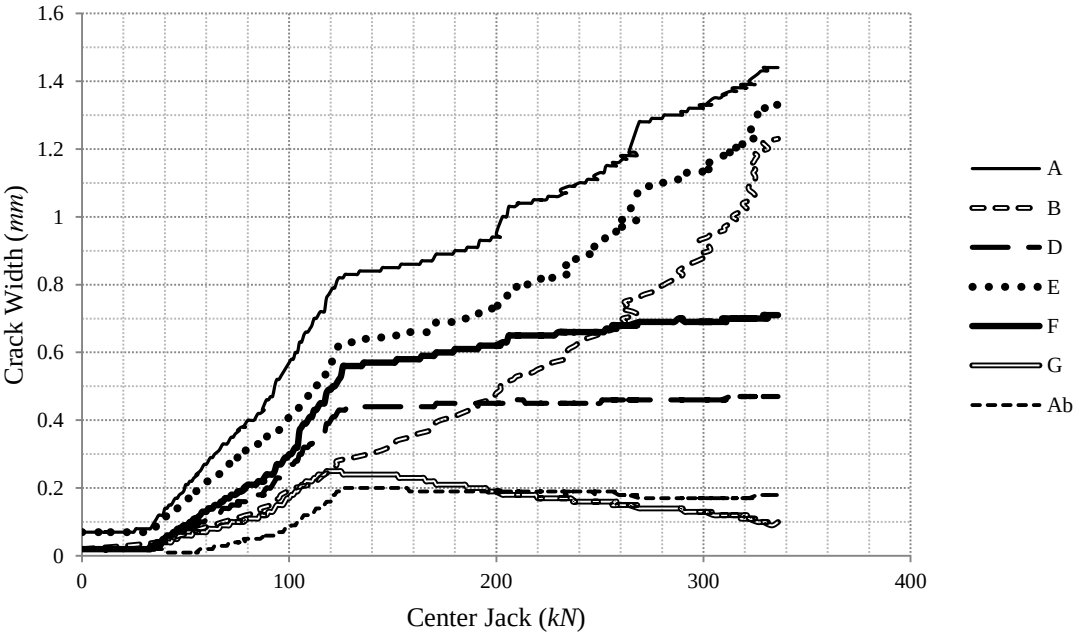
1.6
1.4
1.2
1
0.8
0.6
0.4
0.2
0
Crack Width (mm)
0
100
200
300
400
Center Jack (kN)
A
B
D
E
F
G
Ab

(d)

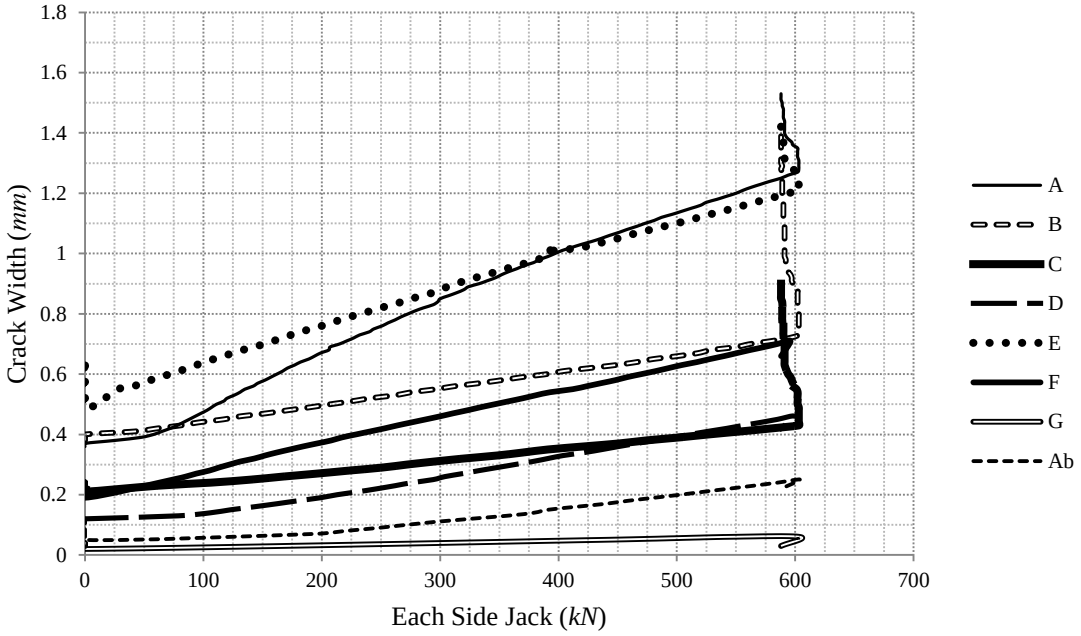

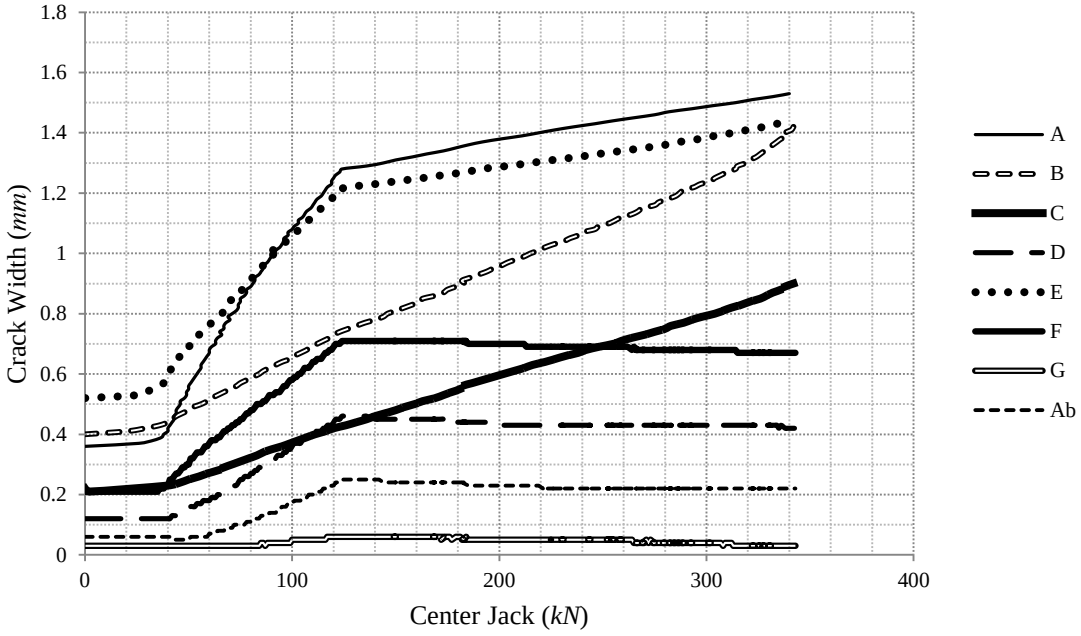

(e)

Fig. A.11 Crack widths in panel C, a) 2nd stage, b) one-way tension, c) one-way bending, d) 3rd stage, e) 4th stage

APPENDIX B

TYPICAL FE INPUT FILES

B.1 Perfect bond model for Kankam test

```
*Heading
** Job name: ... Model name: ...
*Preprint, echo=NO, model=NO, history=NO, contact=NO
**
** PARTS
**
*Part, name=Part-1
*Node
  1,        12.5,          0.
  2,        12.5,          2.
  .
  .
  .
  2193,    10.4,          98.
*Element, type=CAX4R
  1,    1,  113,  234,    2
  2,  113,  114,  235,  234
  .
  .
  .
  2100, 2193,   97,   98,  112
*Nset, nset=_PickedSet7_N, internal
...
*Elset, elset=_PickedSet7_E, internal, generate
...
*Nset, nset=_PickedSet8_N, internal
...
*Elset, elset=_PickedSet8_E, internal
...
*Nset, nset=_PickedSet9_N, internal
...
*Elset, elset=_PickedSet9_E, internal, generate
...
```

```
*Nset, nset=_PickedSet12_N, internal
...
*Elset, elset=_PickedSet12_E, internal, generate
...
*Nset, nset=_PickedSet13_N, internal
...
*Elset, elset=_PickedSet13_E, internal, generate
...
*Elset, elset=_PickedSet12, internal, generate
...
*Elset, elset=_PickedSet13, internal, generate
...
** Section: concrt
*Solid Section, elset=_PickedSet13, controls=EC-1, material=concrete
1.,
** Section: rnfrc
*Solid Section, elset=_PickedSet12, controls=EC-1, material=Steel
1.,
*End Part
**
**
** ASSEMBLY
**
*Assembly, name=Assembly
**
*Instance, name=Part-1-1, part=Part-1
*End Instance
**
*Nset, nset=_PickedSet18, internal, instance=Part-1-1
...
*Nset, nset=_PickedSet23, internal, instance=Part-1-1
...
*Nset, nset=_PickedSet24, internal, instance=Part-1-1
...
*End Assembly
**
** ELEMENT CONTROLS
**
*Section Controls, name=EC-1, second order accuracy=YES
1., 1., 1.
*Amplitude, name=Amp-1, definition=SMOOTH STEP
0., 0., 50., 1.
**
** MATERIALS
**
*Material, name=Steel
```

```
*Density
 0.0078,
*Elastic
181000., 0.3
*Material, name=concrete
*Density
 0.0024,
*Elastic
33000., 0.18
*Concrete Damaged Plasticity
34.,   0.1,  1.16, 0.666,    0.
*Concrete Compression Hardening
20.,       0.
40., 0.000988
*Concrete Tension Stiffening, type=DISPLACEMENT
   3.,   0.
 0.45, 0.02
   0., 0.18
**
** BOUNDARY CONDITIONS
**
** Name: BC-1 Type: Displacement/Rotation
*Boundary
_PickedSet18, 1, 1
** Name: BC-2 Type: Displacement/Rotation
*Boundary
_PickedSet23, 2, 2
** ----------------------------------------------------------------
**
** STEP: Step-1
**
*Step, name=Step-1, nlgeom=NO
*Dynamic, Explicit
, 50.
*Bulk Viscosity
0.06, 1.2
**
** BOUNDARY CONDITIONS
**
** Name: BC-3 Type: Displacement/Rotation
*Boundary, amplitude=Amp-1
_PickedSet24, 2, 2, 0.1
**
** OUTPUT REQUESTS
**
*Restart, write, number interval=1, time marks=NO
```

```
**
** FIELD OUTPUT: F-Output-1
**
*Output, field, number interval=100
*Node Output
A, RF, U, V
*Element Output, directions=YES
E, LE, PE, PEEQ, PEEQT, S
**
** HISTORY OUTPUT: H-Output-1
**
*Output, history, variable=PRESELECT
*End Step
```

B.2 Diagonal link element bond model for Kankam test

```
*Heading
** Job name: ... Model name: ...
*Preprint, echo=NO, model=NO, history=NO, contact=NO
**
** PARTS
**
*Part, name=conc-mesh-1
*Node
     1,        12.5,          0.
     2,        14.5,          0.
     .
     .
     .
     1887,   84.5,         100.
*Element, type=CAX4R
  1,    1,    2,   39,   38
  2,    2,    3,   40,   39
  .
  .
  .
  1800, 1849, 1850, 1887, 1886
*Elset, elset=_PickedSet2, internal, generate
...
** Section: concrt
*Solid Section, elset=_PickedSet2, controls=EC-1, material=concrete
1.,
*End Part
```

```
**
*Part, name=rbr-mesh-1
*Node
      1,           0.,           0.

      2,       0.96,           0.
      .
      .
      .
      1414,        12.5,         100.
*Element, type=CAX4R
  1,    1,    2,   16,   15
  2,    2,    3,   17,   16
  .
  .
  .
  1300, 1399, 1400, 1414, 1413
*Elset, elset=_PickedSet2, internal, generate
...
** Section: rnfrc
*Solid Section, elset=_PickedSet2, controls=EC-1, material=Steel
1.,
*End Part
**
**
** ASSEMBLY
**
*Assembly, name=Assembly
**
*Instance, name=conc-mesh-1-1, part=conc-mesh-1
*End Instance
**
*Instance, name=rbr-mesh-1-1, part=rbr-mesh-1
*End Instance
**
*Element, type=CONN2D2
1, rbr-mesh-1-1.13, conc-mesh-1-1.38
.
.
100, rbr-mesh-1-1.1413, conc-mesh-1-1.1814
*Connector Section, elset=Wire-1-Set-1, behavior=Diagonal
Axial,
*Nset, nset=Wire-1-Set-1, instance=rbr-mesh-1-1, generate
...
*Nset, nset=Wire-1-Set-1, instance=conc-mesh-1-1, generate
...
```

```
*Elset, elset=Wire-1-Set-1, generate
...
*Nset, nset=_PickedSet40, internal, instance=rbr-mesh-1-1, generate
...
*Nset, nset=_PickedSet41, internal, instance=conc-mesh-1-1, generate
...
*Nset, nset=_PickedSet41, internal, instance=rbr-mesh-1-1, generate
...
*Nset, nset=Set-2, instance=rbr-mesh-1-1, generate
...
*End Assembly
*Connector Behavior, name=Diagonal
*Connector Elasticity, nonlinear, component=1
-999999., -0.1
      0.,   0.
**
** ELEMENT CONTROLS
**
*Section Controls, name=EC-1, second order accuracy=YES
1., 1., 1.
*Amplitude, name=Amp-1, definition=SMOOTH STEP
0., 0., 30., 1.
**
** MATERIALS
**
*Material, name=Steel
*Density
 0.0078,
*Elastic
181000., 0.3
*Material, name=concrete
*Density
 0.0024,
*Elastic
33000., 0.18
*Concrete Damaged Plasticity
34.,   0.1,  1.16, 0.666,    0.
*Concrete Compression Hardening
20.,     0.
40., 0.000988
*Concrete Tension Stiffening, type=DISPLACEMENT
   3.,   0.
 0.45, 0.02
   0., 0.18
**
** BOUNDARY CONDITIONS
```

```
**
** Name: BC-1 Type: Displacement/Rotation
*Boundary
_PickedSet40, 1, 1
** Name: BC-2 Type: Displacement/Rotation
*Boundary
_PickedSet41, 2, 2
** ----------------------------------------------------------------
**
** STEP: Step-1
**
*Step, name=Step-1, nlgeom=NO
*Dynamic, Explicit
, 30.
*Bulk Viscosity
0.06, 1.2
**
** BOUNDARY CONDITIONS
**
** Name: BC-3 Type: Displacement/Rotation
*Boundary, amplitude=Amp-1
Set-2, 2, 2, 0.1
**
** OUTPUT REQUESTS
**
*Restart, write, number interval=1, time marks=NO
**
** FIELD OUTPUT: F-Output-1
**
*Output, field, number interval=100
*Node Output
A, RF, U, V
*Element Output, directions=YES
E, LE, PE, PEEQ, PEEQT, S
**
** HISTORY OUTPUT: H-Output-2
**
*Output, history, time interval=0.3
*Element Output, elset=Wire-1-Set-1
CTF1, CU1
**
** HISTORY OUTPUT: H-Output-1
**
*Output, history, variable=PRESELECT
*End Step
```

B.3 Bond layer model for Kankam test

```
*Heading
** Job name: ... Model name: ...
*Preprint, echo=NO, model=NO, history=NO, contact=NO
**
** PARTS
**
*Part, name=Part-1
*Node
      1,        12.5,          0.
      2,        12.5,          2.
      .
      .
      .
     2193,    10.416667,         98.
*Element, type=CAX4R
  1,    1,  113,  234,    2
  2,  113,  114,  235,  234
  .
  .
  .
  2100, 2193,   97,   98,  112
*Nset, nset=_PickedSet7_N, internal
...
*Elset, elset=_PickedSet7_E, internal, generate
...
*Nset, nset=_PickedSet8_N, internal
...
*Elset, elset=_PickedSet8_E, internal
...
*Nset, nset=_PickedSet9_N, internal
...
*Elset, elset=_PickedSet9_E, internal, generate
...
*Nset, nset=_PickedSet12_N, internal
...
*Elset, elset=_PickedSet12_E, internal, generate
...
*Nset, nset=_PickedSet13_N, internal
...
*Elset, elset=_PickedSet13_E, internal, generate
...
*Elset, elset=_PickedSet12, internal, generate
...
*Elset, elset=_PickedSet14, internal
```

```
...
*Elset, elset=_PickedSet15, internal, generate
...
** Section: bond
*Solid Section, elset=_PickedSet15, controls=EC-1, material="bond layer"
1.,
** Section: concrt
*Solid Section, elset=_PickedSet14, controls=EC-1, material=concrete
1.,
** Section: rnfrc
*Solid Section, elset=_PickedSet12, controls=EC-1, material=Steel
1.,
*End Part
**
**
** ASSEMBLY
**
*Assembly, name=Assembly
**
*Instance, name=Part-1-1, part=Part-1
*End Instance
**
*Nset, nset=_PickedSet18, internal, instance=Part-1-1
...
*Nset, nset=_PickedSet23, internal, instance=Part-1-1
...
*Nset, nset=_PickedSet24, internal, instance=Part-1-1
...
*End Assembly
**
** ELEMENT CONTROLS
**
*Section Controls, name=EC-1, second order accuracy=YES
1., 1., 1.
*Amplitude, name=Amp-1, definition=SMOOTH STEP
0., 0., 30., 0.95
**
** MATERIALS
**
*Material, name=Steel
*Density
 0.0078,
*Elastic
181000., 0.3
*Material, name="bond layer"
*Density
```

```
 0.0024,
*Elastic
33000., 0.18
*Concrete Damaged Plasticity
34.,   0.1,  1.16, 0.666,    0.
*Concrete Compression Hardening
20.,       0.
40., 0.000988
*Concrete Tension Stiffening, type=DISPLACEMENT
  0.02,   0.
 0.009, 0.05
    0.,  0.1
*Material, name=concrete
*Density
 0.0024,
*Elastic
33000., 0.18
*Concrete Damaged Plasticity
34.,   0.1,  1.16, 0.666,    0.
*Concrete Compression Hardening
20.,       0.
40., 0.000988
*Concrete Tension Stiffening, type=DISPLACEMENT
   3.,   0.
 0.45, 0.02
   0., 0.18
**
** BOUNDARY CONDITIONS
**
** Name: BC-1 Type: Displacement/Rotation
*Boundary
_PickedSet18, 1, 1
** Name: BC-2 Type: Displacement/Rotation
*Boundary
_PickedSet23, 2, 2
** ----------------------------------------------------------------
**
** STEP: Step-1
**
*Step, name=Step-1, nlgeom=NO
*Dynamic, Explicit
, 30.
*Bulk Viscosity
0.06, 1.2
**
** BOUNDARY CONDITIONS
```

```
**
** Name: BC-3 Type: Displacement/Rotation
*Boundary, amplitude=Amp-1
_PickedSet24, 2, 2, 0.1
**
** OUTPUT REQUESTS
**
*Restart, write, number interval=1, time marks=NO
**
** FIELD OUTPUT: F-Output-1
**
*Output, field, number interval=100
*Node Output
A, RF, U, V
*Element Output, directions=YES
E, LE, PE, PEEQ, PEEQT, S
**
** HISTORY OUTPUT: H-Output-1
**
*Output, history, variable=PRESELECT
*End Step
```

B.4 Internally restrained shrinkage model

```
*Heading
** Job name: ... Model name: ...
*Preprint, echo=NO, model=NO, history=NO, contact=NO
**
** PARTS
**
*Part, name=Part-1
*Node
      1,          10.,           0.
      2,          10.,          10.
                  .
                  .
                  .
   2007,          50.,        1990.
*Element, type=CAX4R
  1,    1,  403,  618,    2
  2,  403,  405,  619,  618
  .
  .
```

```
  .
  1800,  47,   2,   3,  48
*Elset, elset=_PickedSet5, internal, generate
...
*Elset, elset=_PickedSet6, internal
...
** Section: concrt
*Solid Section, elset=_PickedSet6, controls=EC-1, material=concrete
1.,
** Section: rnfrc
*Solid Section, elset=_PickedSet5, controls=EC-1, material=Steel
1.,
*End Part
**
**
** ASSEMBLY
**
*Assembly, name=Assembly
**
*Instance, name=Part-1-1, part=Part-1
*End Instance
**
*Nset, nset=_PickedSet58, internal, instance=Part-1-1
...
*End Assembly
**
** ELEMENT CONTROLS
**
*Section Controls, name=EC-1, second order accuracy=YES
1., 1., 1.
*Amplitude, name=Amp-1, definition=SMOOTH STEP
0., 0., 200., 1.
**
** MATERIALS
**
*Material, name=Bond
*Density
 0.0023,
*Elastic
34000., 0.18
*Expansion
 1e-05,
*Concrete Damaged Plasticity
34.,   0.1,  1.16, 0.666,    0.
*Concrete Compression Hardening
  15.,       0.
```

```
 41.9, 0.000968
*Concrete Tension Stiffening, type=DISPLACEMENT
   0.02,   0.
 0.009, 0.05
    0.,  0.1
*Material, name=Steel
*Density
 0.0078,
*Elastic
200000., 0.3
*Expansion
0.,
*Material, name=concrete
*Density
 0.0023,
*Elastic
34000., 0.18
*Expansion
 1e-05,
*Concrete Damaged Plasticity
34.,   0.1,  1.16, 0.666,    0.
*Concrete Compression Hardening
  15.,       0.
 41.9, 0.000968
*Concrete Tension Stiffening, type=DISPLACEMENT
 2.97,   0.
 0.45, 0.02
   0., 0.15
**
** BOUNDARY CONDITIONS
**
** Name: BC-1 Type: Displacement/Rotation
*Boundary
_PickedSet58, 1, 1
** Name: BC-2 Type: Displacement/Rotation
*Boundary
_PickedSet59, 2, 2
**
** PREDEFINED FIELDS
**
** Name: Predefined Field-1   Type: Temperature
*Initial Conditions, type=TEMPERATURE
_PickedSet60, 0.
** ----------------------------------------------------------------
**
** STEP: Step-1
```

```
**
*Step, name=Step-1, nlgeom=NO
*Dynamic, Explicit
, 200.
*Bulk Viscosity
0.06, 1.2
**
** PREDEFINED FIELDS
**
** Name: Predefined Field-1   Type: Temperature
*Temperature, amplitude=Amp-1
_PickedSet60, -5.
**
** OUTPUT REQUESTS
**
*Restart, write, number interval=1, time marks=NO
**
** FIELD OUTPUT: F-Output-1
**
*Output, field, number interval=100
*Node Output
A, RF, U, V
*Element Output, directions=YES
E, LE, PE, PEEQ, PEEQT, S
**
** HISTORY OUTPUT: H-Output-1
**
*Output, history, variable=PRESELECT
*End Step
```

REFERENCES

ACI Committee 209, 1992, "Prediction of Creep, Shrinkage and Temperature Effects in Concrete Structures", (ACI 209R-92), American Concrete Institute, Farmington Hills, Mich.

ACI Committee 318, 1995, "Building Code Requirements for Structural Concrete (ACI 318-95) and Commentary (ACI 318R-95)," American Concrete Institute, Farmington Hills, Mich.

ACI Committee 318, 1999, "Building Code Requirements for Structural Concrete (ACI 318-99) and Commentary (ACI 318R-99)," American Concrete Institute, Farmington Hills, Mich.

ACI Committee 350, 2001, "Code Requirements for Environmental Engineering Concrete Structures and Commentary," American Concrete Institute, Farmington Hills, Mich.

ACI Committee 350, 2006, "Code Requirements for Environmental Engineering Concrete Structures and Commentary," American Concrete Institute, Farmington Hills, Mich.

ASTM C39/C39M, 2005, "Standard Test Method for Compressive Strength of Cylindrical Concrete Specimens," Annual Book of ASTM Standards, Philadelphia.

ASTM C496/C496M, 2004, "Standard Test Method for Splitting Tensile Strength of Cylindrical Concrete Specimens," Annual Book of ASTM Standards, Philadelphia.

ASTM C78, 2008, "Standard Test Method for Flexural Strength of Concrete (Using Simple Beam with Third-Point Loading," Annual Book of ASTM Standards, Philadelphia.

Bažant, Z. P., 1979, "Material Behavior under Various Types of Loading," Annual Symposium-Society of Flight Test Engineers, Proceedings of Workshop on High Strength Concrete, National Science Foundation, Washington, D.C., pp. 79-92.

Bazant, Z.P., and Oh, B.H., 1983a, "Spacing of Cracks in Reinforced Concrete," Journal of Structural Engineering, American Society of Civil Engineers, Vol. 109, No. 9, pp 2066-2085.

Bažant, Z. P., and Oh, B. H., 1983b, "Crack Band Theory for Fracture of Concrete," Materials and Structures, RILEM, V. 16, No. 93, pp. 155-177.

Beeby, A.W., 1970, "An Investigation of Cracking in Slabs Spanning One Way", Cement and Concrete Association, Technical Report 42.433, London.

Beeby, A.W., 1971, "Prediction and Control of Flexural Cracking in Reinforced concrete Members," Cracking, Deflection and Ultimate Load of Concrete Slab Systems, SP-20, American Concrete Institute, Farmington Hills, Mich., pp. 55-75.

Beeby, A.W., 1971, "An Investigation of Cracking on the Side Faces of Beams," Cement and Concrete Association, Technical Report 42.466, London.

British Standards Institution, 1987, "BS 8007: Design of Concrete Structures for Retaining Aqueous Liquids," London: British Standards Institution.

Broms, B.B., 1965, "Crack Width and Crack Spacing in Reinforced Concrete Members," ACI Journal, Proceedings, Vol. 62, No. 10, pp. 1237-1255.

CEB-FIP Model Code, 1990, "Model Code for Concrete Structures," Comite Euro-International due Beton/Federation Internationale de la Precontrainte, Paris 1990.

Cho, J., Kim, N., Cho, N., and Choi, I., 2004, "Cracking Behavior of Reinforced Concrete Panel Subjected to Biaxial Tension", ACI Structural Journal, Vol. 101, No. 1, pp. 76-84.

CSA Standard A23.3-04, 2004, "Design of Concrete Structures," Canadian Standard Association, Rexdale, Canada.

Dawood, N., and Marzouk, H, 2010, "An Analytical Model for Crack Spacing of Thick Reinforced Concrete Plates," Engineering Structures, Vol. 32, No. 2, pp. 472-482.

Desayi, P., and Kulkarni, A. B., 1976, “Determination of Maximum Crack Width in Two-Way Reinforced Concrete Slabs,” Proceedings of the Institution of Civil Engineers (London), Vol. 61, No. pt 2, pp. 343-349.

Frosch, R.J., 1999, "Another Look at Cracking and Crack Control in Reinforced Concrete," ACI Structural Journal, Vol. 96, No. 3, pp. 437–442.

Gergely, P., and Lutz, L. A., 1968, “Maximum Crack Width in Reinforced Concrete Flexural Members,” Causes, Mechanism, and Control of Cracking in Concrete, SP-20, American Concrete Institute, Farmington Hills, Mich., pp. 87–117.

Gilbert, R.I., 2005, “Time-Dependent Cracking and Crack Control in Reinforced Concrete Structures,” Serviceability of Concrete, SP-225, American Concrete Institute, Farmington Hills, Mich., pp. 223–240.

Goto, Y., and Otsuka, K., 1979, “Experimental Studies on Cracks Formed in Concrete around Deformed Tension Bars,” Technology Reports, Tohoko University, Vol. 44, No. 1, pp. 49-83.

de Groot, A.K., Kusters, G.M.A., and Monnier, Th., 1981, "Numerical Modeling of Bond-Slip Behavior", Heron, Vol. 26, No. 1B, p. 90.

Hibbitt, H.D., Karlson, B.I., and Sorenson, E.P., 2007, “ABAQUS version 6.7, Finite Element Program”, Dassault Systèmes Simulia Corp., Providence, R.I.

Hillerborg, A., Modeer, M, and Petersson, P. E., 1976, “Analysis of Crack Formation and Crack Growth by Means of Fracture Mechanics and Finite Elements,” Cement and Concrete Research, V. 6, pp. 773-782.

Kankam, C. K., 1997, “Relationship of Bond Stress, Steel Stress, and Slip in Reinforced Concrete,” Journal of Structural Engineering, ASCE, Vol. 123, No. 1, pp. 79-85.

Kianoush, M. R., Acarcan, M., and Ziari, A., 2008, "Behavior of Base Restrained Reinforced Concrete Walls under Volumetric Change," Engineering Structures, Vol. 30, No. 6, pp. 1526-1534.

Lee, J., and Fenves, G. L., 1998, "Plastic-Damage Model for Cyclic Loading of Concrete Structures," Journal of Engineering Mechanics, Vol. 124, No.8, pp. 892–900.

Lubliner, J., Oliver, J., Oller, S., and Onate, E., 1989, "A Plastic-Damage Model for Concrete," International Journal of Solids and Structures, Vol. 25, No. 3, pp. 299–326.

MacGregor, J. G., Simmonds, S. H., and Rizkalla, S. H., 1980a, "Test of a Prestressed Concrete Secondary Containment Structure," Structural Engineering Report No. 85, Department of Civil Engineering, University of Alberta.

MacGregor, J. G., Rizkalla, S. H., and Simmonds, S. H., 1980b "Cracking of Reinforced and Prestressed Concrete Wall Segments," Structural Engineering Report No. 82, Department of Civil Engineering, University of Alberta.

Marti, P., Alvarez, M., Kaufmann, W., and Sigrist, V., 1998, "Tension Chord Model for Structural Concrete," Structural Engineering International, Vol. 8, No. 4, pp. 287-298.

Nawy, E. G., and Blair, K. W., 1971, "Further Studies on Flexural Crack Control in Structural Slab Systems," Cracking, Deflection, and Ultimate Load of Concrete Slab systems, SP-30, American Concrete Institute, Farmington Hills, Mich, pp. 1-41.

Nawy, E. G., 1972, "Crack Control through Reinforcement Distribution in Two-Way Acting Slabs and Plates," ACI Journal, Proceedings, Vol. 69, No. 4, pp. 217-219.

NZS 3106, 1986, "Code of Practice for Concrete Structures for the Storage of Liquids," Standards Association of New Zealand, Wellington.

Ngo, D., Scordelis, A. C., 1967, “Finite Element Analysis of Reinforced Concrete Beams,” ACI Journal, Proceedings, Vol. 64, No. 3, pp. 152-163.

Lutz, A. L., and Gergely, P., 1967, “Mechanics of Bond and Slip of Deformed Bars in Concrete,” ACI Journal, Proceedings, Vol. 64, No. 11, pp. 711-721.

Rizk, E., and Marzouk, H., 2010, “A New Formula to Calculate Crack Spacing for Concrete Plates,” ACI Structural Journal, Vol. 107, No. 1, pp. 43-52.

Rizkalla, S. H., Simmonds, S. H., and, MacGregor, J. G., 1979, “Leakage Tests of Wall Segments of Reactor Containments,” Structural Engineering Report No. 80, Department of Civil Engineering, University of Alberta.

Simmonds, S. H., Rizkalla, S. H., and MacGregor, J. G., 1979, “Tests of Wall Segments From Reactor Containments Volume 1,” Structural Engineering Report No. 81, Department of Civil Engineering, University of Alberta.

Tammo, K., and Thelandersson, S., 2009, “Crack Behavior near Reinforcing Bars in Concrete Structures,” ACI Structural Journal, Vol. 106, No. 3, pp. 259-267.

Ziari, A, and Kianoush, M. R., 2009a, “Investigation of Flexural Cracking and Leakage in RC Liquid Containing Structures,” Engineering Structures, Vol. 31, No. 5, pp. 1056-1067.

Ziari, A, and Kianoush, M. R., 2009b, “Investigation of Direct Tension Cracking and Leakage in RC Elements,” Engineering Structures, Vol. 31, No. 2, pp. 466-474.